Inhibiting platelet scramblase activity

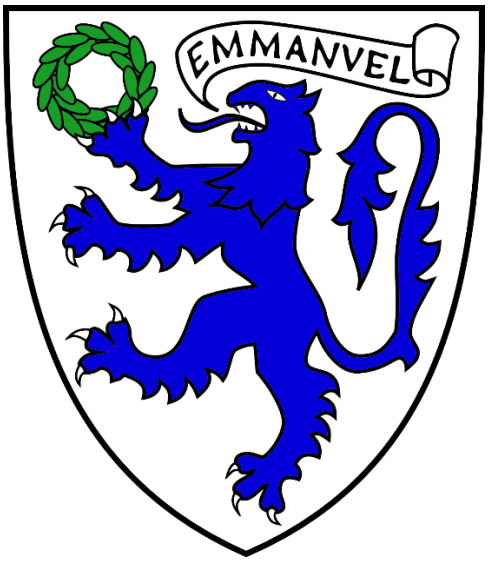

Sarah Louise Millington-Burgess

Emmanuel College

August 2020

This thesis is submitted for the degree of

Doctor of Philosophy

Supervisor: Dr Matthew Harper

Department of Pharmacology

University of Cambridge

Declaration

This thesis is the result of my own work and includes nothing which is the outcome of work done in collaboration except as declared in the Preface and specified in the text. It is not substantially the same as any that I have submitted, or, is being concurrently submitted for a degree or diploma or other qualification at the University of Cambridge or any other University or similar institution except as declared in the Preface and specified in the text. I further state that no substantial part of my thesis has already been submitted, or, is being concurrently submitted for any such degree, diploma or other qualification at the University of Cambridge or any other University or similar institution except as declared in the Preface and specified in the text. It does not exceed the prescribed word limit for the relevant Degree Committee.

Abstract - Inhibiting platelet scramblase activity

Sarah Louise Millington-Burgess

In both thrombosis and haemostasis, two distinct populations of activated platelets form, pro-aggregatory and pro-coagulant platelets. Pro-aggregatory platelets have active integrins and aggregate together via fibrinogen to form the haemostatic plug which prevents bleeding. Pro-coagulant platelets expose phosphatidylserine (PS) which acts as a surface for binding of the tenase (FIXa/VIIIa) and prothrombinase (FXa/Va) complexes that generate a burst of thrombin production responsible for occlusive clot formation. All current anti-platelet drugs are associated with bleeding side effects since they inhibit pro-aggregatory platelet activity. No drug exists which selectively targets the pro-coagulant platelet population, though this could be an alternative anti-thrombotic approach associated with fewer bleeding side effects if pro-aggregatory activity remains. In order to test such an approach, a selective inhibitor of pro-coagulant platelet activity must be developed. Critical to platelet PS exposure is activity of the main platelet scramblase, TMEM16F. This thesis aimed to develop inhibitors of TMEM16F and platelet scramblase activity.

R5421 was the only previously described inhibitor of platelet scramblase activity. R5421, however, is shown to be a non-selective inhibitor of platelet scramblase activity, also affecting platelet pro-aggregatory activity by inhibiting $\alpha_{IIb}\beta_3$ integrin activation, α-granule release and cytosolic Ca^{2+} signalling in response to a range of agonists. Ligand-based *in silico* methods were applied to identify new inhibitors of platelet scramblase activity. The pesticide thiodicarb was identified as a novel inhibitor of platelet scramblase activity but also acts non-selectively. Since R5421 has wide ranging off-target effects and attempts to improve its selectivity were unsuccessful, other lead compounds were pursued.

The polyphenolic compounds tannic acid and epigallocatechin gallate (EGCG') inhibit TMEM16F activity when over-expressed in cell lines. Both tannic acid and EGCG' are shown to inhibit platelet scramblase activity. An empirical screen of polyphenolic compounds defined an emerging pharmacophore for inhibition of platelet scramblase activity. All catechin gallate compounds inhibited platelet scramblase activity non-selectively. Structure-based *in silico* methods were applied to identify new inhibitors of platelet scramblase activity, first using the fungal nhTMEM16 structure and later the mTMEM16F structure. These screens identified novel inhibitors of platelet scramblase activity which do not affect platelet $\alpha_{IIb}\beta_3$ integrin activation, α-granule release or cytosolic Ca^{2+} signalling. Further work is required to confirm whether these compounds act directly on TMEM16F or inhibit platelet scramblase activity through a different mechanism.

Table of Contents

List of Figures

Chapter 1: Introduction

Chapter 3 - R5421 is not a selective inhibitor of platelet phospholipid scramblase activity

Chapter 4 - An empirical screen of polyphenolic compounds for effects on platelet scramblase activity

Chapter 5 - A structure-based screen using an nhTMEM16 structure

Chapter 6 - A structure-based screen using an mTMEM16F structure

List of abbreviations

ACD	Acid citrate dextrose
ADP	Adenosine 5′-diphosphate
ATP	Adenosine triphosphate
AUC	Area under curve
AV	Annexin V
C	Catechin
CaCC	Ca^{2+} activated Cl^- channel
cAMP	Cyclic adenosine monophosphate
CG’	Catechin gallate
cGMP	Cyclic guanosine monophosphate
COX 1	Cyclooxygenase 1
CRP-XL	Cross-linked collagen-related peptide
DA	Digallic acid
DMSO	Dimethylsulfoxide
EC	Epicatechin
ECG’	Epicatechin gallate
EGC	Epigallocatechin
EGCG’	Epigallocatechin gallate
EM	Electron microscopy
ER	Endoplasmic reticulum
FSC	Forward scatter
GC	Gallocatechin
GCG’	Gallocatechin gallate
GPCR	G-protein-coupled receptor
HBS	HEPES-buffered saline

IP	Prostacyclin receptor
ITAM	Immunoreceptor tyrosine-based activation motif
KO	Knock-out
MCU	Mitochondrial calcium uniporter
MD	Molecular dynamics
MFI	Median fluorescence intensity
mPTP	Mitochondrial permeability transition pore
NEM	N-ethylmaleimide
NO	Nitric oxide
PAR1	Protease-activated receptor 1
PAR1-AP	PAR1-activating peptide (AP) (SFLLRN-amide)
PAR4	Protease-activated receptor 4
PAR4-AP	PAR4-activating peptide (AP) (AYPGKF-amide)
PE	Phosphatidylethanolamine
PFA	Paraformaldehyde
PGE_1	Prostaglandin E_1
PGI_2	Prostacyclin
PI3-K	Phosphoinositide 3-kinase
PIP_3	Phosphoinositide-3,4,5-trisphosphate
PKC	Protein kinase C
PLC	Phospholipase C
PRP	Platelet rich plasma
PS	Phosphatidylserine
RA	Rosmarinic acid
RBC	Red blood cell
RLU	Relative luminescence units

RT	Ambient/room temperature
SB	Silybinin
SEM	Standard error of the mean
SOCE	Store operated Ca^{2+} entry
TA	Tannic acid
TK	Tyrosine kinase
TM	Transmembrane
U	Unstimulated
vWF	von Willebrand factor

Publications

S. L. Millington-Burgess, M. T. Harper
Gene of the issue: ANO6 and Scott Syndrome
Platelets (2019)
https://doi.org/10.1080/09537104.2019.1693039

S. L. Millington-Burgess, A. M. Bonna, T. Rahman, M. T. Harper
R5421 is not a selective inhibitor of platelet phospholipid scramblase activity
British Journal of Pharmacology (2020)
https://doi.org/10.1111/bph.15152

Acknowledgement

First and foremost, I would like to thank Dr Matthew Harper for being an inspiring and supportive supervisor. I would also like to thank all of those in the Harper Lab who have helped me with my work and made this PhD enjoyable. My thanks go to Jessica Berry, Luc Francis, Roxanna Hajbabaie, Ivelin Ivanov, Dora Lopresto, Rebecca Riddle and Hao Wei. Thanks must also go to other members of the Department of Pharmacology for their support, especially Dr Taufiq Rahman for his help with *in silico* work, and all of our blood donors without whom this work would not have been possible. I would also like to thank Dr Andrew Murray for his continued mentorship and encouragement throughout my PhD which has proved invaluable. Thanks also to the British Heart Foundation for their generous funding.

Many of the challenges faced during my PhD have not been scientific and so I would like to thank everyone who has supported me through challenging times to have truly come out the other side stronger and more resilient. I could never thank the medical professionals who have treated me enough but there is no doubt that this thesis would not have been possible without their help. The greatest thanks must go to Professor Franklin Joseph who has never given up on ensuring I have the best quality of life possible since the very start of my studies. Thanks also to other staff at the Countess of Chester Hospital who have helped me along the way; Karen Perkins, Dr Jason Causer and Dr Ravi Jayaram. My eternal gratitude must also go to Dr Natalia Zarate-Lopez and Dr Saul Berkovitz at UCLH whose skill and care have also allowed me to continue doing what I enjoy. I hope that throughout my career I will be able to have as great a positive impact on my future peers and students as everyone who has supported me so far and I hope that I can put into action my drive to improve the academic environment for scientists with long term health problems.

I could also not have completed this thesis without the love and support of my family and friends. Thank you so much to my parents, my brother and my grandparents for your unconditional love throughout everything I do, not just during this PhD. Thank you to all of my friends who have helped me through my PhD with hugs, coffee, cake, advice and sometimes gin. My second family at Emmanuel College will always be one of the greatest things to have come out of my time as a PhD student. And lastly, thank you to my best friend and rock, my greatest support and love, Tom. You have been through every day of this PhD alongside me and I could not have done any of it without you. Thank you for always being there for me, whatever what. Your coding skills are much appreciated too.

And so, I would like to dedicate this thesis with thanks to Professor Joseph and in loving memory of Grandma Felicity and Grandad Fred who I know are looking down on me, incredibly proud.

Chapter 1 – Introduction

1.1 Cardiovascular disease is the world's biggest killer

In 2016 the World Health Organisation estimated that 31% of global deaths (17.9 million) resulted from cardiovascular disease. 85% of these deaths were due to heart attacks and strokes (WHO, 2019). Improving treatments to reduce cardiovascular morbidity and mortality is therefore of paramount importance.

The formation of blood clots, and their consequences, are critical to the pathology of heart attacks and stroke (Steinhubl and Moliterno, 2005). When a clot, known as a thrombus, forms within a blood vessel the flow through that vessel may become reduced or completely occluded. This reduces supply of both oxygen and respiratory substrates to downstream tissue causing ischaemia and irreversible cell damage or death, as occurs during heart attacks and strokes. Preventing the formation of these blood clots (thrombosis) is essential in order to reduce the global burden of cardiovascular disease.

1.2 Platelets are central to thrombosis

Platelets are blood cells with a central role in thrombosis (Libby, 2013). The main physiological roles of platelets occur during haemostasis when they prevent blood loss at the sites of vascular injury (Broos et al., 2011). Following exposure to sub-endothelial collagens, platelets become activated and adhere to the site of injury. Two subpopulations of activated platelets form, pro-aggregatory platelets and pro-coagulant platelets. Pro-aggregatory platelets will aggregate, as their name suggests, to form the primary haemostatic plug which seals the cut. Pro-coagulant platelets interact with circulating coagulation factors to form a clot and prevent further blood loss in secondary haemostasis (Versteeg et al., 2013). The clot is stabilised via fibrin cross-linking by Factor XIII (Muszbek et al., 2011), the clot retracts (Durrant et al., 2017) and the endothelium is repaired. Eventually the clot will be broken down by fibrinolysis (Chapin and Hajjar, 2015). Similar processes of platelet activation, adhesion and aggregation are involved in thrombosis, but the stimulus for activation is not injury to a healthy blood vessel but rupture of an atherosclerotic plaque or other pathological damage to endothelial cells (Lippi et al., 2011).

A healthy endothelium produces a range of anti-platelet factors including prostacyclin (PGI_2), nitric oxide (NO) and ectonucleotidases (Vane et al., 1990). PGI_2 binds the platelet membrane bound $G\alpha_s$ coupled prostacyclin receptor, IP, and raises intracellular cyclic adenosine

monophosphate concentration ([cAMP]) and cyclic guanosine monophosphate concentration ([cGMP]) (Nishimura et al., 1995). NO acts via a soluble guanylyl cyclase to raise intracellular [cGMP] (Wang et al., 1998). Raised cytosolic cyclic nucleotide levels inhibit platelet signalling pathways (Schwarz et al., 2001). Ectonucleotidases break down circulating adenosine triphosphate (ATP) and adenosine diphosphate (ADP) which may otherwise activate platelets via the P2Y receptor family (Marcus et al., 1997).

When endothelial cell damage occurs, which in the absence of vascular injury may be during inflammation or following atherosclerotic plaque formation, these inhibitory factors are no longer produced by the endothelium. Platelets are also exposed to adhesive matrix proteins and a wide range of factors activate platelets at sites of endothelial damage (de Witt et al., 2014). Plaque rupture exposes subendothelial collagens, particularly collagen type I that is a major component of the plaque fibrous cap (Farndale et al., 2004). Endothelial inflammation also leads to secretion of von Willebrand factor (vWF) (Bernardo et al., 2004). Platelets can also adhere to other exposed matrix proteins, such as other collagens, laminins and podoplanin. These matrix proteins activate platelets through their respective receptors (GPVI/α2β1 for collagen and laminin, α6β1 for laminin, CLEC2 for podoplanin, GPIb–V–IX for vWF, α5β1 for fibronectin) (Emsley et al., 2000; Moroi and Jung, 2004; Navarro-Núñez et al., 2013; Schaff et al., 2013; Varga-Szabo David et al., 2008) (Figure 1.1).

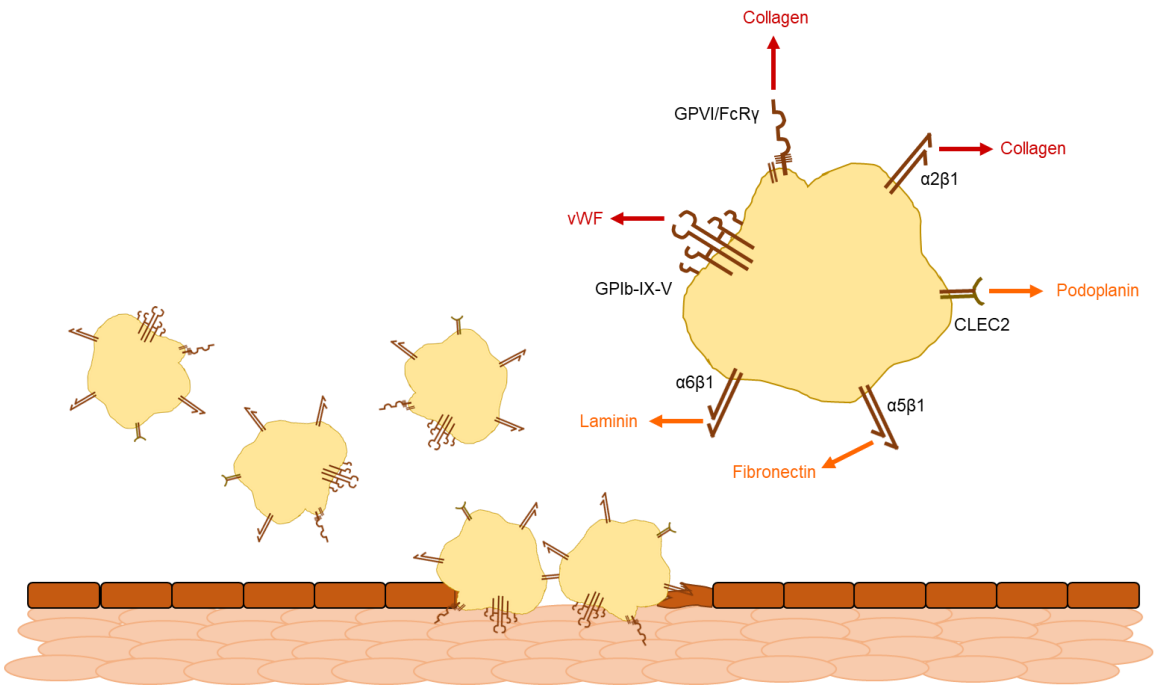

Figure 1.1: Platelet adhesion and activation following exposure to extracellular matrix proteins. GPVI/FcRγ and α2β1 bind collagen, GPIb-IX-V binds von Willebrand Factor (vWF), α6β1 binds laminin, α5β1 binds fibronectin and CLEC2 binds podoplanin.

1.3 Distinct subpopulations of platelets form during thrombosis

As mentioned previously, following activation two distinct subpopulations of platelets are formed within a growing thrombus: pro-aggregatory and pro-coagulant platelets (Figure 1.2) (van der Meijden and Heemskerk, 2019). Pro-aggregatory platelets have active integrin $\alpha_{IIb}\beta_3$ which allows platelets to aggregate together, via fibrinogen, to form the primary haemostatic plug. Pro-coagulant platelets do not have active integrins but are characterised by phosphatidylserine (PS) exposure. The PS acts as a pro-coagulant surface for binding of the tenase (FIXa/VIIIa) and prothrombinase (FXa/Va) complexes that generate a burst of thrombin production responsible for occlusive clot formation (Monroe et al., 2002).

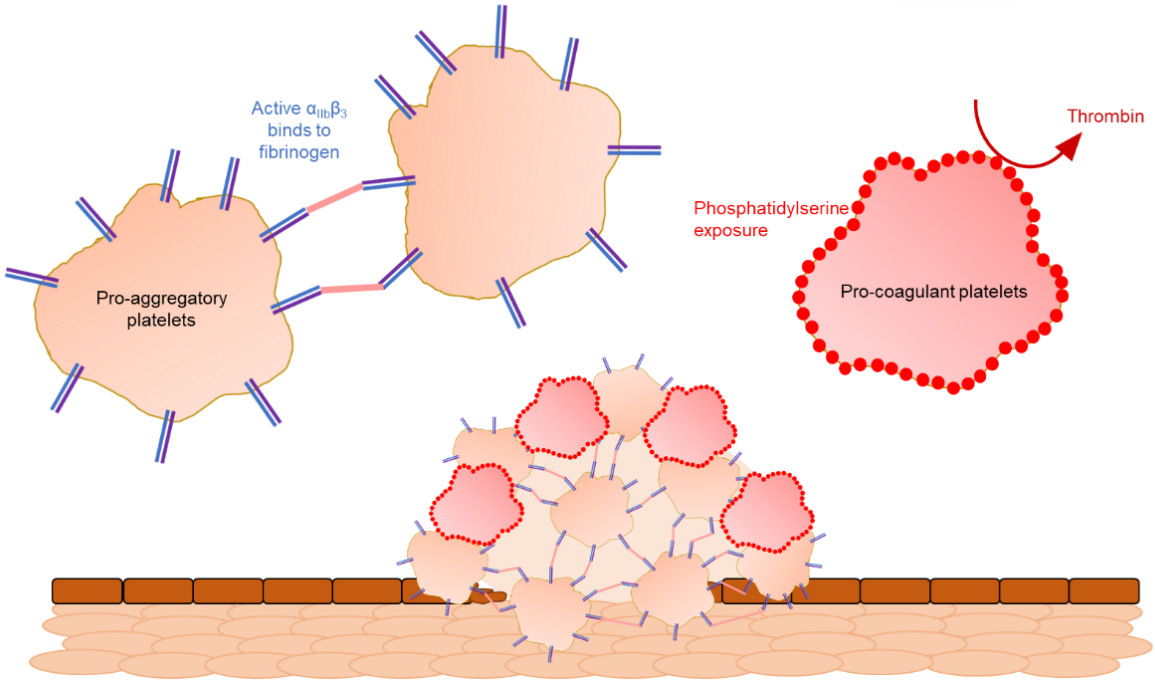

Figure 1.2: Platelet subpopulations in a developing thrombus. Some platelets are pro-aggregatory with active $\alpha_{IIb}\beta_3$ integrins that bind fibrinogen and form the meshwork of the clot. Other platelets are pro-coagulant, exposing phosphatidylserine (PS) on their surface to support thrombin generation.

1.4 Pro-aggregatory platelets have active integrins

Activation of platelets by extracellular matrix proteins (particularly collagen acting at GPVI) leads to increased cytosolic [Ca^{2+}]. Platelets are also activated by thrombin produced by the intrinsic and extrinsic coagulation pathways, also leading to increased [Ca^{2+}] downstream of protease-activated receptors 1 and 4 (PAR1 and PAR4) (Versteeg et al., 2013). Elevated [Ca^{2+}] and protein kinase C (PKC) activation lead to the secretion of ADP from dense granules (Chen et al., 2018) and thromboxane A_2 production by cyclooxygenase 1 (COX1) (O'Donnell et al., 2014). ADP and thromboxane A_2 act via $P2Y_1$ and TP receptors respectively to further

increase cytosolic [Ca^{2+}]. Elevated [Ca^{2+}] activates CalDAG-GEFI (a guanine nucleotide exchange factor) which in turn activates the small G protein, Rap1b. Rap1b promotes binding of talin to cytosolic regions of the β_3 integrin subunit initiating its activation. ADP also acts at the $P2Y_{12}$ receptor and by activating phosphoinositide 3-kinase (PI3-K) leads to increased phosphoinositide-3,4,5-trisphosphate (PIP_3). Adrenaline acting at the α_2 adrenoreceptor can provide an additional or alternative increase in [PIP_3] to the $P2Y_{12}$ receptor (Siess and Lapetina, 1989). PIP_3 inhibits Rasa3, a GTPase activating protein. Rasa3 normally inhibits Rap1b, but in the presence of PIP_3, Rap1b remains active and so maintains $\alpha_{IIb}\beta_3$ activation (Stefanini and Bergmeier, 2019, 2016). This is schematically represented in Figure 1.3. Active $\alpha_{IIb}\beta_3$ binds fibrinogen allowing aggregation of different platelets with active $\alpha_{IIb}\beta_3$ at their surface (Payrastre et al., 2000). These pro-aggregatory platelets do not expose PS on their surface (Munnix et al., 2003).

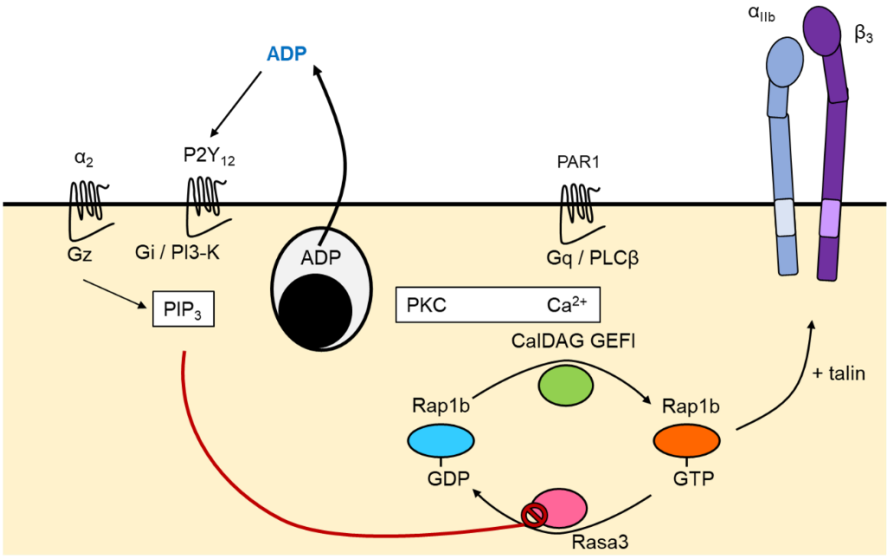

Figure 1.3: Schematic representation of $\alpha_{IIb}\beta_3$ integrin activation. $\alpha_{IIb}\beta_3$ integrin activation requires the activation of Rap1b by CalDAG-GEFI. Rap1b promotes the binding of talin to the cytosolic region of the β_3 integrin initiating its activation. Rasa3 must also be inhibited by increased [PIP_3] to maintain $\alpha_{IIb}\beta_3$ activation.

1.5 Current anti-platelet drugs target pro-aggregatory platelet activity and are associated with bleeding side effects

Since platelet activation drives thrombosis, inhibition of platelet activity is a key anti-thrombotic strategy in patients with a high risk of cardiovascular disease (McFadyen et al., 2018). Most of the currently approved anti-thrombotic drugs work by targeting platelet aggregation (Jamasbi et al., 2017). These include aspirin (a cyclooxygenase inhibitor, which prevents the production of platelet thromboxane A_2) and $P2Y_{12}$ receptor antagonists (which prevent ADP

stimulation e.g. clopidogrel, ticagrelor and prasugrel). These drugs act on factors which are released by activated platelets to stimulate others in a positive feedback mechanism. Other clinically used anti-platelet drugs include vorapaxar, a PAR1 antagonist, and eptifibatide, an integrin $\alpha_{IIb}\beta_3$ antagonist (Patrono et al., 2017). These anti-thrombotic drugs effectively reduce the risk of acute coronary events but individual responses to treatment are variable and they are associated with increased bleeding (Swieringa et al., 2014). This is because without pro-aggregatory platelet function, primary haemostasis is impaired. Current anti-platelet drugs are consequently contraindicated in some patient populations where both thrombotic and bleeding risks are high, such as cancer patients undergoing chemotherapy or those with thrombocytopenia, patients recovering from haemorrhagic stroke, transient ischaemic attacks or with severe hypertension, patients undergoing major surgery or recovering from severe trauma and those with active bleeding (BNF: British National Formulary – NICE)[1].

There is thus an unmet clinical need for novel anti-platelet therapies which prevent thrombosis without significant bleeding risks. There are currently no anti-thrombotic therapies that specifically target pro-coagulant platelet activity. Patients with hypertension (Preston et al., 2003), type 1 and type 2 diabetes (Sabatier et al., 2002; Tan et al., 2005), coronary artery disease (Mallatet al., 2000; Pasalic et al., 2018), carotid atherosclerosis (Lukasik et al., 2013), cortical stroke (Prodan and Dale, 2008), transient ischaemic attacks (Prodan et al., 2011), pulmonary arterial hypertension (Nadaud et al., 2013) and end stage renal disease (Valaydon et al., 2009) all show increased pro-coagulant platelet activity or increased pro-coagulant microparticle counts. This indicates that reducing pro-coagulant activity could serve as a novel anti-thrombotic target.

1.6 Pro-coagulant platelets expose PS

PS exposure, the hallmark of pro-coagulant platelet activity, increases local thrombin generation up to 1000 fold (Heemskerk et al., 2013). PS acts as a negatively charged surface for assembly of the vitamin K-dependent coagulation factors FVa and FXa (Schreuder et al., 2019; Zwaal et al., 1998). Pro-coagulant platelets also swell into balloon-like structures due to activation of Ca^{2+} activated Cl^- channels and the influx of water through aquaporin 1 (AQP1) (Agbani et al., 2018, 2015) and release microparticles which also have PS exposed on their surface (Agbani et al., 2015; Fujii et al., 2015; Sims et al., 1989) acting to increase the pro-coagulant surface area (Figure 1.4). The balloon-like structures support prolonged pro-coagulant activity during the later stages of platelet activation compared to the body (Agbani

[1] https://bnf.nice.org.uk accessed 6/8/2020

et al., 2017). Blocking platelet ballooning with AQP1 deletion or carbonic anhydrase inhibitors acetazolamide and methazolamide inhibit thrombus formation *in vivo* and do not increase bleeding (Agbani et al., 2020, 2018, 2015). Some pro-coagulant platelets, termed “coated platelets” will also have additional pro-coagulant proteins bound to their surface such as fibrin and the contents of secreted granules (Dale, 2005).

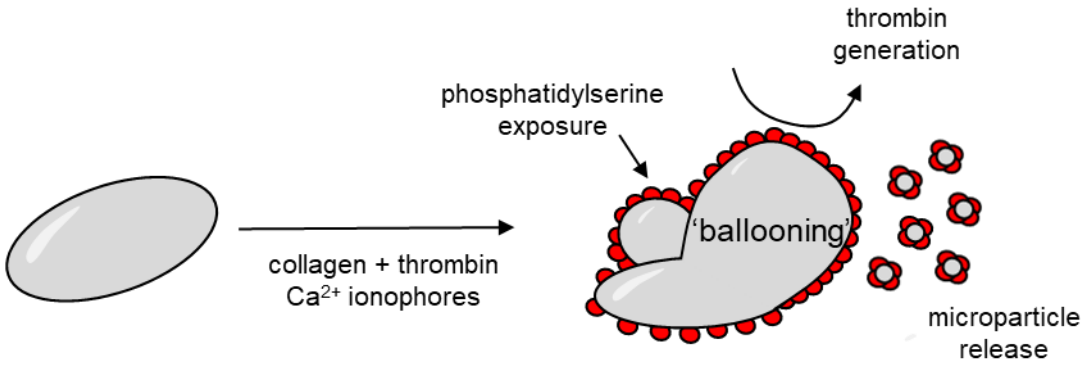

Figure 1.4: Pro-coagulant platelets are formed in response to strong stimuli such as dual collagen and thrombin stimulation or Ca^{2+} ionophores. Pro-coagulant platelets expose surface phosphatidylserine (PS) which supports local thrombin generation. Pro-coagulant platelets also swell to form balloon like structures and release microparticles to increase the pro-coagulant surface area. Figure adapted from Millington-Burgess and Harper, 2019.

All plasma membranes have an asymmetrical distribution of phospholipids across their two bilayers. PS and phosphatidylethanolamine (PE) are normally confined to the inner leaflet of the plasma membrane (Schick et al., 1976). At rest there is a low level of flip-flop movement of phospholipids between the bilayers but there is a large energy barrier to this movement as the hydrophilic headgroup of the phospholipid must cross the hydrophobic core of the bilayer. This phospholipid asymmetry is maintained by an active flippase protein, possibly a member of the P4-ATPase family, which reverses any movement of PS to the outer membrane (Daleke, 2003; Tang et al., 1996).

In activated platelets, but only in the subpopulation that becomes pro-coagulant, there is inactivation of the flippase and activation of a scramblase protein (Wolfs et al., 2005). The scramblase protein is non-specific and transports all phospholipids in both directions across the bilayer, but the net result is a movement of PS to the outer surface of the plasma membrane which is not reversed by the now-inactive flippase (Figure 1.5). Platelets, and other blood cells, from individuals with Scott Syndrome show impaired PS exposure and platelet pro-coagulant activity. These patients display a moderate bleeding phenotype with significant bleeding following a substantial haemostatic challenge such as surgery or childbirth, but

without excessive bleeding from superficial cuts or easy bruising (Millington-Burgess and Harper, 2019).

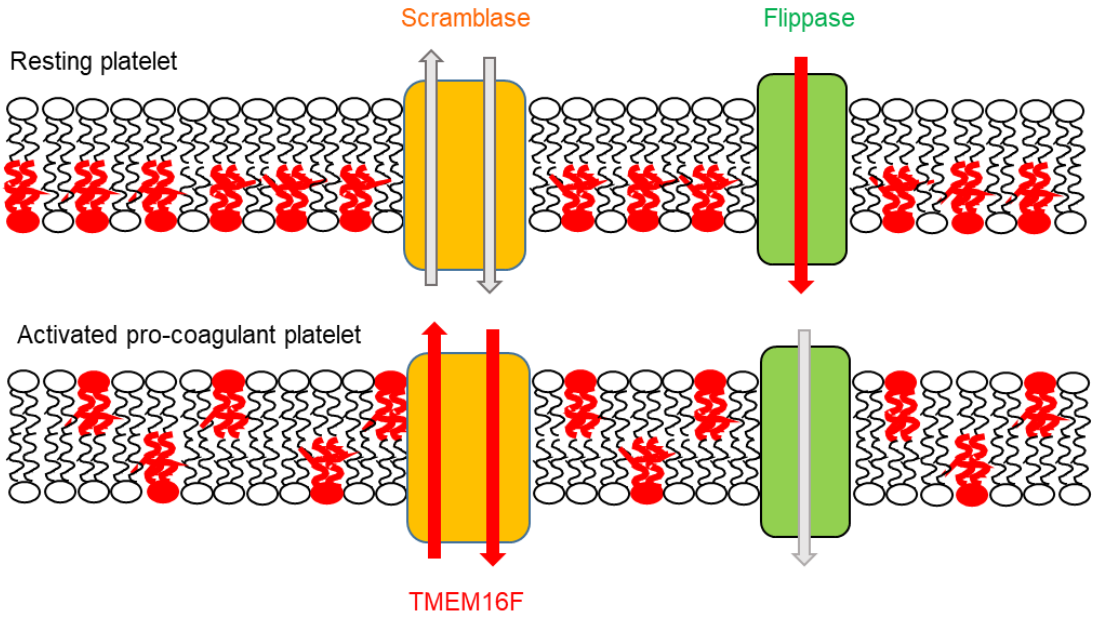

Figure 1.5: Plasma membrane mechanism of PS exposure. Schematic showing (top) a resting, unstimulated platelet plasma membrane with an inactive scramblase and an active flippase. PS is confined to the inner leaflet of the bilayer. (Bottom) A stimulated pro-coagulant platelet membrane which is exposing PS due to an active scramblase and an inhibited flippase. PS is shown in red. Red arrows denote movement of PS, grey arrows represent inactive or inhibited action. The scramblase is represented in yellow and the flippase in green. TMEM16F is a platelet scramblase.

PS exposure in pro-coagulant platelets occurs through a mechanism entirely distinct to the apoptotic mechanism of PS exposure in other cells. Unlike apoptosis, caspases are not involved in platelet pro-coagulant activity (White et al., 2012), nor are the Bcl-2 family member proteins Bak and Bax (Schoenwaelder et al., 2009) and cytochrome c is not lost from the intermembrane space (Choo et al., 2017).

1.7 Differences in Ca^{2+} signalling underlie the formation of distinct subpopulations of activated platelets

PS exposing platelets have sustained high cytosolic Ca^{2+} signals compared with transient Ca^{2+} signals in pro-aggregatory platelets (Choo et al., 2012; Heemskerk et al., 1997). Initial agonist induced cytosolic Ca^{2+} signals in platelets result from Ca^{2+} release from internal stores and entry across the plasma membrane, mainly via store operated Ca^{2+} entry (SOCE). Targeting cytosolic Ca^{2+} signalling would be unlikely to be a successful anti-thrombotic approach since

many of the same signalling pathways and Ca^{2+} channels are involved in both pro-aggregatory and pro-coagulant platelets, as well as many other cell types (Braun et al., 2011). Additionally, mutations leading to loss of SOCE cause severe immunodeficiency, illustrating the critical roles of these pathways (Feske, 2011). Similarly, targeting PAR1, PAR4 or GPVI would not selectively inhibit pro-coagulant platelet activity. The sustained Ca^{2+} signals in pro-coagulant platelets lead to an increase in mitochondrial [Ca^{2+}] and opening of the mitochondrial permeability transition pore (mPTP) when the mitochondrial [Ca^{2+}] rises above a critical threshold (Jobe et al., 2008). We have recently shown that this leads to a 'supramaximal' cytosolic Ca^{2+} signal, a very high signal in the order of 100 µM, which is characteristic of pro-coagulant platelets as it does not occur in pro-aggregatory platelets (Abbasian et al., 2020) (Figure 1.6). This model is consistent with computational modelling of platelet Ca^{2+} dynamics following stimulation by Pantaleev's group (Obydennyy et al., 2016). These signalling events lead to the activation of the scramblase and inhibition of the flippase, though the exact mechanism is unknown. It could be that the supramaximal Ca^{2+} signal is sufficient to induce PS exposure or there could be additional, as yet undetermined, regulatory signals required.

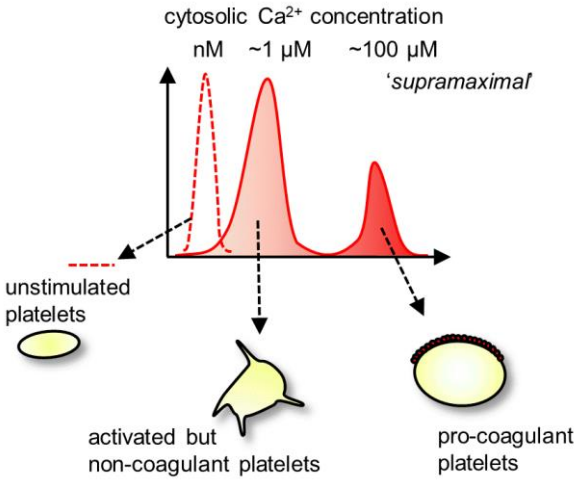

Figure 1.6: A "supramaximal" Ca^{2+} signal is necessary for pro-coagulant platelet formation. Figure taken from Abbassian et al., 2020.

Genetic loss of the pore component of the mitochondrial calcium uniporter (MCU), which is essential for mitochondrial Ca^{2+} uptake, inhibits PS exposure (Kholmukhamedov et al., 2018). Pharmacological inhibition of mitochondrial Ca^{2+} uptake by the reported MCU blocker Ru360 reduces PS exposure, as does disrupting the electrochemical gradient driving Ca^{2+} uptake with the uncoupler FCCP or complex 1 inhibitor metformin (Choo et al., 2012). Pharmacological inhibition of mPTP formation by cyclosporin A, coenzyme Q or bongkrekic

acid inhibits PS exposure whilst potentiation of mPTP formation by the oxidants phenylarsine oxide and diamide or H_2O_2 stimulates PS exposure (Jobe et al., 2008; Remenyi et al., 2005). Cyclophilin D is a critical regulator of mPTP formation, modulating its sensitivity to [Ca^{2+}] (Baines et al., 2005) and is the target of cyclosporin A (Kajitani et al., 2008). Genetic loss of cyclophilin D in mice significantly inhibits the formation of pro-coagulant platelets and leads to a reduction in arterial thrombosis (Jobe et al., 2008) and brain injury following ischaemic stroke in mouse models (Denorme et al., 2019). Contrastingly, some studies have shown that loss of cyclophilin D leads to an increase in thrombosis since cyclophilin D-dependent inactivation of integrin $\alpha_{IIb}\beta_3$ is necessary to limit thrombus growth (Liu et al., 2013). Pro-coagulant platelets tend to localise to concentrated “cap” structures on the surface of thrombi (Podoplelova et al., 2016) and have been shown to be extruded to the surface as thrombi contract (Nechipurenko et al., 2019), maximising interactions with circulating coagulation factors and consequent thrombin generation.

1.8 TMEM16F: a platelet scramblase

The identity of the phospholipid scramblase in platelets and other blood cells was a long-standing problem, finally solved in 2010. TMEM16F was identified as a Ca^{2+} activated phospholipid scramblase protein in a screen of mouse B cell lines (Ba/F3). One line was found to constitutively express PS due to a mutated and constitutively active TMEM16F (Suzuki et al., 2010). In the same study, a patient with Scott Syndrome was found to carry a mutation in a splice acceptor site resulting in a truncation of TMEM16F in the 3rd transmembrane domain. TMEM16F has since been shown to scramble all phospholipids at a rate of 4.5×10^4 lipids per second at 25 °C (Watanabe et al., 2018). TMEM16F is not involved in apoptotic PS exposure (Kmit et al., 2013). There is evidence for some low-level platelet PS exposure which occurs following stimulation with collagen and thrombin which is TMEM16F- independent (van Kruchten et al., 2013).

1.9 Scott Syndrome

It is now established that Scott syndrome is caused by mutations in the *ANO6* gene leading to a lack of TMEM16F expression, as we have recently reviewed (Millington-Burgess and Harper, 2019). The *ANO6* gene, which encodes TMEM16F, was first described *in silico* in 2004 (Katoh and Katoh, 2004). It is a member of the anoctamin family, so called as they were predicted to encode proteins with 8 transmembrane domains. ANO6 has 4 splice variants, 3 of which have been shown to traffic to the membrane and support phospholipid scrambling

(Scudieri et al., 2015). Of the other TMEM16 family proteins, TMEM16A and 16B are Ca^{2+}-activated Cl^- channels whilst TMEM16C, 16D, 16F, 16G, 16J and 16K have been shown to have some scramblase activity (Bushell et al., 2019; Suzuki et al., 2013). The functions of TMEM16E and TMEM16H remain unclear.

Only 6 cases of Scott Syndrome have been reported to date (Flores-Nascimento et al., 2012; Halliez et al., 2015; Munnix et al., 2003; Toti et al., 1996; Weiss et al., 1979), though it may be underdiagnosed due to its relatively mild clinical presentation until a significant haemostatic challenge and lack of routine diagnostic test. Scott Syndrome patients have prolonged prothrombin times and high residual plasma prothrombin levels, but a definitive diagnosis requires measurement of platelet PS exposure by flow cytometry. After diagnosis, management involves appropriate platelet transfusions during procedures to prevent excessive blood loss (Parry et al., 1980).

The original patient, Mrs Scott (MS), had deficient platelet pro-coagulant activity but all other platelet functions, including adhesion, aggregation and secretion, were normal (Weiss et al., 1979). The description of a second patient (FS) and her family indicated that Scott Syndrome was a genetic condition following an autosomal recessive inheritance pattern (Toti et al., 1996). FS and her two older sisters, who had both died from post-partum haemorrhage, were suggested to be homozygous for the Scott mutation. Platelets from two of FS' asymptomatic children displayed intermediate pro-coagulant activity between those of their mother and controls, suggesting they were heterozygous for the Scott mutation. MS' asymptomatic mother, father and son also showed intermediate platelet prothrombinase activity (Weiss and Lages, 1997), again indicating an autosomal recessive trait. It may be a coincidence that all of the small number of Scott patients described to date are female, but the 3 patients known to have had children all suffered with post-partum haemorrhage, perhaps illustrating the particular importance of platelet-based coagulation post-partum

Scott Syndrome platelets were originally described as lacking "platelet factor 3", leading to reduced factor Va and Xa binding to the surface of activated platelets (Miletich et al., 1979) and consequent reduced subendothelial fibrin deposition (Weiss et al., 1986). Platelet factor 3 was later identified as the exposure of the negatively-charged phospholipid PS on the surface of activated platelets. Studies on resealed red blood cell (RBC) ghosts showed that the Scott Syndrome defect was in an intrinsic membrane component responsible for PS exposure (Bevers et al., 1992).

Flippase activity is unaffected in Scott Syndrome patients but the scramblase activity is defective (Bettache et al., 1998; Dekkers et al., 1998). Platelet microparticle release which requires PS exposure, is also abolished (Sims et al., 1989) and pro-coagulant ballooning is

diminished in Scott Syndrome platelets (Mattheij et al., 2016). Scott Syndrome RBCs also display defective PS exposure, microparticle release and echinocytosis (Bevers et al., 1992). Immortalised Scott Syndrome B-lymphocytes also have impaired PS exposure and pro-coagulant activity (Kojima et al., 1994).

Two proteins were previously proposed to be the phospholipid scramblase: PLSCR1 and ABCA1. PSLCR1 was initially described as a putative scramblase in RBCs (Zhou et al., 1997). However, PSLCR1 mRNA and protein levels (Zhou et al., 1998), and later sequence (Janel et al., 1999), were all normal in Scott Syndrome patients (MS and FS). Furthermore, *Pslcr1*$^{-/-}$ mice have normal haemostasis and platelet and RBC PS exposure (Zhou et al., 2002), excluding PSLCR1. A missense mutation in the ABCA1 gene was identified in a third Scott patient (c.6064G>A (ABCA1 R1925Q)) (Albrecht et al., 2005) which reduced its expression in lymphocytes. This mutation, however, has not been found in any other Scott Syndrome patients and ABCA1 is now known to play a role in cholesterol efflux (Zarubica et al., 2007). ABCA1 mutations cause Tangier disease, patients of which expose normal platelet PS (Nofer et al., 2004; Schmitz and Schambeck, 2006). The study by Suzuki et al., described previously, finally identified TMEM16F as the scramblase underlying Scott Syndrome (Suzuki et al., 2010).

Scott Syndrome platelets show additional differences beyond TMEM16F. A proteomic screen of a Scott Syndrome patient's platelets found differential expression of 134 proteins, with aquaporin 1 expression being particularly strongly upregulated, and increased protein phosphorylation following stimulation (Solari et al., 2016). Further differences in tyrosine phosphorylation have also been determined between Scott Syndrome platelets and controls (Dekkers et al., 1998). It is possible that these differences contribute to the Scott Syndrome phenotype in addition to the loss of TMEM16F scramblase activity.

1.10 TMEM16F in animal models

Several TMEM16F knockout mice have been characterised. *Tmem16f*$^{-/-}$ mice have decreased platelet PS exposure and thrombin peak in response to the Ca^{2+} ionophore A23187 compared to wild type (Yang et al., 2012). These mice are protected from $FeCl_3$-induced arterial thrombosis and have an approximately doubled bleeding time, which is relatively minor compared to many mice with deletion of important platelet proteins involved in aggregation (e.g. $\beta_3^{-/-}$ or $P2Y_{12}^{-/-}$). Platelets from a platelet-specific TMEM16F knock-out (KO) mouse also have reduced PS exposure and microparticle release but other platelet functions are maintained (Baig et al., 2016; Fujii et al., 2015). Apart from these haemostatic effects, the TMEM16F KO mice appear generally healthy.

Table 1.1 Haemostatic effects of TMEM16F KO mice and Scott Syndrome German Shepherd dogs. Wild type – WT. ETP- endogenous thrombin potential.

Animal Model	Mouse global TMEM16F knockout: *TMEM16F*$^{-/-}$ (Yang et al., 2012)	Mouse global TMEM16F knockout: *Ano6*$^{Avor-/-}$ (Mattheji et al., 2015)	Mouse megakaryocyte/ platelet specific knockout: *TMEM16F*$^{fl/fl;Pf4\text{-}CRE}$ (Fujii et al., 2015)	Mouse megakaryocyte/ platelet specific knockout: *TMEM16F*$^{fl/fl;Pf4\text{-}CRE}$ (Baig et al., 2016)	Naturally occurring population of German Shepherd dogs (Brooks et al., 2002)
Platelet PS exposure	Reduced but not absent following A23187 stimulation.	Reduced but not absent following ionomycin or thrombin + convulxin stimulation.	Reduced but not absent following thrombin + collagen or A23187 stimulation.	Reduced but not absent following thrombin + CRP or ionomycin stimulation. PS positive platelets which still formed showed a lower degree of AV binding.	Reduced but not absent following thrombin + collagen or A23187 stimulation.
RBC PS exposure	Absent following A23187 stimulation.	Not reported.	Not reported.	Not reported.	Not reported.
Thrombin generation	Reduced ETP and thrombin peaks.	Not reported.	5-10 fold lower rate of thrombin production.	Reduced rate of thrombin production and fibrin formation.	Virtually no thrombin generation.
Thrombosis	Protected from $FeCl_3$ model: no occlusion in 25 minutes by which time all WTs had occluded.	Normal thrombus formation on collagen with reduced PS, though in anticoagulated blood.	Smaller more fragile thrombi after laser injury.	$FeCl_3$ injury model and 50% of cKO mice did not form a stable occlusion and those that did so occurred significantly later than WT. Increased embolism.	No occlusive clots formed in clot signature analyses.
Bleeding time	Approximately doubled compared to WT. Heterozygote bleeding time similar to WT.	Approximately 5 times as long as WT.	No difference in tail bleeding times.	Bleeding times over 3x as long as WT.	Normal bleeding times.
Other platelet functions	None reported.	Normal collagen induced aggregation. Reduced swelling and blebbing. Normal integrin activation and P-selectin in response to ADP, thrombin and convulxin.	Reduced microparticle release. Normal cytosolic Ca^{2+} signals following stimulation with thrombin + collagen. Normal α- and dense granule release.	No differences in integrin activation or P-selectin exposure.	Normal platelet aggregation.
Other	Fertile, viable, grossly normal morphology. Reduced B cell PS exposure.	Reduced viability ~30% homozygotes survive. Reduced calpain dependent protein cleavage. Moderately affected apoptosis dependent PS exposure. Reduced high level but increased moderate PS exposure.	Normal clot retraction.	Similar brain infarcts in models of ischaemic stroke.	Normal clot retraction.

Table 1.1 summarises the haemostatic effects of the TMEM16F KO mice studied to date as well as the phenotype of a naturally occurring population of German Shepherd dogs with Scott Syndrome (Brooks et al., 2002) .

TMEM16F has also been implicated in a number of other processes including bone mineralisation (Ousingsawat et al., 2015), T cell signalling (Hu et al., 2016), enveloped virus entry into cells e.g. HIV (Chua et al., 2019), motor neuron excitability (Soulard et al., 2020), microglial function (Zhao and Gao, 2019), airway mucus secretion (Cabrita et al., 2019) and membrane repair (Wu et al., 2020). TMEM16F has also recently been shown to play a role in placental development with loss of TMEM16F leading to increased perinatal mortality, which might explain in part why Scott Syndrome is so rare (Zhang et al., 2020).

Some roles of TMEM16F may be unrelated to its scramblase activity. There is debate in the literature as to whether TMEM16F is a dual function protein acting as a Ca^{2+} activated ion channel as well as a phospholipid scramblase. Some reports show TMEM16F to be a Ca^{2+} activated Cl^- channel (Scudieri et al., 2015; Shimizu et al., 2013), others to be a non-selective cation channel (Yang et al., 2012) whilst others report TMEM16F has no recordable ion channel activity (Duran et al., 2011; Suzuki et al., 2013). Ye et al., report that TMEM16F's selectivity for Cl^- increases as intracellular Ca^{2+} rises (Ye et al., 2019). It does not seem, however, that ion channel activity is necessary for the protein to function as a phospholipid scramblase (Kmit et al., 2013).

1.11 TMEM16F: a potential anti-thrombotic target?

TMEM16F is therefore a protein critical for platelet PS exposure and hence the formation of pro-coagulant platelets. This makes it a candidate target protein for novel anti-thrombotic drug development. Based on the evidence from *Tmem16f*$^{-/-}$ mice and patients with Scott Syndrome, a TMEM16F inhibitor would prevent the formation of pro-coagulant platelets whilst leaving the function of the pro-aggregatory platelets intact. As other roles of TMEM16F seem relatively restricted, inhibiting this protein pharmacologically may be associated with fewer undesirable side effects than targeting other platelet proteins. Conversely, inhibiting TMEM16F may increase bleeding risk or significantly influence other roles of TMEM16F to an unacceptable degree. In order to test this hypothesis, however, a selective inhibitor of TMEM16F must be developed.

An understanding of the structure of TMEM16F and the mechanism by which it acts as a phospholipid scramblase will be essential for the design of novel inhibitors of TMEM16F.

1.12 Fungal TMEM16 homologues

nhTMEM16, from *Nectria haematococca,* and afTMEM16, from *Aspergillus fumigatus,* are 2 fungal phospholipid scramblase homologues of TMEM16F which have been structurally and mechanistically characterised.

1.13 nhTMEM16

The X-ray crystal structure of nhTMEM16 was the first scramblase structure to be solved with a resolution of 3.3 – 3.4 Å (Brunner et al., 2014). nhTMEM16 is a homodimer. Each subunit has 10 transmembrane spanning α-helices (TM1-10; the gene family name anoctamins was in fact a misnomer). Both N and C termini are cytosolic, and a ferrodoxin-like fold is seen near the N-terminal domain. This structure, notable for its' resemblance to a butterfly shape, is now known as the classical TMEM16 structure (Figure 1.7 A). There is a large dimer interface (9650 $Å^2$), mostly due to the interaction of the N-terminal domain of one monomer with the C terminal domain of the other, and a small dimer cavity, the functional relevance of which remains unclear but is presumed to be packed with phospholipids when in the membrane. Ca^{2+} binding is co-ordinated by 6 acidic residues on TM6, 7 and 8 that are highly conserved throughout the TMEM16 family (Figure 1.7 B).

TM3-7 form a spiralling hydrophilic cavity, 8 – 11 Å wide, which is exposed on one side to the membrane lipids, illustrated in pink in Figure 1.7. This is believed to be the main pathway for phospholipid movement between the membrane bilayers (Brunner et al., 2014). TM4 and TM6 line the hydrophilic groove, termed an "aqueduct" by some groups for its transport functions and hydrophilic nature (Jiang et al., 2017).

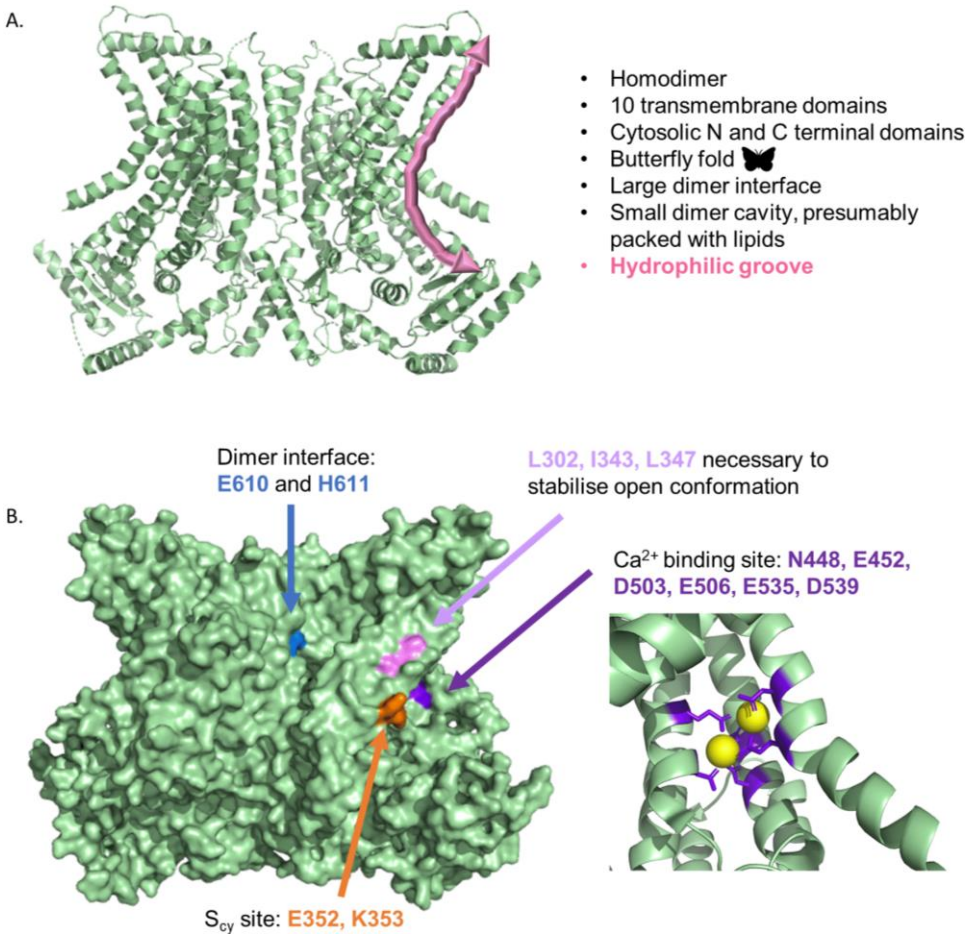

Figure 1.7: Structural features of nhTMEM16. (A) Ribbon representation of nhTMEM16 structure PDB ID: 4WIS (Brunner et al., 2014). Bullet points highlight common structural features of the TMEM16 family. Pink arrow indicates the hydrophilic groove believed to be the main site of phospholipid scrambling. (B) 3D space-filling representation of the nhTMEM16 structure. Highlighted in blue are residues E610 and E611 important for interactions at the dimer interface. Highlighted in violet are residues L302, I343 and L347 which stabilise the open conformation of nhTMEM16. Highlighted in purple are the Ca^{2+} co-ordinating residues N448, E452, D503, E506, E535, D539. Highlighted in orange are the residues E352 and K353 which form the S_{cy} site. More information about these residues is detailed in the main text.

Several theories have been proposed as to how this groove mediates phospholipid scrambling, though most evidence indicates some involvement of a “credit-card mechanism” (Pomorski and Menon, 2006), schematically presented in Figure 1.8. Here the hydrophilic groove is proposed to act as a conduit for the movement of the phospholipid headgroups through the hydrophobic membrane core whilst the long acyl chains remain within the lipid environment.

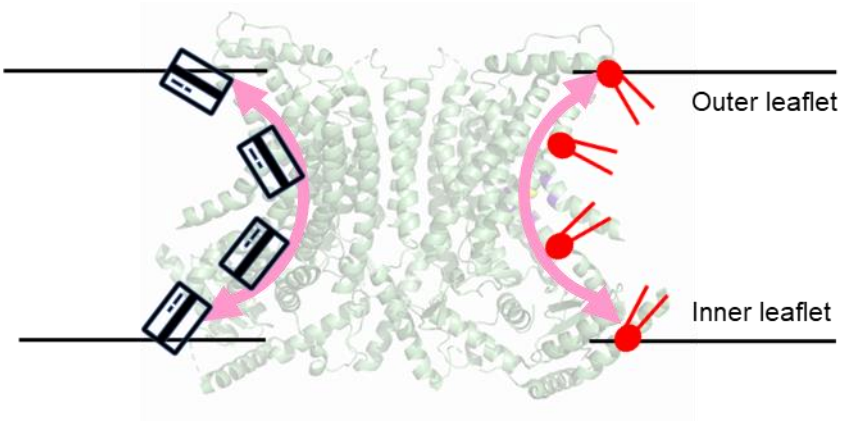

Figure 1.8: Schematic of the credit card mechanism of phospholipid scrambling. The charged phospholipid head groups interact with residues in the hydrophilic groove to facilitate movement between bilayers of the membrane whilst the hydrophobic acyl chains remain within the lipid core.

The hydrophilicity of the groove is not uniform; hydrophilic residues concentrate at the intracellular end of TM4 and extracellular end of TM6. This causes local deformation of the membrane bilayer, acting to thin the membrane and cause a slight curvature near to the groove to match the hydrophobic surfaces of the protein. These local membrane disruptions lower the energy barrier for diffusion of phospholipids across the membrane and optimally orient phospholipids to access the groove. Such membrane distortions were predicted in molecular dynamics (MD) simulations of nhTMEM16 scrambling (Bethel and Grabe, 2016; Jiang et al., 2017) with nhTMEM16 thinning the membrane locally from 28.5 Å to 18.3 Å. Similar membrane thinning was predicted to occur for TMEM16F (reducing membrane thickness to 20.5 Å). Models where all residues within the groove were neutralised reduced the predicted membrane distortion but did not eliminate it, suggesting that the whole protein structure is complicit in this deformation (Bethel and Grabe, 2016). Membrane distortion was later confirmed in cryo-electron microscopy (EM) structures when nhTMEM16 was reconstituted in lipid nanodiscs (Kalienkova et al., 2019). This is schematically presented in Figure 1.9.

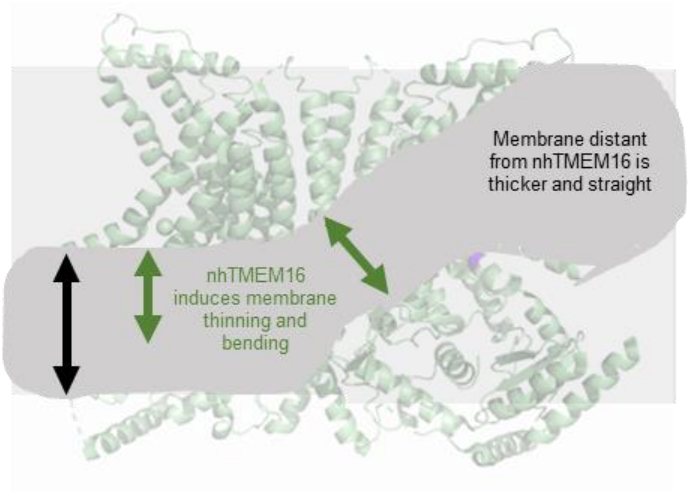

Figure 1.9: Schematic representation of local membrane distortion induced by nhTMEM16. Due to relative differences in the hydrophilicity of the nhTMEM16 structure, within the groove and at distant sites, local deformations are induced within the surrounding membrane. This causes membrane thinning and a slight curvature to orient phospholipids optimally for transport through the groove. These local membrane distortions lower the energy barrier for phospholipid scrambling.

However, membrane distortion alone is not sufficient for full scrambling activity by nhTMEM16. A "stepwise" mechanism of Ca^{2+}-dependent activation of nhTMEM16 has been proposed (Kalienkova et al., 2019). In the absence of Ca^{2+}, nhTMEM16 exists in a closed, inactive state. When nhTMEM16 is reconstituted in lipid nanodiscs, the groove is blocked from the membrane core by association of TM4 and TM6. The absence of Ca^{2+} means the acidic residues involved in Ca^{2+} binding repel each other and cause TM6 to block the groove. During MD simulations some lipids were observed in the Ca^{2+} free conformation of nhTMEM16 which may explain the phospholipid scrambling exhibited by fungal homologues in the absence of Ca^{2+} when expressed in liposomes (Bethel and Grabe, 2016).

Following Ca^{2+} activation, the most substantial movement occurs in the intracellular end of TM6 with Q468 moving 15 Å. The groove is already wider at this intracellular end, however, so it is likely that the movements which occur higher up the groove, particularly a 5 Å movement of TM4 residues 325-345, act as a gating strategy to allow the movement of phospholipids. Further movement of TM4 appears to be limited by the interaction of TM3 with TM10 on the other subunit of the dimer.

In the active Ca^{2+}-bound state, TM4 is stabilised by an association with TM3 and residue L302 is important for this interaction. The L302A mutant can conduct ions but cannot scramble lipids suggesting this stabilisation of TM4 cannot take place (Khelashvili et al., 2019). Hydrophobic

interactions between I343 and L347 in TM4 and L302 in TM3 keep the groove open to allow phospholipid scrambling, highlighted in violet in Figure 1.7 B.

MD simulations of phospholipid movement through nhTMEM16 found that some residues in the groove were disproportionately involved in phospholipid movements. Bethel and colleagues found 2 sites within the groove which were important during phospholipid movement (Bethel and Grabe, 2016). One site at the extracellular end of the groove, involving E313 and R432, was proposed to act as a stepping-stone for phospholipids. A site at the cytosolic end of the groove was identified which was important but not obligatory for phospholipid movement involving E352 and K353 (S_{cy}). Jiang and colleagues used similar methods to identify 3 sites in overall agreement with Bethel et al. External, central and internal sites were identified (S_{ext}, S_{cen}, S_{int} respectively) and mutations of residues in these sites reduced phospholipid scrambling, consistent with the fact that these sites are important (Jiang et al., 2017). These sites are illustrated in Figure 1.10.

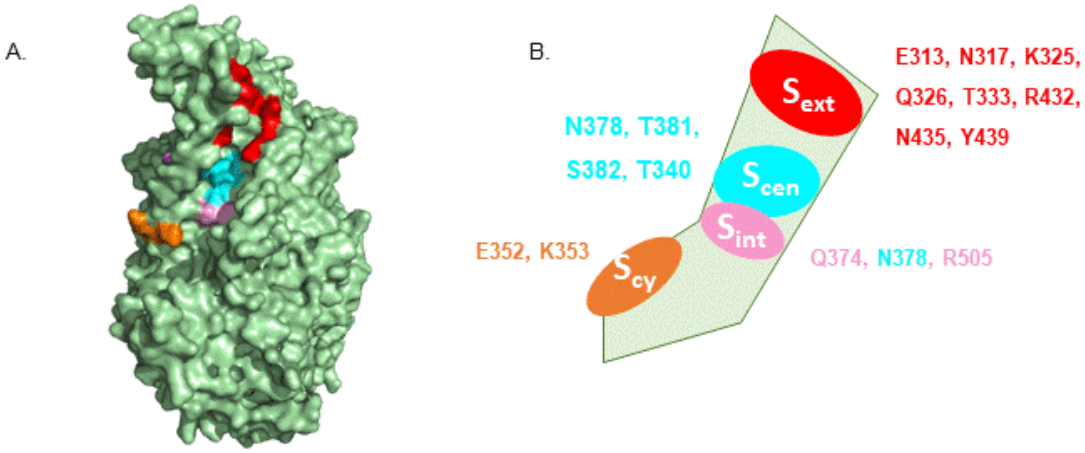

Figure 1.10: The hydrophilic groove of nhTMEM16. (A) 3D representation of a side-on view of the hydrophilic groove which when open will be exposed to the membrane core. Residues predicted to be particularly important in phospholipid conduction by MD simulations are highlighted in colour and schematically presented in (B).

An intermediate state of the nhTMEM16 protein was also detected where the groove is blocked from the membrane core at the extracellular end, where TM4 and TM6 are still in close association, but the dimensions of the pore have widened compared to the closed state. This state may allow pore formation to permit ion conduction without the scrambling of phospholipids. Hydrophobic interactions between V337 and V447 are important for this channel-like state (Kalienkova et al., 2019).

Together these structural and functional data suggest that different states of the nhTMEM16 protein mediate ionic conductance and phospholipid scrambling and an equilibrium exists between the intermediate and open state depending upon intracellular [Ca^{2+}] and the lipid environment. Table 1.2 details key residues in nhTMEM16 highlighted by the structural and functional studies discussed above.

nhTMEM16		
Residues	**Roles**	**Reference**
N448, E452, D503, E506, E535, D539	Involved in Ca^{2+} co-ordination. Highly conserved throughout the TMEM16 family.	(Brunner et al., 2014)
E610 and H611	Interact at dimer interface	
E313, R432	Extracellular phospholipid interaction site in groove. A "stepping stone" site.	(Bethel and Grabe, 2016)
E352, K353	Cytosolic phospholipid interaction site in groove.	
E313, N317, K325, Q326, T333, R432, N435, Y439	External site: phospholipid interaction site in groove.	(Jiang et al., 2017)
N378, T381, S382, T340	Central site: phospholipid interaction site in groove.	
Q374, N378, R505	Internal site: phospholipid interaction site in groove.	
N310, E313, G329, T333, Q436, Y439	Na^{+} interaction site: co-ordination by oxygen atoms on residues.	
Q374, E496, E497	Transient interactions with Na^{+}.	
L302, I343, L347	Residues on TM3 (L302) and TM4 (I343 and L347) necessary to stabilise the open groove conformation.	(Khelashvili et al., 2019)
Mutants	**Effect**	**Reference**
Triple mutant E452Q/E535Q/D539N	Three residues involved in Ca^{2+} co-ordination. Mutant shows weak scrambling activity which is not increased by raising intracellular Ca^{2+}.	(Brunner et al., 2014)
R505Q	Reduced scrambling and ionic currents.	(Jiang et al., 2017)
N378K	Reduced scrambling and ionic currents.	
T333V	Reduced scrambling and ionic currents.	
R432W	10-100 times greater inhibitory effect on scrambling of smaller phospholipids than PEGylated phospholipids in presence of Ca^{2+}. Same effect on all sizes of phospholipid in absence of Ca^{2+}.	(Malvezzi et al., 2018)
L302A	Severely impaired lipid scrambling, but ion channel activity.	(Khelashvili et al., 2019)
L302A/I343A	>100 fold reduction in scrambling rates.	
L347A	~10 fold reduction in scrambling rate.	
I343A/L347A	Complete loss of scrambling activity.	
D503A	Reduced potency for Ca^{2+} but still some scrambling activity.	(Kalienkova et al., 2019)
P341A	No detectable effect.	
G339A and P332A	Decreased scrambling in presence and absence of Ca^{2+} but no change in Ca^{2+} binding. 2 residues involved in movement of TM4 upon Ca^{2+} activation.	

Table 1.2 Key residues for nhTMEM16 function and effects of mutations. Colour coding matches Figures 1.7 and 1.10.

1.14 afTMEM16

afTMEM16 was identified during a screen for eukaryotic homologues of TMEM16F and is a non-selective Ca^{2+}-gated ion channel and a Ca^{2+}-dependent phospholipid scramblase (Malvezzi et al., 2013). Ionic conduction and phospholipid scrambling were differentially affected by the lipid environment and ionic conductance was not necessary for phospholipid scrambling. Both functions, however, are controlled by a single Ca^{2+} binding site (Malvezzi et al., 2013).

The afTMEM16 structure was solved by cryo-EM (Falzone et al., 2019). afTMEM16 shows all the characteristic structural features of the TMEM16 family, being a homodimer with 10 transmembrane domains. There are 2 dimer cavities which are larger than those in nhTMEM16. TM3-6 form a hydrophilic groove at least 5 Å in diameter which is exposed to the membrane when Ca^{2+}-bound.

Two states of the afTMEM16 structure were found. In the absence of Ca^{2+} the hydrophilic groove is closed to the membrane due to constriction between TM4 and TM6 with hydrophobic surfaces exposed to the membrane. Ion conduction is prevented in this state by aromatic and hydrophobic side chains around TM3-7; the narrowest part of the groove is just 1 Å. Two Ca^{2+} are co-ordinated by each monomer at binding sites located between TM6, TM7, and TM8 (Table 1.3 and Figure 1.11). Upon Ca^{2+} binding TM6 moves around A437 by 20°, straightening and opening up the hydrophilic groove, moving away from its association with TM4. TM4 also bends away from TM6 around P324 and P333 and TM3 also moves up to 6 Å (Figure 1.11) (Falzone et al., 2019).

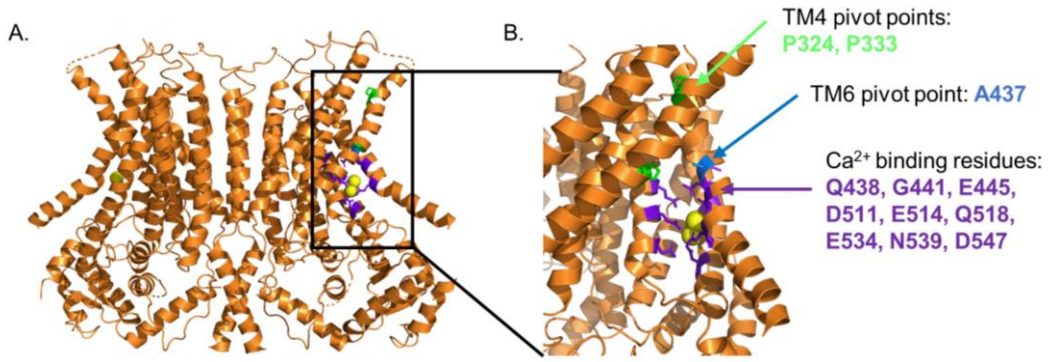

Figure 1.11: afTMEM16 structure and critical residues. (A) Ribbon representation of afTMEM16 structure PDB ID: 6EOH (Falzone et al., 2019). (B) Enlarged view of critical residues. Highlighted in green are P324 and P333 which are pivot points for TM4 upon Ca^{2+} binding. Highlighted in blue is A437 which is the TM6 pivot point upon Ca^{2+} binding. Highlighted in purple are Ca^{2+} binding residues Q438, G441, E445, D511, E514, Q518, E534, N539 and D547. More information about these residues is detailed in the main text and Table 1.3.

afTMEM16 also induces Ca^{2+}-independent membrane bending and thinning to prime for phospholipid scrambling. This is particularly due to the different lengths of the helices lining the dimer cavity. afTMEM16 scrambling is inhibited by C24:0 ceramide and is slower in thicker membranes indicating that the physico-chemical properties of the membrane are important for scrambling (Malvezzi et al., 2018).

afTMEM16 additionally demonstrates out-of-the groove phospholipid scrambling. afTMEM16 can scramble PEGylated lipids with headgroups much larger than the dimensions of the groove, albeit at a slower rate than smaller lipids. This suggests a potential out-of-the-groove mechanism facilitated by local membrane deformation in addition to the credit-card transport of smaller phospholipids (Malvezzi et al., 2018). Ion movement, however, likely does occur through the groove as this is not inhibited by larger PEGylated phospholipids. Larger ions, such as NMDG are still unable to be conducted through afTMEM16 in the presence of PEGylated lipids, indicating these lipids do not distort the dimensions of the groove (Malvezzi et al., 2018). Similar evidence for out-of-the-groove scrambling was found for nhTMEM16 (Malvezzi et al., 2018).

afTMEM16		
Residues	**Roles**	**Reference**
Q438, G441, E445, D511, E514, Q518, E534, N539, D547	Ca^{2+} co-ordination.	(Falzone et al., 2019)
P324, P333	TM4 pivot following Ca^{2+} binding.	
A437	TM6 pivot following Ca^{2+} binding	
Mutant	**Effect**	**Reference**
D511A/E514A	No longer Ca^{2+} sensitive. Very little phospholipid scrambling or ion conduction.	(Malvezzi et al., 2013)
D511A/E514A	Similar Ca^{2+} independent scrambling of N-NBD-PE to wild type.	(Malvezzi et al., 2018)

Table 1.3: Key residues for afTMEM16 function and effects of mutations. Colour coding matches Figure 1.11.

Overall, the sequence homology between these fungal scramblase homologues and human TMEM16F is low (~25%). However, their structures reveal critical insights into the functional mechanisms of the TMEM16 scramblase family which will guide inhibitor design.

To summarise our insights from these fungal homologues: TMEM16 scramblase proteins are homodimers with 10 transmembrane spanning α helices, cytosolic N and C terminal domains and dimer cavities presumed to be packed with lipids in the membrane environment. Each monomer contains a hydrophilic groove. This groove is shielded from the membrane core in the absence of Ca^{2+} and in this state the proteins do not scramble phospholipids or conduct ions. Ca^{2+} binding induces conformational changes in the protein which opens the groove to the membrane core allowing access to phospholipid headgroups and phospholipid scrambling

via a credit-card mechanism. The most notable conformational changes involved in groove opening occur to TM6 and more subtle changes to TM4 and TM3. In nhTMEM16 there is additional evidence for an intermediate protein conformation which conducts ions but does not scramble phospholipids. Both fungal homologues induce a degree of membrane deformation to thin and bend the membrane in the vicinity of the groove which will further lower the energy barrier for movement of lipids and potentially allow out-of-the-groove phospholipid scrambling.

1.15 TMEM16A is a calcium activated chloride channel

Both mouse and human TMEM16F share a much higher sequence homology to TMEM16A than the fungal homologues.

TMEM16A is a member of the same protein family as TMEM16F and in 2008 it was identified as the long sought after Ca^{2+} activated Cl^- channel (CaCC) (Caputo et al., 2008; Yang et al., 2008). The structure of mTMEM16A was determined by cryo-EM, first at a low resolution (6.6 Å) and later the same year at a higher resolution (3.75 - 4.06 Å) (Paulino et al., 2017b, 2017a) and using nanodiscs (3.8 Å) (Dang et al., 2017). Like nhTMEM16, mTMEM16A is a homodimer with cytosolic N and C termini and a transmembrane domain containing 10 α-helices. The N terminal ferrodoxin-like fold resembles that in nhTMEM16. Unlike nhTMEM16, the mTMEM16A dimer interface is relatively small, accounting for only 1.3% of the combined molecular surface. The ion conduction pore is also formed by TM 3-7, though it instead has an hourglass shape and is shielded from the membrane lipid environment by interactions between TM4 and TM6. The pore is lined with basic amino acids conferring a positive electrostatic environment in the pore for anion selectivity. Activation occurs following Ca^{2+} co-ordination which causes a conformational change in the intracellular half of TM6. The lower half of the helix moves like a hinge around G644, which increases the diameter of the neck of the pore and allows permeation of ions (Figure 1.12). There are also thought to be smaller conformational changes higher up in the channel which affect permeability of the pore (Paulino et al., 2017b).

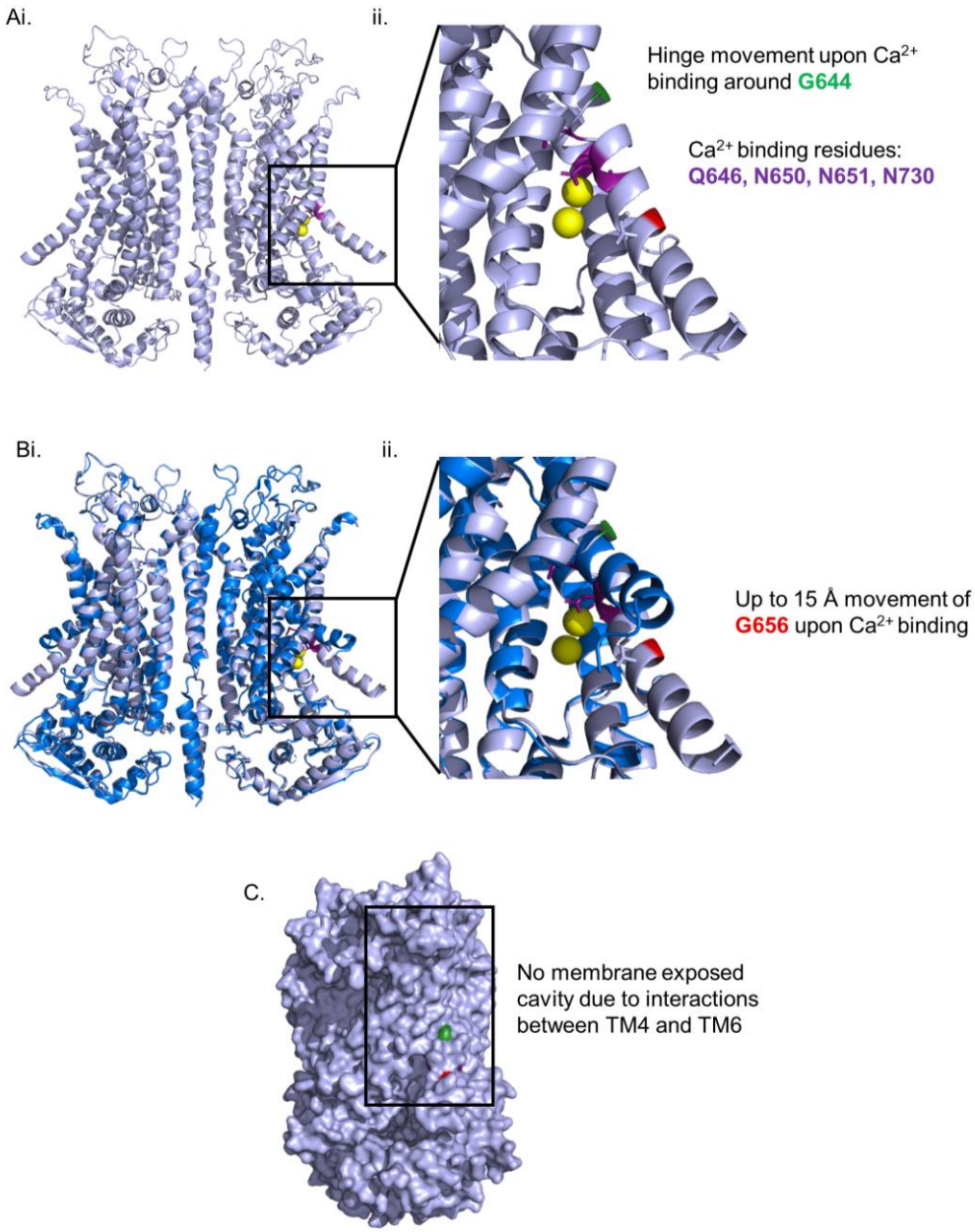

Figure 1.12: mTMEM16A structure and critical residues. (Ai) Ribbon representation of Ca^{2+} bound mTMEM16A structure PDB ID: 5OYB (Paulino et al., 2017). (Aii) Enlarged view of critical residues. Highlighted in green is G644 around which TM6 hinges following Ca^{2+} binding. Highlighted in purple are the Ca^{2+} binding residues Q646, N650, N651 and N730. (Bi) Overlaid ribbon representations of Ca^{2+} bound mTMEM16A structure 5OYB in light blue with Ca^{2+} free mTMEM16A structure 5OYG in dark blue. (Bii) Enlarged view of critical residues. Highlighted in red is G656 which moves 15 Å upon Ca^{2+} binding. (C) Space filling representation of Ca^{2+} bound mTMEM16A. More information about these residues is detailed in the main text and Table 1.4.

Despite the low sequence identity between nhTMEM16 and mTMEM16A, there is a generally conserved secondary structure with 447 Cα residues being within 4 Å of each other in the superimposition of mTMEM16A and nhTMEM16. TMEM16A does not normally scramble phospholipids. However, a so called “scramblase domain” from TMEM16F is able to confer scrambling activity to TMEM16A in a chimeric protein (Yu et al., 2015) as are scramblase domains from other TMEM16 scramblases; 16C, 16D, 16E, 16G, 16J and 16K though these show differing efficiencies and selectivity for phospholipids (Gyobu et al., 2017). In contrast, the N-terminal regions of TMEM16F (amino acids 1-250) and TMEM16A (amino acids 1-285) were functionally interchangeable, as were the C termini (16A: 869-956, 16F: 844-911) (Suzuki et al., 2014). Table 1.4 details residues critical to mTMEM16A function and the effects of mutations studied to date.

TMEM16A		
Residue	**Role**	**Reference**
Q646, N650, N651, N730	Co-ordinates Ca^{2+}. Mutation of all residues to alanine lowers potency towards Ca^{2+}.	(Paulino et al., 2017a)
G644	Hinge for movement of TM6.	
G656	TM6 moves up to 15 A proximal to G656.	
Mutation	**Effect**	**Reference**
K588A	Channel shows outward rectification.	(Paulino et al., 2017b)
K645A	Channel shows outward rectification.	
R535A	Channel shows inward rectification.	
R515A	Channel shows deviation from the linear current-voltage relationship in both directions.	
G644A, G644P	Left-shift in the half-maximal effective concentration (EC_{50}).	(Paulino et al., 2017a)
G644P	Constitutive current observed in the absence of Ca^{2+} indicates basal activity of the mutant.	
I550A	Increases the potency of Ca^{2+} and gives rise to basal currents. Pore lining residue.	

Table 1.4: Key residues for mTMEM16A function and effects of mutations. Colour coding matches Figure 1.12.

The TMEM16A structure is important to consider when developing an inhibitor of TMEM16F. If the inhibitor is to act selectively, it must show a mechanism of action which distinguishes between the TMEM16F scramblase and the TMEM16A ion channel functions of these structurally similar proteins.

1.16 mTMEM16F

The mouse TMEM16F (mTMEM16F) structure was solved in 2019 (Alvadia et al., 2019). mTMEM16F shares over 90% sequence homology to human TMEM16F (hTMEM16F) and shows all the classical structural features of the TMEM16 family (homodimer, 10 transmembrane domains and a dimer interface packed with lipids). The mTMEM16F structure is most similar to the mTMEM16A structure (with an amino acid identity of 35.4% and similarity of 52.1% throughout the protein, higher in transmembrane regions (Suzuki et al., 2014)), perhaps reflecting the low sequence homology to the fungal homologues, though general architectures match. Unlike the fungal homologues, no obvious membrane distortion was apparent when mTMEM16F was reconstituted in lipid nanodiscs, though the resolution of these structures was relatively low (Alvadia et al., 2019).

Two distinct conformations of mTMEM16F were found by Alvadia et al. The Ca^{2+} free, inactive mTMEM16F structure closely resembles that of the Ca^{2+} free and inactive nhTMEM16. The hydrophilic groove is closed off from the membrane core by close association of TM4 and TM6. Upon Ca^{2+} binding TM6 moves by almost 20° around G615 away from TM4 to open the groove. The Ca^{2+} bound mTMEM16F structure, however, does not show a fully open groove; this structure more closely resembles the intermediate state of nhTMEM16 where there is still a constriction at the extracellular end of the groove (Figure 1.13). It remains to be determined whether the captured structure truly represents an intermediate or fully activated mTMEM16F. A fully open structure might not have been found due to its transient nature or instability during sample preparation. It is also possible that the mechanism of scrambling in mTMEM16F differs significantly to that observed in fungal homologues.

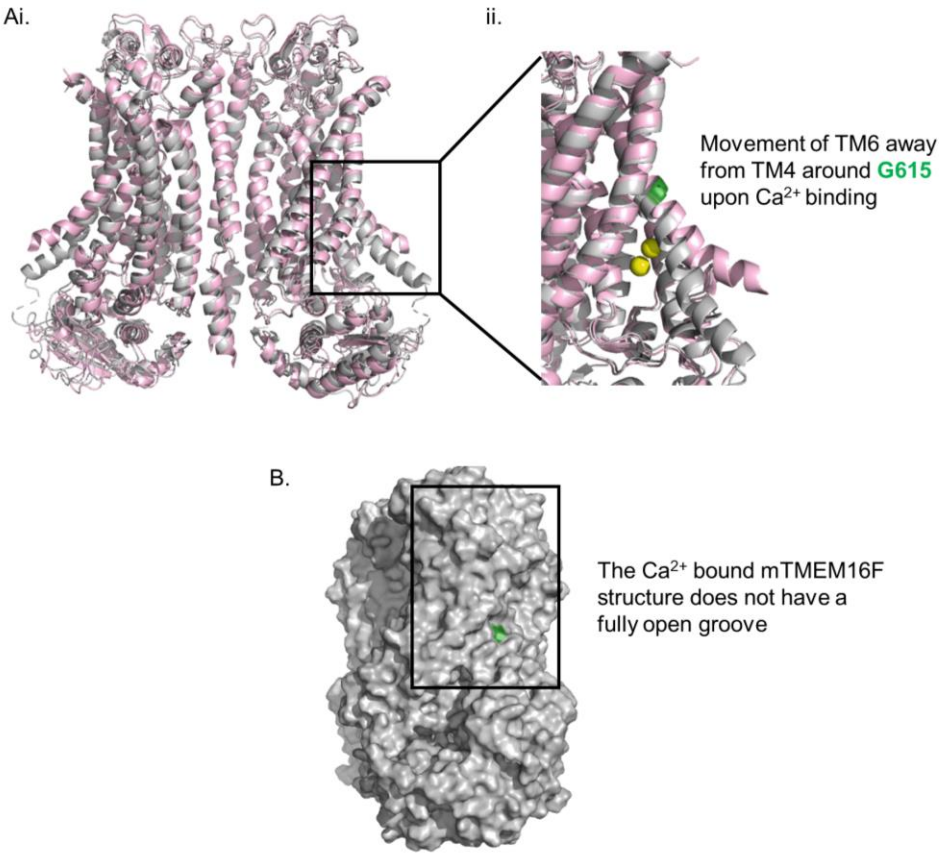

Figure 1.13: Ca^{2+} bound and Ca^{2+} free mTMEM16F structures. (Ai) Ribbon representation of Ca^{2+} bound mTMEM16F structure PDB ID: 6QP6 (grey) overlaid with the Ca^{2+} free mTMEM16F structure PDB ID: 6QPB (Alvadia et al., 2019). (Aii) Enlarged view of hinge residue G615 highlighted in green. (B) Space filling representation of Ca^{2+} bound mTMEM16F.

If the captured structure represents a fully activated mTMEM16F, then following Ca^{2+} binding, two thirds of the groove remains shielded from the membrane core. Scrambling may occur via an out-of-the-groove mechanism whereby the opening of the cytosolic end of the groove causes local membrane distortion and lowers the energy barrier for out-of-the-groove transport.

Functional studies, however, suggest that a fully open state may exist. Ion conductance and phospholipid scrambling are both regulated by Ca^{2+} binding but differentially affected by various mutations around the groove. Alvadia et al. proposed that in the presence of Ca^{2+} an equilibrium exists between the intermediate and fully open states of mTMEM16F, as proposed for the fungal scramblases, with the intermediate state supporting ionic conductance and the complete opening of the groove required for lipid scrambling. Movement of the extracellular portions of TM3 and TM4 may be responsible for the further opening of the extracellular end of the groove and transition to a fully open state (Alvadia et al., 2019).

Mutations in mTMEM16F sites corresponding to the S_{ext} and S_{cy} site in nhTMEM16 of Bethel and Grabe (R478, K530, E604) reduce or inhibit scrambling activity, suggesting these hydrophilic residues are critical for PS exposure (Gyobu et al., 2017). Further mutational studies identified that an inner activation gate was established by the 3 hydrophobic residues F518, Y563 and I612. F518K and Y563K are constitutively active phospholipid scramblases which no longer need to be activated by Ca^{2+} (Figure 1.14). Mutation of L543K in TMEM16A in the analogous inner gate position conferred scrambling activity to the channel (Le et al., 2019) though other studies found that a longer 35 amino acid "scrambling domain" needed to be engineered into mTMEM16A to confer scrambling activity in this region (Gyobu et al., 2017; Yu et al., 2015).

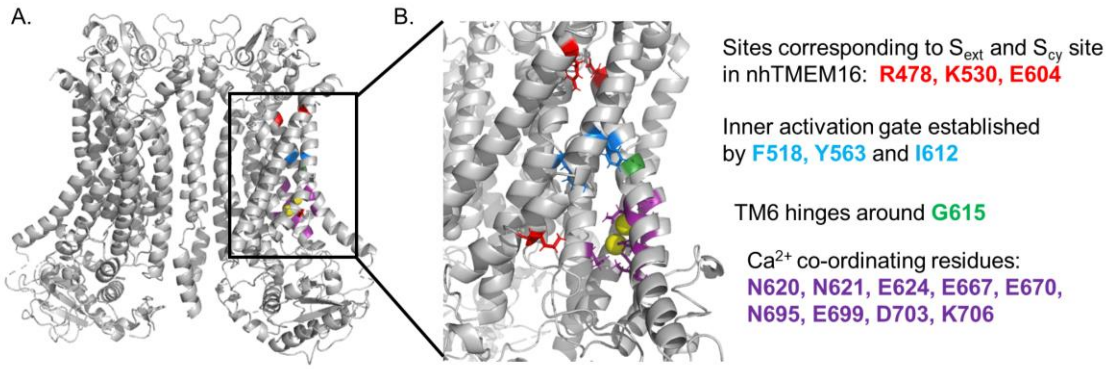

Figure 1.14: Critical groove residues in mTMEM16F. (A) Ribbon representation of Ca^{2+} bound mTMEM16F structure PDB ID: 6QP6 (Alvadia et al., 2019). (B) Enlarged view of critical residues in the groove. Highlighted in red are R478, K530, E604 which are residues corresponding to S_{ext} and S_{cy} in nhTMEM16. Highlighted in blue are F518, Y563 and I612 which establish an inner activation gate. Highlighted in purple are the Ca^{2+} co-ordinating residues N620, N621, E624, E667, E670, N695, E699, D703 and K706. More information about these residues is detailed in the main text and Table 1.5.

A second series of mTMEM16F structures were published, additionally showing that PIP_2 regulates conformational changes of mTMEM16F. Particularly, with PIP_2 supplementation, TM6 was found to kink at P628 causing membrane distortion around TM6 and pre-TM1 as well as membrane thinning around TM3 and TM4. mTMEM16F was able to thin the membrane locally by up to 40%, enabling lipid scrambling in the Ca^{2+} bound, PIP_2 supplemented state (Feng et al., 2019). This group also found that more lipids were bound to the Ca^{2+} activated structure compared to the Ca^{2+} free structure (Figure 1.15). Two different states were found in PIP_2 supplemented structures, termed class 1 and class 2, with class 2 demonstrating more prominent membrane thinning and phospholipids at most slanted angles. This group also did not find any structures with a fully open groove but again found evidence for different states

since mutations affected scrambling and channel activity separately. A difference between these structures and those of Alvadia et al., was that only a single Ca^{2+} was resolved in each monomer.

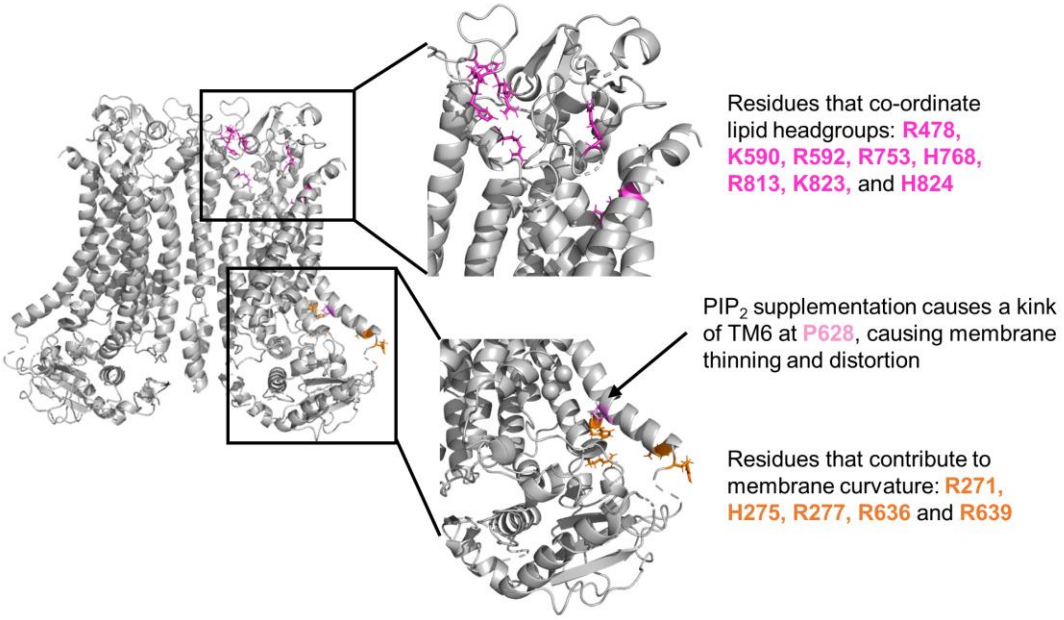

Figure 1.15: Residues involved in membrane distortion and lipid binding in mTMEM16F. Ribbon representation of Ca^{2+} bound mTMEM16F structure PDB ID: 6QP6 (Alvadia et al., 2019). Enlarged views of critical residues. Highlighted in magenta are R478, K590, R592, R753, H768, R813, K823, H824 which are residues that co-ordinate lipid headgroups. Highlighted in pink is P628 where TM6 kinks following PIP_2 supplementation. Highlighted in orange are R271, H275, R277, R636 and R639, which contribute to membrane curvature. More information about these residues is detailed in the main text and Table 1.5.

Table 1.5 details important residues within the mTMEM16F structure and the functional effects of mutations which have informed our current understanding of the mechanism of TMEM16F scramblase activity.

mTMEM16F		
Residue	**Roles**	**Reference**
G615, N620, N621, E624, E667, E670, N695, E699, D703, K706	Co-ordinate Ca^{2+} on TM6, TM7 and TM8.	(Alvadia et al., 2019)
E395, K398, S854, I857, P858, D859	Putative Ca^{2+} binding site at end of α10.	
F518, Y563, I612	Inner activation gate of hydrophobic residues.	(Le et al., 2019)
N621, E670, D703 (likely E624)	Co-ordinate Ca^{2+} on TM6, TM7 and TM8.	(Feng et al., 2019)
G615	Straightening of TM6 upon Ca^{2+} binding.	
R478, K590 and R592	Co-ordinate a lipid in PIP_2 supplemented TMEM16F in nanodiscs. R478 corresponds to E313 in nhTMEM16 where MD simulations show phospholipid headgroups being scrambled.	
E604	E604 corresponds to R432 in nhTMEM16 where MD simulations show phospholipid headgroups being scrambled.	
R753 and H768 **R813, K823, and H824**	Co-ordinate lipid headgroups in Ca^{2+} bound TMEM16F in digitonin on TM9-TM10 and TM9-TM10 loop. R573 and H768 important for lipid scrambling but not channel function.	
P628	PIP_2 required for a kink of TM6 at P628, causing membrane thinning and distortion.	
R271, H275, R277, R636, R639	Cluster to attract lipid headgroups contributing to membrane curvature and distortion.	
R542	On TM4-TM5 loop, only contacts TM2-TM3 loop in absence of Ca^{2+}.	
K706	On TM8, within proximity of E624 only in Ca^{2+} bound TMEM16F.	
K526	Essential for PS exposure – a “stepping stone”.	(Gyobu et al., 2017)
Mutations	**Effects**	**Reference**
K370A	No effect on lipid scrambling – outside groove.	(Alvadia et al., 2019)
R478A	Reduced current conduction, located in pore. Increases Ca^{2+} potency. Decreased rate of lipid scrambling.	
Q559K	Lower Ca^{2+} potency, located in pore. Change in ion selectivity but unaffected lipid scrambling.	
G615A	Increased potency for Ca^{2+} due to stabilisation of open state of the channel.	
Q623F	No effect on lipid scrambling – outside groove.	
E624Q	Virtually no detectable scrambling activity.	
E667Q	Decreased potency for Ca^{2+} for both scrambling and ion conduction.	
mTMEM16F^{SCRD}	Reduced scrambling activity. Some ion conduction although lower.	
D409G	Accelerated scrambling in HEK293T cells.	(Le et al., 2019)
F518A	Increased PS exposure compared to WT following ionomycin.	
F518W	Mild gain of function mutation to increase scrambling.	
F518L	Reduced scramblase activity.	
F518E and I612E	Spontaneous PS exposure.	
F518K and Y563K	Constitutively active scramblases.	
F518K-D703R	Show constitutive PS exposure.	
F518A-Y563A-I612A	Additive effect of the triple mutants, more enhanced PS exposure compared to the single mutants.	
Y563A	Constitutive PS exposure, even in absence of Ca^{2+}. Enhanced ion channel activity, no desensitisation.	

	Likely induces cytotoxicity.	
Y563W	Reduced phospholipid scrambling.	
Y563K-D703R	Show constitutive PS exposure.	
I612A	Increased PS exposure compared to WT following ionomycin.	
I612W	Reduced phospholipid scrambling.	
I612Q	Modest gain of function for scrambling.	
I612K	Less destabilising than F518K and Y563K.	
D703R	Abolished phospholipid scrambling.	
R271A/H275A/R277A	Accelerated onset of Ca^{2+} influx, PS exposure and GPMV generation.	(Feng et al., 2019)
R478A **R478A/K590A**	Delayed onset of GPMV formation.	
R478A/K590A/R592A	Delayed onset of PS exposure. No GPMV formation.	
E529A	Delayed onset of Ca^{2+} influx, PS exposure and GPMV formation. Reduced channel activity, reduced sensitivity to Ca^{2+}.	
E530A	Milder effect than E529A.	
R542A	Accelerated onset of Ca^{2+} influx, PS exposure, and GPMV formation.	
E604A	More delayed PS exposure and GPMV formation compare to E29A. Reduced channel activity, reduced sensitivity to Ca^{2+}.	
N621A	Reduced Ca^{2+}, GPMV formation and PS exposure.	
R636A/R639A	Accelerated onset of PS exposure, no effect on Ca^{2+} influx. Residues important for lipid scrambling but not channel function.	
K706A	Reduced Ca^{2+} and GPMV formation.	
R753A/H768A	Delayed onset of PS exposure, no effect on onset of Ca^{2+} influx .	
R813A/K823A/H824A	Slowed Ca^{2+} influx, PS exposure and GPMV formation.	
Q559K	Increases permeability to Cl^- as intracellular Ca^{2+} increases.	(Ye et al., 2019)
R478A	Ca^{2+} induced PS exposure abolished but phospholipid internalising activity was unaffected.	(Gyobu et al., 2017)
K530C	Reduced PS exposure to 40% WT and NBD-PS incorporating activity to 70% WT. No effect on NBD-PC incorporation.	
E604A	Reduced PS exposure to 20% WT and NBD-PS incorporating activity to 50% WT. No effect on NBD- PC incorporation.	
D409G	Constitutive PS exposure. Increase calcium sensitivity of TMEM16F.	(Scudieri et al., 2015)
Q559K	No channel activity but unaffected scramblase activity.	
D409G	Constitutive PS exposure – identification of TMEM16F. Increased sensitivity to calcium.	(Suzuki et al., 2010)

Table 1.5: Key residues for mTMEM16F function and effects of mutations. Colour coding matches Figures 1.13-1.15.

1.17 TMEM16K

TMEM16K is a Ca^{2+}-dependent endoplasmic reticulum (ER) associated lipid scramblase, which maintains PS on the cytoplasmic leaflet of the ER membrane (Tsuji et al., 2019) and also shows non-selective ion channel activity. TMEM16K has recently been shown to regulate endosomal sorting (Petkovic et al., 2020). TMEM16K is also of note as mutations are associated with the autosomal recessive disorder spinocerebellar ataxia type 10 (SCAR10) (Nanetti et al., 2019). It would be critical that any inhibitor of TMEM16F did not disrupt these functions of TMEM16K if it were to be used clinically.

The hTMEM16K structure was solved by X-ray crystallography (3.2 Å) (Bushell et al., 2019). Like other TMEM16 family members, hTMEM16K is a homodimer which adopts the classic butterfly TMEM16 fold with cytosolic N and C terminal domains and 10 transmembrane domains. The cytoplasmic domains differ more significantly compared to TMEM16F and TMEM16A. TM3-7 form the hydrophilic groove associated with phospholipid scrambling and residues on TM6-8 bind Ca^{2+}. These residues are highlighted in Figure 1.16 and detailed in Table 1.6. Ca^{2+} activates TMEM16K scramblase activity, though generally TMEM16K scrambles lipids at slower rates compared with other scramblases. Scramblase activity is higher in thinner membranes, suggesting TMEM16K has a preference for shorter lipids and appears to be more phospholipid selective.

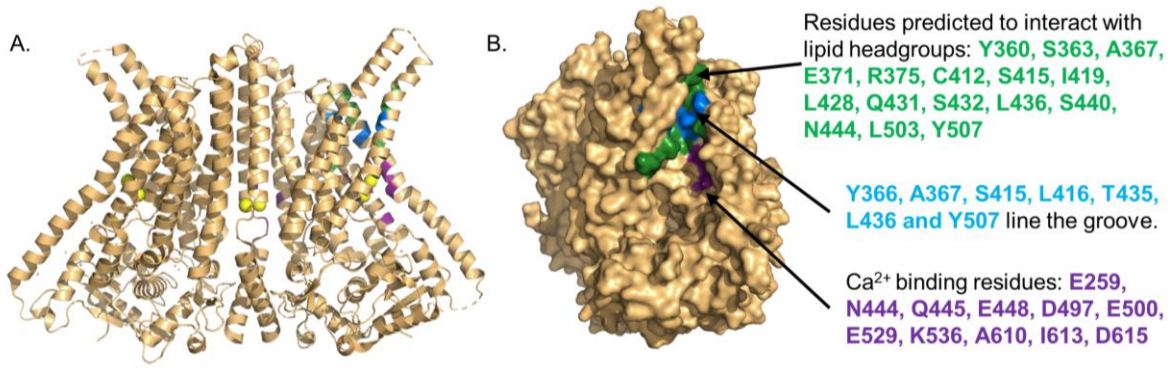

Figure 1.16: hTMEM16K structure and critical residues. (A) Ribbon representation of Ca^{2+} bound hTMEM16K structure PDB ID: 5OC9 (Bushell et al., 2019). (B) Space filling representation of hTMEM16K. Highlighted in green are Y360, S363, A367, E371, R375, C412, S415, I419, L428, Q431, S432, L436, S440, N444, L503 and Y507 which are residues predicted to interact with lipid headgroups. Highlighted in blue are Y366, A367, S415, L416, T435, L436, Y507 which line the groove. Highlighted in purple are the Ca^{2+} binding residues E259, N444, Q445, E448, D497, E500, E529, K536, A610, I613, D615. More information about these residues is detailed in the text and Table 1.6.

TMEM16K		
Residue	**Role**	**Reference**
E259, A610, I613, D615	Co-ordinate the TM10 and α10 Ca^{2+} ion	(Bushell et al., 2019)
N444, Q445, E448, D497, E500, E529, K536	Co-ordinate the TM6-8 Ca^{2+} ions.	
Y366, A367, S415, L416, T435, L436, Y507	Residues from TM4-7 line the hydrophobic neck of the closed groove.	
Y360, S363, A367, E371 R375 C412, S415, I419, L428, Q431, S432, L436, S440, N444, L503, Y507	Residues that MD simulations revealed had substantial interactions with lipid headgroups.	
Mutation	**Effect**	**Reference**
D615N	Mutation seen in once case of ataxia. This mutation did not affect lipid scrambling in the presence of saturating or no Ca^{2+}.	(Bushell et al., 2019)

Table 1.6: Residues and mutations key to hTMEM16K function. Colour coding matches Figure 1.16.

Over the past year a wealth of structural and mechanistic insight into the TMEM16 family of proteins has been gained. An understanding of this information will be critical to the design of inhibitors of TMEM16F. An inhibitor could be expected to act to stabilise the Ca^{2+} free inactive form of the protein, disrupt interactions of lipid headgroups in the hydrophilic groove or prevent local membrane deformations necessary for phospholipid scrambling.

1.18 Pharmacology of TMEM16F

No specific inhibitors of TMEM16F are currently available and to date knowledge of the pharmacology of TMEM16F has been limited.

R5421 was described as an inhibitor of platelet scramblase activity (Dekkers et al., 1998) and has been used to investigate the role of phospholipid scramblase activity across a range of cells and systems including erythrocytes, viral infection and placental function (Berghold et al., 2015; Wesseling et al., 2016; Younan et al., 2018). Whether R5421 directly interacts with TMEM16F is not known.

Polyphenolic compounds such as tannic acid and epigallocatechin gallate (EGCG') have also been shown to inhibit scramblase activity in mTMEM16F-overexpressing cell lines with low IC_{50} values (<1 μM) (Suzuki et al., 2014; Watanabe et al., 2018). In addition, various flavonoids have been shown to reduce platelet PS exposure including catechin and quercetin (Bucki et al., 2003), although it is not clear whether they directly block scramblase activity or inhibit signalling pathways leading towards scramblase activation. Polyphenolic compounds are known to be pleotropic and have many other effects on platelets unrelated to pro-coagulant

activity. EGCG' inhibits cyclooxygenase-1 and thromboxane synthase more potently than aspirin (Lee et al., 2013), inhibits thrombin proteolytic activity (Deana et al., 2003) and thrombin-, ADP- or collagen-induced aggregation, reducing phosphorylation of p38 MAPK and ERK-1/2 or heat shock protein 27 (Iida et al., 2014; Joo et al., 2018; Lill et al., 2003). EGCG' also increases platelet [cAMP] and inhibits PLCγ2, reducing Ca^{2+} mobilisation and thus platelet activation (Jin et al., 2008; Ok et al., 2012) and prolongs tail bleeding times in mice (Kang et al., 1999), which could be in part due to reduced PS exposure. Gallotannins have been shown to inhibit TMEM16A activity (Namkung et al., 2010), suggesting that these polyphenols may interact with multiple TMEM16 family members. These polyphenolic compounds are therefore clearly non-specific inhibitors of platelet scramblase activity. CaCC blockers, such as $T16A_{inh}$-A01 or NPPB, also inhibit TMEM16F activity but with lower potency (Suzuki et al., 2014). It is possible that these drugs are relatively selective for TMEM16A and related Cl^- channels, and only block TMEM16F at higher concentrations.

Little is known about the mechanism of action of these inhibitors of TMEM16F and many have not been tested for effects on platelet scramblase activity. For most of these inhibitors, however, there is clear evidence that they inhibit other proteins or pathways in addition to TMEM16F and would not be suitable compounds to test the effects of selectively inhibiting platelet pro-coagulant activity.

1.19 Aims

The aim of this thesis was to identify an inhibitor of TMEM16F to be used in order to test the hypothesis that TMEM16F inhibition could be a novel anti-thrombotic approach. Evidence from TMEM16F knock out mice and patients with Scott Syndrome suggest that targeting platelet pro-coagulant activity could be a novel anti-thrombotic approach associated with fewer bleeding side effects than current therapies.

To do this, I used a combination of *in silico* and wet lab techniques. First, I characterised the selectivity (or lack of it) of the previously described scramblase inhibitor R5421, and used a ligand-based approach to characterise a series of related molecules. Second, I investigated the inhibitory effects of polyphenolic catechin-based compounds on platelet phospholipid scrambling. Finally, I used a structure-based approach based around polyphenolic compounds to try to identify a new scaffold which more selectively inhibits platelet scramblase activity. Together, these studies increase our understanding of the pharmacology of TMEM16F and platelet phospholipid scramblase activity.

Chapter 2 - Materials and Methods

2.1 Materials

Chemical	Supplier	Code
A23187	Sigma-Aldrich	C7522
Adenosine 5′-diphosphate (ADP)	Sigma-Aldrich	01905
Adrenaline hydrochloride	Sigma-Aldrich	E4642
Apyrase	Sigma-Aldrich	A6535
Bovine thrombin	Sigma-Aldrich	T4648
$CaCl_2$	Sigma-Aldrich	21115
Catechin (C)	Cayman Chemical	18644
Catechin gallate (CG')	Cayman Chemical	24963
Citric acid	Sigma-Aldrich	C1909
Cross-linked collagen-related peptide (CRP-XL)	Prof. Richard Farndale, Department of Biochemistry, University of Cambridge	(Morton et al., 1995)
D-glucose	Fisher Scientific	G/0500/53
Digallic acid (DA)	Cayman Chemical	21224
Dimethylsulfoxide (DMSO)	Sigma-Aldrich	D2650
Epicatechin (EC)	Cayman Chemical	11807
Epicatechin gallate (ECG')	Cayman Chemical	11808
Epigallocatechin (EGC)	Cayman Chemical	11809
Epigallocatechin gallate (EGCG')	Cayman Chemical	70935
Gallocatechin (GC)	Cayman Chemical	16944
Gallocatechin gallate (GCG')	Cayman Chemical	24962
HEPES	Sigma-Aldrich	H3375
KCl	Sigma-Aldrich	P3911
$MgCl_2.6H_2O$	Sigma-Aldrich	M2670
NaCl	Sigma-Aldrich	S7653
$NaHCO_3$	VWR Chemicals	10247
Na_2HPO_4	Acros Organics	AC207802500
N-ethylmaleimide (NEM)	Sigma-Aldrich	E3876
PAR1-activating peptide (AP) (SFLLRN-amide trifluoroacetate salt)	Bachem	4031274

PAR4-activating peptide (AP) (AYPGKF - amide)	Peptide Synthetics	N/A
Paraformaldehyde (PFA)	Alfa Aesar	J61899
PGE_1	Santa Cruz	sc-201223
R5421 (ethaninidothioic acid)	EndoTherm	ENG071
Rosmarinic acid (RA)	Sigma-Aldrich	536954
Silybinin (SB)	Sigma-Aldrich	S0417
Tannic acid (TA)	Sigma-Aldrich	403040
Tri-sodium citrate	Sigma-Aldrich	71405

Conjugated antibody/protein	Supplier	Code
Alexa 47-conjugated anti-glycoprotein VI	BD Pharmingen	564701
FITC-conjugated PAC-1	BD Biosciences	340507
PE-Cy7-conjugated anti-CD41a	eBioscience	25-0419-42
PE-conjugated anti-CD62P	BD Pharmingen	555524
Annexin V (AV)-FITC	eBioscience	BMS306FI

Supplier information and codes for all screening compounds (A1-16, S1-15 and G1-21) are detailed in Table 3.1, Table 5.3 and Table 6.1 in the respective chapters which describe their use.

2.2 Washed platelet preparation

Blood was taken by venepuncture from healthy, drug-free volunteers who had given informed, written consent in accordance with the Declaration of Helsinki and with approval from the Human Biology Research Ethics Committee, University of Cambridge.

Blood was drawn into sodium citrate (3.2% v/v) vacutainers (Greiner Bio-One). Acid citrate dextrose (ACD; in mM: 85 tri-sodium citrate, 71 citric acid, 111 D-glucose) was added (1:7 v/v) and platelet rich plasma (PRP) was separated by centrifugation (200 g, 10 minutes, ambient temperature and without brake).

Washed platelets were prepared as previously described (Wei et al., 2018). PRP was collected and diluted 1:1 v/v with HEPES-buffered saline (HBS; in mM: 135 NaCl, 3 KCl, 10 HEPES, 1 $MgCl_2.6H_2O$, 0.34 Na_2HPO_4, 12 $NaHCO_3$; pH 7.4) supplemented with 5 mM D-glucose (HBS-glucose). 100 nM prostaglandin E_1 (PGE_1) and apyrase (grade VII; 0.02 U/ml) were added to

prevent platelet activation. Platelets were pelleted by centrifugation (600 g, 10 minutes, ambient temperature). The platelet pellet was resuspended in HBS-glucose, counted on a BD Accuri C6 flow cytometer and then diluted to 5 x 10^7 platelets per ml unless otherwise specified. Apyrase was added (0.02 U/ml) and platelets were rested in a 30°C water bath for 30 minutes before use. Prior to use, $CaCl_2$ was added so stimulations occurred at 2mM Ca^{2+}.

2.3 Red blood cell (RBC) preparation

For RBC preparation, all PRP was removed and the remaining fraction was diluted 1:5 v/v in HBS-glucose. Cells were centrifuged twice (2000 g, 5 minutes, ambient temperature) and the supernatant discarded each time. Cell purity and count were measured by flow cytometry. The percentage of platelets remaining was controlled to always be less than 0.5%, based on forward and side scatter profiles. RBCs were re-suspended at desired density in HBS-glucose and rested at ambient temperature before use.

2.4 Flow cytometry of platelets

Platelets were pre-treated with compounds for testing at temperatures, concentrations and for durations specified in the main text. Compounds were dissolved in dimethylsulfoxide (DMSO) or HBS as appropriate. An equivalent amount of solvent was added to vehicle controls. Platelets were stimulated with agonists for durations and at temperatures as specified in the main text in the presence of 2 mM Ca^{2+}. Following stimulations, platelets were stained with fluorescently conjugated antibodies or proteins for 2 minutes at ambient temperature, then fixed with 1% paraformaldehyde (PFA) and diluted 1:5 v/v with HBS for analysis by flow cytometry (BD Accuri C6). PE-Cy7-conjugated anti-CD41a antibody (1:100) was used to positively identify platelets. Annexin V (AV)-FITC (1:100 in 2.5 mM Ca^{2+} HBS-glucose) was used to detect surface PS exposure. “No PS exposure” gates were set so that >99% of unstimulated platelets did not expose PS. “High level PS exposure” gates were set so that A23187-stimulated platelets all displayed high level PS exposure and the “medium level PS exposure” gate was set between the two. PS-positive platelet-derived microparticles were defined as $CD41^+/AV^+$ events that were smaller than 1 µm. Microparticle count was given as event count/µl of stimulated platelet suspension read. The 1 µm gate was set in forward scatter (FSC) using 1 µm silica beads as previously described (Wei et al., 2018). $\alpha_{IIb}\beta_3$ integrin activation was measured using FITC-conjugated PAC-1 antibody (1:20). P-selectin surface exposure was measured using PE-conjugated anti-CD62P antibody (1:20) as a marker of α-granule release. To measure surface expression of glycoprotein VI, Alexa 647-conjugated

anti-glycoprotein VI antibody (1:100) was used. For end-point analysis, 20,000 events were collected. Compensation was performed when necessary using OneComp eBeads (Invitrogen, 01-1111-41) according to the manufacturer's instructions.

2.5 RBC PS Exposure Assay

RBCs were incubated with 10 mM N-ethylmaleimide (NEM) (to inhibit flippase activity) for 15 minutes at 1.6 x 10^8 cells per ml. RBCs were washed to remove excess NEM and resuspended at 1.6 x 10^7 cells per ml. RBCs were incubated with vehicle (0.1% DMSO) or 100 µM compound for 10 minutes. RBCs were then stimulated with 100 µM Ca^{2+} and 0.4 µM A23187 for 30 minutes and compared to unstimulated RBCs (100 µM Ca^{2+} and HBS-glucose). NEM incubation, compound incubation and stimulations were all carried out at 37°C. RBCs were then stained with AV buffer (annexin V-FITC 1:100 in HBS, 2.5 mM Ca^{2+}) on ice for 30 minutes. Samples were diluted in HBS 2.5 mM Ca^{2+} and read immediately by flow cytometry. 20,000 RBC events were recorded. "No PS exposure" gates were set so that >99% of unstimulated RBCs did not expose PS. "Medium level PS exposure" gates were set such that ~10% of A23187-stimulated RBCs showed medium level PS exposure and the "high level PS exposure" gate was set above this.

2.6 Real-time AV binding assay

This assay was performed in white flat-bottomed 96-well plates; 90 µl platelet suspension at 1 × 10^8 per ml was pre-incubated with screening compounds or DMSO as a vehicle control for 10 minutes in the presence of 2 mM Ca^{2+} and then stimulated using 10 µM A23187 (dispensed via on-board injectors) to make a final volume of 100 µl, all at 37°C. Promega RealTime-Glo™ Annexin V Apoptosis Detection Assay kit (JA1001) was used according to manufacturer's instructions. Detection buffer containing 1 × Annexin V-SmBiT Reagent, Annexin V-LgBiT Reagent and Annexin V NanoBiT Substrate diluted in HBS-glucose was added in equal volume (100 µl) and luminescence was detected every 10 seconds for 10 minutes following stimulation using a FLUOstar Omega plate reader (BMG Labtech). The luminescence of an unstimulated control sample was subtracted from the stimulated samples to account for small increases in baseline luminescence over time. Peak scrambling rates were calculated from the gradients of luminescence traces using GraphPad Prism v.8.

2.7 Cal520 fluorescent signals

Undiluted PRP was loaded with 1 μM Cal520-AM (AAT Bioquest, 21130) for 10 minutes at 30°C. Apyrase (0.02 U/ml) and PGE_1 (100 nM) were present throughout. PRP was diluted 1:1 v/v with HBS-glucose and excess dye was washed away during the second centrifugation step, as above. Platelets were re-suspended at 5 x 10^7 platelets per ml in HBS-glucose, apyrase (0.02 U/ml) added and rested in a water bath at 30°C for 30 minutes before use. Cal520-loaded platelets were incubated with compounds for durations and at temperatures described in the main text in the presence of 2 mM Ca^{2+}. Cal520 florescence was monitored at ambient temperature using a FLUOStar Omega Plate Reader ((BMG Labtech); Excitation: 485nm, Emission: 520nm) in black, flat-bottomed 96-well plates. Fluorescence in unstimulated Cal520-loaded platelets was measured every 5 seconds for 1 minute before stimulation with the indicated agonist (dispensed via the onboard reagent injectors) and fluorescence was measured every 5 seconds for a further 10 minutes after stimulation. Fluorescence values were normalised to initial fluorescence values of vehicle controls containing DMSO. This F/F_0 normalisation accounts for variation in Cal520 loading between different experiments. Area under curve (AUC) represents the sum of fluorescence readings above baseline following stimulation.

2.8 *In silico* ligand-based screen around R5421

The 3D structure of R5421 was obtained from PubChem (ID: 124220090) and was then energy-minimised using MMFF94 forcefield implemented in Open Babel 3.0 (O'Boyle et al., 2011). Using the energy-minimised R5421 as a query, a subset of the Molport database comprising 10,000 readily purchasable diverse chemical scaffolds was screened, using ROCS (Rapid Overlay of Chemical Structures, version 3.1, OpenEye Scientific Software. Santa Fe, NM, USA) (Rush et al., 2005). The top 100 hits were ranked based on Tanimoto combo scores and the top 16 molecules purchased for wet testing. Alignments of compounds and similarity scores to R5421 were calculated using Forge software (Forge, version 10.6, Cresset) (Cheeseright et al., 2006).

2.9 *In silico* structure-based screen based on polyphenolic compounds

The 3D structures of all compounds were obtained from PubChem and were energy-minimised using MMFF94 forcefield implemented in Open Babel 3.0. These structures were then blindly docked using Autodock Vina (Trott and Olson, 2010) with an exhaustiveness of 64 into the nhTMEM16 (PDB ID: 4WIS) and mTMEM16F structures (PDB ID: 6QP6) prepared

for docking using UCSF Chimera (Pettersen et al., 2004). Docking poses were analysed as detailed in chapter 5 using a program developed by Tom Millington (attached in appendix). Highest ranked poses were re-docked using GOLD (Jones et al., 1997) and used as a query for FRED (McGann, 2011). The top 500 ranking hits from each FRED screen were re-docked using GOLD and the highest scoring compounds were selected for wet screening.

2.10 Statistics and data analysis

The number of biological repeats in each experiment is detailed in figure legends and represents independent platelet or RBC preparations from different donors. Wherever possible, experiments were repeated to at least n = 5 (Curtis et al., 2018). Homogeneity of variance was tested using Levene's test and normality of data tested using Shapiro-Francia test (both in Excel) to determine whether parametric analyses were justified. Statistical analyses were performed in GraphPad Prism v.8. All statistical tests were carried out using matched analyses of independent values (not technical replicates). Where individual treatment conditions were compared to DMSO controls, two-tailed Student's paired t-tests were used. Where multiple treatment conditions were compared to DMSO controls, data were analysed using one-way repeated measures ANOVA or two-way ANOVAs, both ways matching, and Sidak's or Dunnett's multiple comparison tests as appropriate (and only when F in ANOVA achieved statistical significance). p values <0.05 were taken to be statistically significant. * $p<0.05$, ** $p<0.01$, ***$p<0.001$.

Chapter 3 – R5421 is not a selective inhibitor of platelet phospholipid scramblase activity

R5421 (ethaninidothioic acid) was the only previously described inhibitor of platelet scramblase activity (Dekkers et al., 1998). Despite being used as a scramblase inhibitor by several groups in different systems (Berghold et al., 2015; Wesseling et al., 2016; Younan et al., 2018), the specificity of R5421 had not been well characterised. This chapter aimed to determine whether R5421 selectively inhibits platelet scramblase activity and perform a ligand-based screen focused around R5421 to try and identify new inhibitors of platelet scramblase activity. Figure 3.1 illustrates the chemical structure of R5421.

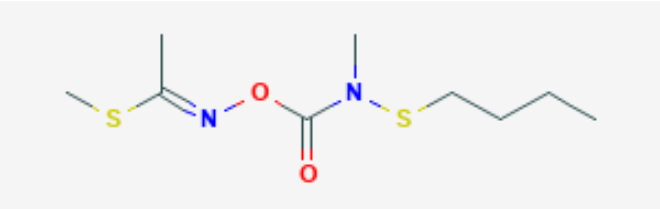

Figure 3.1: Chemical structure of R5421. Image taken from Pubchem.

3.1 R5421 slows platelet scrambling rate following stimulation with A23187 in a plate-based AV binding assay

A real-time plate-based annexin V (AV) binding luminescence assay was used to measure the rate of platelet scramblase activity. This assay uses two AV fusion proteins containing complementary subunits of NanoBiT Luciferase. PS exposure allows the AV fusion proteins to bind in proximity on the plasma membrane and generate a luminescence signal. The peak rate of PS exposure was slowed following incubation with 50 µM R5421 for 10 minutes at 37°C compared with 0.1% DMSO. The pIC_{50} for inhibition of peak scrambling rate by R5421 was 4.81 ± 0.06 (pIC_{50} values are given as mean ± standard error of the mean (SEM)) (Figure 3.2).

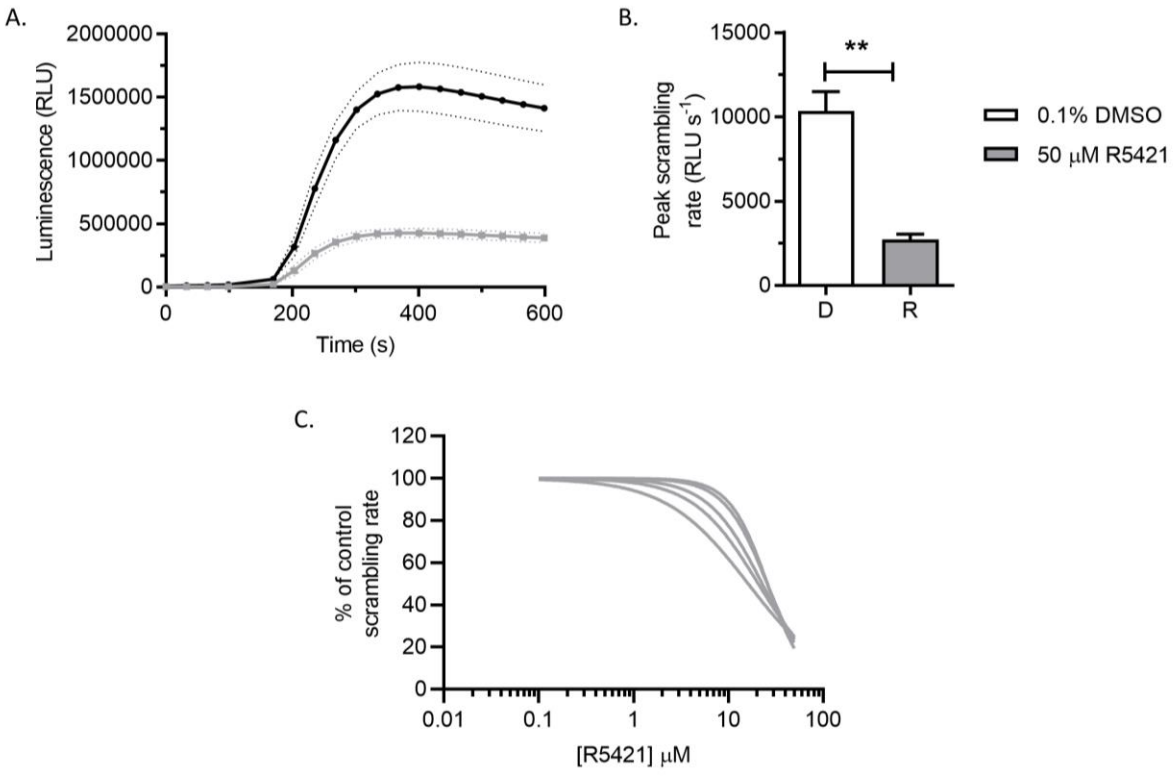

Figure 3.2: R5421 slows platelet scrambling rate. (A) Luminescence traces from a real-time plate-based AV binding assay following stimulation with 10 µM A23187 using platelets incubated with 50 µM R5421 or 0.1% DMSO. RLU: relative luminescence units. s: seconds. (B) Peak scrambling rate in platelets incubated with 50 µM R5421 or 0.1% DMSO. (C) Inhibition curves for R5421 slowing peak scrambling rate compared to 0.1% DMSO control. Bar chart and traces show mean ± SEM. N = 5. Data were analysed using a two-tailed Student's paired t-test. Black lines and white bar: 0.1% DMSO. Grey lines or bar: 50 µM R5421.

3.2 R5421 inhibits platelet PS exposure following stimulation with A23187 or thrombin + CRP-XL in a time- and temperature-dependent manner in a flow cytometry AV binding assay

Platelet PS exposure was measured by endpoint flow cytometry at 2 and 10 minutes post stimulation with 10 μM A23187. In contrast to the luminescence-based assay, a 10-minute incubation with 50 μM R5421 did not affect endpoint AV binding measured by flow cytometry under any conditions tested. A 60-minute incubation of R5421 at both ambient temperature and 37°C inhibited PS exposure at 2 minutes following stimulation. A 60-minute incubation of 50 μM R5421 at 37°C also inhibited PS exposure at 10 minutes following stimulation. Maximal endpoint inhibition was seen following incubation with R5421 for 60 minutes at 37°C and following 2 minutes of stimulation, consistent with an inhibition of the rate of PS exposure as more platelets become PS positive by 10 minutes post stimulation (Figure 3.3 A). The pIC_{50} value for inhibition by R5421 of PS exposure following stimulation with A23817 was 4.41 ± 0.04 (Figure 3.3 D). 50 μM R5421 also inhibited endpoint platelet PS exposure following a 10-minute stimulation with 1U/ml thrombin + 1 μg/ml cross-linked collagen-related peptide (CRP-XL; a glycoprotein VI (GPVI) agonist) (Figure 3.3 C). This inhibition was achieved following only a 10-minute incubation at ambient temperature and had a pIC_{50} value of 5.01 ± 0.40 (Figure 3.3 E).

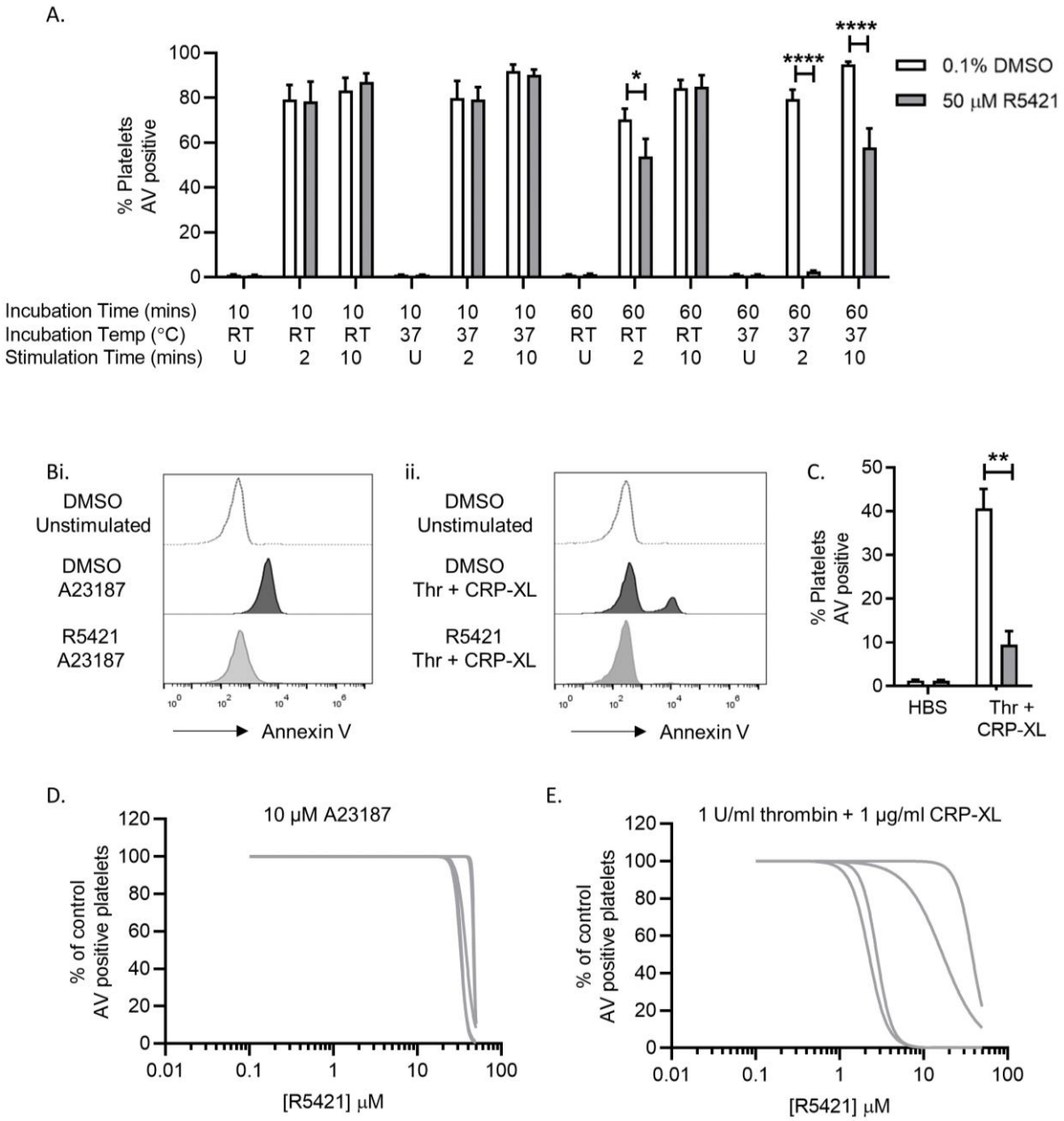

Figure 3.3: R5421 inhibits platelet PS exposure in a flow cytometry AV binding assay. (A) Flow cytometry AV binding after stimulation with 10 μM A23187 following different incubation conditions with 50 μM R5421 or 0.1% DMSO (10- or 60-minute incubations at ambient temperature (RT) or 37°C) and stimulation times (2 or 10 minutes; U, unstimulated). All stimulations were at ambient temperature. (B) Representative histograms of AV binding measured by flow cytometry following stimulation with (i) 10 μM A23187 or (ii) 1 U/ml thrombin + 1 μg/ml CRP-XL. Unshaded: unstimulated platelets. Black shading: 0.1% DMSO-treated platelets. Grey shading: 50 μM R5421-treated platelets. (C) Flow cytometry AV binding after a 10-minute incubation with 50 μM R5421 or 0.1% DMSO at ambient temperature and a 10-minute stimulation with 1 U/ml thrombin + 1 μg/ml CRP-XL at ambient temperature. (D) Inhibition curves for inhibition of platelet PS exposure by R5421 following stimulation with 10 μM A23187. (E) Inhibition curves for inhibition of platelet PS exposure by R5421 following stimulation with 1 U/ml thrombin + 1 μg/ml CRP-XL. White bars: 0.1% DMSO. Grey bars: 50 μM R5421. Bar charts show mean ± SEM. N = 4-5. Data were analysed using two-way ANOVA, both factors matching and Sidak's multiple comparisons test.

3.3 R5421 inhibits platelet $\alpha_{IIb}\beta_3$ integrin activation and α-granule release following stimulation with PAR1-AP

To determine whether R5421 has off-target effects in platelets, R5421-treated platelets were stimulated with protease-activated receptor 1-activating peptide (PAR1-AP; 10 μM). This stimulus was chosen as it effectively stimulates platelets to become pro-aggregatory but very few become pro-coagulant (Harper and Poole, 2011). R5421 inhibited $\alpha_{IIb}\beta_3$ integrin activation, measured by PAC-1 binding (Figure 3.4 A,B), with a mean pIC_{50} value of 5.32 ± 0.09 (Figure 3.4 G), and α-granule release, measured by an anti-CD62P antibody (Figure 3.4 C,D), with a mean pIC_{50} value of 4.67 ± 0.06 (Figure 3.4 H). These inhibitions were observed after a 10-minute incubation with R5421 at ambient temperature. R5421 inhibited $\alpha_{IIb}\beta_3$ activation and α-granule secretion even when platelets were co-stimulated with 10 μM PAR1-AP and 10 μM ADP or when platelets were co-stimulated with 10 μM PAR1-AP and 10 μM adrenaline (Figure 3.4 E,F).

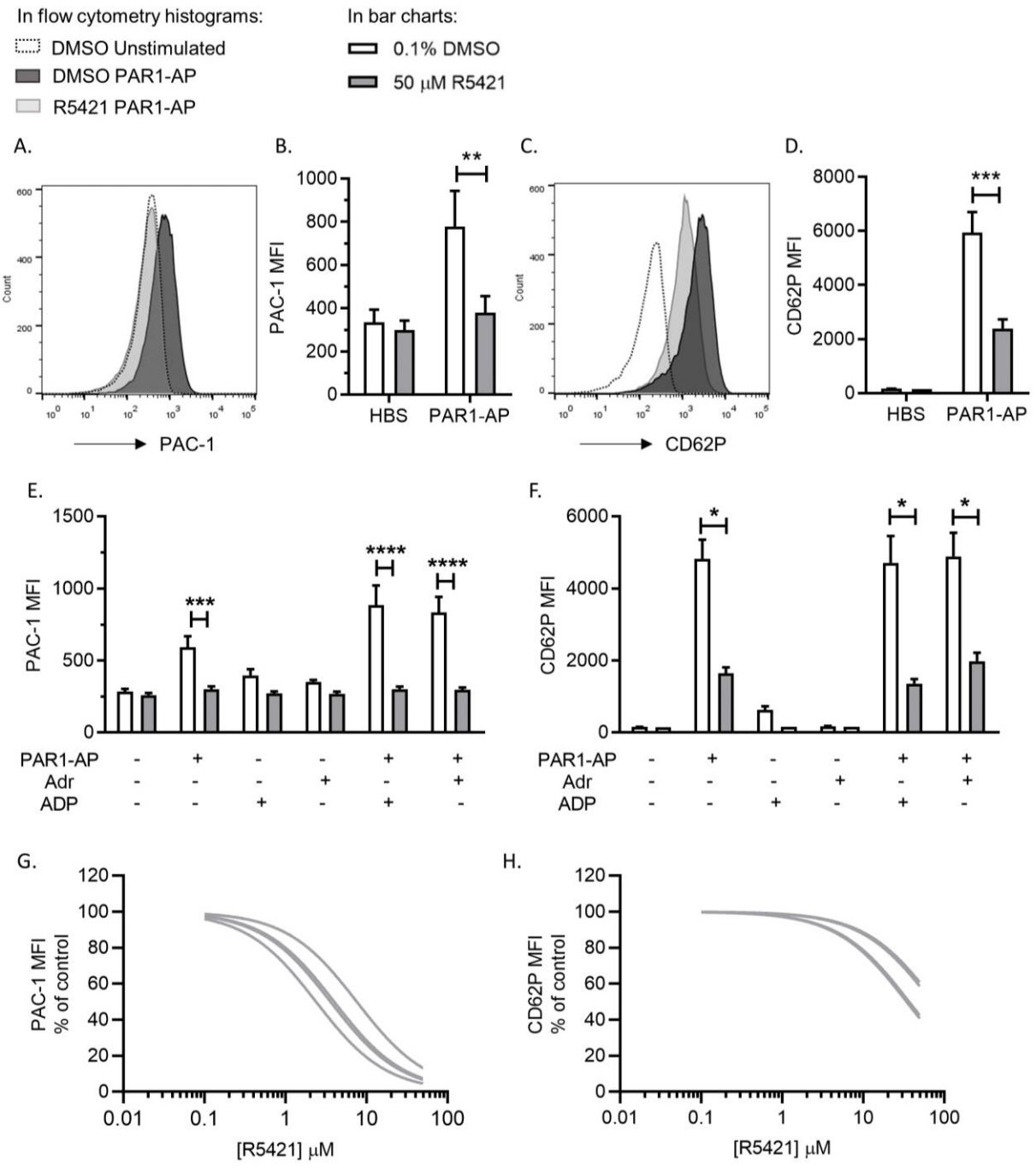

Figure 3.4: R5421 inhibits platelet $\alpha_{IIb}\beta_3$ integrin activation and α-granule release following stimulation with PAR1-AP. Platelets were treated with 50 μM R5421 or 0.1% DMSO for 10 minutes at ambient temperature prior to stimulation for 10 minutes. $\alpha_{IIb}\beta_3$ activation was measured by flow cytometry as PAC-1 binding (FITC conjugated). α-granule secretion was measured by anti-CD62P (P-selectin) antibody binding (phycoerythrin (PE) conjugated). (A) Representative histograms of PAC-1 binding. (B) PAC-1-FITC median fluorescence intensity (MFI) following stimulation with 10 μM PAR1-AP. (C) Representative histograms of anti-CD62P-PE fluorescence. (D) CD62P-PE MFI following stimulation with 10 μM PAR1-AP. (E) PAC-1 binding following stimulation with 10 μM PAR1-AP ± 10 μM ADP or 10 μM adrenaline. (F) CD62P binding following stimulation with PAR1-AP ± 10 μM ADP or 10 μM adrenaline. (G) Inhibition curves for R5421 inhibiting PAC-1 binding. (H) Inhibition curves for R5421 inhibiting CD62P binding. Bar charts show mean ± SEM. N = 5. White bars: 0.1% DMSO. Grey bars: 50-μM R5421. Inhibition curves N = 4. Data were analysed using two-way ANOVA, both factors matching and Sidak's multiple comparisons test.

3.4 R5421 inhibits platelet cytosolic Ca^{2+} signalling in response to a range of agonists

To investigate whether R5421 affected platelet Ca^{2+} signalling, platelets were loaded with the Ca^{2+}-sensitive fluorescent dye, Cal520. Stimulation with 10 µM A23187 resulted in a rapid and sustained increase in Cal520 fluorescence, which was not significantly affected by 50 µM R5421 pre-treatment (Figure 3.5 A). In contrast, R5421 inhibited Cal520 fluorescence following co-stimulation with 1 U/ml thrombin + 1 µg/ml CRP-XL. Although the peak F/F_0 was not significantly different, R5421 inhibited the sustained Ca^{2+} signal, whether quantified by area under the curve (AUC) or F/F_0 10 minutes post stimulation when samples were taken for flow cytometry analysis (Figure 3.5 B). R5421 inhibited platelet Cal520 fluorescence following stimulation with 10 µM PAR1-AP quantified by AUC, peak F/F_0 or F/F_0 at 10 minutes post stimulation, although the magnitude of this effect was relatively small (Figure 3.5 C). Similarly, although R5421 partially inhibited the peak F/F_0 following stimulation with 100 µM PAR4-AP, it did not significantly affect the sustained signal, quantified by AUC or F/F_0 at 10 minutes post stimulation (Figure 3.5 D). In contrast, R5421 significantly inhibited the Cal520 fluorescence signal in response to 1 µg/ml CRP-XL, when quantified by AUC, peak F/F_0 or F/F_0 at 10 minutes post stimulation (Figure 3.5 E). All Ca^{2+} signals were measured following incubations with R5421 that had been shown to inhibit platelet PS exposure, $\alpha_{IIb}\beta_3$ integrin activation or α-granule release above in Figures 3.2 – 3.4.

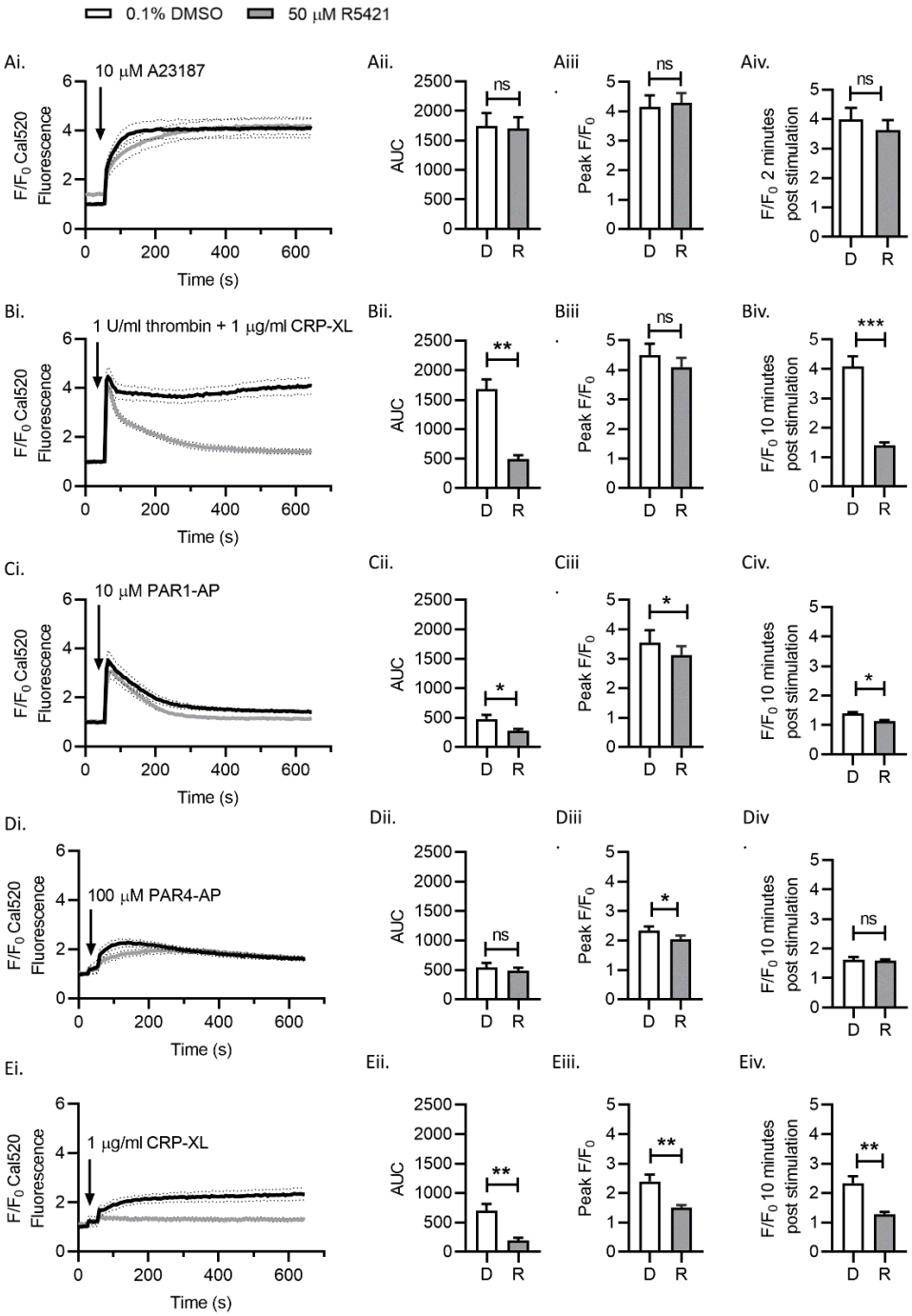

Figure 3.5: R5421 inhibits platelet Ca^{2+} signalling in response to a range of agonists. Platelets were loaded with the Ca^{2+}-sensitive fluorescence dye, Cal520. Fluorescence values were normalised to the initial fluorescence values of vehicle controls containing 0.1% DMSO in matched samples to account for variation in dye loading (F/F_0). Platelets were treated with 50 μM R5421 (grey lines and bars) or 0.1% DMSO (black lines and white bars) under conditions that inhibited PS exposure or integrin activation in previous experiments (i.e., in (A), 60-minute incubation at 37°C and in (B)–(E), 10-minute incubation at ambient temperature). Where indicated, platelets were stimulated with (A) 10 μM A23187; (B) 1 U/ml thrombin + 1 μg/ml CRP-XL; (C) 10 μM PAR1-AP; (D) 100 μM PAR4-AP; and (E) 1 μg/ml CRP-XL. All stimulations were at ambient temperature. Data are presented as (i) F/F_0 Cal520 fluorescence following stimulation; (ii) AUC above baseline ($F/F_0 = 1$); (iii) peak F/F_0 following stimulation; and (iv) F/F_0 at corresponding time of inhibition of PS exposure or integrin activation in flow cytometry (i.e., in (A), 2 minutes and in (B)–(E), 10 minutes). In (ii)–(iv) for each stimulation mean ± SEM is also given. N = 5. Data were analysed using two-tailed Student's paired t-tests.

3.5 A ligand-based screen around R5421 identified 16 compounds with similar physical and electrochemical properties

Since R5421 appeared to have multiple inhibitory effects on platelets, it was decided to see if it was possible to pharmacologically separate these effects by using molecules similar to R5421. An *in silico* ligand-based screen around R5421 identified 16 commercially available compounds that were tested using the plate-based AV binding assay. The structures for these compounds are given in Table 3.1 alongside compound similarity scores, accounting for fields and shape, to R5421 generated using Forge v10.6 (Cresset). Figure 3.6 illustrates the lowest energy 3D conformation of R5421 and its electrostatic fields.

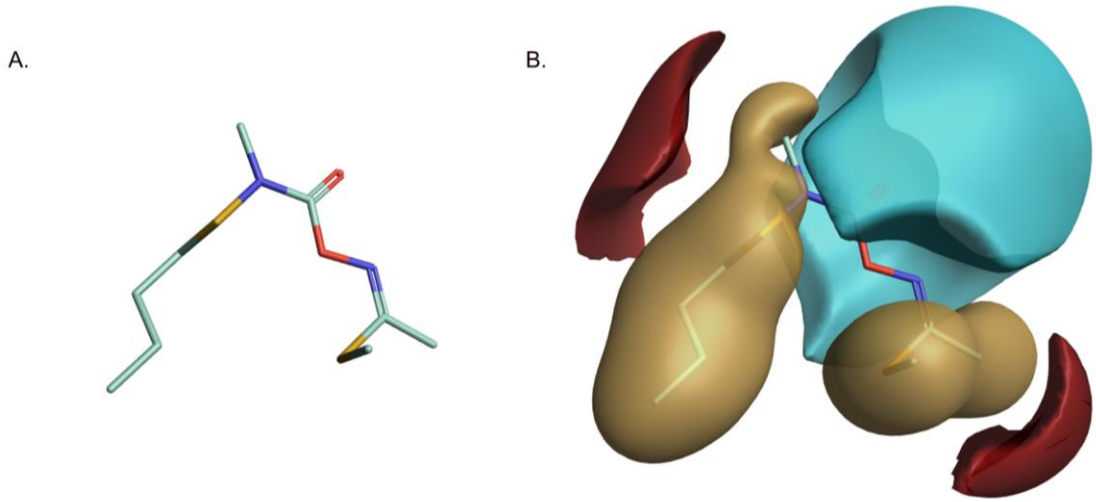

Figure 3.6: Electrostatic fields around R5421. (A) Lowest energy 3D conformation of R5421 calculated using Forge. (B) Electrostatic fields around R5421 calculated using Forge. Negative electrostatic fields shown in blue, positive electrostatic fields shown in red, hydrophobic fields shown in yellow.

Table 3.1: Chemical structures and supplier information of compounds A1-A16 identified by ligand-based screen around R5421. Similarity scores calculated using Forge. MW- molecular weight.

Compound	Molport ID	IUPAC	MW	Similarity	Structure
A1 Thiodicarb	006-131-791	[1-(methylsulfanyl)ethylidene]amino N-methyl-N-[(3-methyl-6-oxo-5-oxa-2-thia-4,7-diazaoct-3-en-7-yl)sulfanyl]carbamate	354.46	0.705	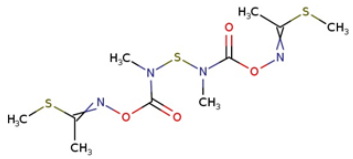
A2	003-035-355	1-(2,4-dichlorobenzoyl)-2-(ethylsulfanyl)-4,5-dihydro-1H-imidazole	303.20	0.639	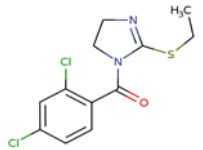
A3	019-921-409	N-(but-3-yn-1-yl)cyclopropanesulfonamide	173.23	0.684	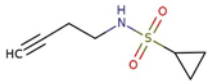
A4	019-921-413	N-(but-3-yn-1-yl)-1-(3-methylphenyl)methanesulfonamide	237.32	0.659	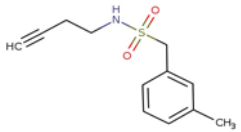
A5	028-614-144	3-methyl-N-[3-(propan-2-yloxy)propyl]-1,2,4-thiadiazole-5-carboxamide	243.33	0.674	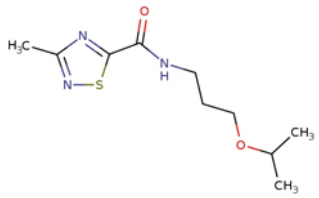

A6	035-671-151	N-[2-(furan-2-yl)-2-methoxyethyl]butanamide	211.26	0.678	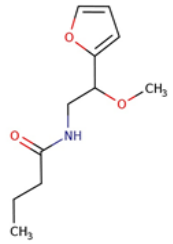
A7	039-214-408	2-[(tert-butylsulfanyl)methyl]-1-cyclopropanecarbonylpiperidine	255.42	0.683	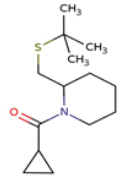
A8	039-214-429	1-{2-[(tert-butylsulfanyl)methyl]piperidin-1-yl}-2-methoxyethan-1-one	259.41	0.691	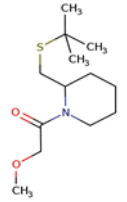
A9	002-892-383	ethyl 2-(methylsulfanyl)-1,4,5,6-tetrahydropyrimidine-1-carboxylate	202.27	0.656	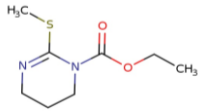
A10	002-905-880	4,4-dimethyl-1,1-bis(methylsulfanyl)pent-1-en-3-one	204.35	0.751	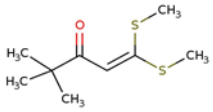

A11	002-911-246	2-(ethylsulfanyl)-5,6-dimethyl-3,4-dihydropyrimidin-4-one	184.26	0.703	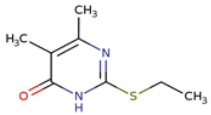
A12	002-913-559	ethyl 2-{[(methylsulfanyl)methanethioyl]amino}acetate	193.28	0.655	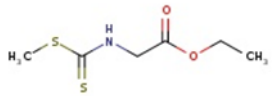
A13	002-466-999	N-[4-(chloromethyl)-1,3-thiazol-2-yl]-N-ethylacetamide	218.70	0.747	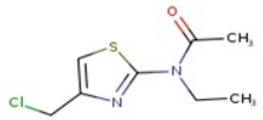
A14	002-470-805	N-ethyl-N-(4-formyl-1,3-thiazol-2-yl)acetamide	198.24	0.732	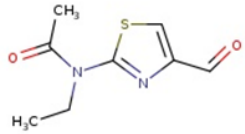
A15	002-479-974	N,N-dibutylsulfamoyl chloride	227.75	0.700	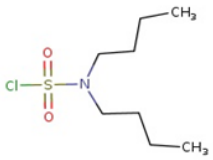
A16	028-299-557	N-[1-(ethylsulfanyl)propan-2-yl]-N-methyl-2-(5-methyl-1,2-oxazol-3-yl)acetamide	256.36	0.719	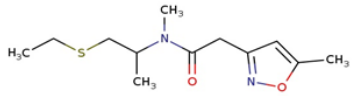

3.6 Compounds A1 and A2 slow platelet scrambling rate following stimulation with A23187 in a plate-based AV binding assay

The compounds A1-A16 were blinded for screening purposes. All compounds were screened at 100 µM. Compounds A1 and A2 slowed the rate of scrambling following stimulation with 10 µM A23187 compared to 0.1% DMSO-treated control following a 10-minute incubation of platelets with compounds at 37°C (Figure 3.7).

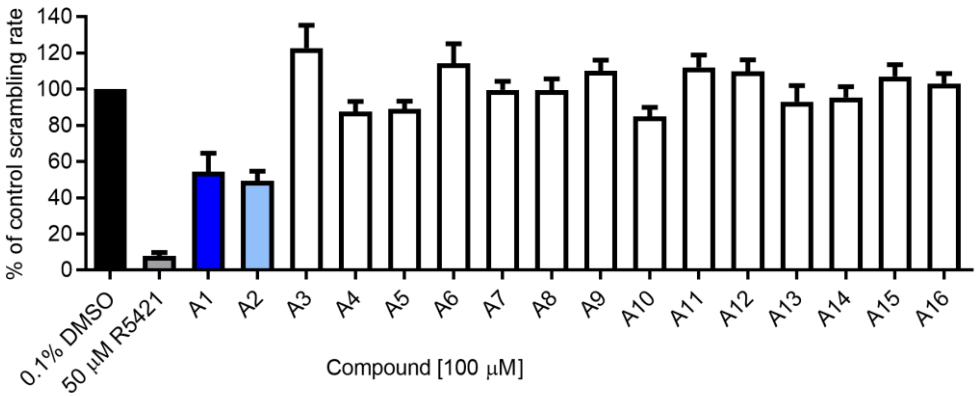

Figure 3.7: A1 and A2 slow platelet scrambling rate. Peak scrambling rate in platelets incubated with 50 µM R5421 or 100 µM A1-A16 as a percentage of 0.1% DMSO-treated control. Bars show mean ± SEM. N =5. Statistical tests were not applied to this initial screen.

3.7 A1 inhibits platelet PS exposure following stimulation with A23187 or thrombin + CRP-XL in a flow cytometry AV binding assay

Compounds A1 and A2 were tested in a flow cytometry-based AV binding assay, to exclude any inhibition due to assay-dependent effects. Only compound A1 (100 µM) inhibited platelet PS exposure following a 2-minute stimulation with 10 µM A23187 after a 60-minute incubation at 37°C. Under these incubation conditions, A1 treatment also tended towards increased PS exposure in unstimulated platelets and increased AV positive microparticle release from unstimulated platelets, though these did not reach statistical significance (Figure 3.8 A). A1 inhibited PS exposure and AV microparticle formation following a 10-minute incubation at ambient temperature and a 10-minute stimulation with 1U/ml thrombin + 1 µg/ml CRP-XL, as did R5421, when measured by flow cytometry (Figure 3.8 B). A2 had no effect on PS exposure following stimulation with A23187 or thrombin + CRP-XL when measured by flow cytometry.

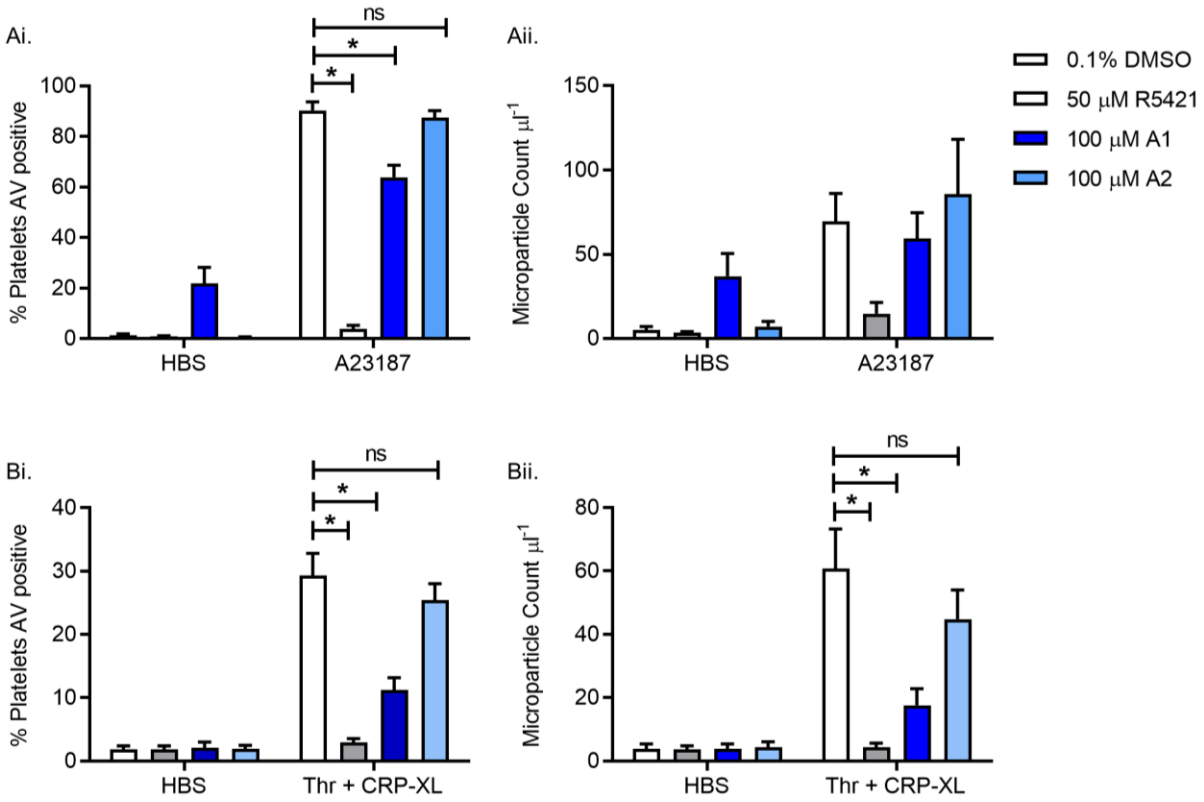

Figure 3.8: A1 inhibits platelet PS exposure in a flow cytometry AV binding assay. (Ai) Flow cytometry AV binding after a 2-minute stimulation with 10 µM A23187 following incubation with 50 µM R5421, 100 µM A1 or A2 or 0.1% DMSO for 60 minutes at 37°C. (Aii) AV positive microparticle count following stimulation with 10 µM A23187. (Bi) Flow cytometry AV binding after a 10-minute incubation with 50 µM R5421, 100 µM A1 or A2 or 0.1% DMSO at ambient temperature and a 10-minute stimulation with 1 U/ml thrombin + 1 µg/ml CRP-XL at ambient temperature. (Bii) AV positive microparticle count following stimulation with 1 U/ml thrombin + 1 µg/ml CRP-XL. White bars: 0.1% DMSO, grey bars: 50 µM R5421, dark blue bars: 100 µM A1, light blue bars: 100 µM A2. Bar charts show mean ± SEM. N = 5. Data were analysed using two-way ANOVA, both factors matching and Dunnett's multiple comparisons test.

3.8 A1 (Thiodicarb) inhibits platelet $\alpha_{IIb}\beta_3$ integrin activation and α-granule release following stimulation with PAR1-AP

A1 also inhibited platelet $\alpha_{IIb}\beta_3$ integrin activation (pIC_{50} 5.03 ± 0.27, Figure 3.9 A,C) and α-granule release (pIC_{50} 4.52 ± 0.12, Figure 3.9 B,D) following a 10-minute stimulation with 10 µM PAR1-AP after a 10-minute incubation at ambient temperature. When the compounds were unblinded, A1 was revealed to be thiodicarb, a pesticide.

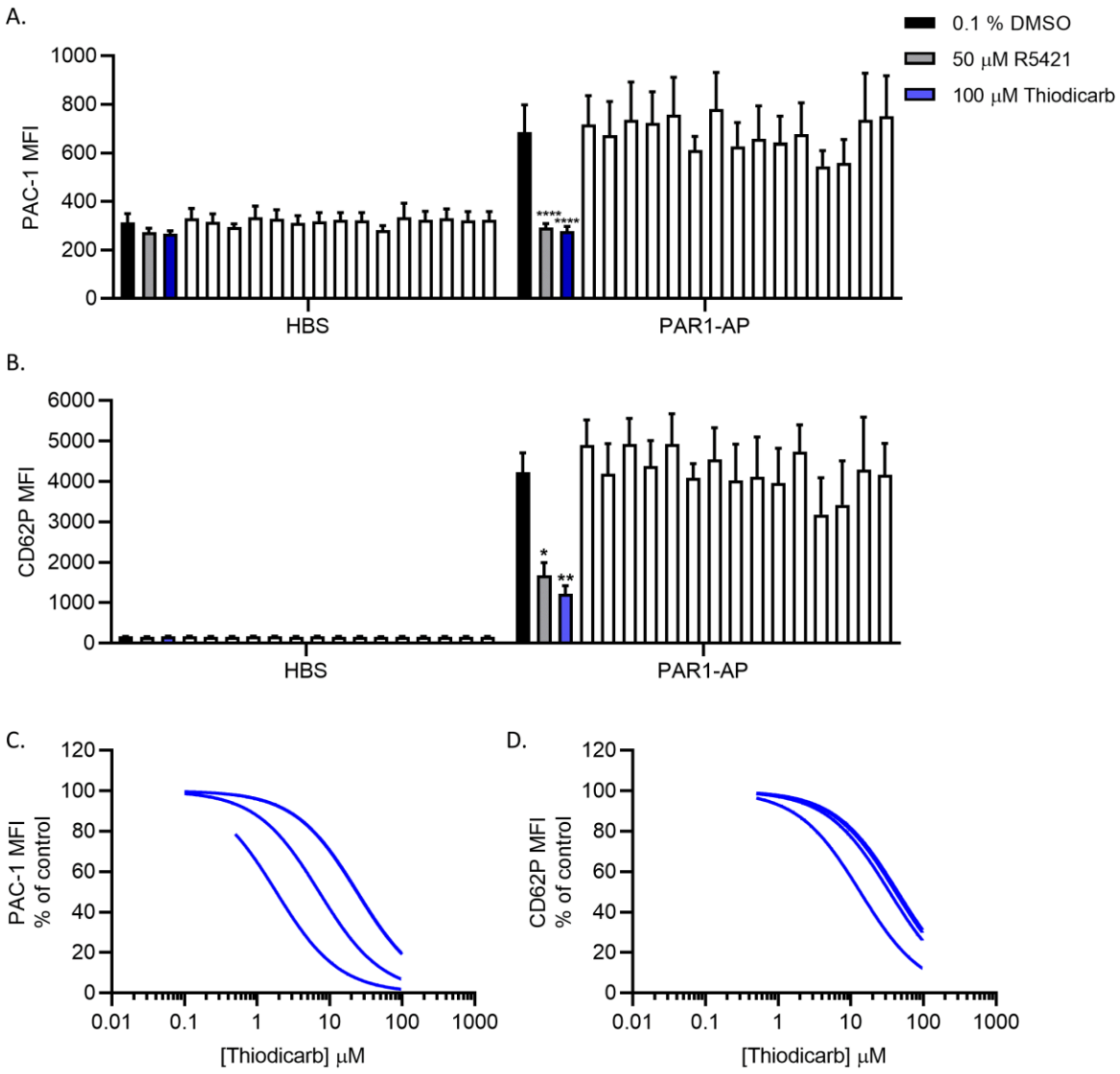

Figure 3.9: A1 (Thiodicarb) inhibits platelet $\alpha_{IIb}\beta_3$ integrin activation and α-granule release following stimulation with PAR1-AP. Platelets were treated with 50 μM R5421, 100 μM A1-A16 or 0.1% DMSO for 10 minutes at ambient temperature prior to stimulation for 10 minutes. $\alpha_{IIb}\beta_3$ activation was measured by flow cytometry as PAC-1 binding (FITC conjugated). α-granule secretion was measured by anti-CD62P (P-selectin) antibody binding (phycoerythrin (PE) conjugated). (A) PAC-1-FITC MFI following stimulation with 10 μM PAR1-AP. (B) CD62P-PE MFI following stimulation with 10 μM PAR1-AP. (C) Inhibition curves for A1/thiodicarb inhibiting PAC-1 binding. (D) Inhibition curves for A1/thiodicarb inhibiting CD62P binding. Bar charts show mean ± SEM. N = 5. Black bars: 0.1% DMSO., grey bars: 50 μM R5421, blue bars 100 μM A1 (thiodicarb). Inhibition curves N = 4. Data were analysed using two-way ANOVA, both factors matching, and Dunnett's multiple comparisons tests.

3.9 Thiodicarb inhibits platelet Ca^{2+} signalling in response to a range of agonists

100 µM thiodicarb did not affect Cal520 fluorescence following stimulation with 10 µM A23187 quantified as AUC, peak F/F_0 or F/F_0 at 2 minutes following stimulation (Figure 3.11 A). However, it was noted that there was increased Cal520 fluorescence at the beginning of traces following a 60-minute incubation of thiodicarb at 37°C (Figure 3.11 Ai). Addition of 100 µM thiodicarb to Cal520-loaded platelets caused a slow, sustained increase in fluorescence after a 10-minute incubation at 37°C which further increased by 60 minutes of incubation (Figure 3.10), suggesting disruption of Ca^{2+} homeostasis. 50 µM R5421 caused a slight increase in Cal520 fluorescence after a 10-minute incubation at 37°C but this was not significant after 60 minutes of incubation. A 10-minute incubation at ambient temperature with thiodicarb inhibited Cal520 fluorescence following stimulation with 1U/ml thrombin + 1 µg/ml CRP-XL. Although the peak F/F_0 was unaffected, the sustained signal at 10 minutes post stimulation was reduced (Figure 3.11 B). There was a small increase in the PAR1-AP-stimulated signal measured by AUC or F/F_0 at 10 minutes post stimulation (Figure 3.11 C). Thiodicarb did not affect cytosolic Ca^{2+} signals following stimulation with 100 µM PAR4-AP (Figure 3.11 D). Consistent with R5421, thiodicarb inhibited Cal520 fluorescence following stimulation with 1 µg/ml CRP-XL quantified by AUC, peak F/F_0, and F/F_0 at 10 minutes post stimulation (Figure 3.11 E).

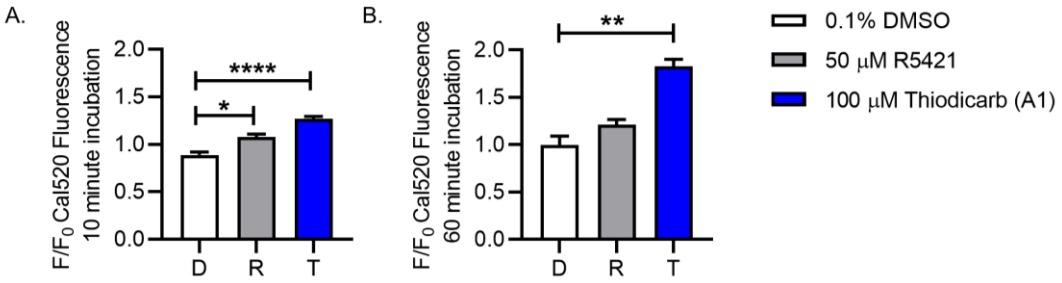

Figure 3.10: Thiodicarb disrupts platelet Ca^{2+} homeostasis. Cal520-loaded platelets were treated with 50 µM R5421, 100 µM thiodicarb or 0.1% DMSO (as vehicle control) and fluorescence monitored for 60 minutes at 37°C. The relative increase in fluorescence (F/F_0) at 10 minutes (A) and 60 minutes (B) after drug treatment is shown. Bar charts show mean ± SEM. N = 5. Data analysed using repeated measures one-way ANOVA and Dunnett's multiple comparisons tests.

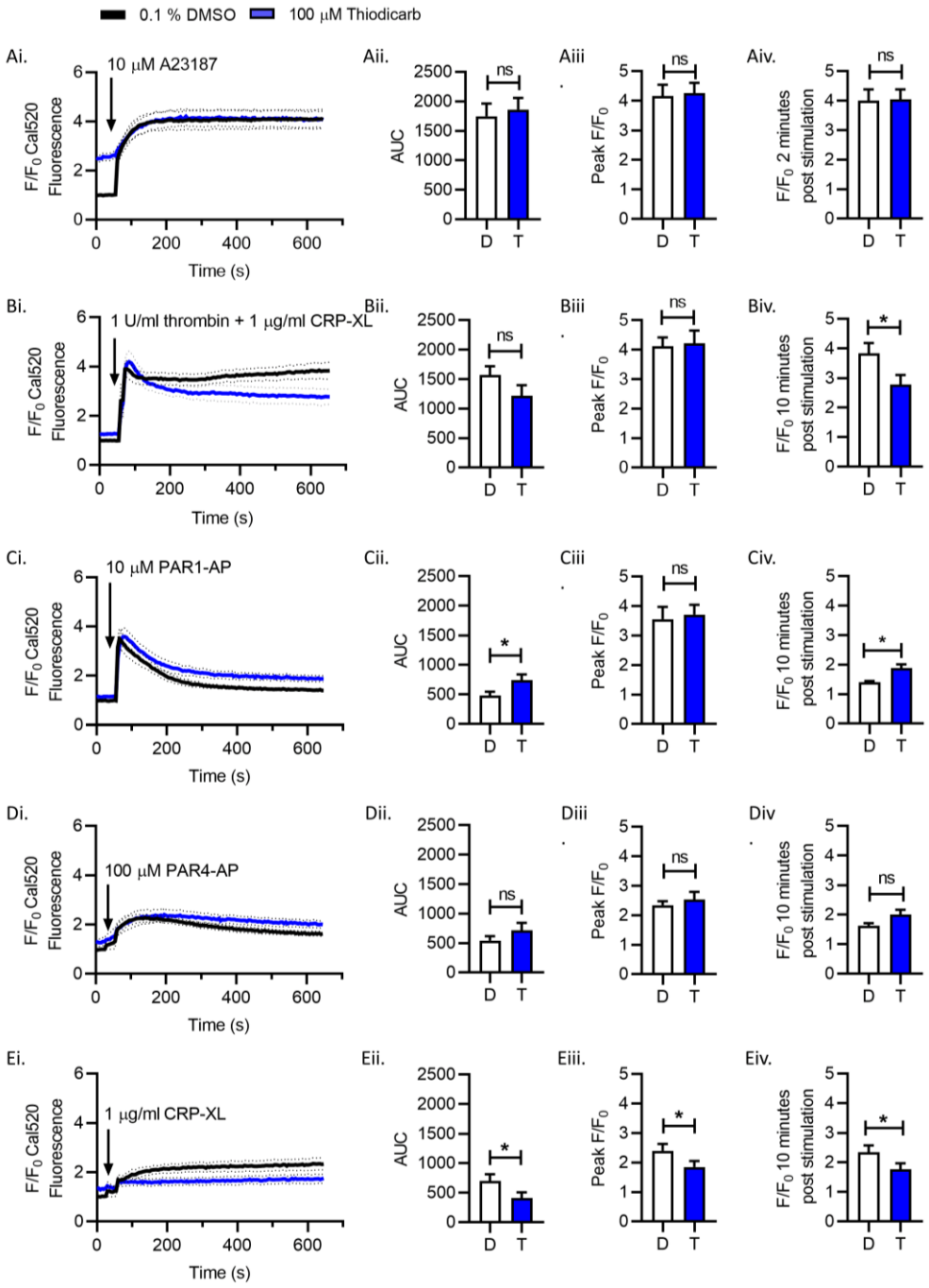

Figure 3.11: Thiodicarb inhibits platelet Ca^{2+} signalling in response to a range of agonists. Platelets were loaded with the Ca^{2+}-sensitive fluorescence dye, Cal520. Fluorescence values were normalised to the initial fluorescence values of vehicle controls containing 0.1% DMSO in matched samples to account for variation in dye loading (F/F_0). Platelets were treated with 100 μM Thiodicarb (blue lines and bars) or 0.1% DMSO (black lines and white bars) under conditions that inhibited PS exposure or integrin activation in previous experiments (i.e., in (A), 60-minute incubation at 37°C and in (B)–(E), 10-minute incubation at ambient temperature). Where indicated, platelets were stimulated with (A) 10 μM A23187; (B) 1 U/ml thrombin + 1 μg/ml CRP-XL; (C) 10 μM PAR1-AP; (D) 100 μM PAR4-AP; and (E) 1 μg/ml CRP-XL. All stimulations at ambient temperature. Data are presented as (i) F/F_0 Cal520 fluorescence following stimulation; (ii) AUC above baseline (F/F_0 = 1); (iii) peak F/F_0 following stimulation; and (iv) F/F_0 at corresponding time of inhibition of PS exposure or integrin activation in flow cytometry (i.e., in (A), 2 minutes and in (B)–(E), 10 minutes). In (ii)–(iv) for each stimulation mean ± SEM is also given. N = 5. Data were analysed using two-tailed Student's paired t-tests.

3.10 R5421 and thiodicarb do not induce shedding of GPVI from the platelet surface

Since R5421 and thiodicarb cause significant inhibition of cytosolic Ca^{2+} signalling following stimulation with CRP-XL, GPVI surface expression was tested to determine whether R5421 or thiodicarb caused shedding of GPVI from the surface, as is seen following prolonged stimulation with A23187 (Montague et al., 2018). Neither 50 μM R5421 nor 100 μM thiodicarb caused any shedding of GPVI from the platelet surface (Figure 3.12).

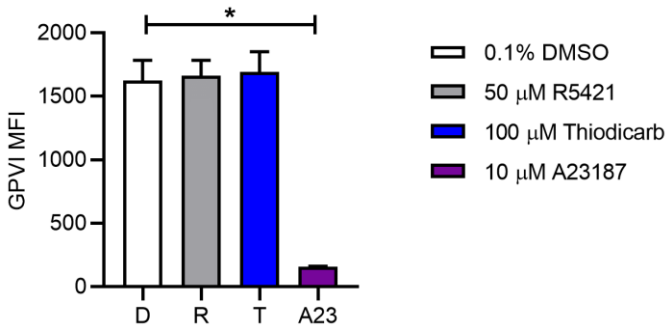

Figure 3.12: R5421 and thiodicarb do not cause GPVI shedding. Platelets were treated with 50 μM R5421, 100 μM thiodicarb, 10 μM A23187 (as positive control) or 0.1% DMSO (as vehicle control) for 60 minutes at 37°C. Surface GPVI expression was detected using an Alexa 47-conjugated antibody and analysed by flow cytometry. The MFI is shown. Bar charts show mean ± SEM. N = 5. Data were analysed using a repeated measures one-way ANOVA and Dunnett's multiple comparisons tests.

3.11 Discussion

R5421 was first described as an inhibitor of scramblase activity in 1998 (Dekkers et al., 1998) and has been used to investigate the roles of phospholipid scrambling in several models. R5421 might therefore provide a useful scaffold for further development of potent and selective TMEM16F inhibitors. However, the pharmacology of R5421 had not been previously thoroughly characterised.

The data in this chapter confirmed that R5421 directly inhibits platelet scramblase activity. Using the calcium ionophore A23187 to stimulate platelet PS exposure, the receptors and intracellular signalling required for PS exposure using physiological agonists is bypassed and intracellular $[Ca^{2+}]$ directly raised to activate the scramblase protein, TMEM16F. R5421 slowed the rate of platelet scramblase activity in our real-time plate-based luminescence AV binding assay following stimulation with A23187. R5421 also inhibited platelet PS exposure following A23187 stimulation in a time- and temperature-dependent manner when measured by flow

cytometry. R5421 did not affect A23187-induced intracellular Ca^{2+} signals under the same incubation conditions that led to inhibition of A23187-induced PS exposure. Therefore, R5421 does not interfere with the calcium ionophore actions of A23187 but has a direct effect on scramblase activity.

Maximum inhibition was achieved following a 60-minute incubation of 50 μM R5421 at 37°C. This is consistent with the original report (Dekkers et al., 1998), which found a similar time dependency to the inhibition. They also reported that the inhibition was not readily reversed by washing the platelets, suggesting that the action of R5421 is either irreversible or has a very slow off-rate. Dekkers et al., reported that R5421 slowed the rate of PS exposure. This was also demonstrated by our plate-based assay (Figure 3.2) and the complete inhibition of end point flow cytometry AV binding 2 minutes following stimulation with A23187, though more platelets become PS positive by 10 minutes after stimulation (Figure 3.3). The percentage of PS positive platelets following a 10 minute stimulation, however, is still reduced compared to DMSO controls.

It is important that R5421 appears to inhibit the rate of PS exposure as we believe this could explain some differences between results in the plate-based and flow cytometry AV binding assays. The plate-based assay requires two different conjugated AVs (Annexin V-SmBiT and Annexin V-LgBiT) to combine in proximity to generate a luminescence signal, which likely requires high cell surface density of PS to be effective. In contrast, the flow cytometry assay requires only a single annexin V-FITC to bind to the platelet to generate a signal. The signal strength of the flow cytometer assay is therefore likely to be less dependent on the PS surface density of a single cell. Notably, a time-resolved FRET assay of AV binding showed a similar lower sensitivity to PS exposure compared to flow cytometry; this TR-FRET assay also required two differently labelled AV monomers to oligomerise to generate a signal (Gasser et al., 2009). This means that the plate-based assay is likely to be more sensitive when detecting inhibition of scrambling rate compared to flow cytometry since the plate-based assay may require a greater density of PS on the platelet surface.

Moreover, AV oligerimises into a 2D lattice when it binds to a PS-exposing membrane. Annexin V-FITC oligomerisation on binding to a PS-exposing membrane may result in a fluorescence signal that is disproportionate to the PS surface density. Flow cytometry analysis of platelet PS exposure often results in an all-or-nothing response, with platelets characterised as positive or negative for AV binding (Abbasian et al., 2020; Harper et al., 2013). The AV-positive platelets all have the same high fluorescence. The detection of AV binding to PS using flow cytometry rapidly saturates with small increases in the percentage of PS exposed in the

membrane, as shown by experiments with bilayers of defined phospholipid composition adsorbed to glass beads (Stuart et al., 1998). Similarly, the fluorescence of AV-FITC bound to liposomes of varying PS percentage showed an all-or-nothing response above a threshold percentage of PS (Shi et al., 2006). Lactadherin-FITC, which does not oligomerise, gave a graded fluorescence signal that was proportional to the PS percentage.

The two-part AV detection system (as in the luminescence assay here or the TR-FRET assay described above) may mean that the signal is less likely to be saturated by small increases in the surface density of PS and may give a signal that is more proportional to the degree of PS exposure, as oligomerisation is required for its signal. In both cases, partial inhibition of PS exposure may be sufficient to show inhibition in the luminescence assay, but not sufficient to reduce the PS exposure below the all-or-nothing threshold for the flow cytometry assay. This suggests that almost complete inhibition of TMEM16F may be required to see an inhibitory effect in flow cytometry. In contrast, a potential benefit of the luminescence-based assay is that it can be used to detect drugs that reduce the rate of scrambling even when endpoint flow cytometry does not show a difference. Complete inhibition of TMEM16F may be required for a therapeutic benefit, however. In an unstimulated platelet, PS that becomes exposed on the surface is transported back into the inner leaflet by a flippase. This flippase activity is inhibited in pro-coagulant platelets, meaning that PS exposure by TMEM16F is unopposed. If the rate of scrambling is substantially reduced but not abolished, PS will still eventually accumulate in the outer leaflet of the membrane. A potential example of such a compound is A2 from the ligand-based screen presented in this chapter.

R5421 also inhibited platelet PS exposure following stimulation with thrombin + CRP-XL, more physiologically relevant agonists, but with a different time and temperature dependency to following A23187. Complete inhibition of thrombin + CRP-XL induced PS exposure was observed by flow cytometry following a 10-minute incubation with R5421 at room temperature (Figure 3.3 C,E). Notably, under these conditions, there was no inhibition of A23187-induced PS exposure. This suggests that following thrombin + CRP-XL stimulation R5421 might be inhibiting platelet PS exposure through a different mechanism. Since PS exposure is dependent on intracellular Ca^{2+} signalling, it was investigated whether this was affected by R5421. R5421 significantly inhibited cytosolic Ca^{2+} signalling following thrombin + CRP-XL stimulation. Although the initial peak increase in fluorescence was unaffected, the sustained Ca^{2+} signal was almost completely inhibited. Since the increase in intracellular [Ca^{2+}] must be sustained to trigger PS exposure (Keuren et al., 2005), the inhibition of PS exposure by R5421 under these conditions is likely to be due to inhibition of Ca^{2+} signalling rather than direct inhibition of the scramblase.

To further investigate the effect of R5421 on intracellular Ca^{2+} signalling, platelets were stimulated separately with agonists of PAR1, PAR4, and GPVI, the main receptors activated during stimulation with thrombin + CRP-XL. There were some small effects on Ca^{2+} signalling downstream of PAR1 and PAR4, though these are unlikely to account for the large inhibition of Ca^{2+} signalling described above. In contrast, Ca^{2+} signalling downstream of GPVI was almost completely abolished. The signalling between receptor and Ca^{2+} signal is notably different downstream of PAR1 or PAR4 and GPVI. PAR1 and PAR4 are G-protein-coupled receptors (GPCRs), predominately coupled to activation of $G\alpha_q$ (Gieseler et al., 2013) and subsequent activation of PLCβ (Nieman, 2016). GPVI is a member of the immunoglobulin family of receptors. It is associated with an immunoreceptor tyrosine-based activation motif (ITAM)-containing protein, FcR γ chain (Moroi and Jung, 2004). Activation of GPVI triggers phosphorylation of the ITAM motif by Src family tyrosine kinases (TKs), followed by recruitment and activation of spleen associated tyrosine kinase (Syk TK) and subsequent phosphorylation of PLCγ2 (Watson et al., 2005). Phosphoinositide 3-kinases and Bruton tyrosine kinase (Btk), a Tec family TK, are also involved in regulating PLCγ2 (Quek et al., 1998; Suzuki-Inoue et al., 2003). Although the molecular target of R5421 is not known, the different pathways between receptor activation and PLC activation provide a potential explanation for the different effect of R5421 on Ca^{2+} signalling downstream of PAR1 or PAR4 and GPVI. R5421 does not induce GPVI shedding from the platelet surface (Figure 3.12), which eliminates this as a potential explanation of reduced Ca^{2+} signalling downstream of GPVI agonists.

R5421 also inhibits platelet $\alpha_{IIb}\beta_3$ integrin activation and α-granule release following stimulation of PAR1, despite having only a small effect on intracellular Ca^{2+} signalling. The inhibition in α-granule secretion could result from decreased $\alpha_{IIb}\beta_3$ activation as outside-in signalling through this integrin enhances α-granule secretion (Tucker et al., 2008). The signalling pathway from PAR1 to $\alpha_{IIb}\beta_3$ activation has been intensively investigated (Stefanini and Bergmeier, 2016) and is illustrated in Figure 1.3. R5421 could, in principle, act at any step of integrin activation, however, R5421 is unlikely to be solely acting to inhibit ADP release by dense granule secretion, as $\alpha_{IIb}\beta_3$ activation could not be rescued by co-stimulation with PAR1-AP and ADP (Figure 3.4 E). Similarly, although loss of dense granule secretion reduces α-granule secretion, this would also be rescued by co-stimulation with ADP (Harper et al., 2015; Savage et al., 2013). In addition, R5421 is unlikely to inhibit $P2Y_{12}$, as $\alpha_{IIb}\beta_3$ activation could not be rescued when adrenaline was used to activate α_2-adrenoceptors (Figure 3.4 F), which are coupled to $G\alpha_z$ and can also provide PI3-K-dependent signalling to maintain integrin activation (Gurbel et al., 2015). Together, these data suggest that R5421 may inhibit

$\alpha_{IIb}\beta_3$ activation by acting distal to receptor signalling, perhaps on Rap1b activation, though the precise target remains to be identified.

Since multiple off-target effects of R5421 on platelet function were identified, it was decided to try and find a more selective inhibitor of platelet scramblase activity using a ligand-based *in silico* screen. 16 compounds were identified during this screen for testing with high shape and field similarity to R5421 (similarity scores over 0.6 calculated using Forge software), and two of these, A1 and A2, were found to inhibit the rate of scrambling in the plate-based AV binding assay. However, only A1 (thiodicarb) was also effective at inhibiting platelet PS exposure in flow cytometry experiments following stimulation with A23187 or thrombin + CRP-XL. This again indicates that there are differences between the sensitivities of the plate-based and flow cytometry AV binding assays, which remain to be fully understood as discussed above. The plate-based assay may be a valuable approach for further investigating the mechanisms of PS exposure. However, as the reduction in scrambling rate was not sufficient to affect endpoint AV binding measured by flow cytometry, the widely used approach to measure platelet PS exposure, A2 was not investigated further at this time.

As with R5421, A1/thiodicarb inhibited platelet PS exposure following A23187 stimulation after a 60-minute incubation at 37°C. Under these conditions, thiodicarb tends towards increasing PS exposure in unstimulated platelets, likely by disrupting calcium signalling and causing an increase in cytosolic [Ca^{2+}] which was not seen with R5421 (Figure 3.10). Thiodicarb did not affect Cal520 signals following A23187 stimulation, and so, as for R5421, we can conclude that thiodicarb does have some direct effects on platelet scramblase activity. Again, similarly to R5421, thiodicarb also inhibited platelet PS exposure following stimulation with thrombin + CRP-XL following a 10-minute incubation at room temperature, suggesting thiodicarb may too inhibit PS exposure through a different mechanism to that seen after stimulation with A23187 (Figure 3.8). Thiodicarb also disrupted Ca^{2+} signalling following stimulation with thrombin + CRP-XL, as seen with R5421, indicating that we had not successfully separated the ability to inhibit platelet scramblase activity from the effects on cytosolic Ca^{2+} signalling (Figure 3.11). Furthermore, thiodicarb also inhibited platelet $\alpha_{IIb}\beta_3$ integrin activation and α-granule release following stimulation with PAR1-AP (Figure 3.9) meaning that we had also not successfully separated the ability to inhibit platelet scramblase activity from platelet pro-aggregatory activity.

Thiodicarb is a synthetic carbamate pesticide that is extensively used for crop protection. It has been shown to have some toxicity including systemic organ damage, occasional signs of haemorrhage and inhibition of AChE activity (Dias et al., 2013; Hoizey et al., 2008). No effects on platelets have been previously described. The effects of thiodicarb on platelet function and

Ca^{2+} signalling detailed may underlie some of the compound's toxicity. Whatever its targets, the toxicity of thiodicarb suggests that it, and the related R5421, may not be a suitable scaffold for the development of future scramblase inhibitors. Figure 3.13 illustrates the lowest energy 3D conformation of thiodicarb and the compound's electrostatic fields calculated using Forge. Thiodicarb did not have the highest similarity score to R5421 of the compounds tested but its chemical structure shows that it is essentially a double unit of the R5421 functional groups, highlighted in green (Figure 3.13). Presumably these groups are responsible for the effects on scramblase activity of both of these compounds but also their off-target effects, meaning little more can be deduced to guide improved compound design.

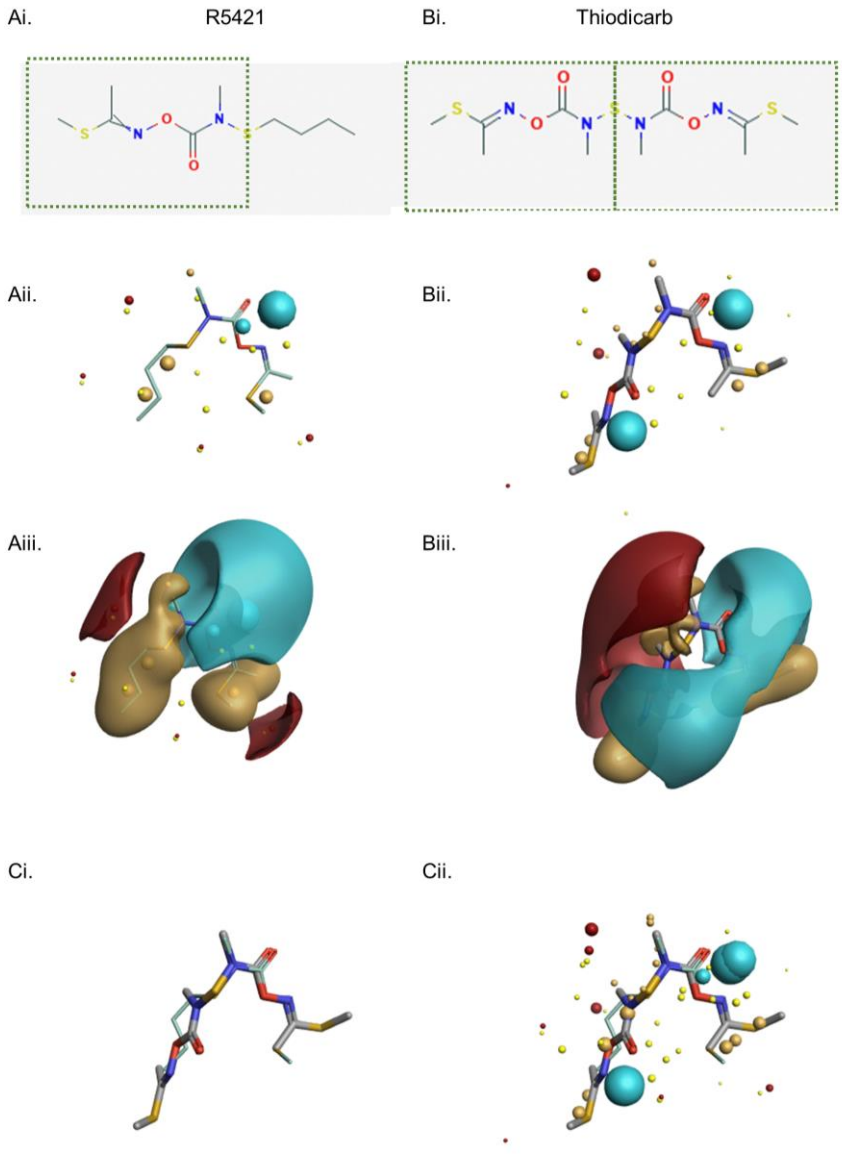

Figure 3.13: Comparison of the electrostatic fields of R5421 and Thiodicarb. (A) R5421; (B) Thiodicarb. (i) 2D representation of chemical structures, images taken from Pubchem. Equivalent groups highlighted in green; (ii) lowest energy 3D aligned conformations generated using Forge with electrostatic fields illustrated as spheres; (iii) electrostatic fields illustrated as 3D clouds. (Ci) Overlaid R5421 and thiodicarb 3D conformations. (Cii) Overlaid R5421 and thiodicarb 3D conformations with electrostatic fields shown as spheres. Negative electrostatic fields shown in blue, positive electrostatic fields shown in red, hydrophobic fields shown in yellow.

In conclusion, as multiple off-target effects of R5421 have been identified, this compound is not suitable for use as a scramblase inhibitor, as it was previously described. Although a ligand-based approach to find a more selective inhibitor of scramblase function was unsuccessful, thiodicarb was identified as a novel inhibitor of platelet scramblase activity. Thiodicarb has similar off-target effects on platelet function as R5421 and additional disruptive effects on Ca^{2+} signalling in unstimulated platelets. The multiple off-target effects of R5421 and the inability to isolate some of these effects using ligand-based screening approaches further suggest that R5421 is not a suitable scaffold to use in design of a selective scramblase inhibitor and other scaffolds should be investigated.

Chapter 4 – An empirical screen of polyphenolic compounds for effects on platelet scramblase activity

Since R5421, the only previously described inhibitor of platelet scramblase activity (Dekkers et al., 1998), acts non-selectively (Millington-Burgess et al., 2020) and ligand-based attempts to improve R5421 were unsuccessful, as detailed in chapter 3, alternative leads must be considered for the design of a selective inhibitor of platelet pro-coagulant activity.

As detailed in the Introduction, two polyphenols – tannic acid (TA) and epigallocatechin gallate (EGCG') – have been shown to inhibit TMEM16F activity in TMEM16F-transfected IFET cells (T. Suzuki et al., 2014) and in artificial lipid bilayers (Watanabe et al., 2018). Whether tannic acid and EGCG' inhibit TMEM16F activity in platelets has not yet been tested.

These polyphenolic compounds are known to be pleotropic, however, and have many other effects on platelet function, including inhibiting platelet pro-aggregatory activity, and hence are not selective inhibitors of scramblase activity. EGCG' inhibits platelet aggregation in response to a range of agonists, (Iida et al., 2014; Joo et al., 2018; Lill et al., 2003) raises intracellular [cAMP] and inhibits PLCγ2, reducing Ca^{2+} mobilisation (Jin et al., 2008; Ok et al., 2012). Both tannic acid and EGCG' also inhibit TMEM16A, the Ca^{2+} activated Cl^- channel closely structurally related to TMEM16F (Namkung et al., 2010; T. Suzuki et al., 2014). Though tannic acid and EGCG' have multiple effects on platelet function, if they are also shown to inhibit platelet scramblase activity, they could be additional leads upon which to base the development of more selective inhibitors of platelet pro-coagulant activity.

This chapter aimed to test the ability of tannic acid and EGCG' to inhibit platelet scramblase activity and to characterise the effects of related polyphenolic compounds to develop a structure-activity relationship of this inhibition to guide future compound design.

4.1 Tannic acid inhibits high level platelet and red blood cell (RBC) PS exposure following stimulation with A23187 or thrombin + CRP-XL in a flow cytometry AV binding assay

100 µM tannic acid inhibited platelet PS exposure, measured by AV binding by flow cytometry, after a 10-minute incubation at ambient temperature and stimulation with either 10 µM A23187 (Figure 4.1) or dual stimulation with 1U/ml thrombin and 1 µg/ml CRP-XL (Figure 4.2). Tannic acid specifically inhibited high level PS exposure in platelets, although some medium level PS exposure still occurred, particularly in platelets stimulated with A23187 (Figures 4.1 A and 4.2 A). Tannic acid inhibited AV-positive microparticle formation following stimulation; this did not reach significance following A23187 stimulation where microparticle formation in DMSO treated controls was particularly variable (Figure 4.1 B) but was statistically significant following stimulation with thrombin + CRP-XL (Figure 4.2 B).

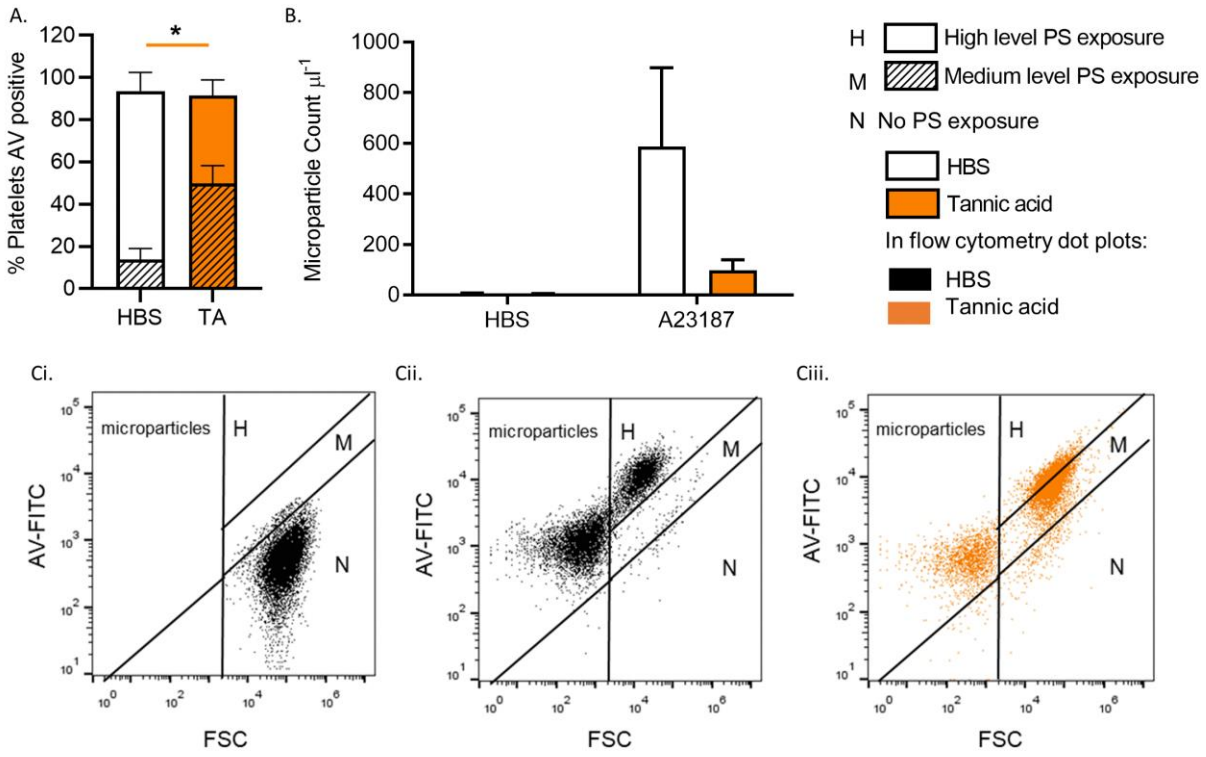

Figure 4.1: Tannic acid inhibits high level platelet PS exposure following stimulation with A23187. Flow cytometry AV binding after stimulation with 10 µM A23187 following a 10-minute incubation with 100 µM tannic acid or HBS at ambient temperature. (A) % of platelets with high level or medium level AV binding. (B) AV positive microparticle count. (C) Flow cytometry dot plots showing representative AV binding of (i) unstimulated platelets incubated with HBS; (ii) platelets incubated with HBS following stimulation with 10 µM A23187; (iii) platelets incubated with 100 µM tannic acid following stimulation with 10 µM A23187. White bars/black dots - platelets pre-incubated with HBS, orange dots/bars – platelets pre-incubated with 100 µM tannic acid. Hatching – medium level PS exposure. No hatching – high level PS exposure. Bar charts show mean ± SEM. N = 4. Orange statistic in A represents a significant interaction between tannic acid treatment and level of PS exposure in a two-way ANOVA, both factors matching.

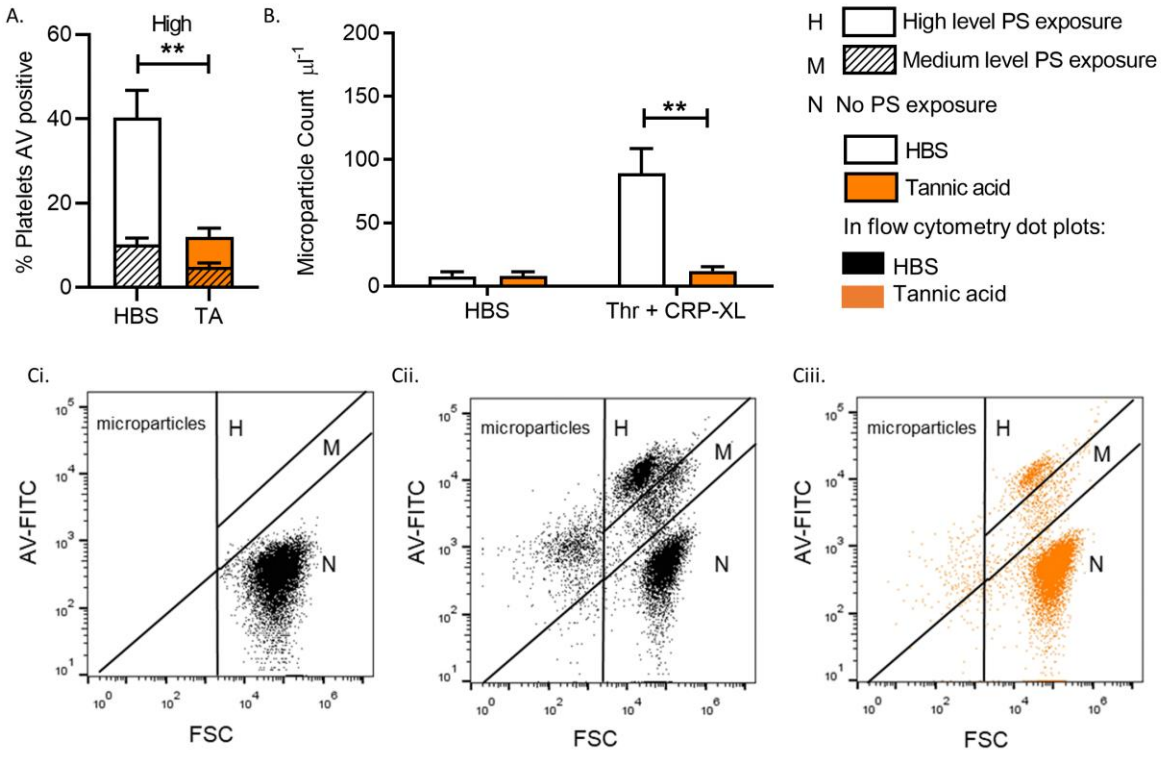

Figure 4.2: Tannic acid inhibits high level platelet PS exposure following stimulation with thrombin + CRP-XL. Flow cytometry AV binding after stimulation with 1 U/ml thrombin + 1 µg/ml CRP-XL following a 10-minute incubation with 100 µM tannic acid or HBS at ambient temperature. (A) % of platelets with high level or medium level AV binding. (B) AV positive microparticle count. (C) Flow cytometry dot plots showing representative AV binding of (i) unstimulated platelets incubated with HBS; (ii) platelets incubated with HBS following stimulation with 1 U/ml thrombin + 1 µg/ml CRP-XL; (iii) platelets incubated with 100 µM tannic acid following stimulation with 1 U/ml thrombin + 1 µg/ml CRP-XL. White bars/black dots - platelets pre-incubated with HBS, orange dots/bars – platelets pre-incubated with 100 µM tannic acid. Hatching – medium level PS exposure. No hatching – high level PS exposure. Bar charts show mean ± SEM. N = 5. Data analysed using two-way ANOVA, both factors matching, and Sidak's multiple comparisons test.

100 µM tannic acid also eliminated high level PS exposure in RBCs following stimulation with 0.4 µM A23187, though some medium level PS exposure still occurred (Figure 4.3).

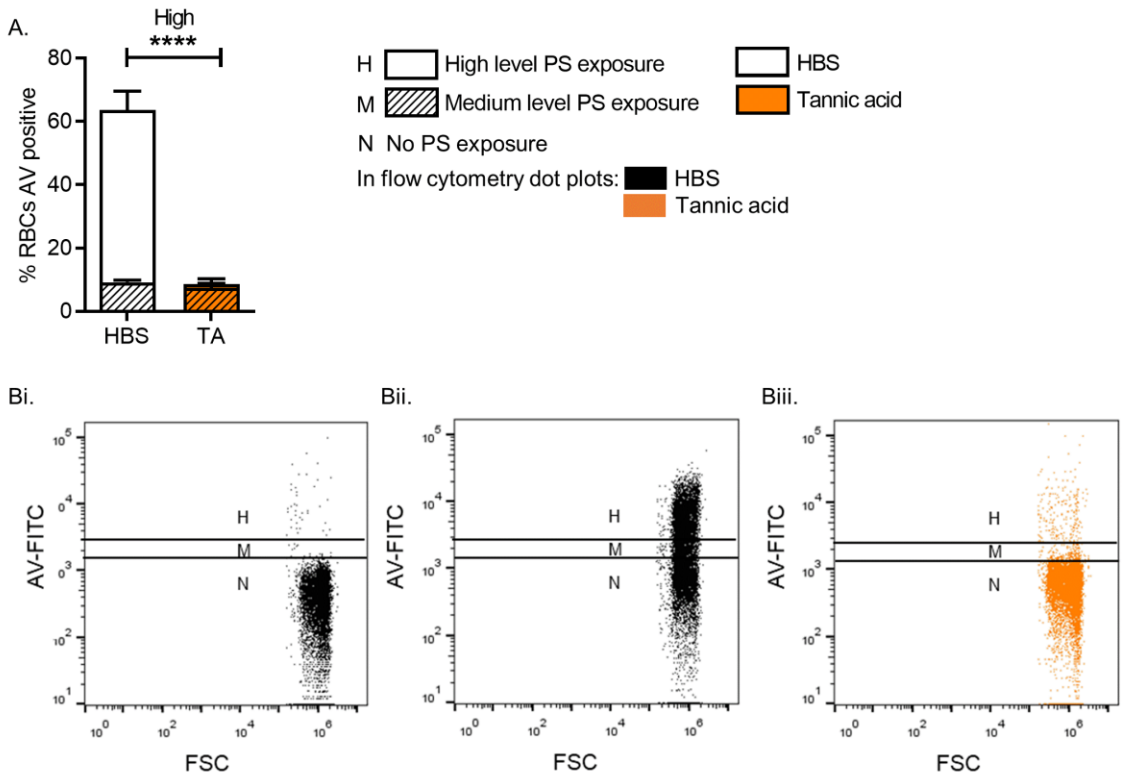

Figure 4.3: Tannic acid inhibits high level RBC PS exposure following stimulation with A23187. Flow cytometry AV binding after stimulation with 0.4 µM A23187 following a 10-minute incubation with 100 µM tannic acid or HBS. (A) % of RBCs with high level or medium level AV binding. (B) Flow cytometry dot plots showing representative AV binding of (i) unstimulated RBCs incubated with HBS; (ii) RBCs incubated with HBS following stimulation with 0.4 µM A23187; (iii) RBCs incubated with 100 µM tannic acid following stimulation with 0.4 µM A23187. White bars/black dots - RBCs pre-incubated with HBS, orange dots/bars – RBCs pre-incubated with 100 µM tannic acid. Hatching – medium level PS exposure. No hatching – high level PS exposure. Bar charts show mean ± SEM. N = 7. Data analysed using a two-way ANOVA, both factors matching, and Sidak's multiple comparisons test.

4.2 Tannic acid inhibits platelet α-granule release and enhances $\alpha_{IIb}\beta_3$ integrin activation following stimulation with PAR1-AP

A 10-minute incubation of 100 μM tannic acid at ambient temperature inhibited platelet α-granule release, measured by anti-CD62P antibody binding by flow cytometry, following a 10-minute stimulation with 10 μM PAR1-AP (Figure 4.4 A). Tannic acid trended towards increasing $\alpha_{IIb}\beta_3$ integrin activation, measured by PAC-1 antibody binding by flow cytometry, following a 10-minute stimulation with 10 μM PAR1-AP (Figure 4.4 B).

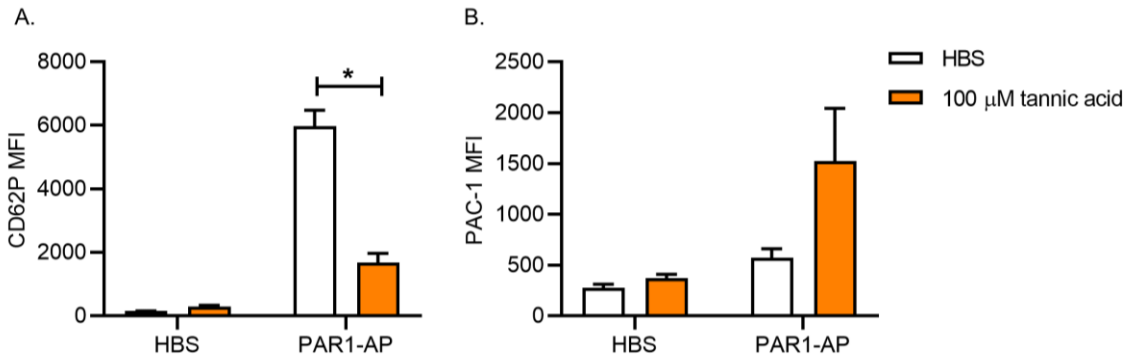

Figure 4.4: Tannic acid inhibits platelet α-granule release and enhances $\alpha_{IIb}\beta_3$ integrin activation following stimulation with PAR1-AP. (A) Platelet CD62P MFI, showing α-granule release, following stimulation with 10 μM PAR1-AP. (B) Platelet PAC-1 MFI, showing $\alpha_{IIb}\beta_3$ integrin activation, following stimulation with 10 μM PAR1-AP. White bars represent platelets pre-incubated with HBS, orange bars represent platelets pre-incubated with 100 μM tannic acid. Bar charts show mean ± SEM. N = 3. Data analysed using a two-way ANOVA, both factors matching, with Sidak's multiple comparisons tests.

4.3 EGCG' inhibits high level PS exposure in platelets and RBCs following stimulation with A23187 or thrombin + CRP-XL in a flow cytometry AV binding assay

As tannic acid is a large pleotropic compound known to have multiple effects on platelet function, it is an unsuitable lead for development of a selective inhibitor of platelet scramblase activity. I therefore screened a set of smaller polyphenolic compounds related to tannic acid to find a more suitable lead for further investigation. The structures of the 5 compounds tested are illustrated in Figure 4.5. Epigallocatechin gallate (EGCG'), gallocatechin (GC) and digallic acid (DA) were chosen as they share structures based upon the galloyl moiety, similar to tannic acid (TA). Rosmarinic acid (RA) and silybinin (SB) were also chosen as plant polyphenols which are more structurally distinct to tannic acid.

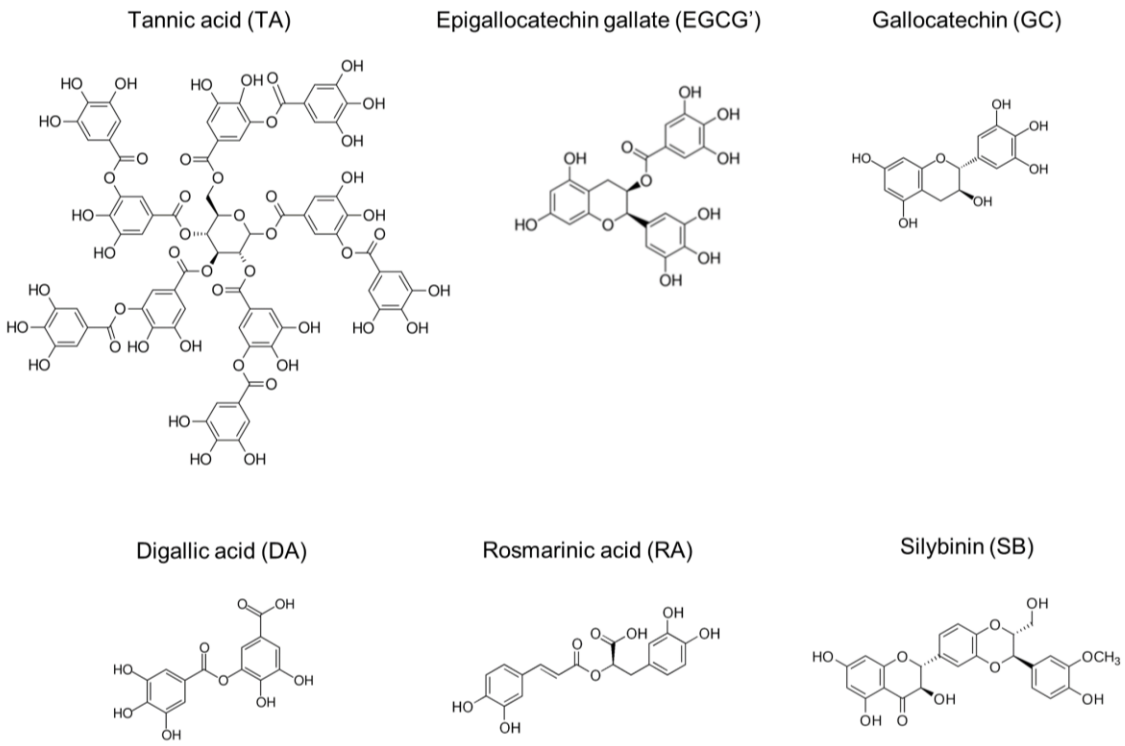

Figure 4.5: Structures of polyphenolic compounds screened.

Of the 5 compounds tested, 100 μM EGCG' inhibited high level PS exposure in platelets following stimulation with 10 μM A23187, though higher levels of medium PS exposure were observed (Figure 4.6). The exact nature of this medium level PS exposure remains to be determined, though it is high level PS exposure which has been shown to be TMEM16F-dependent and contributes to thrombosis. Medium level PS exposure has been documented previously in response to apoptotic stimuli, such as ABT-737. Following stimulation with ABT-737, medium level PS exposure remains in platelets from individuals with Scott Syndrome (van Kruchten et al., 2013) and is seen in *Tmem16f*$^{-/-}$ mouse platelets (Mattheij et al., 2016). This medium level PS exposure following apoptotic stimuli may be driven by other platelet scramblases such as Xkr8 (J. Suzuki et al., 2014). EGCG' also inhibited high level PS exposure in platelets following dual 1 U/ml thrombin + 1 μg/ml CRP-XL stimulation (Figure 4.7). EGCG' inhibited AV positive microparticle formation following stimulation with A23187 (Figure 4.6 B) and trended towards decreasing AV positive microparticle formation following stimulation with thrombin + CRP-XL, though this was not statistically significant due to a higher variability within controls. 100 μM EGCG' also inhibited high level PS exposure in RBCs following 0.4 μM A23187 stimulation (Figure 4.8). 100 μM GC reduced high level PS exposure in platelets following stimulation with A23187, whilst medium level PS exposure increased (Figure 4.6 A). 100 μM RA and SB had no effect on platelet or RBC PS exposure but SB increased the number of AV positive microparticles formed following stimulation with 1 U/ml thrombin + 1 μg/ml CRP-XL (Figure 4.7 B).

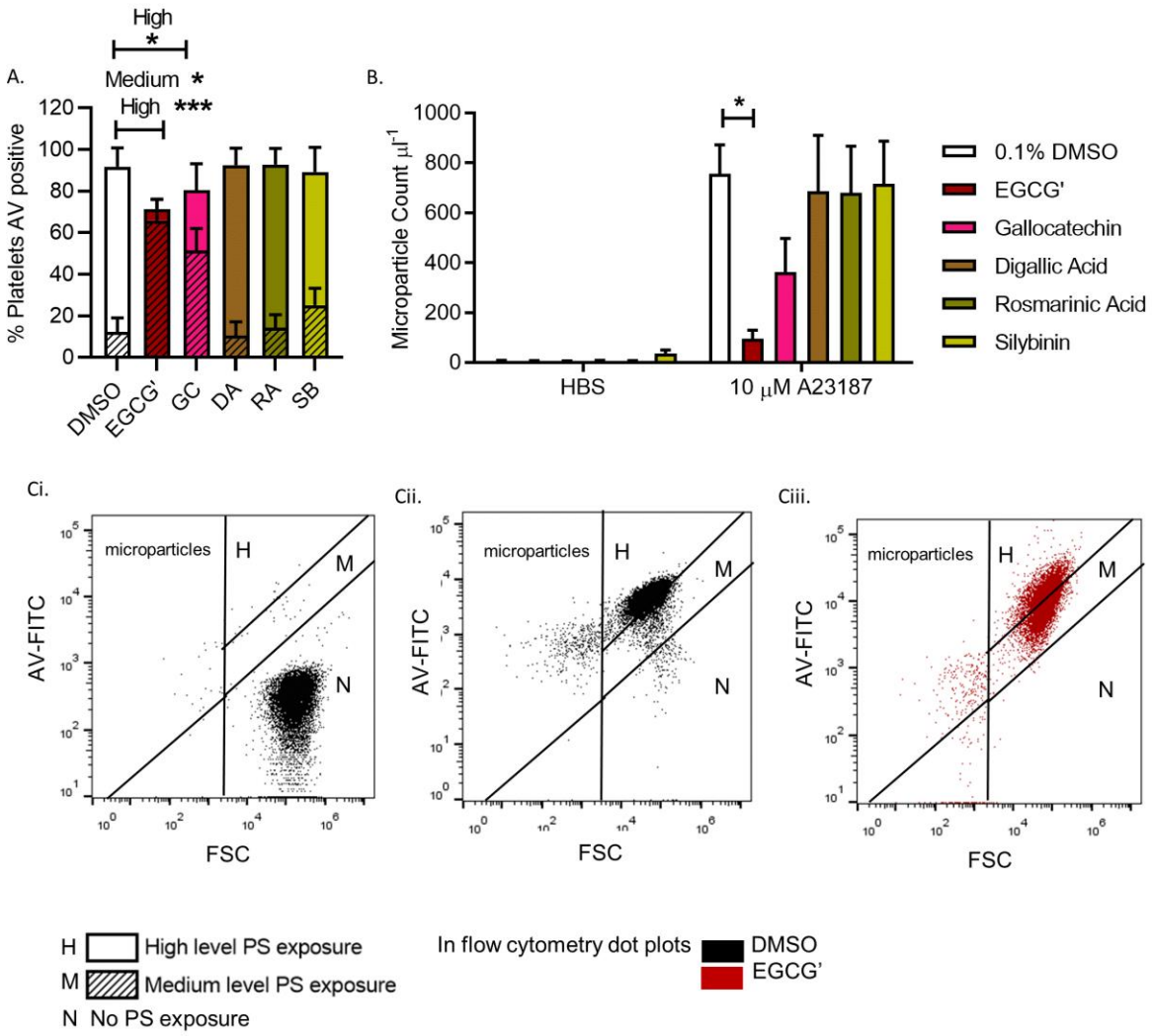

Figure 4.6: EGCG' inhibits high level platelet PS exposure following stimulation with A23187. Flow cytometry AV binding after stimulation with 10 µM A23187 following a 10-minute incubation with 100 µM polyphenolic compound or 0.1% DMSO at ambient temperature. EGCG' – epigallocatechin gallate; GC- gallocatechin; DA – digallic acid; RA – rosmarinic acid; SB – silybinin. (A) % of platelets with high level or medium level AV binding following stimulation with 10 µM A23187. (B) AV positive microparticle count. (C) Flow cytometry dot plots showing representative AV binding of (i) unstimulated platelets incubated with 0.1% DMSO; (ii) platelets incubated with 0.1% DMSO following stimulation with 10 µM A23187; (iii) platelets incubated with 100 µM EGCG' following stimulation with 10 µM A23187. White bars/black dots - platelets pre-incubated with 0.1% DMSO, dark red dots/bars – platelets pre-incubated with 100 µM EGCG'. Hatching – medium level PS exposure. No hatching – high level PS exposure. Bar charts show mean ± SEM. N = 4. Data analysed using two-way ANOVA, both factors matching, and Sidak's multiple comparisons test in (A) and Dunnett's multiple comparisons test in (B).

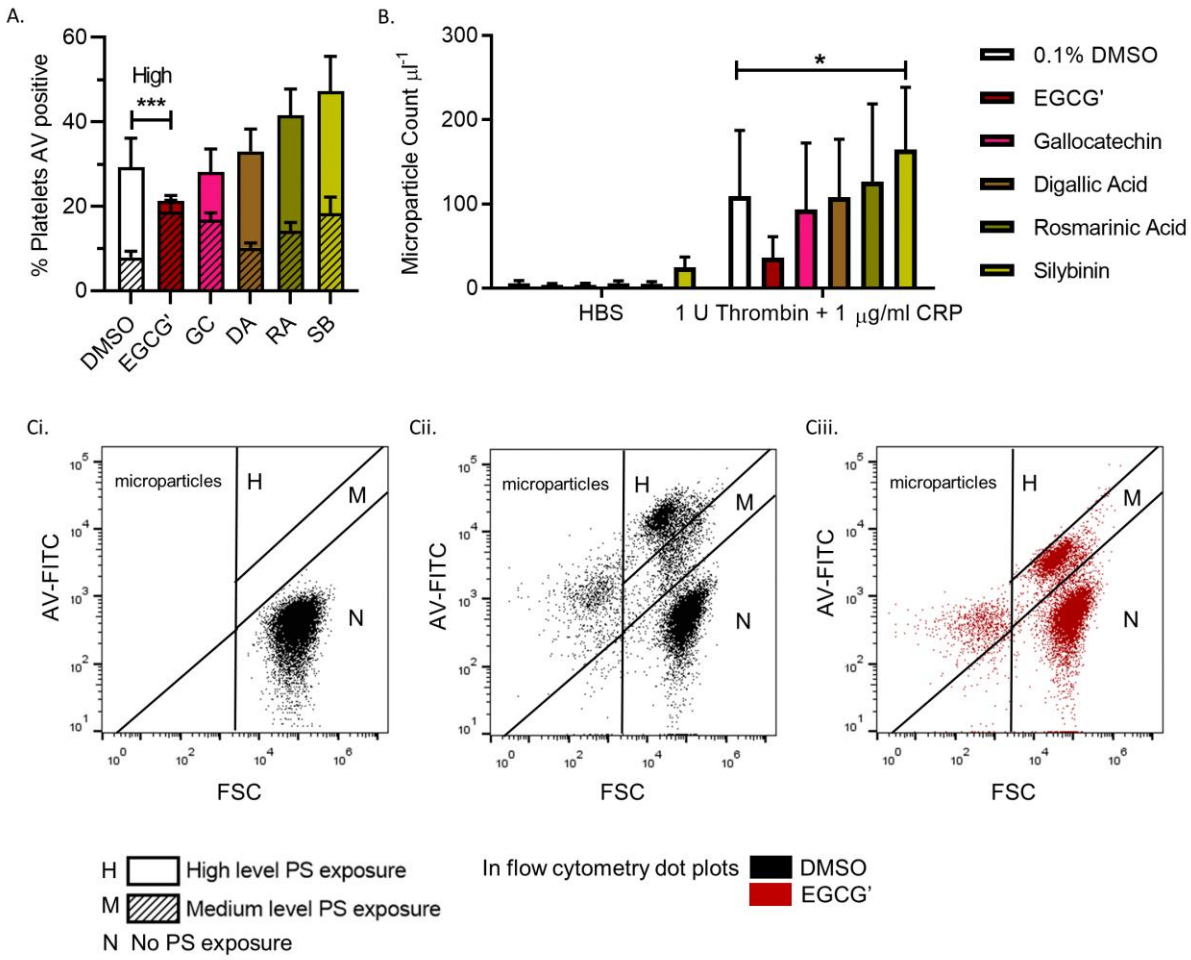

Figure 4.7: EGCG' inhibits high level platelet PS exposure following stimulation with thrombin + CRP-XL. Flow cytometry AV binding after stimulation with 1 U/ml thrombin + 1 µg/ml CRP-XL following a 10-minute incubation with 100 µM polyphenolic compound or 0.1% DMSO at ambient temperature. EGCG' – epigallocatechin gallate; GC- gallocatechin; DA – digallic acid; RA – rosmarinic acid; SB – silybinin. (A) % of platelets with high level or medium level AV binding following stimulation with 1 U/ml thrombin + 1 µg/ml CRP-XL. (B) AV positive microparticle count. (C) Flow cytometry dot plots showing representative AV binding of (i) unstimulated platelets incubated with 0.1% DMSO; (ii) platelets incubated with 0.1% DMSO following stimulation with 1 U/ml thrombin + 1 µg/ml CRP-XL; (iii) platelets incubated with 100 µM EGCG' following stimulation with 1 U/ml thrombin + 1 µg/ml CRP-XL. White bars/black dots - platelets pre-incubated with 0.1% DMSO, dark red dots/ bars – platelets pre-incubated with 100 µM EGCG'. Hatching – medium level PS exposure. No hatching – high level PS exposure. Bar charts show mean ± SEM. N = 4-5. Data analysed using two-way ANOVA, both factors matching, and Sidak's multiple comparisons test in (A) and Dunnett's multiple comparisons test in (B).

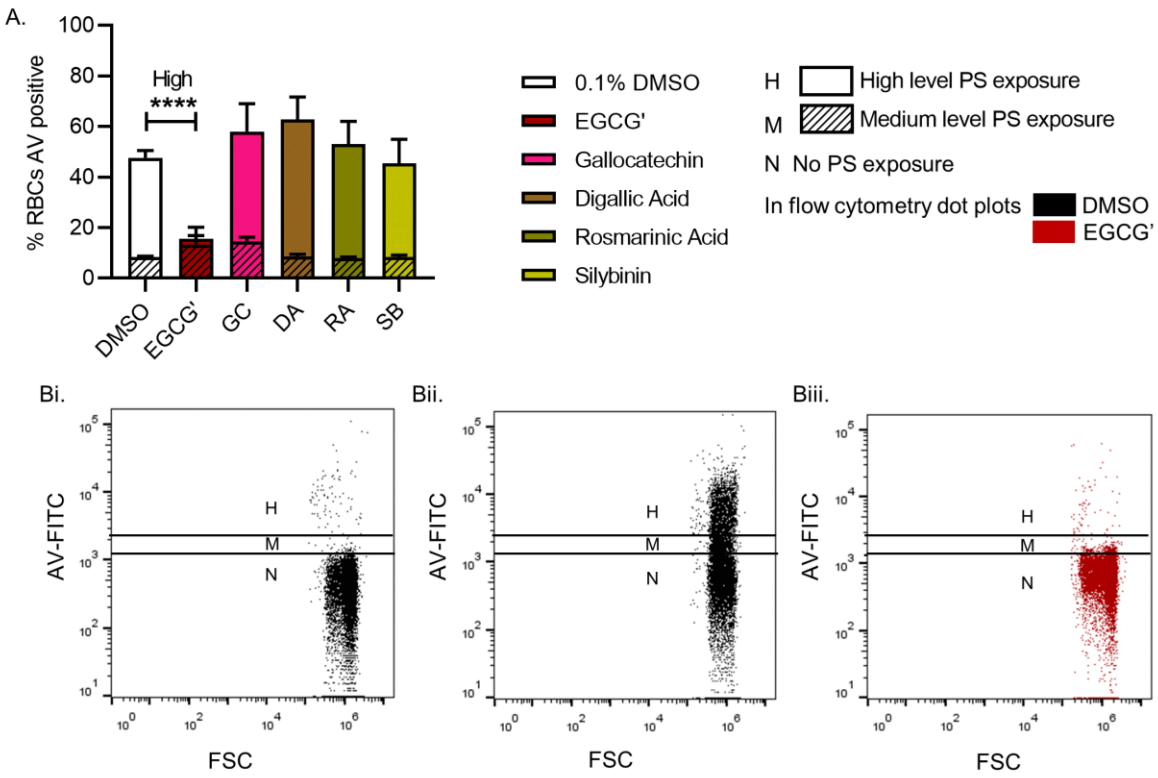

Figure 4.8: EGCG' inhibits high level RBC PS exposure following stimulation with A23187. Flow cytometry AV binding after stimulation with 0.4 μM A23187 following a 10-minute incubation with 100 μM polyphenolic compound or 0.1% DMSO. (A) % of RBCs with high level or medium level AV binding following stimulation with 0.4 μM A23187. (B) Flow cytometry dot plots showing representative AV binding of (i) unstimulated RBCs incubated with 0.1% DMSO; (ii) RBCs incubated with 0.1% DMSO following stimulation with 0.4 μM A23187; (iii) RBCs incubated with 100 μM EGCG' following stimulation with 0.4 μM A23187. White bars/black dots - RBCs pre-incubated with 0.1% DMSO, dark red dots/bars – RBCs pre-incubated with 100 μM EGCG'. Hatching – medium level PS exposure. No hatching – high level PS exposure. Bar charts show mean ± SEM. N = 5. Data analysed using two-way ANOVA, both factors matching, and Dunnett's multiple comparisons test.

4.4 Catechin gallate compounds inhibit high level PS exposure in platelets and RBCs in a flow cytometry AV binding assay

Both EGCG' and GC inhibited high level PS exposure in platelets, and EGCG' in RBCs, following A23187 stimulation (Figures 4.6 and 4.8). In order to better identify the substructures responsible for this activity and identify related compounds which may have a similar effect, I conducted an empirical screen of catechin and catechin gallate compounds, the structures of which are presented in Figure 4.9.

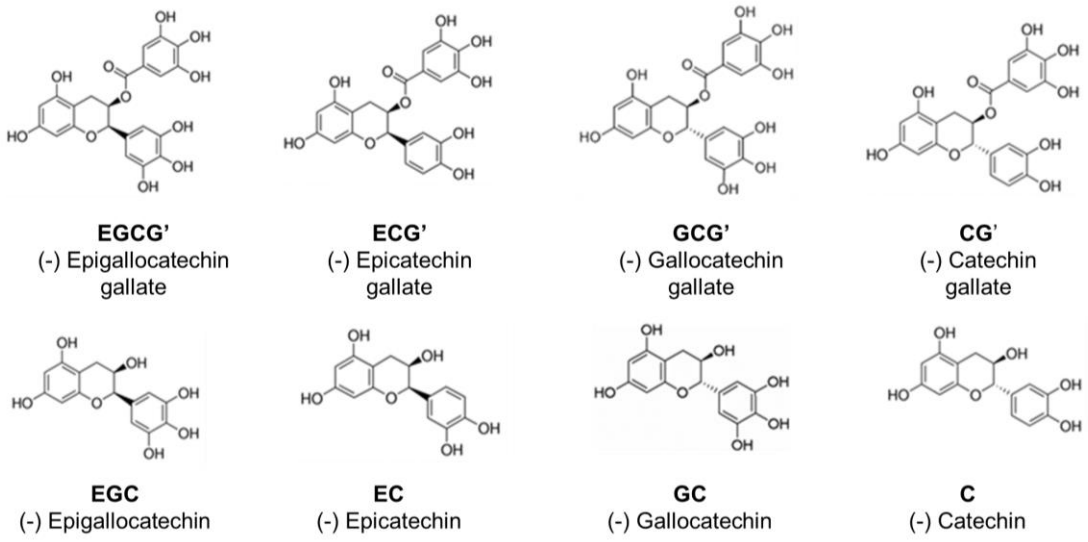

Figure 4.9: Structures of catechin and catechin gallate compounds screened.

All catechin gallate compounds (EGCG', ECG', GCG', CG') inhibited high level PS exposure in platelets following stimulation with 1 U/ml thrombin and 1 µg/ml CRP-XL. This reached statistical significance for EGCG', ECG' and GCG' but did not quite reach significance for CG' (Figure 4.10 A). Instead, CG' significantly increased the proportion of stimulated platelets with medium level PS exposure. CG' also increased the number of AV positive microparticles formed following stimulation with 1 U/ml thrombin and 1 µg/ml CRP-XL (Figure 4.10 B). All catechin gallate compounds also inhibited high level PS exposure in RBCs following stimulation with 0.4 µM A23187 (Figure 4.10 D). The closely structurally related catechin compounds, lacking the gallate group, had no effect on PS exposure in platelets or RBCs, or were much less effective in the case of GC compared with GCG' in RBCs. Gallocatechin compounds, with and without a gallate group, trended towards causing medium level PS exposure in unstimulated RBCs (Figure 4.10 C).

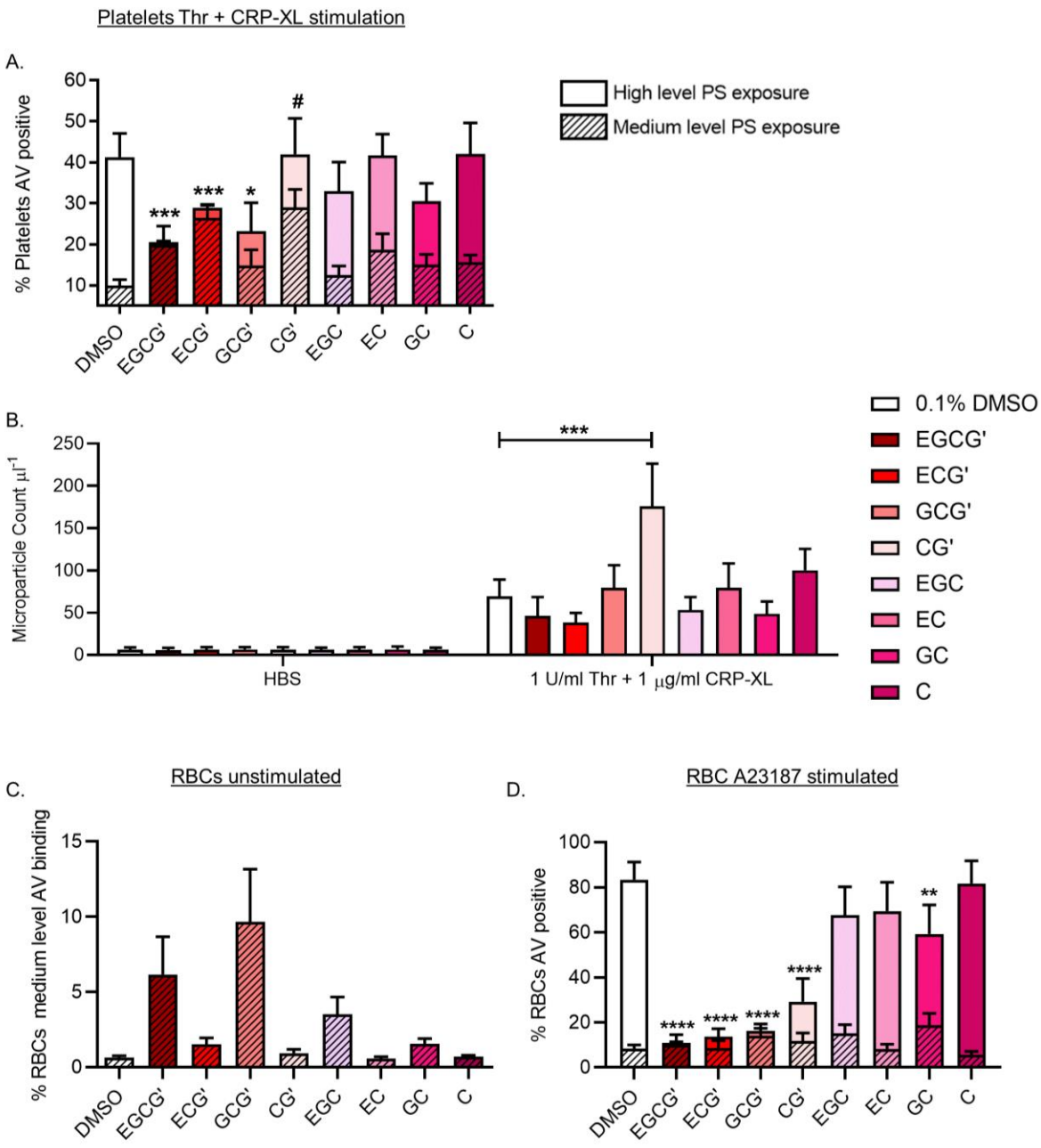

Figure 4.10: Effects of catechin and catechin gallate compounds on platelet and RBC PS exposure. (A) % of platelets with high level or medium level PS exposure following stimulation with 1 U/ml thrombin + 1 µg/ml CRP-XL after incubation with 0.1% DMSO or 100 µM catechin/catechin gallate compound for 10 minutes at ambient temperature. (B) AV positive microparticle count following stimulation with 1 U/ml thrombin + 1 µg/ml CRP-XL. (C) % of unstimulated RBCs with medium level PS exposure after incubation with 0.1% DMSO or 100 µM catechin/catechin gallate compound. (D) % of RBCs with high level or medium level PS exposure following stimulation with 0.4 µM A23187 after incubation with 0.1% DMSO or 100 µM catechin/catechin gallate compound. Hatching – medium level PS exposure. No hatching – high level PS exposure. Bar charts show mean ± SEM. N = 5. Data were analysed using a two-way ANOVA, both factors matching, and Dunnett's multiple comparisons tests in (A), (B) and (D). Data in (C) were analysed using a repeated measures one-way ANOVA and Dunnett's multiple comparisons test. * represents significant changes in high level PS exposure; # represents significant changes in medium level PS exposure.

4.5 Catechin gallate compounds slow platelet scrambling rate following stimulation with A23187 in a plate-based AV binding assay

Real-time scrambling rate following stimulation with 10 µM A23187 was measured using our plate-based luminescence AV binding assay. All catechin gallate compounds (EGCG', ECG', GCG' and CG') slowed scrambling rate compared to 0.1% DMSO (Figure 4.11 A and 4.11 B). GC also inhibited the scrambling rate, though to a lesser extent. The pIC_{50} values for inhibition of peak scrambling rate by the catechin gallate compounds were all similar whereas that for GC was lower (Figure 4.11 C).

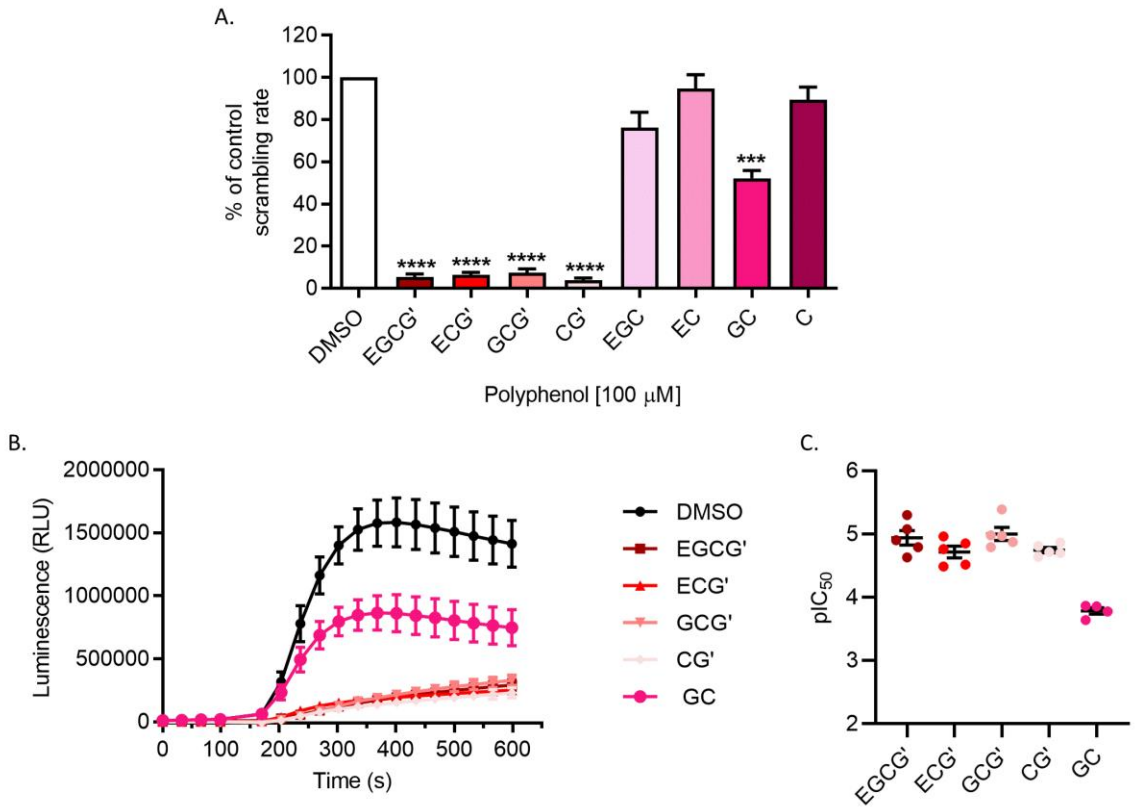

Figure 4.11: Catechin gallate compounds slow platelet scrambling rate. (A) % of control peak scrambling rate in platelets incubated with 100 µM catechin/catechin gallate compounds compared to 0.1% DMSO. (B) Luminescence traces from a real-time plate-based AV binding assay following stimulation with 10 µM A23187 from platelets incubated with 100 µM catechin/catechin gallate compound or 0.1% DMSO. Only traces of compounds which slowed peak scrambling rate are shown here. RLU: relative luminescence units (C) pIC_{50} values for inhibition of peak scrambling rate by catechin compound. Bar charts and traces show mean ± SEM. N = 5. Data were analysed using a repeated measures one-way ANOVA and Dunnett's multiple comparisons test.

4.6 Catechin and catechin gallate compounds do not affect cytosolic Ca^{2+} signalling following stimulation with thrombin and CRP-XL or A23187

Real-time cytosolic Ca^{2+} signals in response to 1 U/ml thrombin + 1 µg/ml CRP-XL dual stimulation or 10 µM A23187 were measured using the fluorescent Ca^{2+} indicator Cal520 on a microplate reader. None of the catechin or catechin gallate compounds significantly affected these cytosolic Ca^{2+} signals when quantified as AUC, peak F/F_0, or F/F_0 at 10 minutes post stimulation (Figure 4.12).

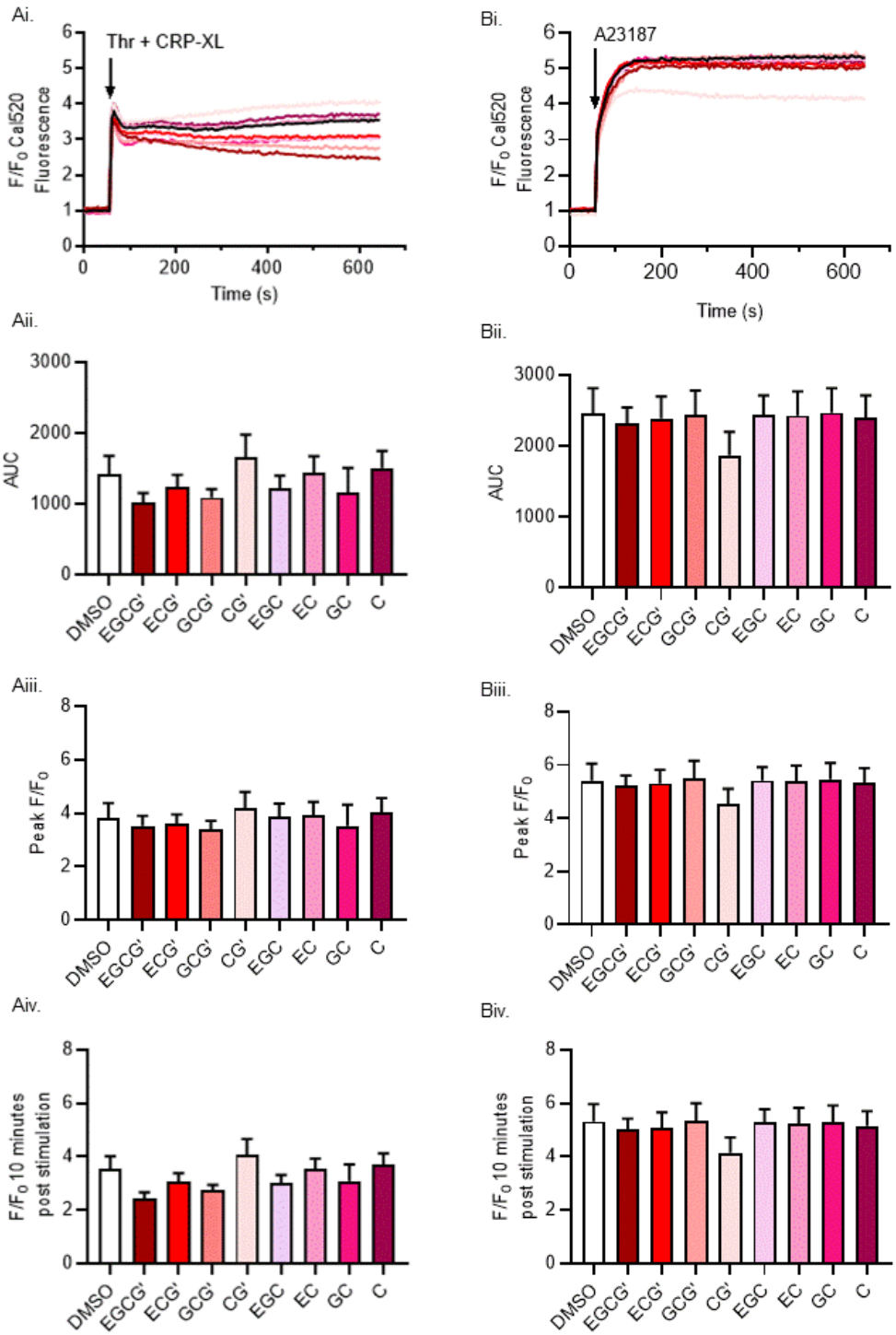

Figure 4.12: Catechin and catechin gallate compounds do not affect platelet cytosolic Ca^{2+} signals following stimulation with thrombin + CRP-XL or A23187. Platelets were loaded with the Ca^{2+}-sensitive fluorescence dye, Cal520. Fluorescence values were normalised to the initial fluorescence values of vehicle controls containing 0.1% DMSO in matched samples to account for variation in dye loading (F/F_0). Platelets were treated with 100 μM catechin/catechin gallate compounds or 0.1% DMSO under conditions that inhibited PS exposure in previous experiments (i.e. a 10-minute incubation and 10-minute stimulation at ambient temperature), Where indicated, platelets were stimulated with (A) 1 U/ml thrombin + 1 μg/ml CRP-XL; (B) 10 μM A23187. Data are presented as (i) F/F_0 Cal520 fluorescence following stimulation; (ii) AUC above baseline ($F/F_0 = 1$); (iii) peak F/F_0 following stimulation; and (iv) F/F_0 at 10 minutes post stimulation. Bar charts show mean ± SEM. N = 5 for all experiments. Data were analysed using repeated measures one-way ANOVA and no statistically significant differences were found between groups.

4.7 Catechin and catechin gallate compounds inhibit platelet $\alpha_{IIb}\beta_3$ integrin activation and α-granule release following stimulation with PAR1-AP

All catechin compounds were additionally tested for effects on PAR1-AP-induced platelet $\alpha_{IIb}\beta_3$ integrin exposure and α-granule release in the same manner as in Figure 4.4, above. Both $\alpha_{IIb}\beta_3$ integrin exposure and α-granule release were significantly inhibited by a range of catechin and catechin gallate compounds (Figure 4.13).

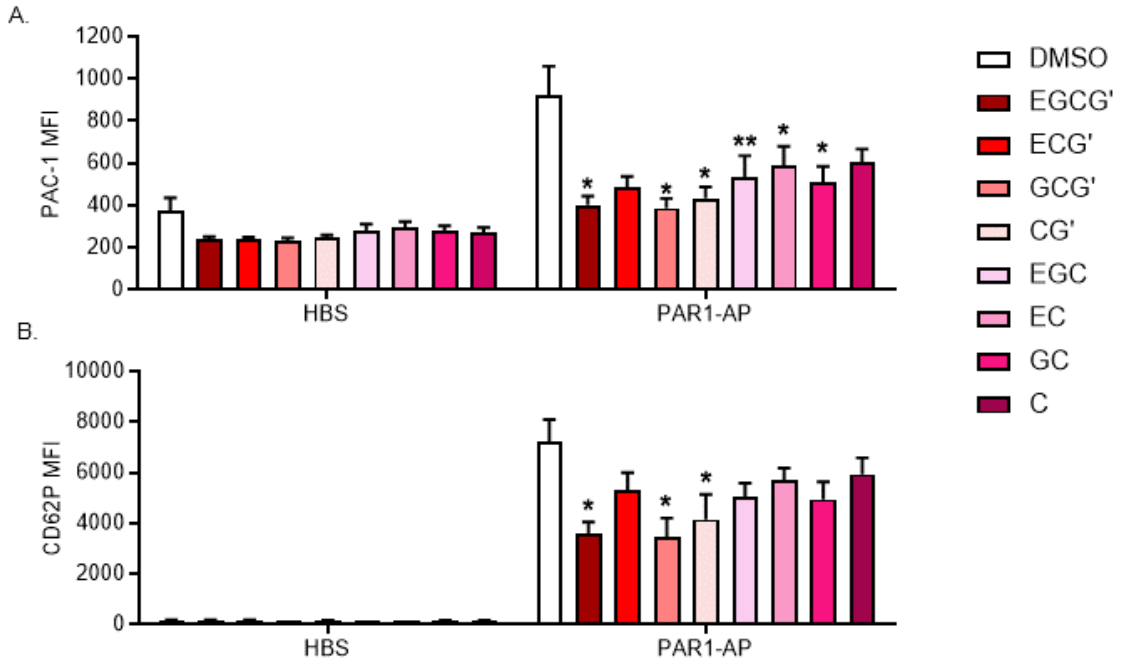

Figure 4.13: Catechin compounds inhibit platelet $\alpha_{IIb}\beta_3$ integrin activation and α-granule release following stimulation with PAR1-AP. Platelets were treated with 100 μM catechin/catechin gallate compound or 0.1% DMSO for 10 minutes at ambient temperature prior to stimulation for 10 minutes. $\alpha_{IIb}\beta_3$ activation was measured by flow cytometry as PAC-1 binding (FITC conjugated). α-granule secretion was measured by anti-CD62P (P-selectin) antibody binding (phycoerythrin (PE) conjugated). (A) PAC-1-FITC MFI following stimulation with 10 μM PAR1-AP. (B) CD62P-PE MFI following stimulation with 10 μM PAR1-AP. Bar charts show mean ± SEM. N = 5. Data analysed using two-way ANOVA, both factors matching, and Dunnett's multiple comparison tests.

4.8 Catechin and catechin gallate compounds do not affect cytosolic Ca^{2+} signalling in response to PAR1-AP

Real-time Ca^{2+} signals in response to 10 μM PAR1-AP, measured using Cal520, showed that none of the catechin or catechin gallate compounds significantly affected these cytosolic Ca^{2+} signals when quantified as AUC, peak F/F_0 or F/F_0 at 10 minutes post stimulation (Figure 4.14).

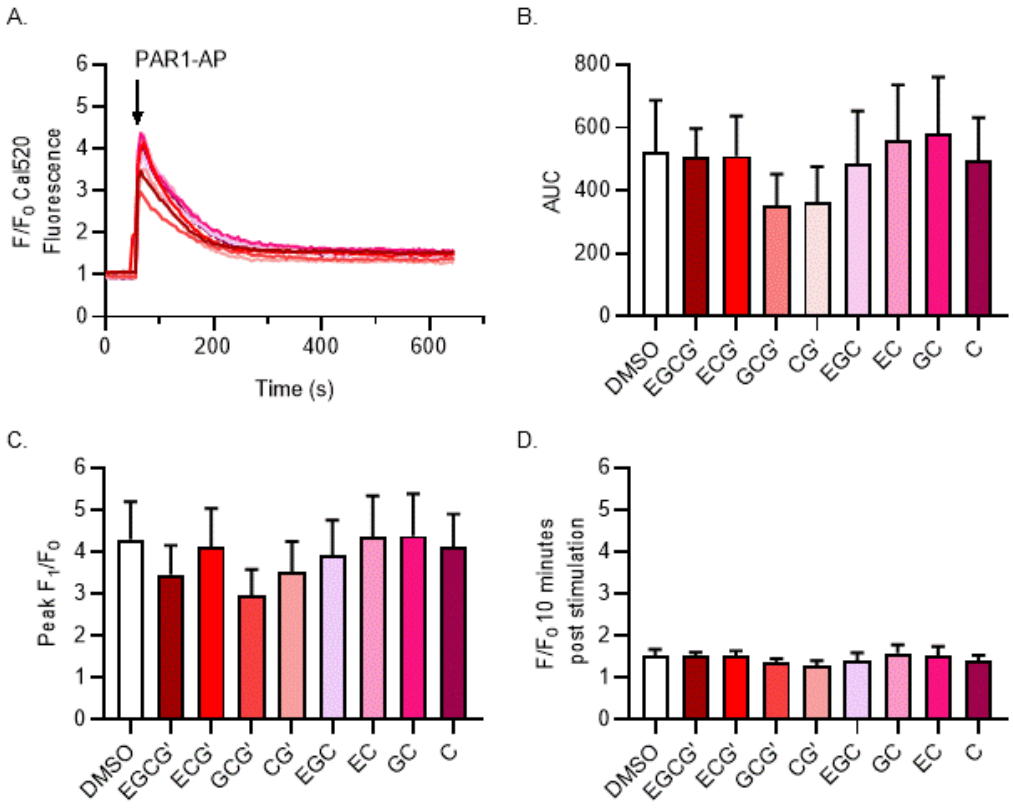

Figure 4.14: Catechin and catechin gallate compounds do not affect platelet cytosolic Ca^{2+} signals following stimulation with PAR1-AP. Cal520-loaded platelets were stimulated with 10 μM PAR1-AP following incubation with 0.1% DMSO or 100 μM catechin/catechin gallate compound. (A) F/F_0 Cal520 fluorescence following stimulation. (B) AUC above baseline ($F/F_0 = 1$). (C) Peak F/F_0 following stimulation. (D) F/F_0 at 10 minutes post stimulation. Bar charts show mean ± SEM. N = 5. Data were analysed using a repeated measures one-way ANOVA and no significant differences compared to DMSO controls were found.

4.9 Discussion

Since the only inhibitor of phospholipid scrambling previously described, R5421 (Dekkers et al., 1998), acts non-selectively in platelets (Millington-Burgess et al., 2020) and ligand-based approaches to improve the selectivity of R5421 were unsuccessful, as detailed in chapter 3, there was a need to pursue other leads for development of a selective inhibitor of platelet scramblase activity.

Polyphenolic compounds including tannic acid and EGCG' have been shown to inhibit TMEM16F-dependent phospholipid scrambling in cell lines and artificial membrane bilayers (Suzuki et al., 2014; Watanabe et al., 2018) but these compounds had not been previously tested on platelet scramblase activity. Here, tannic acid and EGCG' are shown to inhibit platelet scramblase activity for the first time, leading to reduced PS exposure on their surface and reduced AV positive microparticle formation following stimulations with the calcium ionophore A23187 (Figures 4.1 and 4.6) or the more physiologically relevant agonists thrombin and CRP-XL (Figures 4.2 and 4.7).

As discussed in chapter 3, stimulation of platelets with A23187 should bypass intracellular signalling pathways which lead to PS exposure in thrombin + CRP-XL stimulated platelets. As tannic acid and EGCG' inhibit platelet PS exposure following stimulation with A23187 this suggests a direct effect of these compounds on scramblase activity. EGCG' was shown to have no effect on cytosolic Ca^{2+} signals, measured using Cal520, following stimulation with A23187, indicating that EGCG' does not interfere with the action of A23187 itself (Figure 4.6). The effect of tannic acid on platelet cytosolic Ca^{2+} signals following stimulation was not tested, so although it remains possible that tannic acid interferes with the action of A23187, this is unlikely. Further evidence for a direct action of tannic acid and EGCG' on scramblase activity comes from their inhibition of PS exposure in RBCs (Figures 4.3 and 4.8). In the global *Tmem16f*$^{-/-}$ mouse, RBC PS exposure was completely absent (Yang et al., 2012). This suggests that RBC PS exposure might have a simpler mechanism than in platelets, where there is evidence for some lower level TMEM16F-independent PS exposure (van Kruchten et al., 2013). As RBC PS exposure appears only dependent on TMEM16F, RBCS may offer a more direct system in which to measure inhibition of TMEM16F-dependent scramblase activity (Yang et al., 2012). As both tannic acid and EGCG' inhibit RBC PS exposure, this suggests a TMEM16F-dependent effect.

Gallocatechin also inhibited high level platelet PS exposure following stimulation with A23187 (Figure 4.6). The other polyphenolic compounds tested (digallic acid, rosmarinic acid and silybinin) did not affect platelet or RBC PS exposure. This suggests that the galloyl and

catechin structures are important for the inhibitory effects of tannic acid, EGCG' and GC and not all plant polyphenols inhibit scramblase activity.

To probe the structure-activity relationship of compounds for inhibition of platelet scramblase activity, an empirical screen of catechin and catechin gallate compounds was performed, the results of which are summarised in Figure 4.15. EGCG', ECG', GCG' and CG' all inhibited high level PS exposure in platelets and RBCs. None of these catechin or catechin gallate compounds affected platelet cytosolic Ca^{2+} signalling in response to thrombin + CRP-XL or A23187 when measured using Cal520. This indicates that the effects of the catechin gallate compounds on platelet PS exposure are likely mostly independent of effects on Ca^{2+} signalling.

It was noted that EGCG' inhibits high level PS exposure but the percentage of platelets with medium level PS exposure following stimulation with A23187 or thrombin + CRP-XL was increased. The exact nature of this medium level PS exposure remains to be determined. It is possible that it represents a much reduced TMEM16F-dependent activity that allows PS to slowly accumulate due to inhibition of the flippase in pro-coagulant platelets but that does not support enough AV binding for the "all or nothing" signal usually seen in pro-coagulant platelets, discussed in chapter 3. An alternative explanation could be that EGCG' enhances TMEM16F-independent PS exposure. Ideally a scramblase inhibitor would not cause increased medium level PS exposure and this is important to consider in future inhibitor design based around EGCG'. As previously discussed, complete inhibition of TMEM16F activity may be required for therapeutic benefit to prevent thrombosis. Similarly, gallocatechin compounds were found to tend towards causing medium level PS exposure in RBCs. Though this weak activatory effect was not seen in platelets, this should also be avoided in a novel inhibitor of platelet scramblase activity since RBC PS exposure will also contribute to thrombosis (Byrnes and Wolberg, 2017).

Figure 4.15A highlights in red the gallate groups found to be necessary for inhibition of high level PS exposure since the related compounds lacking the gallate groups (EGC, EC, GC, C) did not inhibit high level PS exposure, or did so to a lesser extent as was the case for the effect of GC compared to GCG' on high level RBC PS exposure (Figure 4.10 D). Highlighted in blue are the hydroxyl groups of the gallocatechins which seems to have a week activatory effect on scramblase activity and leads to some medium level PS exposure in unstimulated RBCs. All catechin and catechin gallate compounds inhibited platelet $\alpha_{IIb}\beta_3$ integrin activation and α-granule release following stimulation with PAR1-AP to some degree (Figure 4.13). None of the compounds tested had any effect on cytosolic Ca^{2+} signals following stimulation with PAR1-AP, suggesting the inhibitory effects on integrin activation and α-granule release are

independent of Ca^{2+} signalling (Figure 4.14). This fits with the known multiple inhibitory effects of EGCG' on platelet function (Jin et al., 2008; Lee et al., 2013; Ok et al., 2012). If these catechin gallate compounds all act similarly to EGCG', then raising [cAMP] or inhibiting thromboxane production or ADP-mediated activation could all explain their actions to inhibit integrin activation or α-granule release. This hypothesis could be tested by measuring [cAMP], thromboxane A_2 production by ELISA or performing aggregometry following stimulation with ADP, although this was beyond the scope of this project. Due to these effects on pro-aggregatory platelet functions, none of these compounds are suitable for use in order to investigate the effects of inhibition of platelet scramblase function on thrombosis.

A.

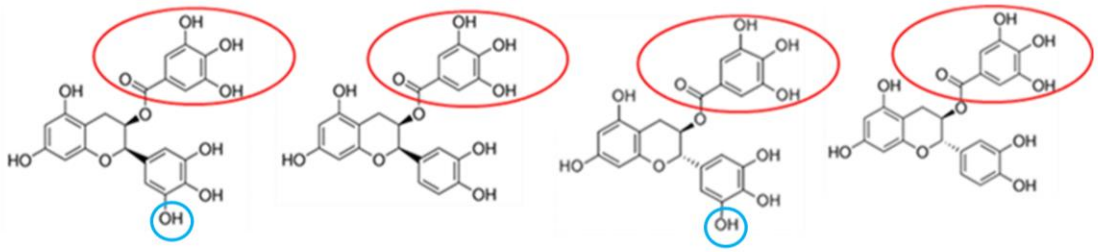

EGCG'
(-) Epigallocatechin gallate

ECG'
(-) Epicatechin gallate

GCG'
(-) Gallocatechin gallate

CG'
(-) Catechin gallate

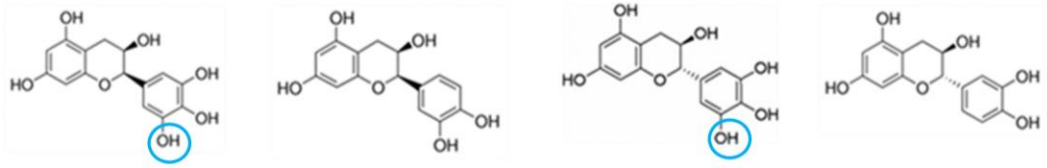

EGC
(-) Epigallocatechin

EC
(-) Epicatechin

GC
(-) Gallocatechin

C
(-) Catechin

B.

	Platelet high level PS exposure	Platelet medium level PS exposure	Platelet microparticle formation	RBC high level PS exposure	Unstimulated RBC medium level PS exposure	Platelet $\alpha_{IIb}\beta_3$ integrin activation	Platelet α-granule release	Platelet cytosolic Ca^{2+} signalling
EGCG'	↓	↑ A23187	↔	↓	↑	↓	↓	↔
ECG'	↓	↔	↔	↓	↔	↓	↓	↔
GCG'	↓	↔	↔	↓	↑	↓	↓	↔
CG'	↓	↑ Thr+CRP-XL	↑	↓	↔	↓	↓	↔
EGC	↔	↔	↔	↔	↑	↓	↓	↔
EC	↔	↔	↔	↔	↔	↓	↓	↔
GC	↔	↔	↔	↓	↑	↓	↓	↔
C	↔	↔	↔	↔	↔	↓	↓	↔

Figure 4.15: Summary of effects of catechin and catechin gallate compounds on platelet and RBC function. (A) Chemical structures of the catechin compounds tested. Highlighted in red are the gallate groups necessary for inhibition of high level PS exposure in platelets and RBCs. Highlighted in blue are the hydroxyl groups of the gallocatechins associated with medium level PS exposure in unstimulated RBCs. (B) Summary table of the effects of catechin compounds on platelet and RBC function. Highlighted in green are desirable functions of compounds. Highlighted in red are undesirable functions of compounds. Highlighted in yellow are effects on platelet medium level PS exposure, the relevance of which remains undetermined.

This empirical screen of catechin compounds has not identified a selective inhibitor of platelet scramblase activity. It has, however, provided information on a structure-activity relationship upon which to base future development of more selective inhibitors of platelet scramblase activity. All catechin gallate compounds were aligned using Forge v10.6 software (Cheeseright et al., 2006) which highlights the electrostatic properties of the inhibitory gallate group (circled in red and showing both positive and negative electrostatic fields around the molecule), which would be desirable to maintain in a new inhibitor, and the activatory galloyl group (highlighted in blue and showing a negative electrostatic field around the molecule) responsible for medium level PS exposure in RBCs, which a new inhibitor would ideally lack (Figure 4.16). In addition to molecular shape and size, these electrostatic properties are an important consideration when developing new inhibitors of phospholipid scramblase activity since they will determine the interactions compounds make with their target to elicit a biological effect.

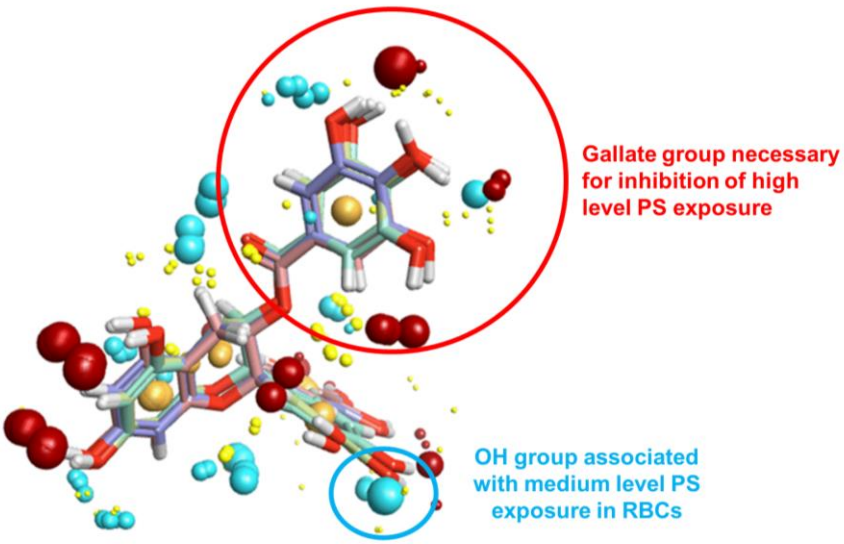

Figure 4.16: Electrostatics of the aligned catechin gallate compounds. Aligned 3D conformations of catechin gallate compounds calculated using Forge. Negative fields shown in blue, positive fields shown in red, hydrophobic fields shown in yellow.

Chapter 5 – A structure-based screen using an nhTMEM16 structure

Chapter 4 showed for the first time that the polyphenolic compounds tannic acid and EGCG' inhibit platelet scramblase activity. An empirical screen determined that catechin gallate compounds (e.g. ECG') inhibit platelet scramblase activity whereas related catechin compounds lacking the gallate group (e.g. EC) do not, suggesting a structure-activity relationship for inhibition of platelet scramblase activity. The catechin gallate compounds, however, are not selective inhibitors of platelet scramblase activity since they also inhibit platelet $\alpha_{IIb}\beta_3$ integrin activation and α-granule release, both of which are necessary for pro-aggregatory platelet activity. This means that the catechin gallates are unsuitable compounds to use to assess the effects of inhibiting platelet pro-coagulant activity and new compounds need to be identified for this use.

This chapter aimed to use a structure-based *in silico* modelling approach to try and identify more selective inhibitors of platelet scramblase activity. When starting this project, the only phospholipid scramblase structure available was that of nhTMEM16 (Brunner et al., 2014) and so this was used for initial screens. Blind *in silico* drug docking studies were performed to predict where the polyphenolic compounds previously tested might interact with the nhTMEM16 structure and this site was then used to screen the Enamine compound library for new structures which might be expected to dock to the same site and could be tested for activity in platelets. Such structure-based drug design methodologies are well established (Batool et al., 2019; Ferreira et al., 2015; van Montfort and Workman, 2017; Wang et al., 2016) and have led to the development of effective and selective compounds against a range of targets including carbonic anhydrase (Supuran, 2012), HIV protease (Wlodawer and Vondrasek, 1998), Pim1-kinase (Ren et al., 2011), STAT3 (Matsuno et al., 2010) aldose reductase (Wang et al., 2013) and cyclo-oxygenase 2 (Dadashpour et al., 2015).

5.1 Binding site prediction for catechin and catechin gallate compounds to nhTMEM16

Energy minimised structures of all catechin and catechin gallate compounds were blindly docked into the prepared X-ray crystallography structure of nhTMEM16 (PDB: 4WIS, 3.3 Å) (Brunner et al., 2014) using Autodock Vina (Trott and Olson, 2010). Docking simulations predict sites where ligands may interact with protein structures, the lowest energy ligand conformation at each site (a pose) and predict the binding energy between ligand and protein at each site. Each run of a docking simulation gives 9 poses per compound, ranked by predicted binding energies with the lowest energy predicting the strongest interaction between compound and protein. Note that for presentation purposes the negative of these binding energies have been used here so that a higher binding energy indicates a stronger predicted interaction.

Each compound was docked into the nhTMEM16 structure during 5 independent runs, to give a total of 45 poses per compound. When multiple compounds are being considered, the number of poses involved becomes too many to reliably or feasibly inspect by eye and comparison of poses could be easily biased. Therefore, an automated method for analysing the localisation of docking poses was developed. This automated method was not intended to replace visual inspection of poses of interest or to be highly relied upon to compare individual poses, rather a rapid way to assess whether compounds are predicted to dock to similar areas of a protein structure. Indeed, to compare individual poses in detail, it would be appropriate to re-dock compounds of interest using more focused docking programs such as GOLD which are known to give better predictions of compound orientation and binding affinities compared to Autodock Vina (Jones et al., 1997).

5.2 Automation of docking pose analysis

A program was written by Tom Millington to automate the analysis of docking poses. The code for this program is attached as appendix 1. The operation of the program can be summarised as follows and is illustrated in Figure 5.1.

Each pose, saved in pdb format from Autodock Vina, is read by the program which extracts the compound name, pose ranking and binding energy from the file name and the co-ordinates of each atom from the file. The centroid of each pose is calculated, as the mean co-ordinate of all atoms in the compound. K-means clustering was applied to the centroids of each pose to identify clusters of poses that approximately co-localise within the protein structure. K-means clustering seeks to sort a sample of n observations (here, docked poses) into k clusters. For the initial program, poses were defined to be within the same cluster as each

other if the centroid of the pose was within 10 Å of the centre co-ordinate of the cluster, which is calculated as the mean of all the pose centroids in the cluster.

To initialise the K-means clustering, k random, non-coincident poses are selected, and their centroids used as cluster centres. Once initialised, the remaining poses are each assigned to the cluster whose centre is closest to the pose centroid. After these allocations, the cluster centroids are re-computed considering all the poses assigned to that cluster. These assignments of poses and computation of cluster centre steps are repeated until no poses are assigned to different clusters between sequential iterations. At this point, the poses will be divided into k clusters.

The program will perform K-means clustering with increasing values of k until a clustering is achieved where every pose centroid is within 10 Å of the cluster centre. If they are, the clustering is accepted. If they are not, k is increased, and the clustering is re-run with the new value of k+1. This is iterated until 1000 clusterings have been accepted and the clustering with the smallest value of k is outputted as the result.

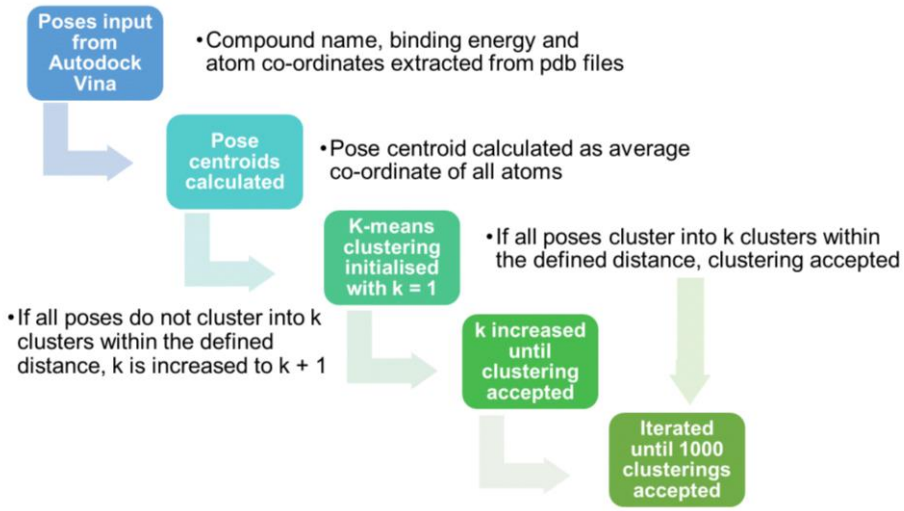

Figure 5.1: Summary of automated program for analysing blind docking poses. K-means clustering is applied until all poses cluster within a defined distance of cluster centre.

5.3 Validation of automated docking pose analysis method

To ensure the automated analysis program was performing as expected, the results were compared with visual inspection. Figures 5.2 and 5.3 illustrate space filling representations of the poses for each catechin and catechin gallate compound docked into the 4WIS structure and the clusters as defined by our program. The program worked well identifying the correct number of clusters for EGCG', ECG', GCG' and GC. However, for CG', EGC, EC and C the number of clusters identified visually and by the program differed.

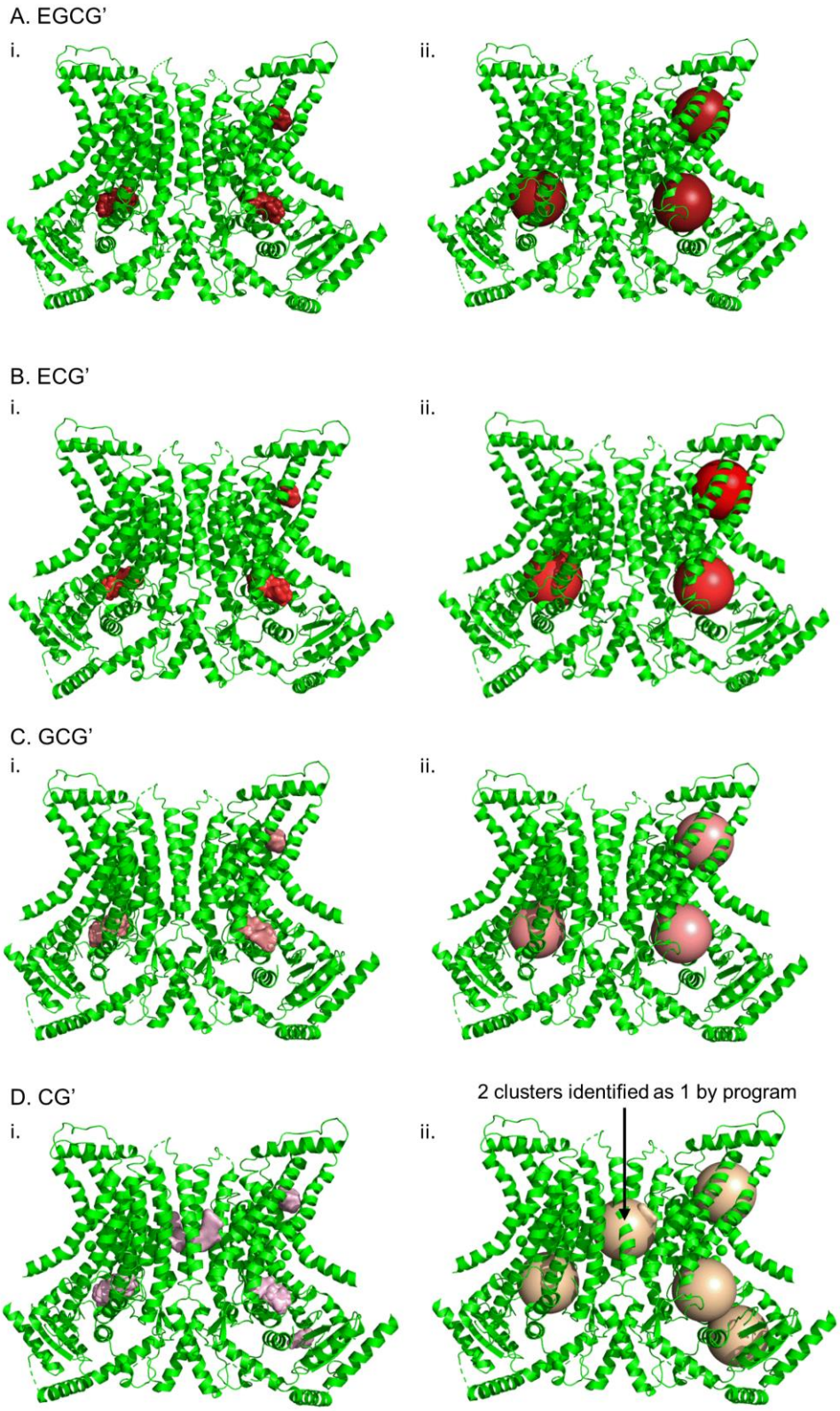

Figure 5.2: Catechin gallate compound clustering analysis in nhTMEM16. (i) Space filling representation of all compound poses in nhTMEM16 structure (4WIS). (ii) Clustering of poses for each compound identified by our automated program in nhTMEM16 structure represented by 10 Å radius spheres. (A) EGCG'; (B) ECG'; (C) GCG'; (D) CG'.

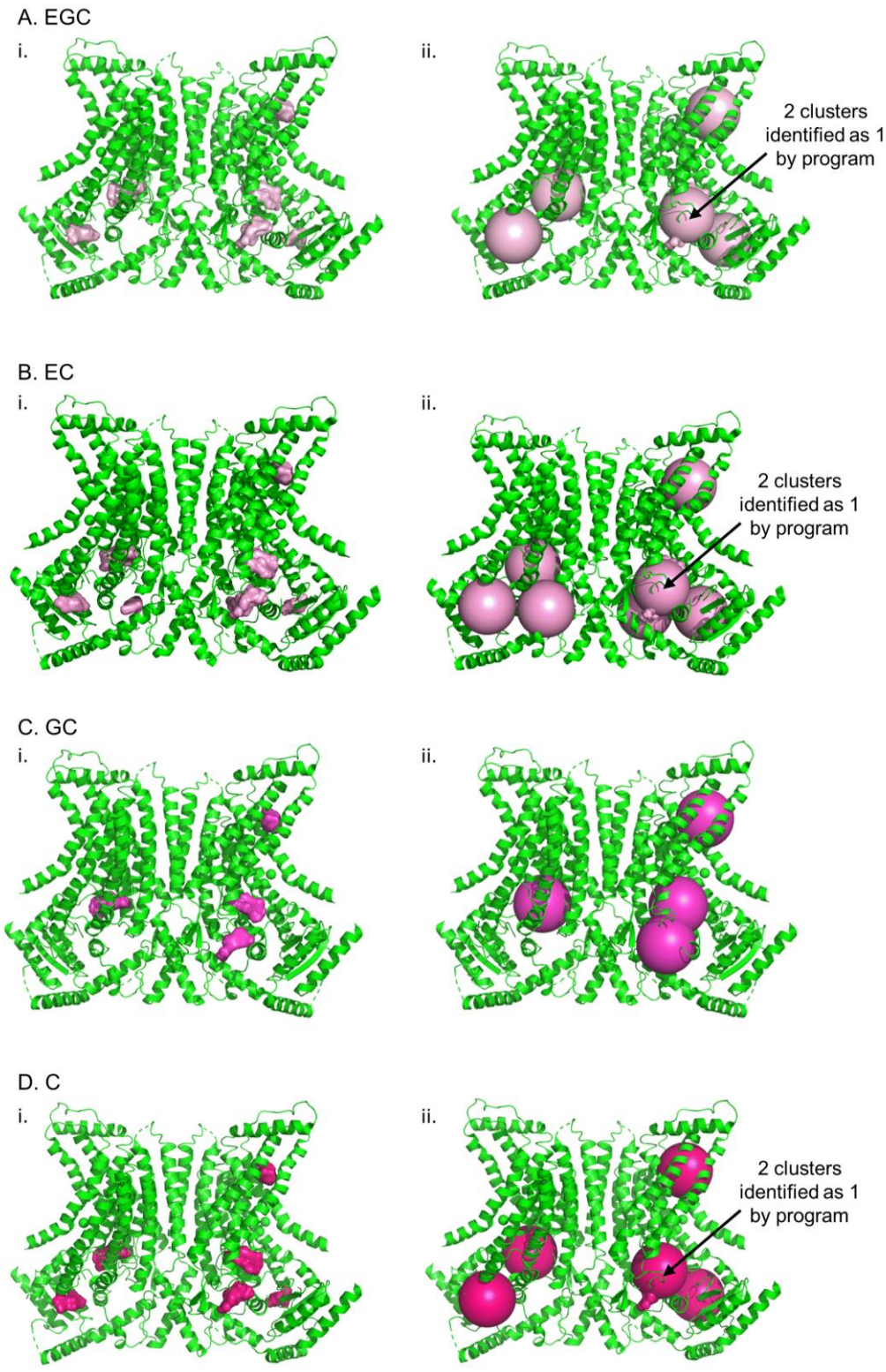

Figure 5.3: Catechin compound clustering analysis in nhTMEM16. (i) Space filling representation of all compound poses in nhTMEM16 structure (4WIS). (ii) Clustering of poses for each compound identified by our automated program in nhTMEM16 structure represented by 10 Å radius spheres. (A) EGC; (B) EC; (C) GC; (D) C.

In all cases where the program correctly identified the number of clusters, all atoms of included poses are contained within the cluster sphere of 10 Å radius. In the cases where the program underestimates the number of clusters, this is not the case and some atoms of poses fall outside the 10 Å radius. A modification was made to the program requiring all atoms of included poses to be within 10 Å of the cluster centre. With this modification, the program correctly identified all clusters for all catechin and catechin gallate compounds, including those previously incorrectly analysed (Figure 5.4). These results are summarised in Table 5.1.

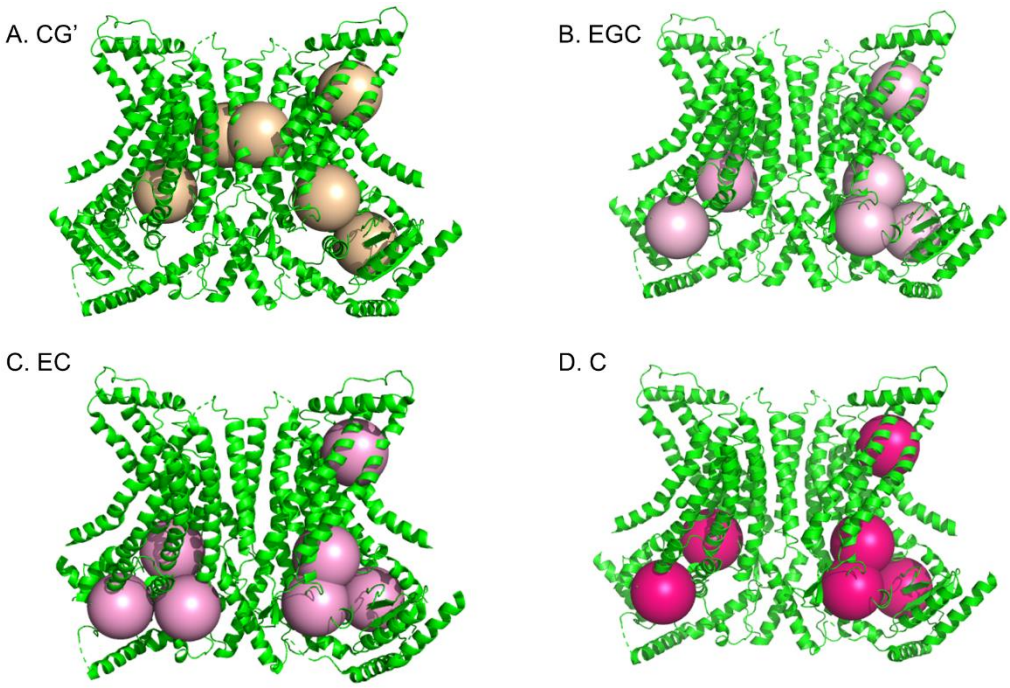

Figure 5.4: Clustering results when all atoms of included poses must be within 10 Å of cluster centre. Clustering of poses for each compound identified by our automated program in nhTMEM16 structure (4WIS) represented by 10 Å radius spheres when all atoms of included poses must be within these spheres. (A) CG'; (B) EGC; (C) EC; (D) C.

Compound	Number of clusters identified visually	Number of clusters identified by program: pose centroids within 10 Å of cluster centre	Number of clusters identified by program: all atoms of poses within 10 Å of cluster centre
EGCG'	3	3	3
ECG'	3	3	3
GCG'	3	3	3
CG'	6	5	6
EGC	6	5	6
EC	8	7	8
GC	4	4	4
C	6	5	6

Table 5.1: Summary of automated docking analysis program validation. The number of clusters of poses for each catechin compound identified by visual inspection, using our initial program where all pose centroids should be within 10 Å of the cluster centre and the modified program where all atoms of included poses should be within 10 Å of the cluster centre. Green shading highlights correct identification of clusters by program, red shading highlights incorrect identification of clusters by program.

Whilst the program correctly identified each cluster, some clusters were in equivalent positions in each monomer subunit of the dimeric structure. Ideally the program would identify these equivalent clusters. Initially it was assumed that the monomers were rotated from each other by 180°, meaning the axis of rotation should fall along the mid-point between equivalent residues. This approach, however, did not give a linear rotation of axis so the "draw_rotation_axis" script[1] was used to identify that the angle of rotation between monomers in the pdb file was 179.2° and define the axis of rotation and transformation matrix.

The rotation matrix and the centre of mass of each monomer chain, A and B, were passed into the program and all poses within clusters that were closer to the centre of mass of chain B were transformed. Once these poses have been transformed the program checks whether they can be merged into existing clusters within the chain A space such that all atoms are within 10 Å of the re-calculated cluster centre. If so, the transformed poses are assigned to that cluster. If not, the mean of the transformed poses' centroids is re-calculated and becomes the new cluster centre. Poses were transformed using both the transformation matrix and the inverse transformation matrix and the transformation that resulted in the tightest final clustering was used. If transformed poses did not merge with an existing cluster, the average of the transformed and inverse transformed poses were used. Figure 5.5 shows the results of these transformations for EGCG' and CG' dockings.

[1] https://pymolwiki.org/index.php/RotationAxis accessed 5/8/20

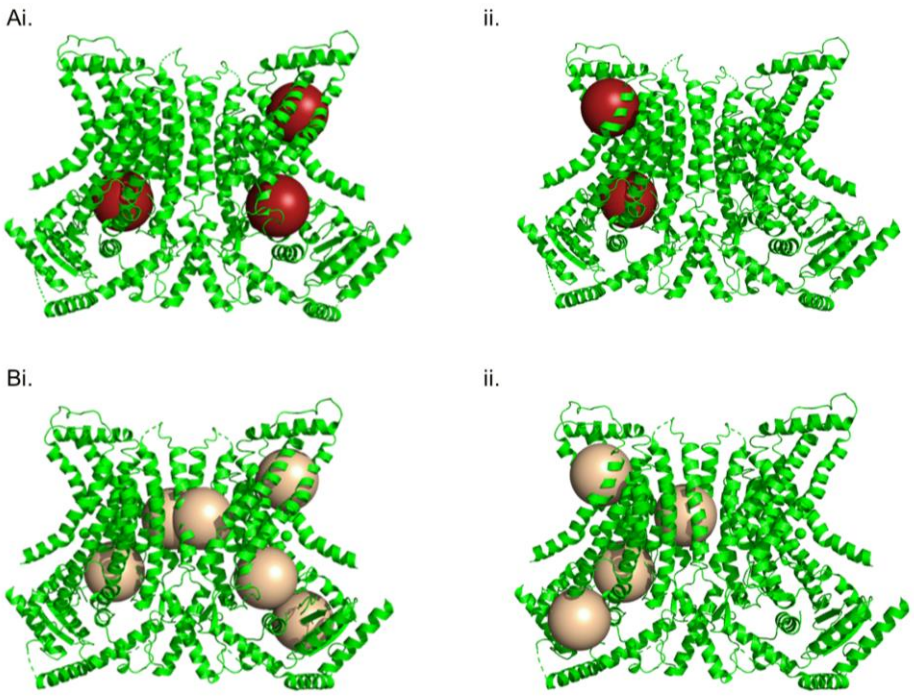

Figure 5.5: Examples of detection of equivalent clusters in each monomer by our program. (i) All clusters detected by program. (ii) Equivalent clusters rotated to be in the same monomer space. (A) EGCG'; (B) CG'. Clusters represented by 10 Å radius spheres.

The program calculates a range of additional parameters as well as the number of clusters identified and their cluster centres as exemplified in Table 5.2. The program will calculate the number of poses in each cluster, the mean predicted binding energies (kcal/mol) of all poses included in a cluster, the standard deviation (STD) of pose centroids from the cluster centre and the maximum dimension of the cluster (Å) which can be compared to the maximum dimension of poses (Å) included for an indication of the spread of poses within the cluster. Additionally, the program will track the clustering of the highest ranked poses from each docking run and output the lowest energy pose in each cluster. These outputs can be compared to give some indication of any differences between compounds which may help explain the biological action of some compared to the ineffectiveness of others.

Compound	No. of clusters	Mean predicted binding energy of poses in most populous cluster (kcal/mol)	STD of poses in cluster	No. of poses in most populous cluster (45)	Max dimension of cluster (Å)	Max dimension of pose (Å)
EGCG'	2	9.03	1.08	36	14.71	12.21
ECG'	2	8.88	1.11	36	14.88	12.06
GCG'	2	8.98	1.13	36	15.51	12.50
CG'	4	8.86	1.16	33	14.60	12.37
EGC	4	7.89	0.92	16	13.44	10.53
EC	5	7.95	1.07	15	12.70	10.44
GC	3	8.25	0.62	32	12.86	10.84
C	4	8.21	0.71	18	12.73	10.76

Mean predicted binding energy (kcal/mol)							
10.0 – 10.39	9.6 – 9.99	9.2-9.59	8.8 – 9.19	8.4 – 8.79	8.0 – 8.39	7.6 – 7.99	7.2 – 7.59
Number of poses in most populous cluster (45)							
40-45	35-39	30-34	25-29	20-24	15-19	10-14	<10

Table 5.2: Example outputs of automated analysis of docking poses. Mean predicted binding energy of poses and the number of poses in most populous cluster are colour coded. This colour coding will be used in subsequent tables. STD – standard deviation.

Figure 5.6A plots the distance of the most populous cluster centres for each compound compared to the most populous EGCG' cluster. Figure 5.6B plots the clusters closest to the second EGCG' cluster identified for each compound. In Figure 5.6A, all the most populous clusters for each compound are at an equivalent site, with their centres all less than 2 Å from each other. Some of this spread could be due to pose centroids being affected by the larger gallate groups. Bubble size represents the number of poses within the cluster and the catechin gallate compounds cluster more commonly to this site compared to the catechin compounds, except for GC. The catechin gallate compounds have higher predicted binding energies compared to the inactive catechin compounds. Figure 5.6B shows that a few poses of all catechin and catechin gallate compounds also localise to the same site as the second EGCG' cluster.

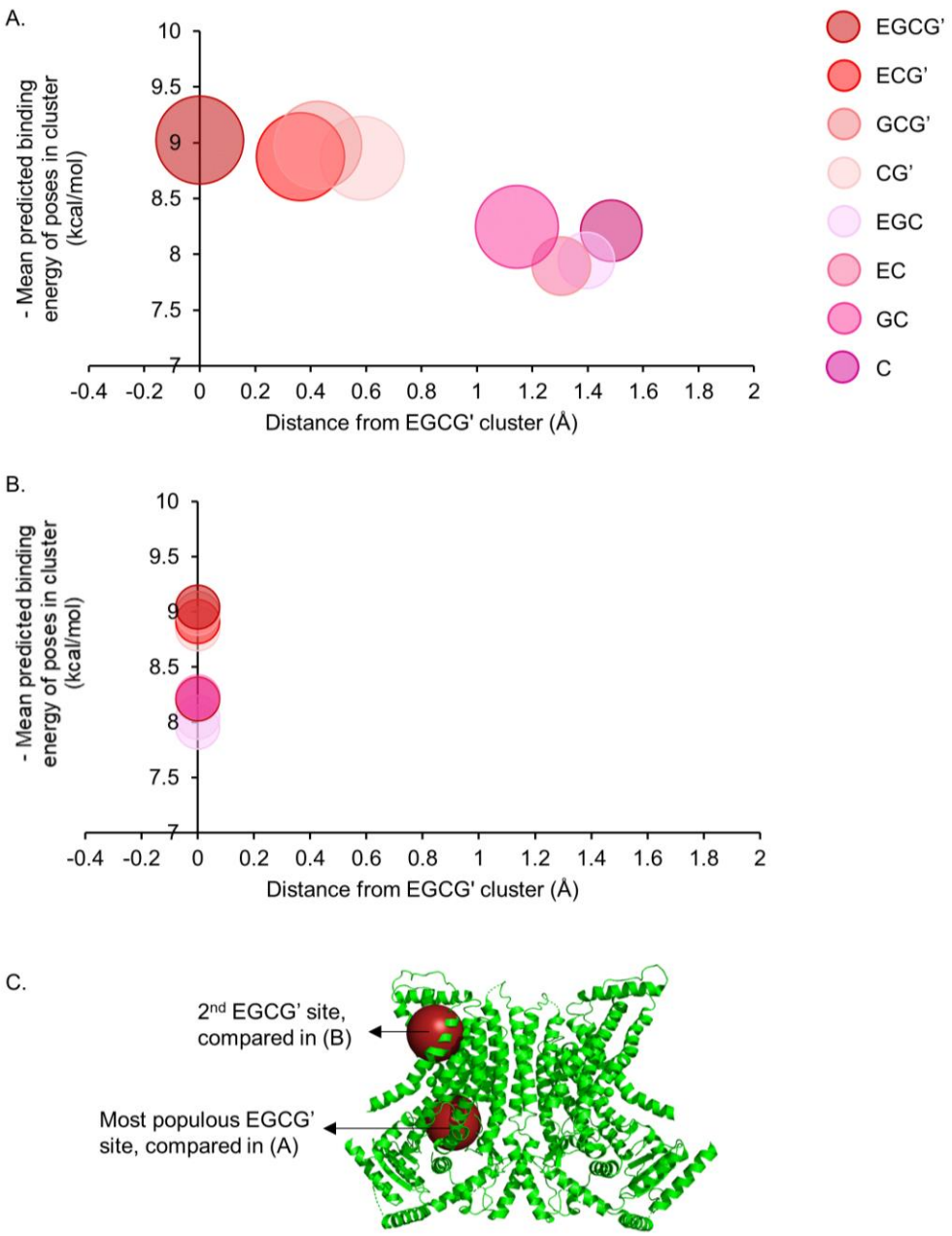

Figure 5.6: Clustering analysis comparing polyphenol cluster distance from EGCG' reference clusters. Distance from EGCG' cluster centres plotted against mean predicted binding energies of poses in cluster. Bubble size represents number of poses in each cluster. (A) Compared to most populous EGCG' cluster. (B) Compared to second EGCG' cluster identified. (C) EGCG' clusters identified by program in nhTMEM16 structure (4WIS) represented as 10 Å radius spheres.

5.4 A structure-based screen around EGCG' dockings in the nhTMEM16 structure

73-80% of catechin gallate compound poses and 72% of GC poses, which did show some degree of inhibition of platelet scramblase activity, dock to the same site in the nhTMEM16 structure. This site is at the cytosolic side of the hydrophilic groove believed to be the pathway for phospholipid movement. It was therefore decided to use this site as the basis for a structure-based screen of the Enamine chemical library using FRED (McGann, 2011). The Enamine Hit Locator library was chosen since it continues a wide range of chemically diverse structures (234240 novel scaffolds) which are commercially available with high purity (>90%) and analogues of scaffolds are obtainable or can be custom synthesised if required. A single reference pose is required for screening using FRED and so the highest energy EGCG' pose from the Autodock Vina runs was re-docked using GOLD, which gives more accurate predictions of ligand poses, and used as the reference query (Figure 5.7). The predicted ligand interactions of the GOLD EGCG' pose were visualised using Poseview (Stierand and Rarey, 2007) (Figure 5.7 C). None of the residues highlighted here by Poseview have been previously described in the literature so their importance to phospholipid scrambling is unknown. Such ligand interactions may underlie the activity of EGCG', however, and can be used for future comparison with any new inhibitors of platelet scramblase activity identified. The compounds from FRED with the highest predicted binding energies from their re-docking in GOLD, were selected for screening. The compounds were blinded for screening purposes and known as S1-S15. The structures of compounds S1-S15 are given in Table 5.3.

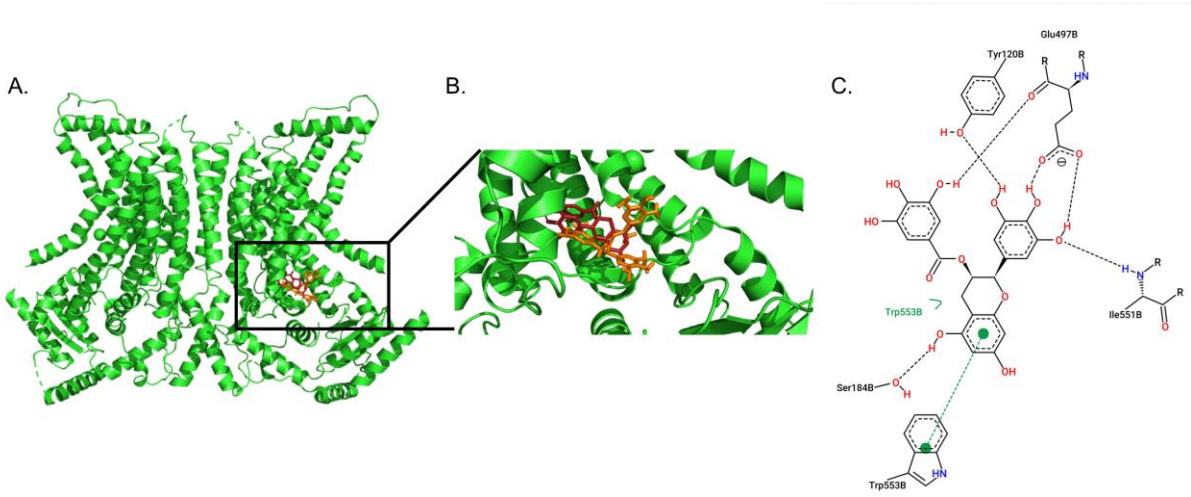

Figure 5.7: EGCG' pose used for FRED screen. (A) Autodock Vina (red) and GOLD (orange) EGCG' pose in nhTMEM16 structure. (B) Close up of Autodock Vina and GOLD EGCG' poses. (C) Poseview result of GOLD EGCG' pose showing predicted ligand interactions.

Table 5.3 Chemical structures and supplier information of compounds S1-S15 identified by structure-based screen around EGCG' dockings in nhTMEM16. MW – molecular weight.

Compound	MolPort ID	IUPAC	MW	Structure
S1	028-548-024	N-benzyl-N-(cyclobutylmethyl)-1-oxo-1,2-dihydroisoquinoline-3-carboxamide	346.4	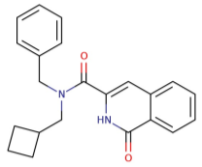
S2	030-027-273	1-cyclopropyl-3-[3-(1-methyl-1H-1,2,4-triazol-3-yl)phenyl]-1-[(pyridin-3-yl)methyl]urea	348.4	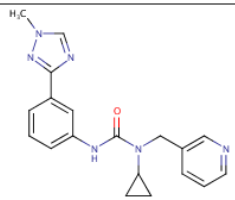
S3	035-827-378	N-(cyclopropylmethyl)-N-[(3-hydroxyphenyl)methyl]-1-oxo-1,2-dihydroisoquinoline-3-carboxamide	348.4	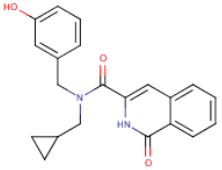
S4	038-979-627	(4aR,7aS)-1-{2-cyclopropyl-5-phenylthieno[2,3-d]pyrimidin-4-yl}-octahydro-1H-pyrrolo[3,4-b]pyridin-5-one	390.5	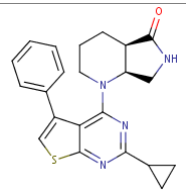
S5	039-001-563	2-(3-methoxyphenyl)-N-[3-methyl-5-(4-methylpiperazin-1-yl)phenyl]acetamide	353.5	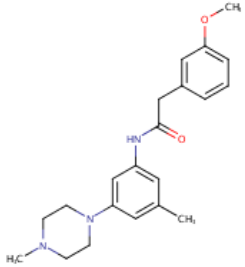

S6	039-276-406	1-[2-(1H-indol-3-yl)acetyl]-4-phenylpiperidine-4-carboxylic acid	362.4	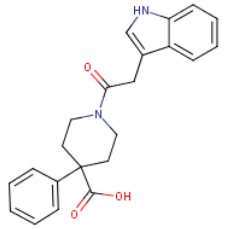
S7	039-293-496	3-hydroxy-N-[2-methyl-5-(1H-pyrazol-1-yl)phenyl]-8-azabicyclo[3.2.1]octane-8-carboxamide	326.4	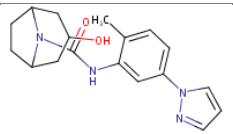
S8	042-690-490	4-{[4-(1H-imidazol-2-yl)piperidin-1-yl]sulfonyl}-N-phenyl-1H-pyrrole-2-carboxamide	399.5	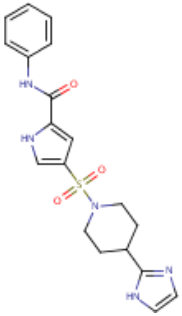
S9	044-506-267	4-[4-(propan-2-yl)pyrimidin-2-yl]-N-[2-(pyrrolidin-1-yl)pyridin-3-yl]piperazine-1-carboxamide	395.5	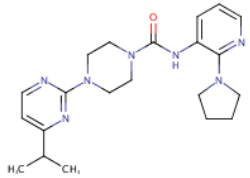
S10	044-507-853	2-[4-(2-oxopyrrolidin-1-yl)phenyl]-N-{4-[(1H-1,2,3,4-tetrazol-5-yl)methyl]phenyl}acetamide	376.4	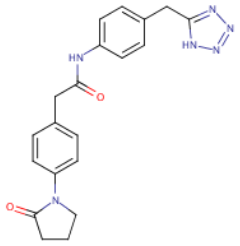

S11	039-168-335	5-[(2S,4R)-4-methoxy-1-[3-(1H-pyrazol-1-yl)benzoyl]pyrrolidin-2-yl]-1H-1,2,4-triazole	338.4	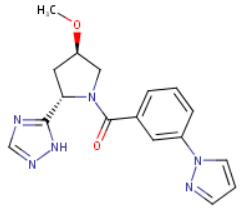
S12	039-168-703	4-[(2S,4R)-4-methoxy-2-(1H-1,2,4-triazol-5-yl)pyrrolidine-1-carbonyl]-1,6-naphthyridine	324.3	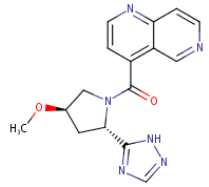
S13	039-150-125	[(3S,4R)-4-(1-methyl-1H-pyrazol-4-yl)-1-{1H-pyrrolo[2,3-b]pyridine-3-sulfonyl}pyrrolidin-3-yl]methanol	361.4	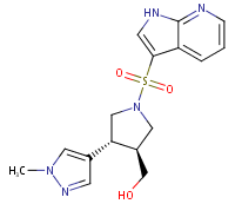
S14	039-168-697	4-fluoro-2-[(2S,4R)-4-methoxy-2-(1H-1,2,4-triazol-5-yl)pyrrolidine-1-carbonyl]-1H-indole	329.3	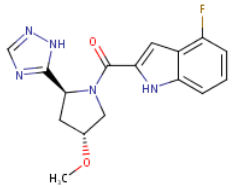
S15	038-994-785	4-(3-benzyl-1,2,4-oxadiazol-5-yl)-4-methoxy-1-(1H-pyrazole-3-carbonyl)piperidine	367.4	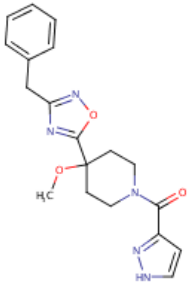

5.5 Docking of S1-S15 into nhTMEM16

Blind docking of energy minimised structures of compounds S1-S15 into the prepared nhTMEM16 structure 4WIS showed that the majority of poses localise to the site they were screened against, the most populous EGCG' cluster (Table 5.4 and Figure 5.8). All S compounds are predicted to bind most commonly to the same site as the polyphenols, with all cluster centres being within 2 Å of the most populous EGCG' cluster centre. The S compounds dock to this site commonly and with a range of predicted binding energies, but all above 8 kcal/mol.

Compound	No. of clusters	No. of poses in most populous cluster (45)	Mean predicted binding energy of poses in most populous cluster (kcal/mol)
S1	2	38	8.53
S2	3	40	8.16
S3	2	44	8.31
S4	3	40	8.78
S5	2	38	8.19
S6	4	36	9.00
S7	2	42	8.96
S8	2	41	8.85
S9	2	35	8.84
S10	4	30	8.98
S11	3	42	8.43
S12	2	41	8.18
S13	4	38	8.44
S14	4	35	8.49
S15	2	44	8.91

Table 5.4: Summary of blind docking of compounds S1–S15 into nhTMEM16 structure. Number of poses in most populous cluster and mean predicted binding energy of poses in most populous cluster are colour coded.

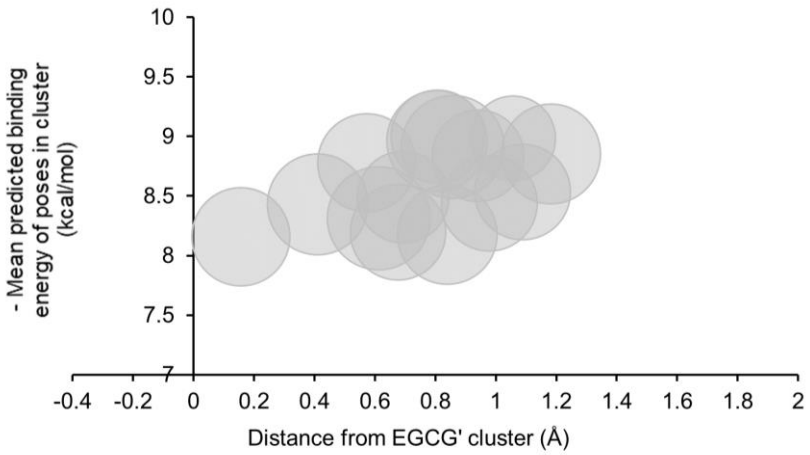

Figure 5.8: Analysis of clustering of compounds S1-S15 compared to most populous EGCG' cluster in nhTMEM16. Distance from most populous EGCG' cluster centre plotted against mean predicted binding energies of poses in cluster. Bubble size represents number of poses in each cluster.

5.6 Five compounds slow platelet scrambling rate following stimulation with A23187 in a plate-based AV binding assay

Compounds S1-S15 were screened using our luminescence-based plate reader AV binding assay that identifies compounds that slow the rate of platelet scramblase activity. Platelets were pre-incubated with 100 μM compounds for 10 minutes at 37°C before stimulation with 10 μM A23187, also at 37°C. 5 compounds: S1, S2, S3, S14 and S15 all slowed peak scrambling rate compared to 0.1% DMSO (Figure 5.9).

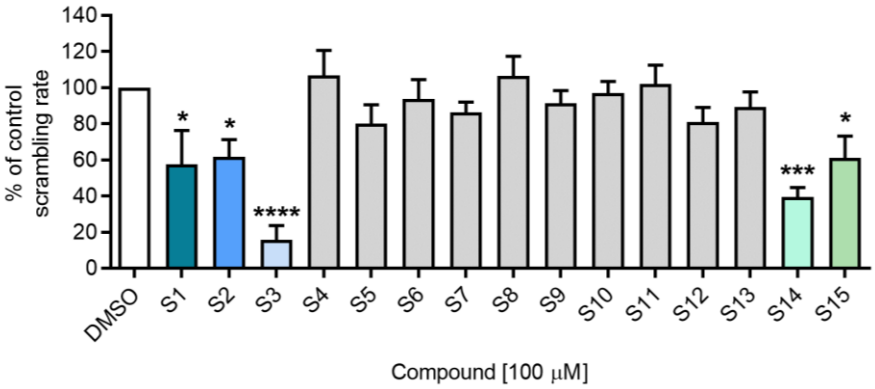

Figure 5.9: Compounds S1, S2, S3, S14, S15 slow platelet scrambling rate. % of control (0.1% DMSO) scrambling rate in luminescence-based AV binding assay when platelets were treated with 100 μM S1-S15 compared to 0.1% DMSO. Bar chart shows mean ± SEM. N = 5. Data analysed using a repeated measures one-way ANOVA and Dunnett's multiple comparisons test.

5.7 S1 inhibits platelet PS exposure following stimulation with thrombin + CRP-XL in a flow cytometry AV binding assay

Compounds S1, S2, S3, S14 and S15 were tested using a flow cytometry-based AV binding assay following a 10-minute stimulation with 1 U/ml thrombin + 1 µg/ml CRP-XL or a 2-minute 10 µM A23187 stimulation at room temperature. Platelets were pre-incubated with 100 µM compounds for 10 minutes (Figure 5.10 A and B) or 60 minutes (Figure 5.10 C and D) at 37°C with 2 mM Ca^{2+} added just prior to stimulation. Only S1 inhibited total platelet PS exposure following stimulation with thrombin + CRP-XL after a 10-minute incubation compared to 0.2% DMSO, though the same trend is seen following a 60-minute incubation of S1. S1 specifically inhibited the proportion of platelets with high level PS exposure following stimulation with thrombin + CRP-XL, the proportion of platelets with medium level PS exposure following stimulation was unaffected (Figure 5.10 E). Compound S2 actually increased the proportion of platelets with high level PS exposure following stimulation with thrombin and CRP-XL compared to controls. None of the compounds tested inhibited total platelet PS exposure following A23187 stimulation, or the proportion of stimulated platelets with high level versus medium level PS exposure, contrary to results seen in the plate-based assay. Note that the DMSO concentration was raised slightly from 0.1% to 0.2% from this point onwards to improve compound solubility and larger volumes of washed platelets were incubated with compounds to prevent precipitation. No compound significantly inhibited AV positive microparticle formation, though S1 did trend towards inhibiting microparticle formation following stimulation with thrombin + CRP-XL after both a 10 minute and 60 minute incubation.

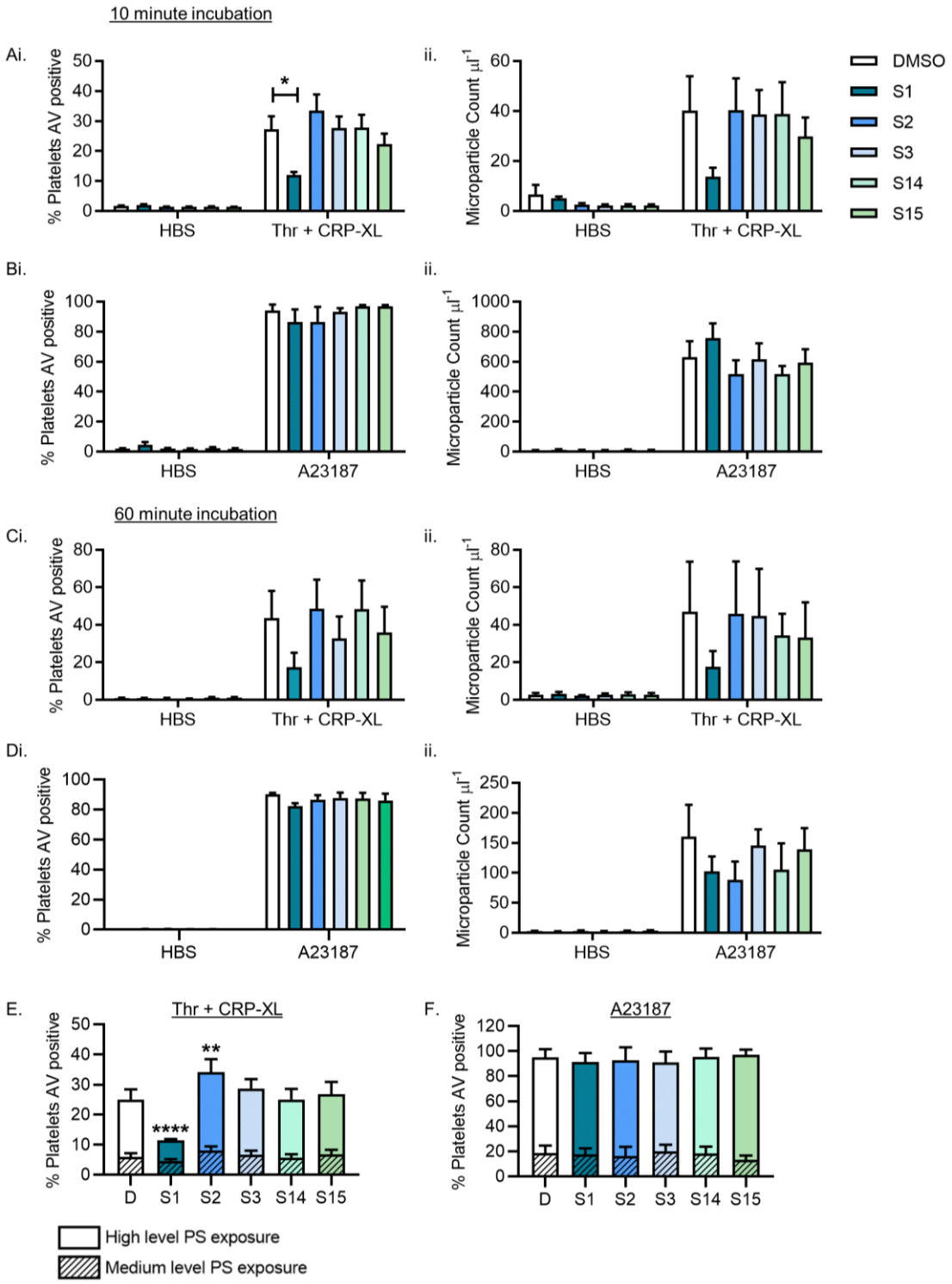

Figure 5.10: Compound S1 inhibits platelet PS exposure following stimulation with thrombin + CRP-XL in a flow cytometry AV binding assay. Platelets incubated with 100 µM compound for 10 minutes at 37°C stimulated with (A) 1 U/ml thrombin + 1 µg/ml CRP-XL for 10 minutes or (B) 2 minutes with 10 µM A23187 at room temperature. (C) Platelets incubated with 100 µM compound for 60 minutes at 37°C stimulated with 1U/ml thrombin + 1 µg/ml CRP-XL for 10 minutes at room temperature or (D) 2 minutes with 10 µM A23187. (i) % platelets AV positive; (ii) AV positive microparticle count. (E) % of platelets with high level or medium level PS exposure following stimulation with 1 U/ml thrombin + 1 µg/ml CRP-XL. (F) % of platelets with high level or medium level PS exposure following stimulation with 10 µM A23187. Bar charts show mean ± SEM. N = 5. Data analysed using two-way ANOVA, both factors matching, and Dunnett's multiple comparisons test.

5.8 S1 does not affect cytosolic Ca^{2+} signalling following stimulation with thrombin + CRP-XL or A23187

Cytosolic Ca^{2+} signals were measured using Cal520 following stimulation with 1 U/ml thrombin + 1 µg/ml CRP-XL or 10 µM A23187 at room temperature following a 60-minute incubation with 100 µM S compound at 37°C. 2 mM Ca^{2+} was added just prior to stimulation. S15 inhibited cytosolic Ca^{2+} signals following thrombin + CRP-XL stimulation when quantified by AUC but not when quantified as peak F/F_0 or F/F_0 at time of flow cytometry sampling (Figure 5.11 A). None of the other compounds tested affected Ca^{2+} signals when quantified by AUC, peak F/F_0 or F/F_0 at time of flow cytometry sampling.

It should be noted here that data are shown for n = 3. Had our lab not been shut down due to COVID-19 the number of replicates would have been increased to at least n = 5, particularly as the data presented here quantified by AUC appears quite variable.

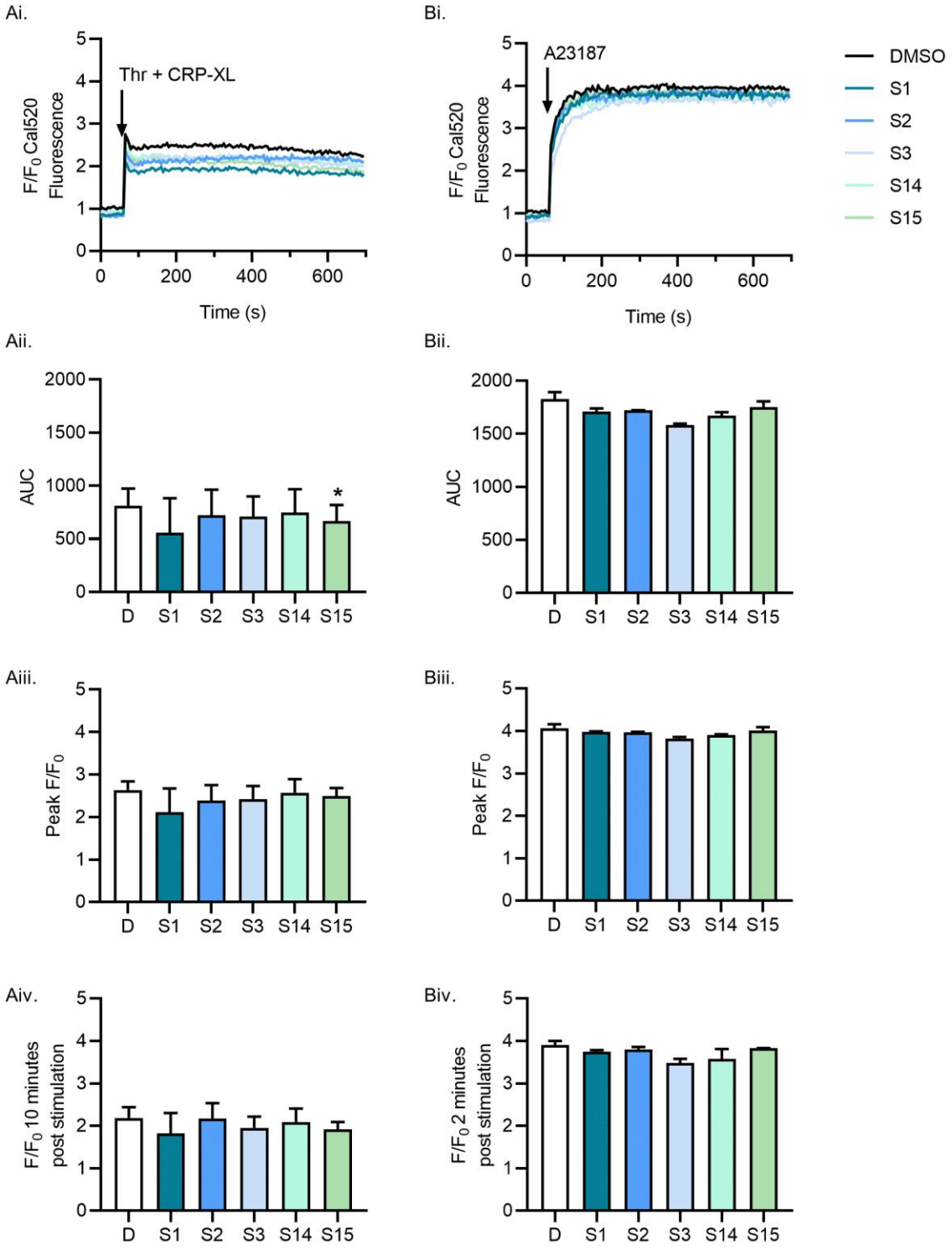

Figure 5.11: S1 does not affect platelet cytosolic Ca^{2+} signals following stimulation with thrombin + CRP-XL or A23187. Platelets were loaded with the Ca^{2+}-sensitive fluorescence dye, Cal520. Fluorescence values were normalised to the initial fluorescence values of vehicle controls containing 0.2% DMSO in matched samples to account for variation in dye loading (F/F_0). Platelets were treated with 100 µM S compound or 0.2% DMSO for 60 minutes at 37°C before stimulations. Where indicated, platelets were stimulated with (A) 1 U/ml thrombin + 1 µg/ml CRP-XL; (B) 10 µM A23187. Data are presented as (i) F/F_0 Cal520 fluorescence following stimulation; (ii) AUC above baseline ($F/F_0 = 1$); (iii) peak F/F_0 following stimulation; and (iv) F/F_0 at 10 minutes post stimulation. Bar charts show mean ± SEM. N = 3. Data analysed using a repeated measures one-way ANOVA and Dunnett's multiple comparisons tests.

5.9 S1 does not affect platelet $\alpha_{IIb}\beta_3$ integrin activation or α-granule release following stimulation with PAR1-AP

A 10 minute incubation of 100 µM S1 at 37°C did not affect platelet $\alpha_{IIb}\beta_3$ integrin activation or α-granule release following a 10-minute stimulation with 10 µM PAR1-AP at ambient temperature (Figure 5.12). This was in contrast to 100 µM EGCG' which inhibited both $\alpha_{IIb}\beta_3$ integrin activation and α-granule release as previously shown.

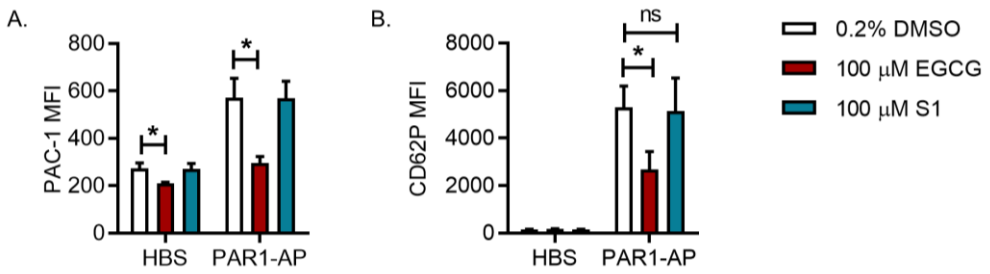

Figure 5.12: S1 does not affect platelet $\alpha_{IIb}\beta_3$ integrin activation or α-granule release following stimulation with PAR1-AP. Platelets were treated with 100 µM S1/EGCG' or 0.2% DMSO for 10 minutes at ambient temperature prior to stimulation for 10 minutes. $\alpha_{IIb}\beta_3$ integrin activation was measured by flow cytometry as PAC-1 binding (FITC conjugated). α-granule secretion was measured by anti-CD62P (P-selectin) antibody binding (phycoerythrin (PE) conjugated). (A) PAC-1-FITC MFI following stimulation with 10 µM PAR1-AP. (B) CD62P-PE MFI following stimulation with 10 µM PAR1-AP. Bar charts show mean ± SEM. N = 5. Data analysed using two-way ANOVA, both factors matching, and Dunnett's multiple comparison tests.

5.10 Active S compounds and catechin gallates dock to the same site in nhTMEM16

The 5 active S compounds that showed inhibition of platelet PS exposure under some conditions are highlighted in Figure 5.13. There is no obvious distinction from the blind docking alone which predicts which compounds are active and which are not. All compounds dock to an equivalent site with similar binding energies.

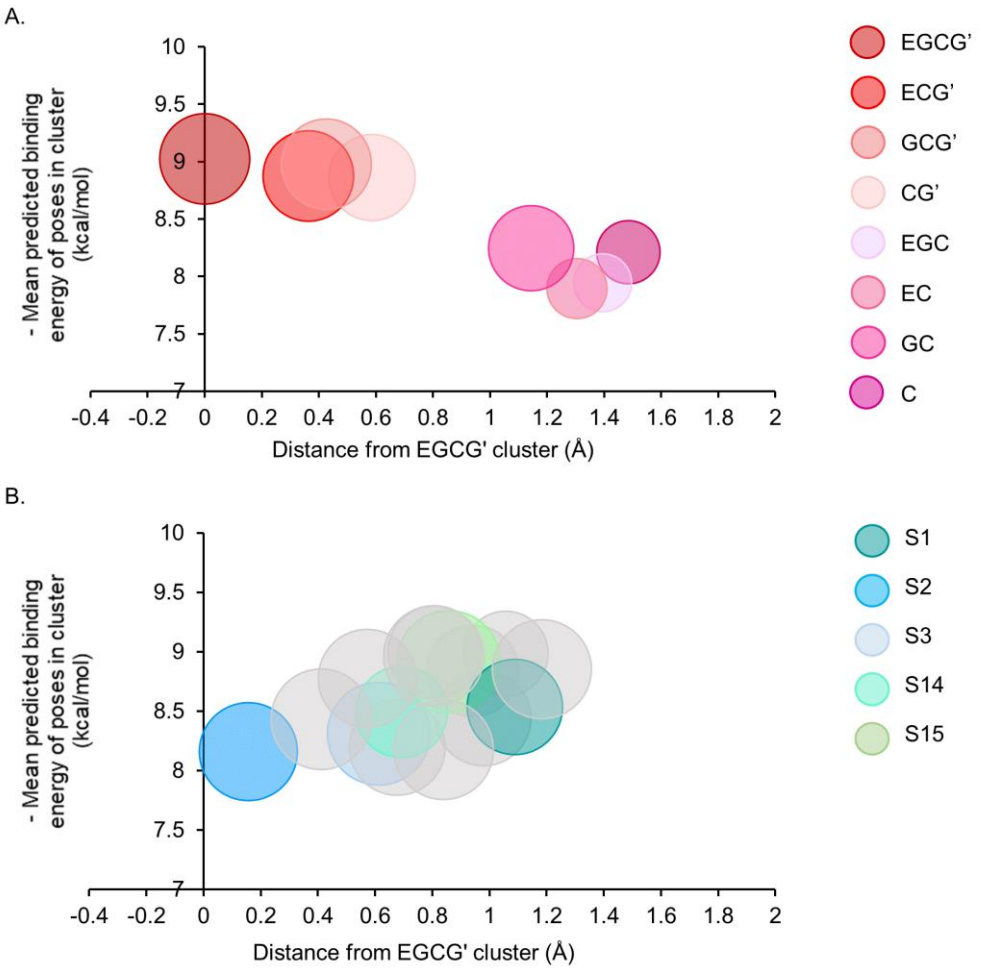

Figure 5.13: Analysis of clustering of S compounds compared to the most populous EGCG' cluster in nhTMEM16. Distance from EGCG' cluster centres plotted against mean predicted binding energies of poses in cluster. Bubble size represents number of poses in each cluster. (A) Analysis of catechin and catechin gallate compound docking for reference. (B) Analysis of S compound docking. Compounds which show some inhibition of platelet scramblase activity are coloured in B.

5.11 Catechin and catechin gallate compound docking in mTMEM16F

The murine TMEM16F structure was published in 2019 (Alvadia et al., 2019), after much of the work reported above had been performed. The mTMEM16F structure shows a similar general architecture to nhTMEM16 but with a much higher sequence homology to hTMEM16F. It may therefore be a more appropriate template for *in silico* predictions of ligand binding to hTMEM16F.

The Ca^{2+} bound structure of mTMEM16F (PDB: 6QP6, 3.2 Å, cryo-EM) was prepared for blind docking and energy-minimised ligand structures were docked using Autodock Vina, as for the nhTMEM16 structure. Surprisingly, compared to nhTMEM16 dockings, there was less

consistency of localisation of catechin gallate compound poses in mTMEM16F and a higher degree of consistency in localisation of the catechin compounds (Table 5.5). For all compounds, except EC, more clusters were identified from dockings in the mTMEM16F structure than the nhTMEM16 structure. In general, the predicted binding energies of poses in the most populous clusters were higher for mTMEM16F than for nhTMEM16.

Compound	No. of clusters	No. of poses in most populous cluster (45)	Mean predicted binding energy of poses in most populous cluster (kcal/mol)
EGCG'	4	27	8.68
ECG'	5	16	9.00
GCG'	4	20	10.04
GCG'	4	20	9.50
CG'	7	11	9.16
EGC	6	19	7.97
EC	4	28	8.10
GC	4	36	8.65
C	5	36	8.16

Table 5.5: Docking analysis of catechin and catechin gallate compounds in mTMEM16F structure 6QP6. Number of poses in most populous cluster and mean predicted binding energy of poses in most populous cluster are colour coded.

Initially, EGCG' was used as the reference compound, as when analysing nhTMEM16 dockings, since EGCG' has been shown to inhibit the activity of purified TMEM16F protein. Figure 5.14 and Table 5.6 summarise the 4 clusters identified by our program for EGCG' in the mTMEM16F structure. Cluster 2 is the most populous but cluster 1 has the highest mean predicted binding energy and all of the highest energy poses from each docking run are in cluster 1.

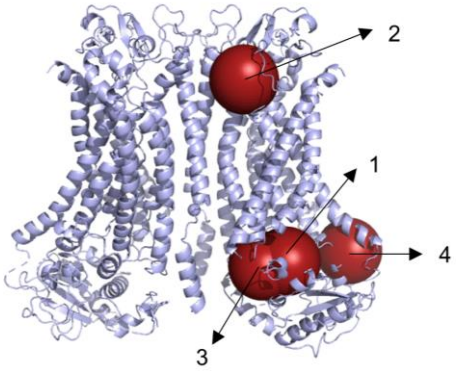

Figure 5.14: EGCG' clusters in mTMEM16F. 10 Å spheres around the 4 cluster centres identified for EGCG' in mTMEM16F structure (6QP6) by our program.

EGCG' Cluster	No. of poses in cluster	No. of highest energy poses	Mean predicted binding energy of poses in cluster (kcal/mol)
1	12	5	8.80
2	27	0	8.68
3	3	0	8.63
4	3	0	8.70

Table 5.6: Summary of EGCG' clusters in mTMEM16F. Number of poses in each cluster and mean predicted binding energy of poses in each cluster are colour coded**.**

When the most populous clusters for each catechin and catechin gallate compound are compared to EGCG' cluster 1, the most populous CG' cluster is in an equivalent location, although most clusters are closer to EGCG' cluster 2. The most populous cluster for ECG' and one of the GCG' clusters localise to a 3rd site (Figure 5.15).

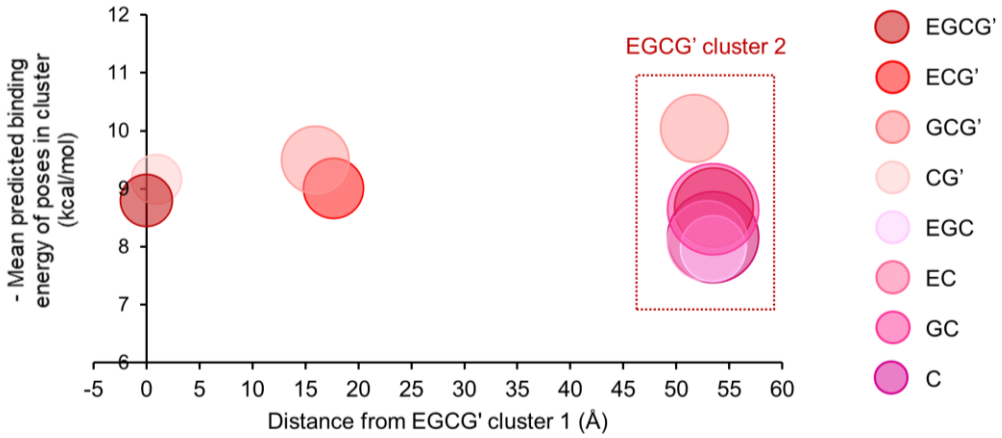

Figure 5.15: Analysis of catechin and catechin gallate clusters in mTMEM16F compared to EGCG' cluster 1. Distance from EGCG' cluster 1 centre plotted against mean predicted binding energies of poses in cluster. Bubble size represents number of poses in each cluster.

Since the catechin gallate compounds do not all cluster most commonly to a single site as in nhTMEM16, the program was re-run with all catechin gallate compounds as "references", being known active compounds, and this gave 9 reference clusters in the mTMEM16F structure (Figure 5.16).

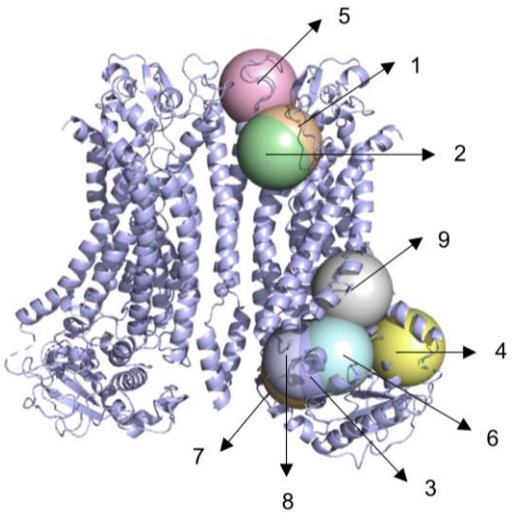

Figure 5.16: Reference clusters in mTMEM16F structure where all catechin gallate poses are considered. Clusters identified by our program in mTMEM16F structure represented by 10 Å spheres.

Each individual catechin and catechin gallate compound cluster was compared to these reference clusters and if they were within 2 standard deviations of the reference cluster centre, the poses in the catechin/catechin gallate cluster were assigned to that reference cluster (Table 5.7).

Reference cluster	Mean predicted binding energy of poses in reference cluster (kcal/mol)	EGCG'	ECG'	GCG'	CG'	EGC	EC	GC	C	Actives	Inactive
1	9.10	27		20		33	28	36	39	47	136
2	9.69		14		10					24	0
3	9.13		10		5					15	0
4	8.7	3								3	0
5	9.38			3	3					6	0
6	8.93	12		2	11		1			25	1
7	8.96										
8	9.01		3		9					12	0
9	9.25	3	16	20	7	3		4	3	46	10
None						9	16	5	3	0	33

Table 5.7: Catechin and catechin gallate compound poses assigned to reference clusters. Table shows the number of poses for each catechin/catechin gallate compound in clusters with centres within 2 standard deviations of reference cluster centres. Mean predicted binding energy of poses in reference cluster is colour coded. The total number of active compound poses assigned to each reference cluster (EGCG', ECG', GCG', CG'), the number of inactive compound poses assigned to each reference cluster (EGC, EC, GC, C). If catechin/catechin gallate compound cluster centres are not within 2 standard deviations of any reference clusters they remained unassigned.

Several reference clusters were in close proximity to each other so the distances between cluster centres were calculated (Table 5.8). If cluster centres were less than 10 Å apart, there was deemed to be sufficient overlap in these clusters to define them as a single site. Clusters 1 and 2 were found to be equivalent, as were 3 and 8. Cluster 6 also had significant overlap with both cluster 3 and 8 and so these were all considered equivalent. When these clusters are merged, the catechin gallates mostly dock to 3 sites (Table 5.9). The average co-ordinates of cluster 1 and 2 became cluster A, the average co-ordinates of 3,6 and 8 became cluster B and cluster 9 became cluster C (Figure 5.17).

Reference cluster	1	2	3	4	5	6	7	8	9
1	0.00								
2	2.07	0.00							
3	53.42	52.32	0.00						
4	60.46	60.25	26.92	0.00					
5	16.31	17.36	68.76	75.08	0.00				
6	52.98	52.03	5.73	22.73	68.67	0.00			
7	60.39	59.57	19.78	28.79	73.65	22.64	0.00		
8	53.23	52.08	2.03	28.56	68.42	7.72	19.20	0.00	
9	39.89	39.36	19.91	22.55	55.54	16.50	30.53	21.01	0.00

Table 5.8: Distances between reference clusters in mTMEM16F. Where the distance between clusters was less than 10 Å, coloured in green, the clusters were defined as equivalent.

Reference cluster	EGCG'	ECG'	GCG'	CG'	EGC	EC	GC	C	Actives	Inactive	Mean predicted binding energy of poses in reference cluster (kcal/mol)
1 & 2 - **A**	27	14	20	10	33	28	36	39	71	136	9.10/9.69
3 & 6 & 8 - **B**	12	13	2	23	0	0	0	0	50	0	9.13/8.93/9.01
4	3								3	0	8.7
5			3	3					6	0	9.38
7		2							2	0	8.96
9 - **C**	3	16	20	7	3		4	3	46	10	9.25
None					9	16	5	3	0	33	

Table 5.9: Catechin and catechin gallate compound poses assigned to amalgamated reference clusters. The number of poses for each catechin/catechin gallate compound in clusters with centres within 2 standard deviations of reference cluster centres. The total number of active compound poses assigned to each reference cluster (EGCG', ECG', GCG', CG'), the number of inactive compound poses assigned to each reference cluster (EGC, EC, GC, C), mean binding energy of each reference cluster. If catechin compound cluster centres are not within 2 standard deviations of any reference clusters they remain unassigned.

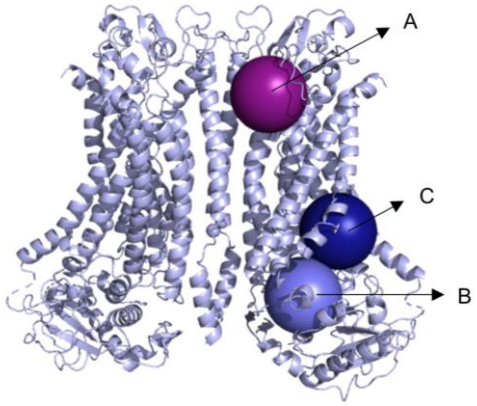

Figure 5.17: Reference clusters A, B and C in mTMEM16F. The mean co-ordinates of the centres of reference clusters 1 and 2 became the centre of cluster A (purple), the mean co-ordinates of the centres of clusters 3,6 and 8 became the centre of cluster B (light blue) and cluster 9 became cluster C (dark blue). Clusters are represented as spheres with 10 Å radius.

5.12 S compound docking in mTMEM16F

Blind dockings of the S compounds were repeated using the mTMEM16F 6QP6 structure and their localisations compared to clusters A, B and C. A new cluster was identified. Cluster D, where many of these S compounds clustered, falls between clusters B and C. Figure 5.18 shows the clustering analysis of S compounds compared to cluster C and highlights how a group of compounds cluster to site D, shaded in violet. Similar to the polyphenols, these clusters were not as highly populated compared to the clustering seen in the nhTMEM16 structure but predicted binding energies were high (Table 5.10). Figure 5.18C highlights in colour the compounds which show some inhibition of platelet scramblase activity. There is no obvious pattern from this docking analysis alone which predicts which compounds show activity. S1, S2 and S15 cluster most closely to cluster D whilst S3 and S14 cluster close to cluster C. There is some overlap between clusters B and D.

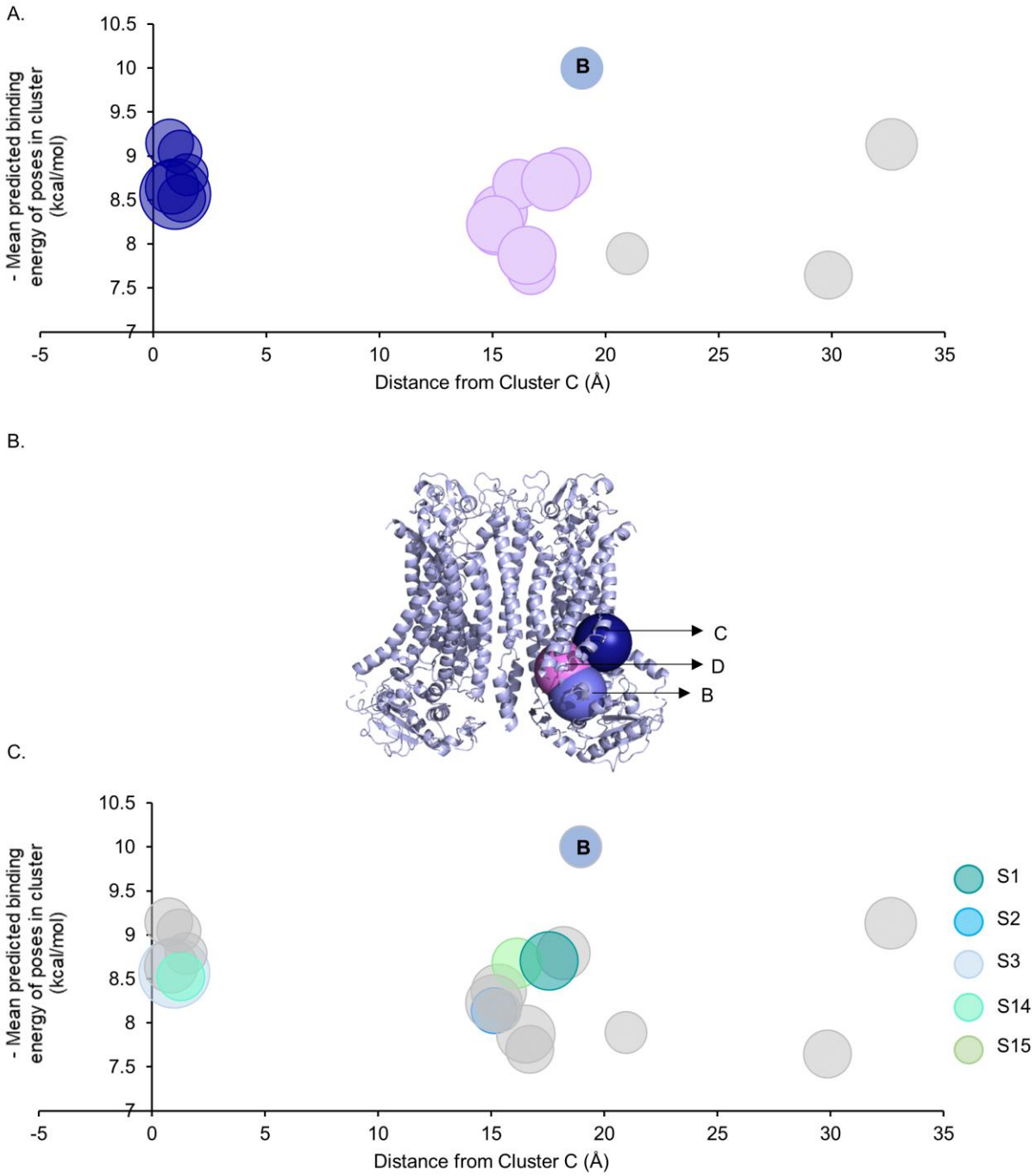

Figure 5.18: S compound clusters in mTMEM16F compared to cluster C. (A & C) Distance from cluster C centre plotted against mean predicted binding energies of poses in cluster. Bubble size represents number of poses in each cluster. (A) S compounds closest to cluster C centre shaded dark blue, compounds closest to cluster D centre shaded in violet. Distance of cluster B from cluster C shown for reference in light blue. (C) compounds showing some inhibition of platelet scramblase activity are shaded. (B) Clusters B (light blue), C (dark blue) and D (violet) in mTMEM16F structure represented as 10 Å spheres.

Compound	No. of clusters	No. of poses in most populous cluster (45)	Mean predicted binding energy of poses in most populous cluster (kcal/mol)	Cluster A distance (Å)	Cluster B distance (Å)	Cluster C distance (Å)	Cluster D distance (Å)
S1	5	19	8.71	47.52	6.22	17.56	2.84
S2	11	12	8.14	43.49	9.87	15.13	1.48
S3	7	28	8.57	39.63	19.43	0.98	16.59
S4	5	16	8.64	39.63	19.11	0.84	16.21
S4		16	8.79	48.06	6.09	18.19	3.36
S5	8	13	8.64	59.57	18.83	29.86	19.81
S5		13	8.79	44.08	9.61	16.70	1.25
S6	7	13	9.15	39.56	19.47	0.74	16.67
S7	7	17	8.36	43.98	9.35	15.33	0.99
S8	8	11	9.05	39.13	19.99	1.19	17.03
S9	10	10	8.79	38.52	20.36	1.50	17.21
S10	5	15	9.13	23.54	37.30	32.66	28.69
S11	8	18	8.23	43.52	9.70	15.11	1.34
S12	5	19	7.87	43.69	10.07	16.53	1.38
S13	11	10	7.89	59.19	24.57	20.96	28.12
S13		10	8.14	43.47	9.90	15.38	1.32
S14	9	13	8.52	39.76	19.65	1.27	16.90
S15	6	14	8.68	44.71	8.71	16.12	0.20

Table 5.10: Docking analysis of S compounds in mTMEM16F structure 6QP6. Table showing the number of clusters identified for each compound, the number of poses in the most populous cluster and the mean predicted binding energy of poses in the most populous cluster. Table also shows the distances from the most populous S compound cluster to cluster centres A, B, C and the newly identified cluster D. Blue shading indicates where the S compound cluster is within 10 Å of the reference cluster. Number of poses in most populous cluster and mean predicted binding energies are colour coded.

When the individual clusters of the active S compounds are compared, the majority of poses are found around the cytosolic side of the hydrophilic groove, however, there is no clear consistency of a single site in this area (Figure 5.19).

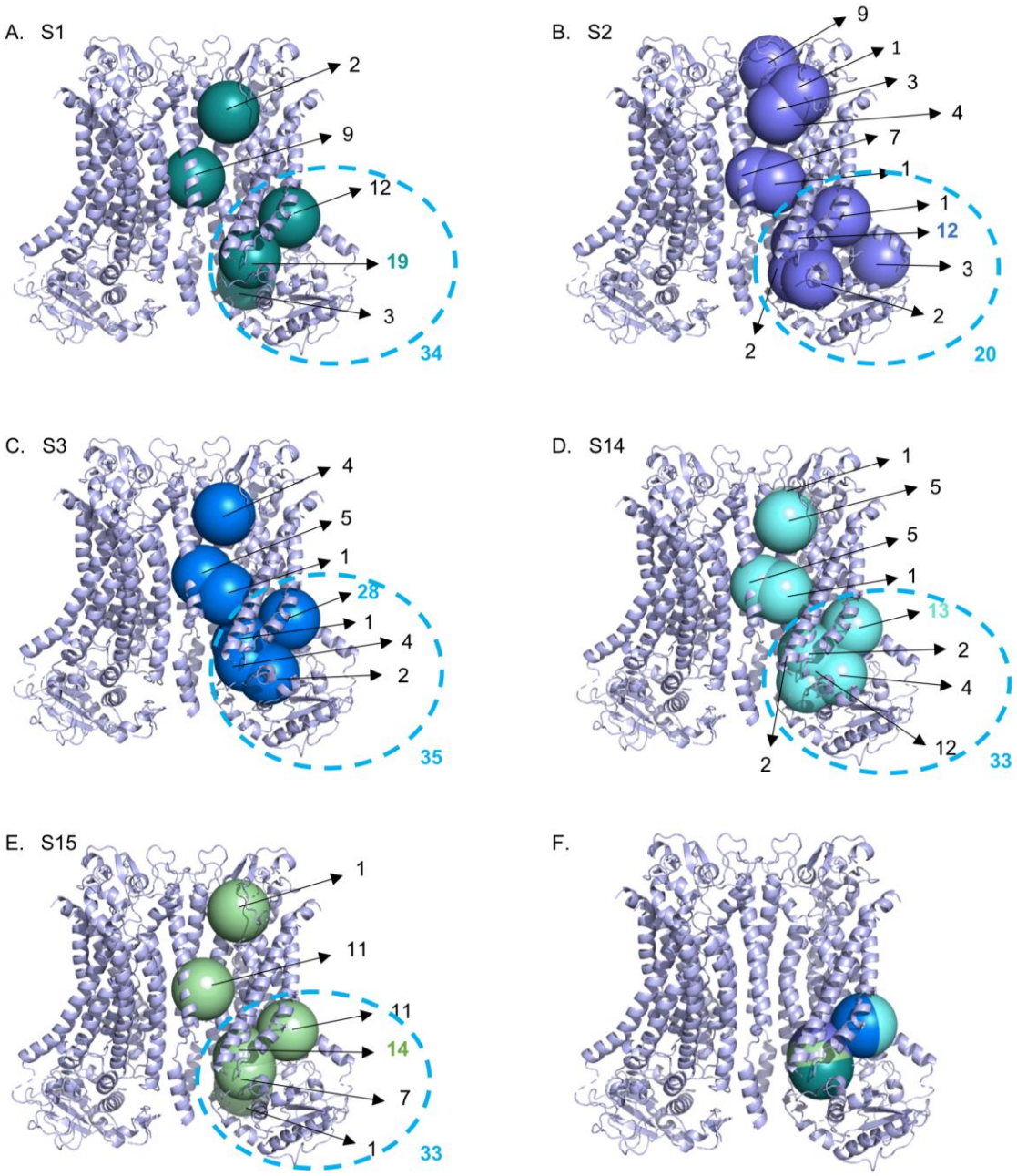

Figure 5.19: All clusters identified for S1, S2, S3, S14, S15 in mTMEM16F. All clusters identified by our program for active S compounds with the number of poses in each cluster labelled. The cytosolic side of the hydrophilic groove is indicated by the blue dotted oval and the number of poses within this oval is given. (A) S1; (B) S2; (C) S3; (D) S14; (E) S15; (F) The most populous clusters for each compound. Clusters are represented by spheres with 10 Å radius.

5.13 Discussion

In Chapter 4 it was shown that each catechin gallate compound tested inhibited platelet PS exposure whilst related catechin compounds lacking the gallate group did not. All catechin gallate compounds, however, additionally inhibited pro-aggregatory platelet functions including $\alpha_{IIb}\beta_3$ integrin activation and α-granule release and are thus unsuitable compounds to test the effects of solely targeting pro-coagulant platelet activity.

In order to try to identify a more selective inhibitor of platelet scramblase activity a structure-based *in silico* approach was pursued. Initially, the only phospholipid scramblase structure available was that of the fungal homologue, nhTMEM16 (Brunner et al., 2014), so this structure informed the screen presented in this chapter.

All catechin and catechin gallate compounds were blindly docked into the nhTMEM16 structure 4WIS and it was found that all compounds, whether active or not, docked most frequently to an equivalent site at the cytosolic side of the hydrophilic groove, believed to be the pathway for phospholipid movement between membrane bilayers. Though the most frequented site was equivalent for all compounds, more variation was seen in dockings of the catechin compounds compared to the catechin gallates with fewer poses localising to this site and more clustering sites identified overall (Table 5.2 and Figure 5.6).

This most frequented clustering site was used as the basis for a structure-based screen of the Enamine chemical library. The highest energy EGCG' pose was re-docked in GOLD and used as a reference for a query using FRED. The top 500 results from FRED were re-docked using GOLD and the highest scoring 15 compounds selected for testing as screening set S. When these compounds were blindly docked into the nhTMEM16 structure, they all most frequently clustered to the correct targeted site with reasonably high predicted binding energies (Table 5.4 and Figure 5.8).

These S compounds were initially tested using our luminescence plate-based AV binding assay. As discussed in Chapter 3 this assay is useful when screening new compounds as it can detect relatively weak inhibitions of scrambling rate that may otherwise be missed by flow cytometry. 5 S compounds were found to slow scrambling rate in this assay: S1, S2, S3, S14 and S15 (Figure 5.9).

When these compounds were tested using a flow cytometry AV binding assay, which is the gold standard in the field, only S1 inhibited platelet PS exposure following stimulation with thrombin + CRP-XL, and none of the compounds tested inhibited PS exposure following A23187. In order to see whether this was a time of incubation-dependent effect, compounds

were pre-incubated for 60 minutes before stimulation but still all except S1 had no effect (Figure 5.10).

Again, this exemplifies differences which remain to be fully understood between our plate-based and flow cytometry AV binding assays. As the inhibition caused by S2, S3, S14 and S15 could not be seen by flow cytometry, their effects were not deemed strong enough to follow up further at this stage, particularly as these screens involved very high concentrations of 100 μM of compound. As in chapter 3, the identification of these weakly inhibiting compounds by the luminescence-based assay could provide interesting insights into the mechanism of platelet scrambling activity by TMEM16F. Future studies where the interactions of these compounds with TMEM16F are predicted and verified may further insights into the mechanism of platelet PS exposure which may not have been gained using flow cytometry screens alone. Further study of compounds S2, S3, S14 and S15 at this point was considered beyond the scope of this thesis, though analysis of the ligand properties of these compounds which slow scrambling rate using Forge could be a future direction for studies.

Since S1 inhibited platelet PS exposure and AV positive microparticle formation following stimulation with thrombin + CRP-XL but not A23187 when measured by flow cytometry (Figure 5.10), we cannot be sure whether S1 has a direct effect on scramblase activity. It may be that S1 has a relatively weak direct inhibitory effect on the scramblase protein since S1 did slow scrambling rate following stimulation with A23187 in our luminescence plate-based AV binding assay. The differing sensitivities to inhibition of the single AV unit flow cytometry assay versus the 2 AV unit plate-based assay may suggest that S1 has a direct but weak effect on scrambling activity that is not strong enough to inhibit the all-or-nothing flow cytometry signal. To further understand the differences between the plate-based and flow cytometry AV assays, the plate-based assay could be repeated with thrombin + CRP-XL stimulation. Real-time flow cytometry AV binding assays could also be performed to look at the rate of scrambling rather than an end point measurement. Furthermore, any differences in incubation and stimulation temperatures between assays should be removed. Incubations for both assays were done at 37°C but stimulations for flow cytometry were performed at ambient temperature, since this generally gives higher AV binding (Ramstrom et al., 2010), whereas the stimulations for the luminescence based assay were performed at 37°C. A FRET-based flow cytometry assay could be established for flow cytometry which would more closely mimic the AV binding kinetics involved in the plate-based assay and may offer some insight into the different results. Similarly, the effect of compounds on fluorescently labelled lactadherin could be investigated since this also binds PS but does not form lattice structures as AV does (Shi et al., 2006).

S1 had no effect on cytosolic Ca^{2+} signalling following stimulation with thrombin + CRP-XL or A23187, measured by Cal520 fluorescence, suggesting S1 does not inhibit platelet PS exposure through effects on Ca^{2+} signalling. It should be noted that the repeats of these Ca^{2+} assays were lower than would be ideal due to the COVID-19 shut down of the lab. If S1 does indeed not affect cytosolic Ca^{2+} signals following stimulation with thrombin + CRP-XL this also supports a direct action of the compound on TMEM16F but does not explain the difference between agonists. S1 specifically inhibited high level PS exposure and did not increase the proportion of stimulated platelets with medium level PS exposure (Figure 5.10), an improvement over EGCG'.

Further work is required to determine whether S1 acts directly on TMEM16F. Though the Cal520 measurements of Ca^{2+} signals acquired to date indicate that compound S1 does not inhibit platelet PS exposure by affecting cytosolic Ca^{2+} signals, these experiments should be repeated with more donors, especially since the AUC data are quite variable. Additionally, the effects of S1 on Fluo-5N Ca^{2+} signals could be tested by flow cytometry. Fluo-5N is a lower affinity Ca^{2+} dye which can detect the supra-maximal Ca^{2+} signal characteristic of pro-coagulant platelets (Abbasian et al., 2020). If S1 directly inhibits the scramblase protein, then this supra-maximal Ca^{2+} signal should remain unaffected. The effects of S1 could also be tested on mitochondrial [Ca^{2+}], using the mitochondrial Ca^{2+}-sensitive dye Rhod-2, and mitochondrial membrane potential, using the dye TMRM. Again, if S1 acts directly on the scramblase protein, both mitochondrial [Ca^{2+}] and membrane potential should be unaffected with the usual "pro-coagulant" portion of the platelet population undergoing mitochondrial permeability transition pore opening, yet not exposing PS. This will help identify whether there are any off-target effects of S1 on the mechanism that leads to PS exposure, which might help understand the differences in results observed between the plate-based and flow cytometry AV binding assays.

If S1 is found to not affect Fluo-5N Ca^{2+} signals or platelet mitochondria then S1 could also be tested for effects on RBC PS exposure when both unstimulated and stimulated to give further indication as to whether S1 is acting directly on the TMEM16F protein and ensure S1 does not cause PS exposure in unstimulated RBCs, as was seen with EGCG'. This project has focused on testing compounds in our main cell of interest, platelets, but if S1 is believed to act specifically on TMEM16F it would be appropriate to test the effects of S1 on TMEM16F in an overexpression system. Eventually it may also be appropriate to perform mutagenesis studies on TMEM16F at predicted sites of action or co-crystalise S1 bound to TMEM16F.

S1 did not affect platelet α-granule release or $\alpha_{IIb}\beta_3$ integrin activation at 100 μM indicating that it is a more selective inhibitor of platelet scramblase activity compared to the catechin gallate compounds, though much less potent.

The identification of S1 as a novel inhibitor of platelet scramblase activity does represent a success rate of 1/15 from this targeted structure-based *in silico* approach which is higher than could be expected from high throughput screening. However, a higher success rate might be expected from such a targeted approach. This might be in part due to the low sequence homology of nhTMEM16 to hTMEM16F. Whilst completing this work the mTMEM16F structure was published (Alvadia et al., 2019). mTMEM16F shares ~90% sequence homology to hTMEM16F and so is a more appropriate structure to use for *in silico* modelling.

When the blind dockings of polyphenolic compounds were repeated using the newly published mTMEM16F structure, there was much less consistency of localisations compared to when the nhTMEM16 structure was used. Less consistent dockings were also found for the S compounds in mTMEM16F. Figure 5.20 illustrates the overlaid nhTMEM16 structure in green with the mTMEM16F structure in grey focussing on the cytosolic side of the hydrophilic groove. There are differences in this region of the protein structure, particularly with transmembrane helices 4 and 6 being further apart in nhTMEM16 than in mTMEM16F and the entrance point to the groove being wider, where many of the compounds cluster in nhTMEM16.

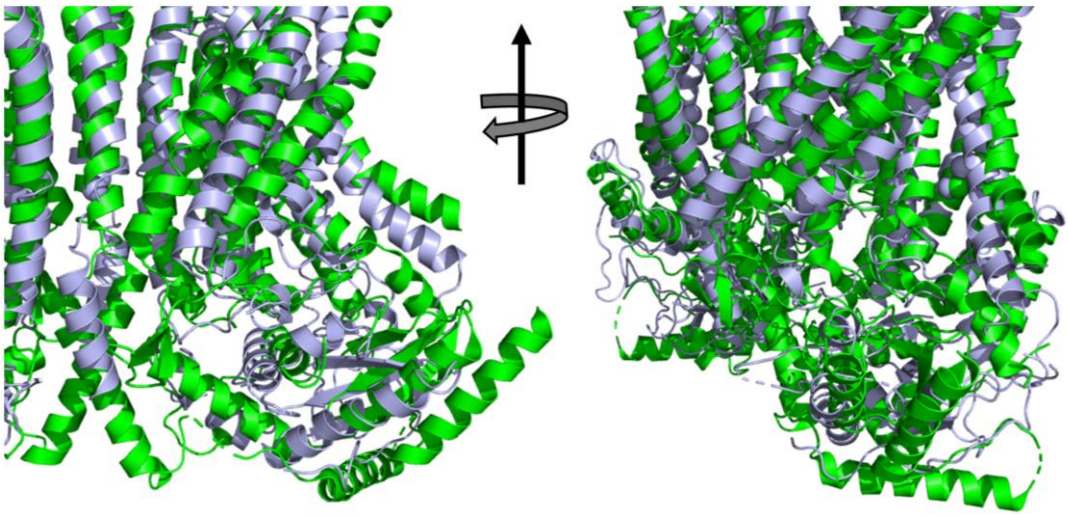

Figure 5.20 Overlay of nhTMEM16 and mTMEM16F structures. nhTMEM16 structure (4WIS) in green and mTMEM16F (6PQ6) in grey overlaid illustrating differences in structures at the cytosolic end of the hydrophilic groove.

These differences in structure may underlie the limited success of our initial screen. Dockings of polyphenolic compounds into the mTMEM16F structure show less consistency than in the nhTMEM16 structure. These *in silico* docking studies only predict areas of protein structures with which compounds may interact, they cannot predict where they interact that is responsible for their biological activity. Although Autodock Vina will also rank dockings based on their predicted binding energies, it is not necessarily the case that the area where a compound docks with the highest predicted binding energy is responsible for its biological activity.

Given the inconsistency of dockings of the active catechin gallate compounds into mTMEM16F, 3 potential sites of action were identified where they may act based on clustering of all of these active compounds, A, B and C. All 3 of these sites could lead future structure-based screens. Site A is notable as it is a site around which PIP_2 has been shown to interact with mTMEM16F and affect its function (Feng et al., 2019). It is plausible that the compounds could alter membrane properties and interactions between phospholipids and the protein at this site. Further investigation of this site would be aided by higher resolution TMEM16F structures in the presence of phospholipids. Sites B and C are at the cytosolic end of the hydrophilic groove, noted to be of interest previously. Either could inform a screen, but the active compound S1 localises closer to site B compared with site C. This rationale led to a screen based around site B presented in the next chapter; with further time and resources, screens based on the other sites could also prove informative. Whether these screens revealed any new active compounds, or not, they may help deduce where the catechin gallate compounds are exerting their biological effect.

As already discussed, the low sequence homology of nhTMEM16 to hTMEM16F likely limited the success of this initial screen, though this was the only phospholipid scramblase structure available throughout most of my PhD. The mTMEM16F structure has a much higher sequence homology compared to hTMEM16F, but differences in sequence remain which may also affect the secondary and tertiary structure of hTMEM16F and subsequent docking predictions. Future work could involve the generation of homology models of hTMEM16F and repeating the blind *in silico* docking studies using these homology structures which may give more reliable predictions of interactions between active compounds and the protein. Additionally, multiple structures of mTMEM16F now exist, including Ca^{2+}-free and PIP_2 supplemented structures in addition to the Ca^{2+} bound structure used here. It is not known whether compounds act to directly inhibit the Ca^{2+} bound form of the protein or prevent proper activation of the Ca^{2+} induced conformational changes. These different structures could be studied *in silico* and hTMEM16F homology models made of each of these states.

A limitation of Auto dock Vina, used for blind docking studies in this thesis, is that it will only output the top 9 poses for each compound with the highest predicted binding energy. It is plausible that compounds exert their biological effect at a site with a lower binding energy that is not output at all by this software. For this reason, future work should also perform similar blind docking studies using a range of software and comparing results may provide more evidence for some sites over others. A further limitation of the docking studies presented here is that TMEM16F is a membrane protein and will be flexible within the phospholipid bilayer. These docking studies, however, were performed *in vacuo* and did not consider protein-membrane interactions, which are known to be critical to the action of TMEM16 phospholipid scramblases (Bethel and Grabe, 2016; Feng et al., 2019). It is plausible that compounds may inhibit scramblase activity by disrupting protein-membrane interactions which could be missed using this current set up. Future molecular dynamic simulations of the protein in phospholipid membranes and dockings involving these simulations could help to better predict the movement of TMEM16F and how compounds may interact with the protein in its native environment.

There are limitations to our automated clustering program, though it does serve its aim of rapidly allowing analysis of many docking poses to see if they fall within the same area. The program does not currently consider the protein structure itself and an improvement of the program may include the protein structure pdb file and automatically split clusters if a protein chain is found to run between them. Secondly, rotations of poses into the same monomer space also do not take account of interactions with protein chains. It is possible that when rotating clusters localised to sites where chains of different monomers interact, these interactions may not be appropriately transformed. This could also potentially be written into an improved version of the program, perhaps where the distance between atoms and each protein chain is measured and these parameters are taken into account during transformation so that the poses remain associated with the correct protein chains. Such detail has not been required for this work, especially since the main sites of interest are not at sites of monomer chain interactions, but such development of the program could prove useful in the future.

A final factor to note is that the solubility of S1 was poor. This was mitigated by raising the [DMSO] to 0.2% and adding drug to a large volume of platelets, but it is possible that some of the variation seen in results for S1 could be due to relatively poor solubility. Certainly, any future development of S1 should look to improve solubility and this is an important consideration for any future medicinal chemistry development of a TMEM16F inhibitor.

The work presented in this chapter has identified S1 as a novel inhibitor of platelet scramblase activity. With the publication of the mTMEM16F structure, this provides new information upon

which to base a structure-based screen as presented here around the nhTMEM16 structure. The 3 sites identified around clusters A, B and C could all inform future screens to increase our understanding of how catechin gallates inhibit platelet scramblase activity and identify novel inhibitors.

Chapter 6 – A structure-based screen using an mTMEM16F structure

Chapter 5 presented a structure-based *in silico* screen focused around blind dockings of polyphenolic compounds into the nhTMEM16 phospholipid scramblase structure. Of 15 compounds tested, 5 showed some inhibition of platelet PS exposure in a plate-based luminescence AV binding assay, but only one compound, S1, inhibited platelet PS exposure in flow cytometry assays. S1 did not affect cytosolic Ca^{2+} signalling, $\alpha_{IIb}\beta_3$ integrin activation or α-granule release, making it a more selective inhibitor of platelet scramblase activity than the catechin gallate compounds studied in Chapter 4. However, the solubility of S1 was poor, making it difficult to work with, and S1 did not inhibit platelet PS exposure in response to A23187 stimulation when AV binding was measured by flow cytometry (as would be expected of a direct inhibitor of platelet scramblase activity). Further work is required to establish whether S1 acts directly on the scramblase protein TMEM16F or via an alternative mechanism.

Whilst a novel inhibitor of platelet scramblase activity was identified from this initial screen, with the publication of the mTMEM16F structure (Alvadia et al., 2019), differences between the fungal and mouse structures became evident and may explain the relatively low success rate of our first screen. This chapter aimed to take a similar structure-based *in silico* approach to the previous chapter, instead using sites identified in the mTMEM16F structure. 3 sites were identified in the mTMEM16F structure where catechin gallate compounds might bind. All 3 of these sites could inform separate *in silico* screens and yield useful results pertaining to the mechanism of action of polyphenolic compounds on scramblase activity. Site B was prioritised for this screen since only active catechin gallate compounds were predicted to dock to this location (Table 5.9) and S1 was predicted to dock most closely to site B.

Some of the lab work for this chapter could not be completed due to the COVID-19 shutdown of our lab. Where this is the case, it is highlighted in the appropriate results section and the experiments I would have ideally completed are detailed in the discussion.

6.1 A structure-based screen focused around ECG' dockings in the mTMEM16F structure

To conduct a structure-based screen using FRED, a reference pose is required. The highest energy ECG' pose in cluster B was used for this screen. The original pose from Autodock Vina was re-docked into the Ca^{2+} bound mTMEM16F structure (6QP6) in a focused docking using GOLD and this was used as the query reference for a screens of the Enamine Hit Locator Library, as in Chapter 5, in addition to the Chembridge CORE library using FRED (Figure 6.1). The Chembridge CORE library contains over 790,000 sp3-enriched, lead-like, small molecule screening compounds with average physiochemical properties that all meet Lipinski's rule of 5. The selected hits were then purchased through Molport. Compounds identified using FRED were re-docked into the mTMEM16F structure using GOLD and the top scoring 21 compounds were selected for screening. Compounds were blinded for screening purposes and known as G1-G21. The structures of compounds G1-G21 are given in Table 6.1.

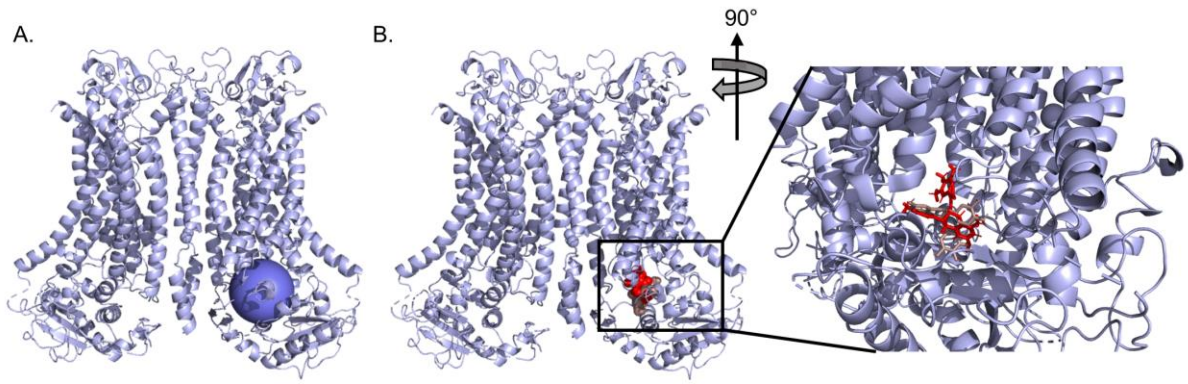

Figure 6.1: Cluster B and refined ECG' pose in mTMEM16F used as reference for FRED screen. (A) Cluster B shown as a 10 Å radius sphere in mTMEM16F structure 6QP6. (B) Space filling representation of the highest energy ECG' pose from Autodock Vina (brown) and refined ECG' pose from GOLD (red). Enlarged view shows stick representations of Autodock Vina and GOLD ECG' poses.

Table 6.1: Chemical structures and supplier information of compounds G1-G21 identified by a structure-based screen around ECG' dockings in mTMEM16F.

IUPAC names were unavailable for some compounds only purchasable from Enamine Chemicals. MW – molecular weight.

Compound	MolPort ID	IUPAC	MW	Structure
G1	003-254-016	3-{[(2H-1,3-benzodioxol-5-yl)methyl]sulfamoyl}-N-[2-(2-methyl-1H-1,3-benzodiazol-1-yl)ethyl]benzamide	492.6	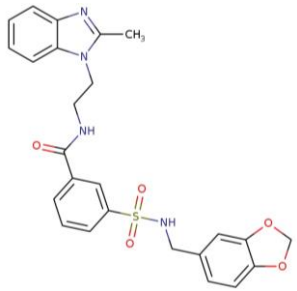
G2	004-164-656	3-(benzylsulfamoyl)-N-[2-(1H-indol-3-yl)ethyl]benzamid	433.5	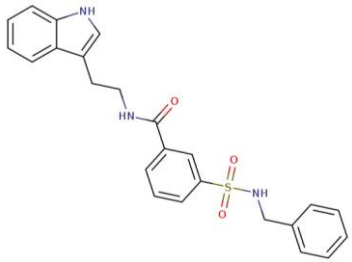
G3	023-232-732	2-(dibenzylamino)-N-({4-[(1H-imidazol-1-yl)methyl]phenyl}methyl)acetamide	424.5	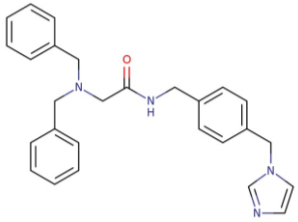

G4	004-201-371	1-(3-{[5-benzyl-4-(2-methoxyethyl)-4H-1,2,4-triazol-3-yl]sulfanyl}propyl)-2,3-dihydro-1H-1,3-benzodiazol-2-one	423.5	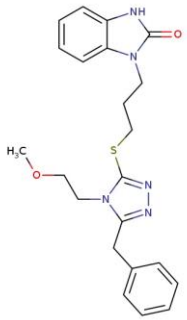
G5	005-517-384	2-({4-[2-(1H-indol-3-yl)acetyl]piperazin-1-yl}methyl)-5,6-dimethyl-3H,4H-thieno[2,3-d]pyrimidin-4-one	435.6	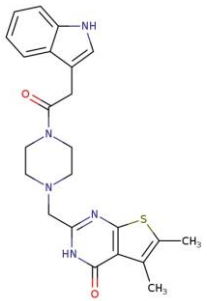
G6	005-658-428	3-{[(2H-1,3-benzodioxol-5-yl)methyl]sulfamoyl}-N-[(1-methyl-1H-1,3-benzodiazol-2-yl)methyl]benzamide	478.5	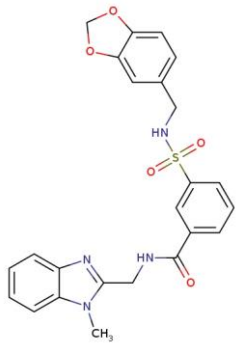

G7	009-464-188	1-[1,3-dimethyl-6-(propan-2-yl)-1H-pyrazolo[3,4-b]pyridine-4-carbonyl]-4-(5,6,7,8-tetrahydronaphthalene-2-sulfonyl)piperazine	495.6	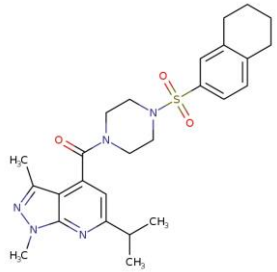
G8	Z56870436 (Enamine)		515.5	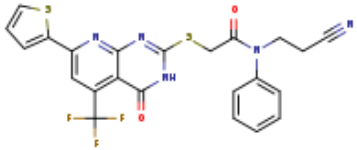
G9	009-465-025	1-{[5-({[2-(furan-2-yl)-1,3-thiazol-4-yl]methyl}sulfanyl)-4-phenyl-4H-1,2,4-triazol-3-yl]methyl}piperidine	437.6	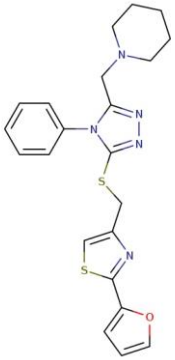
G10	005-536-754	3-{[(4-chlorophenyl)methyl]sulfamoyl}-N-({imidazo[1,2-a]pyridin-2-yl}methyl)-4-methoxybenzamide	485.0	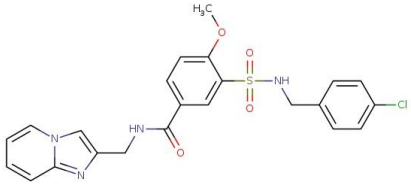

G11	005-818-158	6-(diethylsulfamoyl)-N-{3-[methyl(phenyl)amino]propyl}-2-oxo-1,2-dihydroquinoline-4-carboxamide	470.6	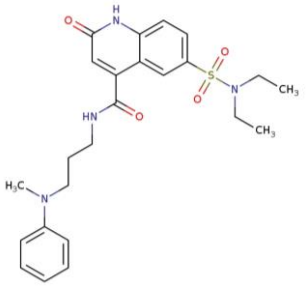
G12	Z226189234 (Enamine)		432.5	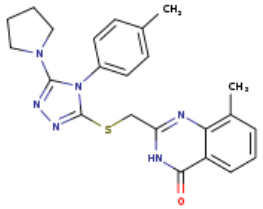
G13	000-434-259	1-[4-(naphthalene-2-sulfonyl)piperazin-1-yl]-4-phenylphthalazine	480.6	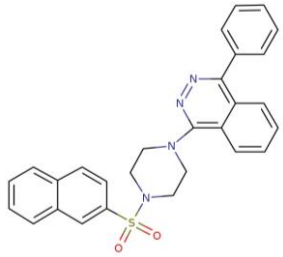
G14	Z29651902 (Enamine)		407.5	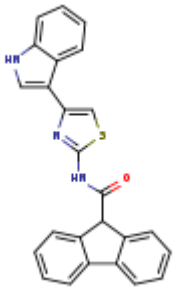

G15	Z102413300 (Enamine)		448.5	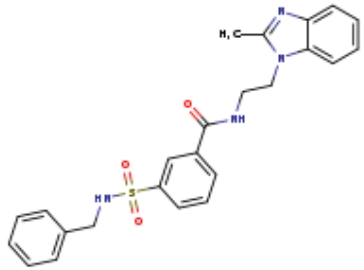
G16	009-320-548	N-{[4-(1H-pyrazol-5-yl)phenyl]methyl}-2-(1H-1,2,3,4-tetrazol-1-yl)benzamide	345.4	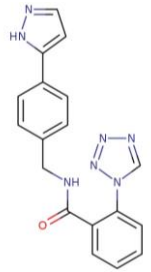
G17	009-492-211	N-[4-(4-acetamidophenyl)-1,3-thiazol-2-yl]-1-(4-methylbenzenesulfonyl)piperidine-4-carboxamide	498.6	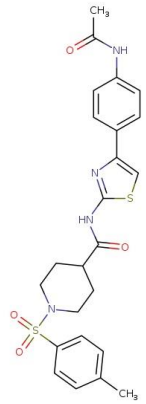

G18	004-582-670	1-(2,3-dihydro-1,4-benzodioxine-6-sulfonyl)-4-{1H-pyrrolo[2,3-b]pyridin-3-yl}-1,2,3,6-tetrahydropyridine	397.5	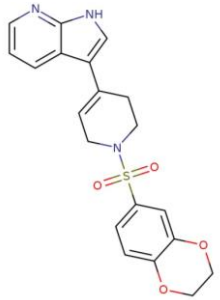
G19	005-828-128	1-(2-methyl-1H-indol-3-yl)-2-{2-[(naphthalen-2-yloxy)methyl]-1H-1,3-benzodiazol-1-yl}ethan-1-one	445.5	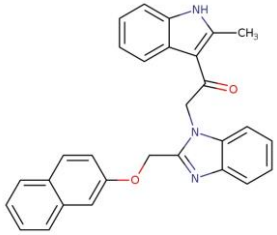
G20	009-442-399	N-(3-oxo-3-{1H,2H,3H,4H,5H-pyrido[4,3-b]indol-2-yl}propyl)naphthalene-2-sulfonamide	433.5	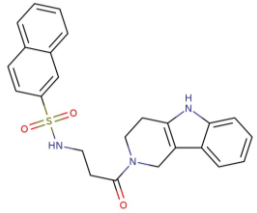
G21	009-434-958	3-({4-benzyl-5-[(piperidin-1-yl)methyl]-4H-1,2,4-triazol-3-yl}sulfanyl)-N-(2-fluorophenyl)propanamide	453.6	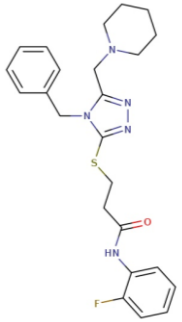

6.2 G compound docking into mTMEM16F dimer

Energy-minimised structures of all G compounds were blindly docked into the prepared mTMEM16F structure (6QP6) using Autodock Vina. The majority of G compounds docked most commonly to the dimer cavity of the mTMEM16F structure (Figure 6.2 and Table 6.2). Many of these clusters have very high predicted mean binding energies above 9 kcal/mol. When analysing G compound clusters, the maximum radius parameter was set to 11 Å, rather than the 10 Å limit used for polyphenolic compounds and the S compounds, since the G compounds themselves were larger.

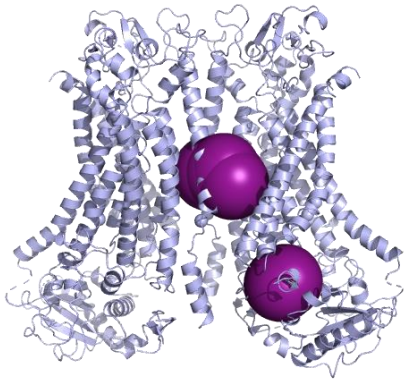

Figure 6.2: Most populous clusters of compounds G1-G21 in mTMEM16F dimer. Most populous clusters represented as 11 Å radius spheres in the mTMEM16F structure (6QP6).

Compound	No. of clusters	No. of poses in most populous cluster (45)	Mean predicted binding energy of poses in most populous cluster (kcal/mol)
G1	4	31	9.99
G2	2	33	9.50
G3	5	18	8.89
G4	5	14	8.45
G5	7	23	10.10
G6	5	22	10.17
G7	3	33	10.79
G8	3	20	9.71
G9	6	18	8.46
G10	3	23	9.41
G11	7	13	8.04
G11	7	13	8.03
G12	6	15	10.12
G13	3	37	12.28
G14	3	30	12.15
G15	6	16	9.77
G16	4	20	9.34
G17	5	29	10.28
G18	5	31	9.67
G19	2	40	11.05
G20	3	37	10.85
G21	3	22	9.51
G21	3	22	9.24

Number of poses in most populous cluster (45)							
40-45	35-39	30-34	25-29	20-24	15-19	10-14	<10
Mean predicted binding energy (kcal/mol)							
10.0 – 10.39	9.6 – 9.99	9.2-9.59	8.8 – 9.19	8.4 – 8.79	8.0 – 8.39	7.6 – 7.99	7.2 – 7.59

Table 6.2: Clustering results for G1-G21 in mTMEM16F dimer. The number of poses in most populous cluster and mean predicted binding energy of poses in most populous cluster are colour coded. This colour coding is used in subsequent tables.

6.3 G compound docking into mTMEM16F monomer

Though initial blind dockings showed that the G compounds docked most commonly to the dimer interface, the predicted binding energies were high. It is possible that the G compounds might also dock elsewhere in the mTMEM16F structure with reasonable binding energies that are not being picked up here since Autodock Vina only outputs the 9 highest energy poses. Blind docking was therefore repeated using the mTMEM16F monomer, extracted from the 6QP6 pdb file. Using the monomer structure, more clusters were identified compared to the

dimer, but many of the most populous of these clusters did correspond to the area around cluster B against which they were screened, with their cluster centres being within 10 Å of the reference pose centroid (Table 6.3 and Figure 6.3).

Compound	No. of clusters	No. of poses in most populous cluster (45)	Mean predicted binding energy of poses in most populous cluster (kcal/mol)
G1	7	13	9.42
G2	8	11	9.06
G3	7	14	8.71
G4	7	17	8.35
G5	7	26	9.53
G6	5	12	9.83
G7	6	19	9.86
G8	9	12	10.13
G9	6	15	8.18
G10	6	14	9.06
G11	10	13	7.35
G12	6	11	10.15
G13	6	14	10.44
G14	6	12	10.45
G15	7	14	9.44
G16	8	11	9.05
G17	4	21	10.00
G18	7	12	9.20
G19	5	16	9.48
G19	5	16	9.38
G20	6	15	10.13
G21	5	23	8.68

Table 6.3: Clustering results for G1-G21 in mTMEM16F monomer. The number of poses in most populous cluster and mean predicted binding energy of poses in most populous cluster are colour coded.

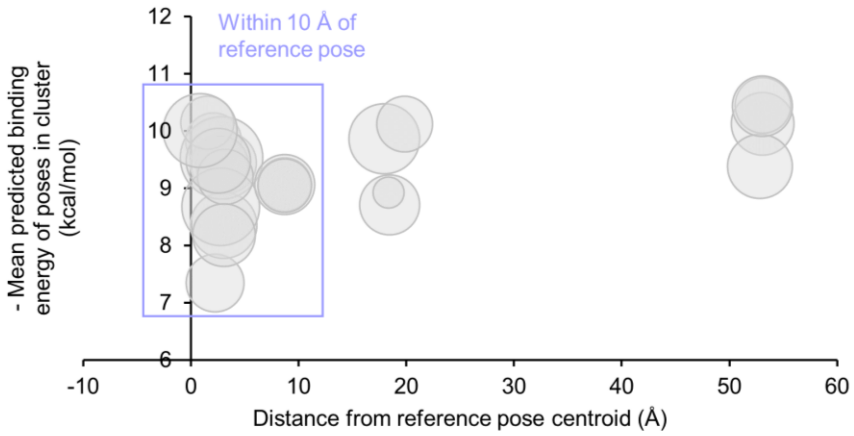

Figure 6.3: Analysis of clustering of G compounds compared to ECG' reference pose. Distance from reference pose centroid plotted against mean predicted binding energy of poses in the cluster. Bubble size represents the number of poses in cluster.

6.4 Five G compounds inhibit platelet PS exposure following stimulation with thrombin + CRP-XL in a flow cytometry AV binding assay

The set of G compounds were split arbitrarily for screening purposes by flow cytometry (G1-G10 in set A and G11-G21 in set B). Following a 60-minute incubation with 100 µM drug at 37°C, platelet PS exposure was measured after a 10-minute stimulation with 1U/ml thrombin + 1 µg/ml CRP-XL at ambient temperature. From set A, compound G9 significantly inhibited PS exposure and in set B G12 significantly inhibited PS exposure. In set B, G11, G17 and G21 were still deemed of interest since they trended towards inhibiting PS exposure but did not reach statistical significance within this large screen. Compound G20 caused PS exposure in unstimulated platelets and G3 trended towards doing so as well. G20 also enhanced platelet PS exposure following stimulation with thrombin + CRP-XL. AV positive microparticle formation was also measured during this screen. Compounds G2, G11, G18, G19 and G20 caused AV positive microparticle release from unstimulated platelets and G20 enhanced AV positive microparticle formation following stimulation with thrombin + CRP-XL (Figure 6.4). The data from Figure 6.4 were re-analysed to look at the proportion of stimulated platelets with high level or medium level PS exposure following treatment with G9, G11, G12, G17 and G21. These data were not statistically analysed since it came from part of a larger screen, but it appeared that G9, G11, G12, G17 and G21 were inhibiting high level PS exposure with no change in medium level PS exposure (Figure 6.5).

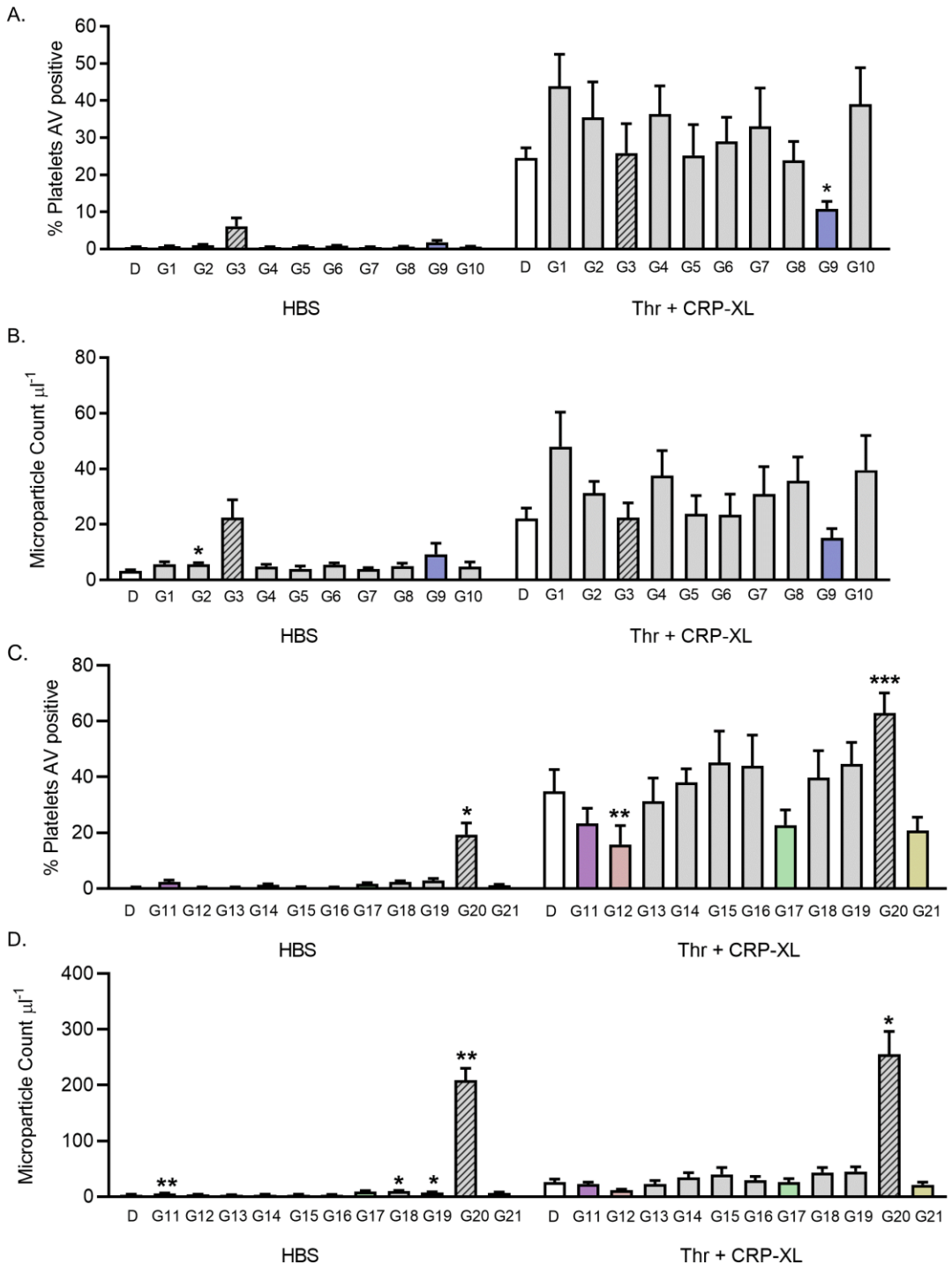

Figure 6.4: Five G compounds inhibit platelet PS exposure following stimulation with thrombin + CRP-XL. Flow cytometry AV binding after stimulation with 1 U/ml thrombin + 1 µg/ml CRP-XL following a 60-minute incubation with 100 µM G1-G21 or 0.1% DMSO at ambient temperature. (A) % of AV positive platelets following pre-incubation with set A compounds. (B) AV positive microparticle count following pre-incubation with set A compounds. (C) % of AV positive platelets following pre-incubation with set B compounds. (D) AV positive microparticle count following pre-incubation with set B compounds. Bar charts show mean ± SEM. N = 5. Data analysed using two-way ANOVA, both factors matching, and Dunnett's multiple comparisons tests.

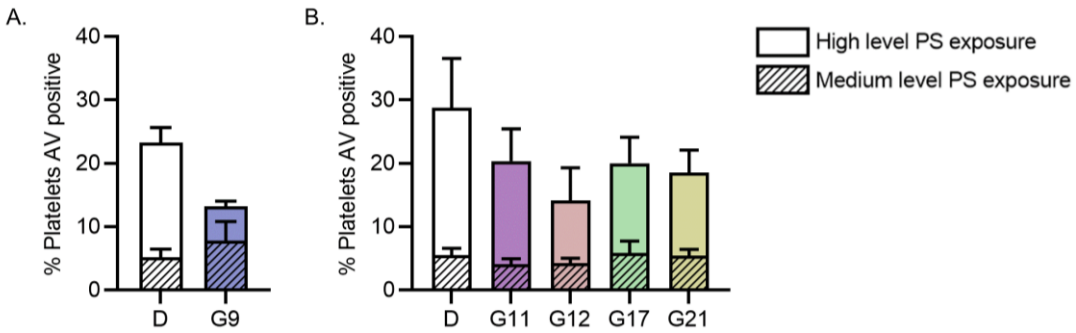

Figure 6.5: Effects of G9, G11, G12, G17 and G21 on high and medium level platelet PS exposure following stimulation with thrombin + CRP-XL. Flow cytometry AV binding after stimulation with 1 U/ml thrombin + 1 µg/ml CRP-XL following a 60-minute incubation with 100 µM G9, G11, G12, G17, G21 or 0.1% DMSO at 37°C. (A) % of platelets with high level or medium level PS exposure following incubation with G9 or DMSO. (B) % of platelets with high level or medium level PS exposure following incubation with G11, G12, G17, G21 or DMSO. Re-analysis of data presented in Figure 6.4. Hatching – medium level PS exposure. No hatching – high level PS exposure. Bar charts show mean ± SEM. N = 5.

6.5 G9, G11, G12, G17 and G21 do not affect cytosolic Ca^{2+} signalling following stimulation with thrombin + CRP-XL

Cytosolic Ca^{2+} signals were measured by Cal520 fluorescence. 100 µM compounds G9, G11, G12 and G17 were not found to affect cytosolic Ca^{2+} signals following stimulation with 1 U/ml thrombin + 1 µg/ml CRP-XL (Figure 6.6, n = 3; due to the COVID-19 shutdown of our lab, experiments could not be repeated to n = 5 as intended). It does appear as though G9 and G12 might inhibit cytosolic Ca^{2+} signalling had I been able to repeat the assay with more donors, so there remains some uncertainty as to whether these compounds affect Ca^{2+} signals. Due to limited compound availability, only a single preliminary run of Ca^{2+} signalling measurements were taken with G21 before the lab shutdown, but this preliminary result also suggested no effect of G21 on cytosolic Ca^{2+} signalling.

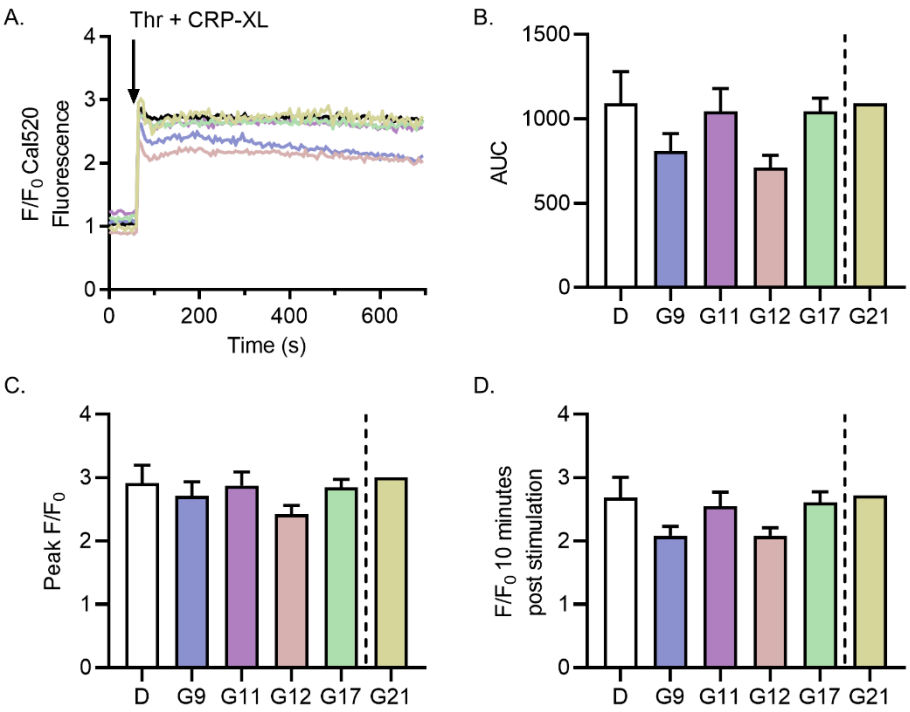

Figure 6.6: G compounds do not affect cytosolic Ca^{2+} signalling following stimulation with thrombin + CRP-XL. Platelets were loaded with the Ca^{2+}-sensitive fluorescence dye, Cal520. Fluorescence values were normalised to the initial fluorescence values of vehicle controls containing 0.1% DMSO in matched samples to account for variation in dye loading (F/F_0). Platelets were treated with 100 µM G compound or 0.1% DMSO for 60 minutes at 37°C before stimulations. Platelets were stimulated with 1 U/ml thrombin + 1 µg/ml CRP-XL. Data are presented as (A) F/F_0 Cal520 fluorescence following stimulation; (B) AUC above baseline ($F/F_0 = 1$); (C) peak F/F_0 following stimulation; and (D) F/F_0 at 10 minutes post stimulation. Bar charts show mean ± SEM. N = 3. Data analysed using a repeated measures one-way ANOVA and Dunnett's multiple comparisons tests.

6.6 G9, G11, G12 and G17 do not inhibit platelet PS exposure following stimulation with A23187 in a flow cytometry AV binding assay

A 60-minute incubation at 37°C with 100 µM G9, G11, G12 and G17 did not inhibit platelet PS exposure following stimulation with 10 µM A23187 measured by flow cytometry (Figure 6.7 A). Under these incubation conditions G9 and G17 caused AV positive microparticle release from unstimulated platelets (Figure 6.7 B). Before the COVID-19 closure of the lab, a single preliminary experiment indicated that these compounds do not affect cytosolic Ca^{2+} signals following stimulation with 10 µM A23187 (Figure 6.7 C). G9, G11, G12 and G17 did not affect the proportion of A23187-stimulated platelets with high level or medium level PS exposure compared to DMSO control (Figure 6.7 D).

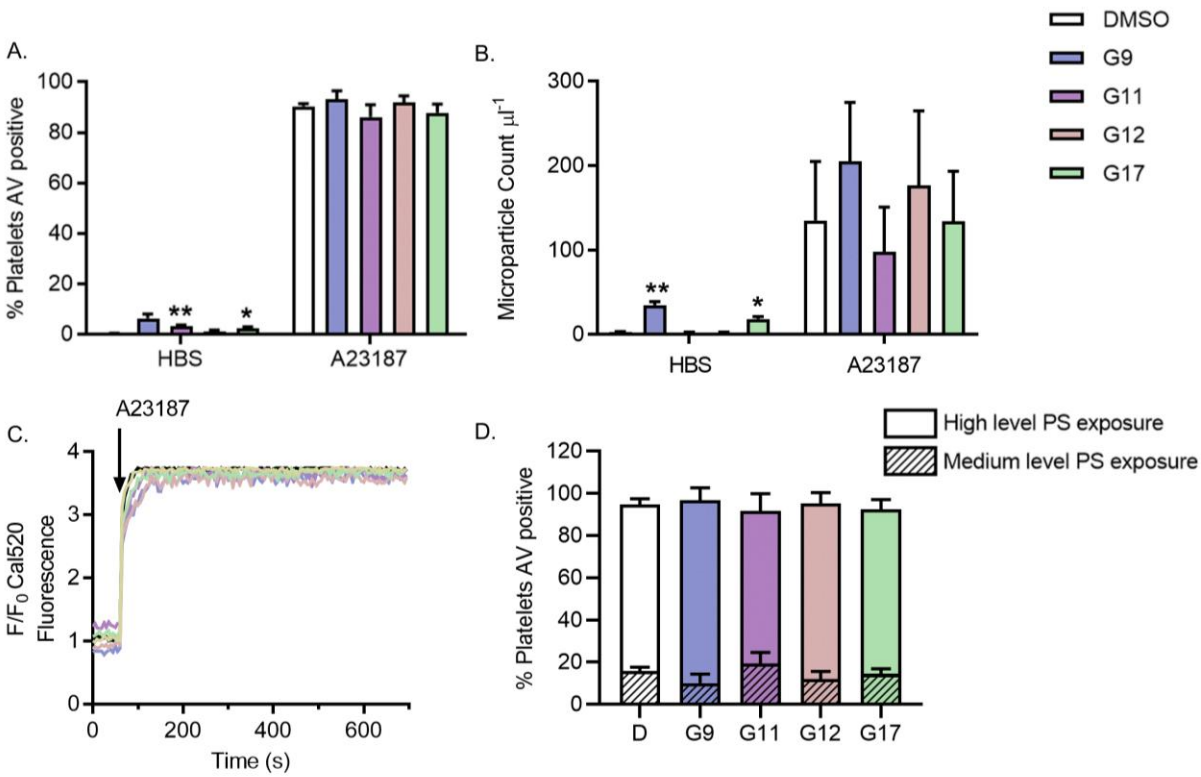

Figure 6.7: G9, G11, G12 and G17 do not inhibit platelet PS exposure following stimulation with A23187 in a flow cytometry AV binding assay. Flow cytometry AV binding after stimulation with 10 µM A23187 following a 60-minute incubation with 100 µM G9, G11, G12, G17 or 0.1% DMSO at 37°C. (A) % platelets AV positive. (B) AV positive microparticle count. (C) Preliminary traces showing F/F_0 Cal520 fluorescence following stimulation with 10 µM A23187. (D) % of platelets with high level or medium level PS exposure following stimulation with 10 µM A23187. Bar charts show mean ± SEM. N = 5. Cal520 trace N =1. Data analysed using two-way ANOVA, both factors matching, and Dunnett's multiple comparisons test.

6.7 G9, G11, G12, G17 and G21 do not affect platelet $\alpha_{IIb}\beta_3$ integrin activation or α-granule release following stimulation with PAR1-AP

G9, G11, G12, G17 and G21 did not affect platelet $\alpha_{IIb}\beta_3$ integrin activation (PAC-1) or α-granule release (CD62P) following stimulation with 10 µM PAR1-AP. $\alpha_{IIb}\beta_3$ integrin activation and α-granule release were measured following a 60-minute incubation with 100 µM G compound at 37°C and a 10-minute stimulation with 10 µM PAR1-AP at ambient temperature. In contrast, G3 inhibited both platelet $\alpha_{IIb}\beta_3$ integrin activation and α-granule release following stimulation with PAR1-AP (Figure 6.8).

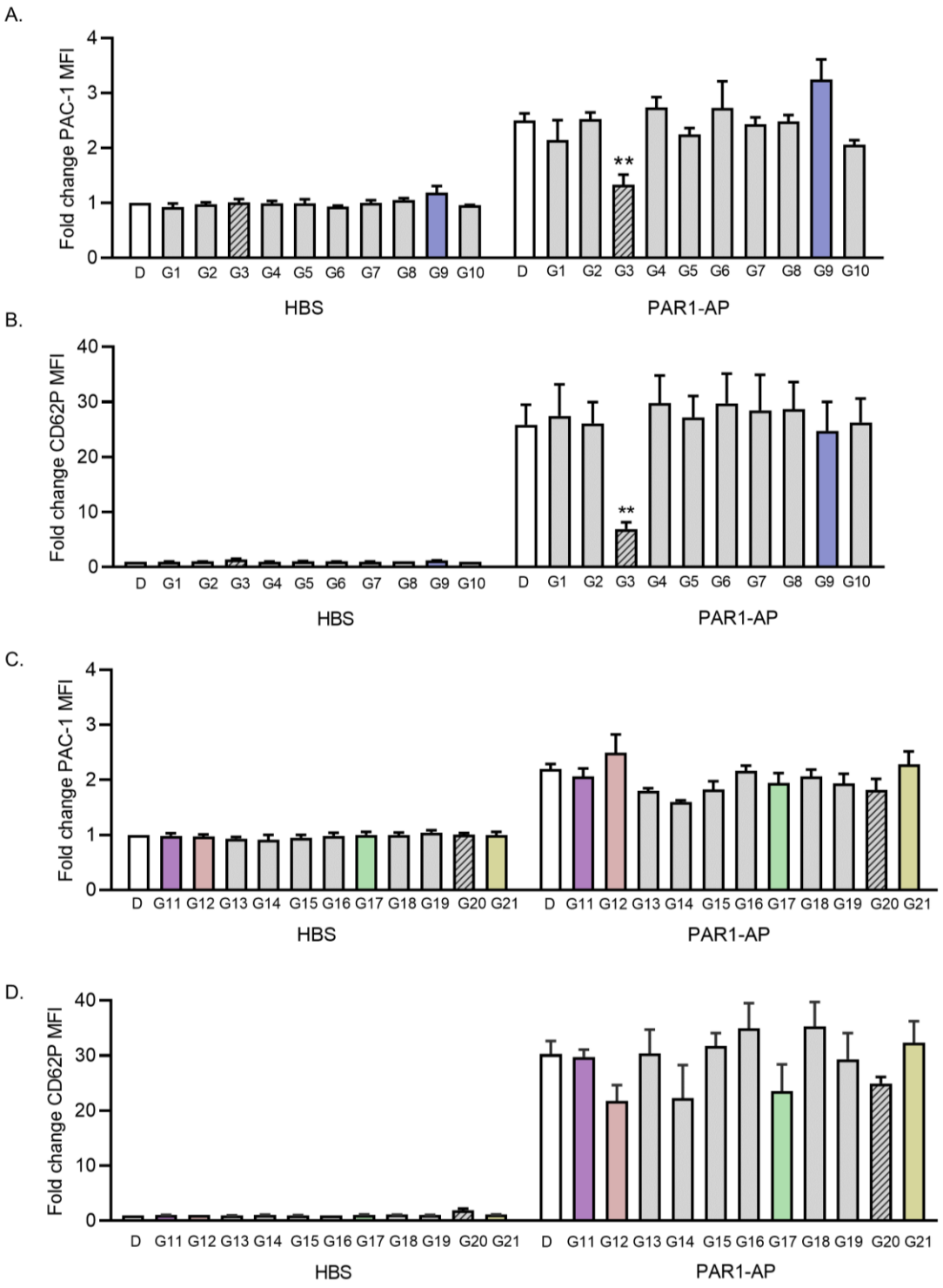

Figure 6.8: G9, G11, G12, G17 and G21 do not affect platelet $\alpha_{IIb}\beta_3$ integrin activation or α-granule release following stimulation with PAR1-AP. Platelets were treated with 100 μM G compound or 0.1% DMSO for 60 minutes at 37°C prior to stimulation for 10 minutes with 10 μM PAR1-AP at ambient temperature. $\alpha_{IIb}\beta_3$ activation was measured by flow cytometry as PAC-1 binding (FITC conjugated). α-granule secretion was measured by anti-CD62P (P-selectin) antibody binding (phycoerythrin (PE) conjugated). (A) Fold change in PAC-1-FITC MFI following incubation with set A compounds. (B) Fold change in CD62P-PE MFI following incubation with set A compounds. (C) Fold change in PAC-1-FITC MFI following incubation with set B compounds. (D) Fold change in CD62P-PE MFI following incubation with set B compounds. Bar charts show mean ± SEM. N = 5. Data analysed using two-way ANOVA, both factors matching and Dunnett's multiple comparison tests.

6.8 G9, G11, G12, G17 and G21 all dock most commonly within 10 Å of the reference pose for cluster B in mTMEM16F monomer

G9, G11, G12, G17 and G21 all inhibit platelet PS exposure following stimulation with thrombin + CRP-XL and dock most commonly into the mTMEM16F monomer within 10 Å of the reference pose for cluster B (Figure 6.9).

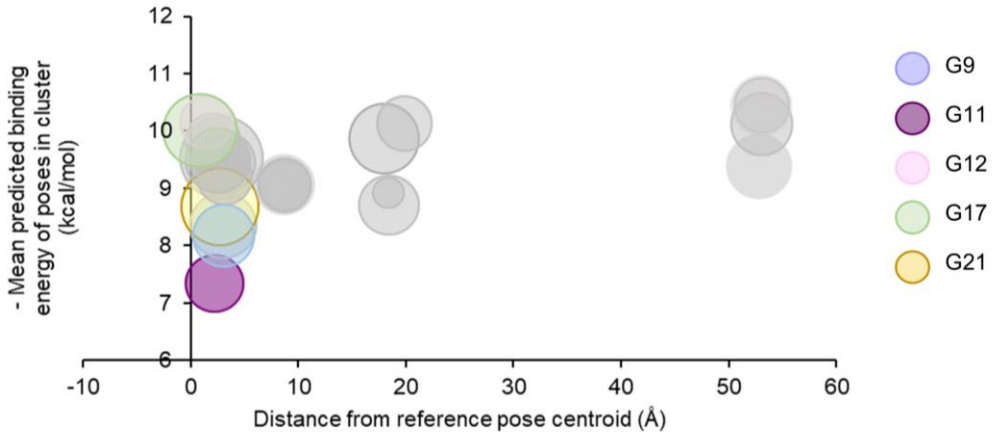

Figure 6.9: Clustering analysis of active G compounds compared to reference pose in mTMEM16F monomer. Distance from reference pose centroid plotted against mean predicted binding energy of poses in the cluster. Bubble size represents the number of poses in cluster.

6.9 G3 may inhibit cytosolic Ca^{2+} signalling in response to a range of agonists

Compound G3 warranted further characterisation as this induced a degree of PS exposure in unstimulated platelets (Figure 6.4) and inhibited PAR1-AP mediated $\alpha_{IIb}\beta_3$ integrin activation and α-granule release (Figure 6.8). Preliminary Cal520 measurements of cytosolic Ca^{2+} signals following stimulation with 1 U/ml thrombin + 1 µg/ml CRP-XL (n = 3) show that G3 inhibited these signals when quantified as AUC, peak F/F_0 and F/F_0 at time of flow cytometry sampling but trended towards increasing F/F_0 prior to stimulation (Figure 6.10 A). Preliminary cytosolic Ca^{2+} signals following stimulation with 10 µM PAR1-AP (n = 2) suggest G3 may also inhibit these (Figure 6.10 B). These experiments were prematurely cut short by the COVID-19 closure of our lab.

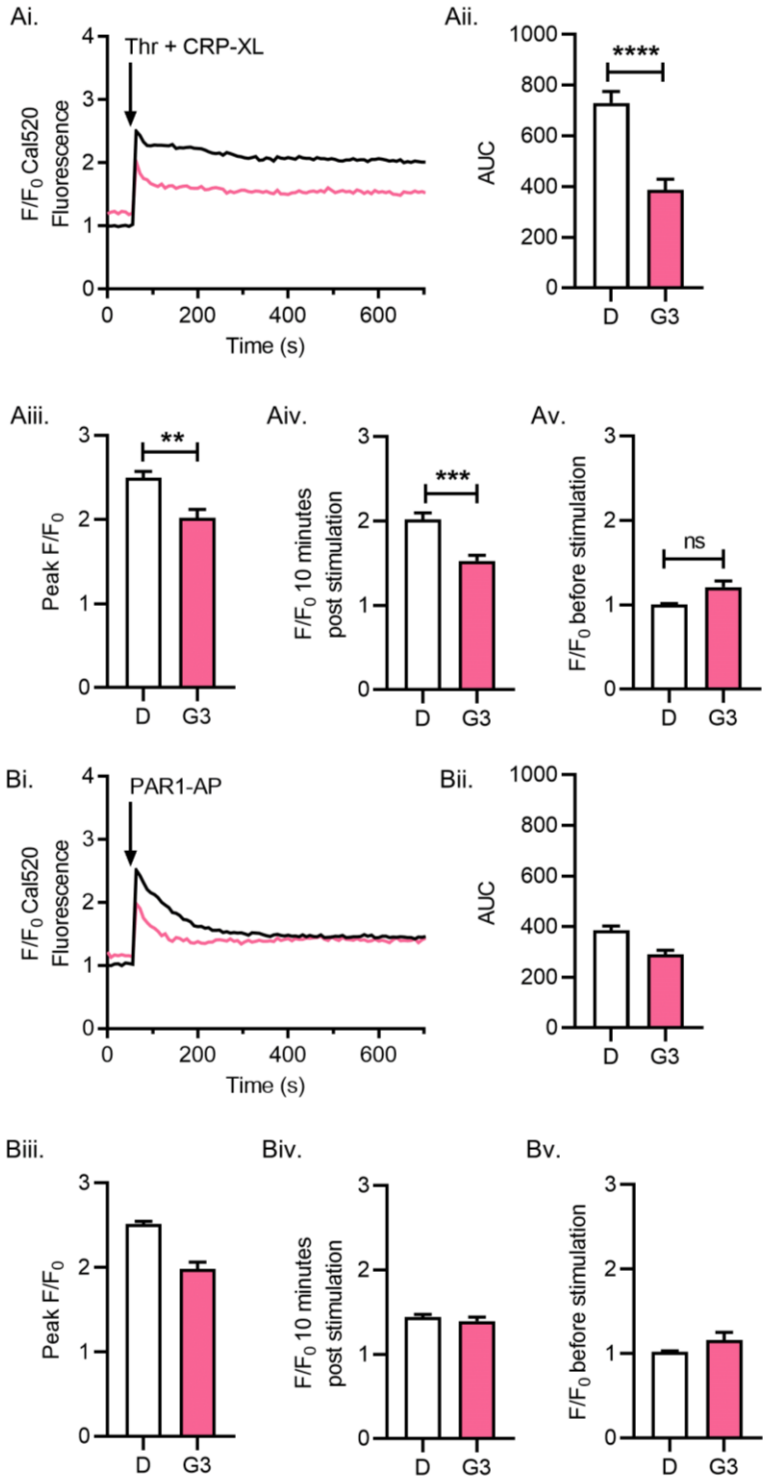

Figure 6.10: Preliminary results suggest G3 inhibits platelet cytosolic Ca^{2+} signalling. Platelets were loaded with the Ca^{2+}-sensitive fluorescence dye, Cal520. Fluorescence values were normalised to the initial fluorescence values of vehicle controls containing 0.1% DMSO in matched samples to account for variation in dye loading (F/F_0). Platelets were treated with 100 μM G3 or 0.1% DMSO for 60 minutes at 37°C before stimulations. Platelets were stimulated with (A) 1 U/ml thrombin + 1 μg/ml CRP-XL or (B) 10 μM PAR1-AP. Data are presented as (i) F/F_0 Cal520 fluorescence following stimulation; (ii) AUC above baseline ($F/F_0 = 1$); (iii) peak F/F_0 following stimulation; (iv) F/F_0 at 10 minutes post stimulation; and (v) F/F_0 before stimulation. Bar charts show mean ± SEM. N = 3 for thrombin + CRP-XL stimulations. Data were analysed using a two-tail Student's paired t-test. N = 2 for PAR1-AP stimulations.

6.10 G20 may enhance cytosolic Ca^{2+} signals following stimulation with thrombin + CRP-XL

G20 warranted further characterisation as it caused PS exposure in unstimulated platelets (Figure 6.4 B). Preliminary experiments suggest that G20 may enhance cytosolic Ca^{2+} signals measured using Cal520 following stimulation with thrombin + CRP-XL (n = 2). These experiments were prematurely cut short by the COVID-19 closure of our lab.

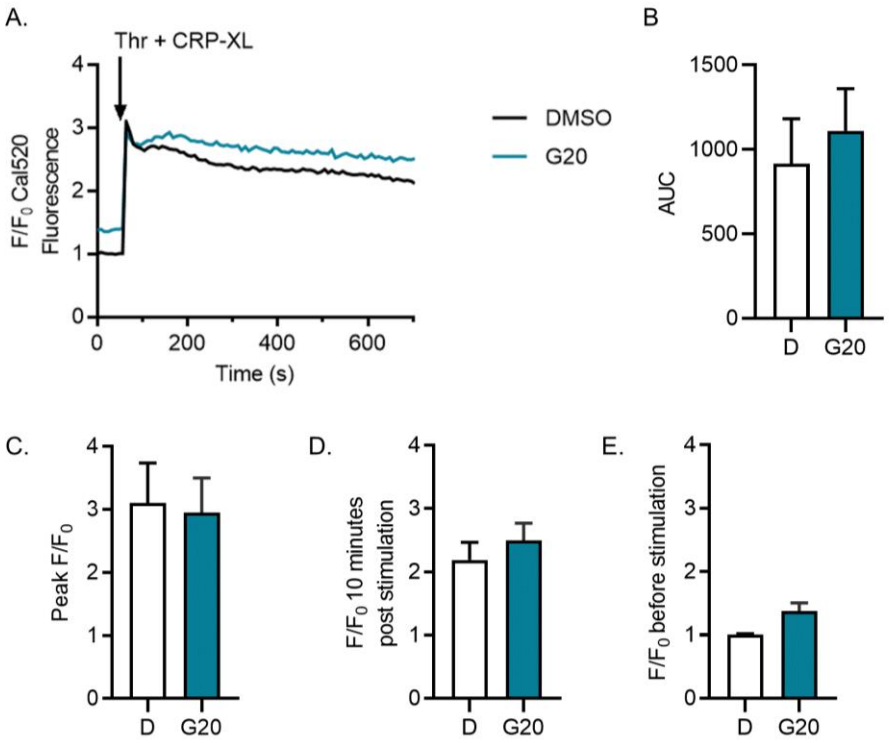

Figure 6.11: Preliminary results of G20 affecting platelet cytosolic Ca^{2+} signalling. Platelets were loaded with the Ca^{2+}-sensitive fluorescence dye, Cal520. Fluorescence values were normalised to the initial fluorescence values of vehicle controls containing 0.1% DMSO in matched samples to account for variation in dye loading (F/F_0). Platelets were treated with 100 µM G20 or 0.1% DMSO for 60 minutes at 37°C before stimulations. Platelets were stimulated with 1 U/ml thrombin + 1 µg/ml CRP-XL. Data are presented as (A) F/F_0 Cal520 fluorescence following stimulation; (B) AUC above baseline (F/F_0 = 1); (C) peak F/F_0 following stimulation; (D) F/F_0 at 10 minutes post stimulation; and (E) F/F_0 before stimulation. Bar charts show mean ± SEM. N = 2.

6.11 Discussion

In chapter 5, three sites (A, B and C) were identified in the Ca^{2+} bound mTMEM16F structure (6QP6) where catechin gallate compounds were predicted to bind and may exert their biological action inhibiting platelet scramblase activity. All three of these sites warrant further investigation to determine where active compounds might interact with the TMEM16F structure and to aid the identification of new selective inhibitors. Site B was chosen for investigation first since no inactive catechin compounds were predicted to dock to this site (Table 5.9), and it was the site closest to the predicted binding location of S1 which also showed some inhibition of platelet scramblase activity.

For this structure-based screen the highest energy ECG' pose from site B was used as the reference, both because the predicted binding energy was slightly higher for ECG' than EGCG' at this site, and due to the more desirable results of ECG' detailed in chapter 4, such as not causing medium level PS exposure in unstimulated RBCs. As in chapter 5, the highest energy ECG' pose was re-docked using GOLD and then used as the reference query for a structure-based screen of the Molport chemical library using FRED. The top 500 results from FRED were re-docked using GOLD and the top 21 scoring compounds selected for testing as the G compounds.

Compounds G1-G21 were blindly docked into the prepared Ca^{2+}-bound mTMEM16F structure using Autodock Vina. Initial dockings indicated that most of the G compounds were predicted to bind within the dimer cavity of mTMEM16F with high predicted binding energies. These docking simulations were carried out *in vacuo* whereas within a membrane the dimer cavity would be expected to be packed with phospholipids. It is not known whether the dimer cavity plays a role in TMEM16F scramblase function. It is plausible that compounds interacting with phospholipid-protein interactions at the dimer cavity may cause local disruption to the membrane environment and affect scrambling in some way. Alternatively, if docking simulations were run in the presence of phospholipids, they might not be able to dock to this dimer cavity site. This means that we cannot rule out any effects of G compounds being due to interactions at the dimer cavity at this stage. However, as discussed in Chapter 5, it is possible for a compound to interact at several sites on a protein's structure that are not responsible for their biological action. Since the G compounds were identified by a structure-based screen at site B, the compounds were blindly docked into the monomeric mTMEM16F structure. When docked into the monomer, 13 of the G compounds docked to within 10 Å of the reference ECG' pose, albeit with lower predicted binding energies compared to within the dimer cavity (Figure 6.3).

Compounds G1-G21 were arbitrarily split for screening for effects on platelet PS exposure following stimulation with thrombin + CRP-XL measured by flow cytometry. If more time had been available, the G compounds could also have been screened using the plate-based luminescence AV binding assay following stimulation with A23187 or thrombin + CRP-XL to look at effects on scramblase rate. As previously discussed, our plate-based assay shows a greater sensitivity when detecting inhibition of scramblase rate compared to end-point flow cytometry. 5 of the G compounds were considered of interest inhibiting platelet PS exposure following stimulation with thrombin + CRP-XL. G9 and G12 reached statistical significance and G11, G17 and G21 trended towards significance as part of these large initial screens. There was no indication of G9, G11, G12, G17 or G21 increasing medium level PS exposure in stimulated platelets, rather they appeared to inhibit high level PS exposure (Figure 6.5).

Cal520 fluorescence traces measuring cytosolic Ca^{2+} signals following stimulation with thrombin + CRP-XL showed that none of G9, G11, G12, G17 or G21 inhibited cytosolic Ca^{2+} signals in the donors tested (n = 1-3). These assays should be repeated in the future to at least an n = 5 before we can confidently conclude that they do not inhibit platelet PS exposure through effects on Ca^{2+} signalling but these experiments were prevented by the COVID-19 shutdown of our lab.

None of the G compounds which inhibited platelet PS exposure inhibited platelet $\alpha_{IIb}\beta_3$ integrin activation or α-granule release following stimulation with PAR1-AP (Figure 6.8). This indicates that G9, G11, G12, G17 and G21 are more selective inhibitors of platelet scramblase activity than the catechin gallate compounds tested in chapter 4 since these important pro-aggregatory platelet functions remain.

However, as was the case for S1 in chapter 5, none of the G compounds tested inhibited platelet PS exposure following stimulation with the Ca^{2+} ionophore A23187 when measured by flow cytometry. As previously discussed, this could indicate a weaker inhibition of scramblase activity or a non-direct action on the scramblase protein to inhibit PS exposure. Future work up of the G compounds should follow that suggested for S1 involving testing the effects of compounds on mitochondrial [Ca^{2+}], mitochondrial membrane potential and permeability transition pore opening, and the supra-maximal Ca^{2+} signal characteristic of pro-coagulant platelets (Abbasian et al., 2020; Choo et al., 2012; Jobe et al., 2008). The active G compounds could be tested in RBCs as an indicator of direct action on TMEM16F and eventual validation against recombinantly expressed TMEM16F protein if compounds are otherwise believed to be acting selectively.

All of the compounds S1, G9, G11, G12, G17 and G21 were analysed using SwissADME which predicts pharmacokinetic parameters of compounds and computes drug-likeness

(Daina et al., 2017). All compounds meet Lipinski's criteria for drug-likeness (Lipinski et al., 2001). S1, G9, G12, and G21 all also fulfil Ghose, Veber, Egan and Muegge filters for drug-likeness (Egan et al., 2000; Ghose et al., 1999; Muegge et al., 2001; Veber et al., 2002). G11 violates both Ghose and Veber filters once and G17 violates the Ghose filter twice and Veber and Egan filters once each. G17 is predicted to have low GI absorption whereas all others have high GI absorption and only S1 is predicted to be blood brain barrier permeant, according to the BOILED-Egg model (Daina and Zoete, 2016). None of the compounds contained any pan assay interference structures (PAINS) (Baell and Holloway, 2010). These predictions are all reassuring that further development of all 6 compounds could potentially result in useful drug leads being developed from them if they are shown to be selective in their action. At this stage it would seem appropriate to continue to pursue all compounds, but the less favourable drug-likeness properties of G11 and G17 and less favourable pharmacokinetic predictions of G17 and S1 are worth noting if prioritisation of compounds was required.

Compounds G3 and G20 were also of interest, though they did not inhibit platelet PS exposure. G3 inhibited $\alpha_{IIb}\beta_3$ integrin activation and α-granule release following stimulation with PAR1-AP (Figure 6.8). Preliminary results indicate that G3 inhibits cytosolic Ca^{2+} signalling downstream of PAR1 (Figure 6.10). Interestingly, despite G3 inhibiting cytosolic Ca^{2+} signals following stimulation with thrombin + CRP-XL, G3 did not have any effect on platelet PS exposure following stimulation but trended towards causing PS exposure in unstimulated platelets. Follow up work could involve testing G3 for any toxic effects on platelets using an LDH assay, which may explain increased PS exposure in unstimulated platelets, or direct activatory effects on scramblase activity which might augment PS exposure in response to a reduced initial Ca^{2+} signal. Ca^{2+} signals downstream of PAR4 and GPVI could also be investigated to determine whether G3 exerts a PAR1-specific effect.

Compound G20 also caused PS exposure in unstimulated platelets and enhanced PS exposure in activated platelets following stimulation with thrombin + CRP-XL. Preliminary results suggest that G20 may augment cytosolic Ca^{2+} signals in both unstimulated and stimulated platelets which may explain the increased PS exposure. These effects on cytosolic Ca^{2+} signalling could be further investigated and G20 should also be tested for toxicity.

The structure-based screen presented here focused around site B in the Ca^{2+} bound mTMEM16F structure has identified 5 novel inhibitors of platelet scramblase activity which do not affect the pro-aggregatory platelet functions of $\alpha_{IIb}\beta_3$ integrin activation or α-granule release. Further work is required to determine whether these compounds act directly on the TMEM16F protein or inhibit platelet PS exposure via a different mechanism.

Chapter 7 - General Discussion

7.1 Summary of results

Inhibiting platelet activation is a key anti-thrombotic strategy used to prevent morbidity and mortality from cardiovascular diseases including heart attacks and strokes (McFadyen et al., 2018). However, all current anti-platelet drugs are associated with increased bleeding and are unsuitable for use in some patient populations (Swieringa et al., 2014). There is therefore an unmet clinical need for effective anti-platelet drugs which do not increase bleeding.

TMEM16F is a platelet phospholipid scramblase protein that has been identified as a potential new anti-thrombotic target (Baig et al., 2016; Fujii et al., 2015; Mattheij et al., 2016; Suzuki et al., 2010; Yang et al., 2012). This thesis aimed to work towards developing a selective inhibitor of TMEM16F. Such an inhibitor would be necessary to test the hypothesis that inhibiting TMEM16F could be a novel anti-thrombotic approach. Evidence from TMEM16F knock out mice and patients with Scott Syndrome suggests that inhibiting TMEM16F may reduce thrombosis and might be associated with fewer bleeding side effects than other anti-platelet drugs since TMEM16F is only involved in pro-coagulant platelet activity and does not play a role in pro-aggregatory activity.

R5421 was the only previously described inhibitor of platelet phospholipid scramblase activity (Dekkers et al., 1998). R5421 had been used to study the effects of scramblase activity in a number of systems but its pharmacology had not been extensively characterised. This thesis demonstrated that R5421 is a non-selective inhibitor of platelet scramblase activity. R5421 also inhibits platelet $\alpha_{IIb}\beta_3$ integrin activation and α-granule release and disrupts cytosolic Ca^{2+} signalling. A ligand-based *in silico* screen identified a set of compounds with similar physical and electrochemical properties to R5421 which were tested for effects on platelet scramblase activity. This screen identified the pesticide thiodicarb as a novel inhibitor of platelet scramblase activity. Thiodicarb, however, also acts non-selectively and inhibits platelet $\alpha_{IIb}\beta_3$ integrin activation, α-granule release and disrupts cytosolic Ca^{2+} signalling (Millington-Burgess et al., 2020). Due to the non-selective action of both R5421 and thiodicarb it was decided not to continue to pursue a ligand-based approach focussed on R5421.

Tannic acid and EGCG' had been shown to inhibit TMEM16F scramblase activity *in vitro* (Suzuki et al., 2014; Watanabe et al., 2018). This thesis showed that both tannic acid and EGCG' inhibit platelet PS exposure. An empirical screen of structurally related polyphenolic compounds showed that all of the catechin-gallate compounds tested inhibited platelet PS exposure whilst catechin compounds lacking the gallate group did not. All catechin gallate

compounds, however, acted non-selectively and also inhibited $\alpha_{IIb}\beta_3$ integrin activation and α-granule release. This screen began to define an emerging pharmacophore for inhibition of platelet PS exposure which can inform future compound design.

Structure-based *in silico* screens were conducted around predicted binding sites of the catechin gallate compounds from docking studies, first using the fungal nhTMEM16 structure and later the mTMEM16F structure. Together, these structure-based screens identified 6 novel inhibitors of platelet scramblase activity when measured by flow cytometry following stimulation with thrombin + CRP-XL: S1, G9, G11, G12, G17 and G21. None of these newly identified inhibitors of platelet scramblase activity inhibited platelet $\alpha_{IIb}\beta_3$ integrin activation or α-granule release following stimulation with PAR1-AP. Four further compounds were identified which inhibited platelet scramblase activity in a plate-based AV binding assay following stimulation with A23187: S2, S3, S14 and S15. Further work is required to establish whether these compounds inhibit platelet scramblase activity via a direct action on TMEM16F or whether they act elsewhere in the mechanism of platelet PS exposure.

7.2 Limitations and future work

The main limitations of this work have been discussed in detail previously and mostly relate to the *in silico* studies performed. Inevitably, *in silico* modelling can only predict possible ligand-protein interactions between the compounds tested and TMEM16F. It is imperative that future studies aim to both improve the accuracy of these predictions and confirm them experimentally to increase our understanding of TMEM16F function and aid the identification of a selective inhibitor.

Our initial structure-based screen was conducted using a fungal nhTMEM16 structure which only shares ~25% sequence identity to hTMEM16F and the second screen used an mTMEM16F structure with ~90% sequence identity to hTMEM16F. Even when using the mTMEM16F structure for *in silico* modelling, key differences between the mTMEM16F and hTMEM16F structures may exist which influence our docking predictions. Homology models of hTMEM16F could be generated and used in future *in silico* work until a hTMEM16F crystal structure becomes available. Furthermore, multiple mTMEM16F structures are now available in Ca^{2+} bound and Ca^{2+} free states, as well as supplemented with PIP_2 (Alvadia et al., 2019; Feng et al., 2019). Further docking studies could be conducted using all of these structures, and human homology models of each, to improve our understanding of whether the inhibitors of platelet scramblase activity identified are most likely acting on the inactive or activated (or a putative intermediate) state of the TMEM16F protein. More extensive dockings studies should be carried out using a range of additional docking programs, such as Autodock 4.

Molecular dynamics simulations could be run with the protein structure moving within a phospholipid bilayer and predicting how compounds affect its function in this more realistic simulation than the *in vacuo* dockings presented here. These studies may identify more specific, or more likely, binding sites for the active compounds in the mTMEM16F structure which could then become the focus for screens of larger compound libraries or inform *de novo* medicinal chemistry design. Improved predictions of where active compounds could be acting on the TMEM16F structure would also allow these sites to be tested in the lab using mutated TMEM16F proteins.

There are also additional *in silico* approaches which could be pursued. These could involve a structure-based approach around R5421, especially if R5421 is predicted to interact with TMEM16F in a similar location to the catechin gallate compounds. Similarly, a ligand based-approach could be pursued based on the catechin gallate compounds and any of the compounds S1, G9, G11, G12, G17 and G21 which are shown to act directly on TMEM16F. A more detailed pharmacophore could be developed using both the ligand properties of active compounds and the predicted interaction sites in the TMEM16F structure and included as a filter during screens of larger chemical libraries or medicinal chemistry design.

The two other major lines of future work should focus on confirming whether or not the inhibitors of platelet scramblase activity identified truly selectively inhibit pro-coagulant activity without affecting pro-aggregatory activity, and if so whether these compounds act directly on TMEM16F or whether they inhibit platelet PS exposure via a different mechanism. All of the compounds S1, G9, G11, G12, G17 and G21 have been shown to not affect platelet $\alpha_{IIb}\beta_3$ integrin activation or α-granule release following stimulation with PAR1-AP. Platelet $\alpha_{IIb}\beta_3$ integrin activation and α-granule release should also be measured following stimulation with other platelet agonists that act via different signalling pathways to PAR1, particularly CRP and ADP to confirm whether pro-aggregatory activity downstream of GPVI and $P2Y_{12}$ respectively remains unaffected by the compounds. It would also be necessary to complete full inhibition curves for these compounds looking at both $\alpha_{IIb}\beta_3$ integrin activation and α-granule release in response to a range of agonists to ensure that lower concentrations of compounds act similarly to the high concentrations used in initial screens and bell shaped inhibition curves have not been missed. Similar inhibition curves should also be completed for each compound and platelet PS exposure. As previously outlined, none of the newly reported inhibitors of platelet scramblase activity affect cytosolic Ca^{2+} signals when measured at the population level in a plate-based Cal520 fluorescence assay. Each compound should be tested to establish whether they affect supramaximal Ca^{2+} signals characteristic of pro-coagulant platelet formation using the low affinity Ca^{2+} dye, Fluo-5N (Abbasian et al., 2020). A direct inhibitor of TMEM16F would not be expected to have any effect on these supramaximal Ca^{2+} signals.

Similarly, a direct TMEM16F inhibitor would not be expected to have any effect on mitochondrial Ca^{2+} uptake, measured using a mitochondrial specific Ca^{2+} dye such as Rhod-2, or mPTP formation, measured using the inner mitochondrial membrane potential dye TMRM. Red blood cell (RBC) PS exposure is TMEM16F dependent but not reliant on mPTP formation and so a direct TMEM16F inhibitor would also be expected to inhibit RBC PS exposure, as the catechin gallate compounds were shown to do. If these experiments indicate that compounds are acting directly on TMEM16F, this could be confirmed in a TMEM16F overexpression system in cell culture. Alternatively, these experiments might identify that the compounds are inhibiting platelet PS exposure by disrupting mitochondrial Ca^{2+} handling or mPTP formation. This would be unexpected due to the targeted structure-based approach which led to their identification but would nevertheless be interesting to pursue since inhibitors of mitochondrial Ca^{2+} uptake and mPTP formation are limited and of potential research and clinical interest in the field of thrombosis and beyond. An additional possibility could be that compounds are inhibiting TMEM16F function by disrupting the local membrane environment rather than binding to the TMEM16F protein itself. This could be investigated using a cellular thermal shift assay (CESTA) to confirm whether compounds directly bind to purified TMEM16F protein. Additionally, CESTA could be used to confirm predicted binding sites of compounds to TMEM16F from docking studies by measuring binding to wild type and mutated forms of the protein.

If compounds are found to be acting directly on TMEM16F then these could be used for proof of principle experiments to determine whether inhibiting TMEM16F could be an effective anti-thrombotic strategy. These might involve testing compounds to see if they inhibit thrombin generation, as would be expected, whilst not affecting aggregation. Testing compounds which are believed to only weakly inhibit TMEM16F would also offer insight into whether complete inhibition of TMEM16F is likely to be necessary for therapeutic effect or whether slowing the rate of platelet scramblase activity would be enough to have some clinical benefit. Compounds could also be tested using *in vitro* thrombosis models to see if occlusion is delayed or prevented. If the proof of concept is shown, further rounds of screening and refinement would be appropriate before testing in *in vivo* thrombosis models. Extensive medicinal chemistry would then need to be applied to transform a lead compound into a future therapeutic.

Compounds would also need to undergo extensive selectivity testing for effects on proteins closely structurally related to TMEM16F such as the Ca^{2+} activated Cl^- channel, TMEM16A, and the endoplasmic reticulum resident scramblase, TMEM16K. It is important that the functions of both TMEM16A and TMEM16K are unaffected by an inhibitor. Other proteins found to have sites similar to the predicted interaction site to TMEM16F, which could be identified using *in silico* methods, should also be prioritised for assessment of off-target effects.

Ultimately a selective TMEM16F inhibitor should be tested using *in vivo* thrombosis models and careful analysis for effects on the roles of TMEM16F in non-blood cells previously identified in animal models (Hu et al., 2016; Ousingsawat et al., 2015; Soulard et al., 2020; Wu et al., 2020). A TMEM16F inhibitor may not be appropriate in certain clinical situations, such as in pregnant women or those undergoing significant surgery as suggested by some observations in Scott Syndrome patients, but in other patient populations could prove a successful alternative or additional anti-thrombotic treatment.

To conclude, the studies presented in this thesis have identified novel inhibitors of platelet scramblase activity that will inform future design of a novel inhibitor and increase our understanding of the pharmacology of TMEM16F and platelet phospholipid scramblase activity.

Bibliography

Abbasian, N., Millington-Burgess, S.L., Chabra, S., Malcor, J.-D., Harper, M.T., 2020. Supramaximal calcium signaling triggers procoagulant platelet formation. Blood Adv. 4, 154–164. https://doi.org/10.1182/bloodadvances.2019000182

Agbani, E.O., Hers, I., Poole, A.W., 2017. Temporal contribution of the platelet body and balloon to thrombin generation. Haematologica 102, e379–e381. https://doi.org/10.3324/haematol.2017.166819

Agbani, E.O., van den Bosch, M.T.J., Brown, E., Williams, C.M., Mattheij, N.J.A., Cosemans, J.M.E.M., Collins, P.W., Heemskerk, J.W.M., Hers, I., Poole, A.W., 2015. Coordinated Membrane Ballooning and Procoagulant Spreading in Human Platelets. Circulation 132, 1414–1424. https://doi.org/10.1161/CIRCULATIONAHA.114.015036

Agbani, E.O., Williams, C.M., Li, Y., Bosch, M.T.J. van den, Moore, S.F., Mauroux, A., Hodgson, L., Verkman, A.S., Hers, I., Poole, A.W., 2018. Aquaporin-1 regulates platelet procoagulant membrane dynamics and in vivo thrombosis. JCI Insight 3. https://doi.org/10.1172/jci.insight.99062

Agbani, E.O., Zhao, X., Williams, C.M., Aungraheeta, R., Hers, I., Swenson, E.R., Poole, A.W., 2020. Carbonic Anhydrase Inhibitors suppress platelet procoagulant responses and in vivo thrombosis. Platelets 31, 853–859. https://doi.org/10.1080/09537104.2019.1709632

Albrecht, C., McVey, J.H., Elliott, J.I., Sardini, A., Kasza, I., Mumford, A.D., Naoumova, R.P., Tuddenham, E.G.D., Szabo, K., Higgins, C.F., 2005. A novel missense mutation in ABCA1 results in altered protein trafficking and reduced phosphatidylserine translocation in a patient with Scott syndrome. Blood 106, 542–549. https://doi.org/10.1182/blood-2004-05-2056

Alvadia, C., Lim, N.K., Clerico Mosina, V., Oostergetel, G.T., Dutzler, R., Paulino, C., 2019. Cryo-EM structures and functional characterization of the murine lipid scramblase TMEM16F. eLife 8. https://doi.org/10.7554/eLife.44365

Baig, A.A., Haining, E.J., Geuss, E., Beck, S., Swieringa, F., Wanitchakool, P., Schuhmann, M.K., Stegner, D., Kunzelmann, K., Kleinschnitz, C., Heemskerk, J.W.M., Braun, A., Nieswandt, B., 2016. TMEM16F-Mediated Platelet Membrane Phospholipid Scrambling Is Critical for Hemostasis and Thrombosis but not Thromboinflammation in Mice—Brief Report. Arterioscler. Thromb. Vasc. Biol. 36, 2152–2157. https://doi.org/10.1161/ATVBAHA.116.307727

Baines, C.P., Kaiser, R.A., Purcell, N.H., Blair, N.S., Osinska, H., Hambleton, M.A., Brunskill, E.W., Sayen, M.R., Gottlieb, R.A., Dorn, G.W., Robbins, J., Molkentin, J.D., 2005. Loss of cyclophilin D reveals a critical role for mitochondrial permeability transition in cell death. Nature 434, 658–662. https://doi.org/10.1038/nature03434

Batool, M., Ahmad, B., Choi, S., 2019. A Structure-Based Drug Discovery Paradigm. Int. J. Mol. Sci. 20. https://doi.org/10.3390/ijms20112783

Berghold, V.M., Gauster, M., Hemmings, D.G., Moser, G., Kremshofer, J., Siwetz, M., Sundl, M., Huppertz, B., 2015. Phospholipid scramblase 1 (PLSCR1) in villous trophoblast of the human placenta. Histochem. Cell Biol. 143, 381–396. https://doi.org/10.1007/s00418-014-1294-y

Bernardo, A., Ball, C., Nolasco, L., Moake, J.F., Dong, J., 2004. Effects of inflammatory cytokines on the release and cleavage of the endothelial cell–derived ultralarge von Willebrand factor multimers under flow. Blood 104, 100–106. https://doi.org/10.1182/blood-2004-01-0107

Bethel, N.P., Grabe, M., 2016. Atomistic insight into lipid translocation by a TMEM16 scramblase. Proc. Natl. Acad. Sci. 113, 14049–14054. https://doi.org/10.1073/pnas.1607574113

Bettache, N., Gaffet, P., Allegre, N., Maurin, L., Toti, F., Freyssinet, J.M., Bienvenüe, A., 1998. Impaired redistribution of aminophospholipids with distinctive cell shape change during Ca^{2+}-induced activation of platelets from a patient with Scott syndrome. Br. J. Haematol. 101, 50–58. https://doi.org/10.1046/j.1365-2141.1998.00658.x

Bevers, E.M., Wiedmer, T., Comfurius, P., Shattil, S.J., Weiss, H.J., Zwaal, R.F., Sims, P.J., 1992. Defective $Ca(^{2+})$-induced microvesiculation and deficient expression of procoagulant activity in erythrocytes from a patient with a bleeding disorder: a study of the red blood cells of Scott syndrome. Blood 79, 380–388.

Braun, A., Vogtle, T., Varga-Szabo, D., Nieswandt, B., 2011. STIM and Orai in hemostasis and thrombosis. Front. Biosci. Landmark Ed. 16, 2144–2160. https://doi.org/10.2741/3844

Brooks, M.B., Catalfamo, J.L., Brown, H.A., Ivanova, P., Lovaglio, J., 2002. A hereditary bleeding disorder of dogs caused by a lack of platelet procoagulant activity. Blood 99, 2434–2441. https://doi.org/10.1182/blood.V99.7.2434

Broos, K., Feys, H.B., De Meyer, S.F., Vanhoorelbeke, K., Deckmyn, H., 2011. Platelets at work in primary hemostasis. Blood Rev. 25, 155–167. https://doi.org/10.1016/j.blre.2011.03.002

Brunner, J.D., Lim, N.K., Schenck, S., Duerst, A., Dutzler, R., 2014. X-ray structure of a calcium-activated TMEM16 lipid scramblase. Nature 516, 207–212. https://doi.org/10.1038/nature13984

Bucki, R., Pastore, J.J., Giraud, F., Sulpice, J.-C., Janmey, P.A., 2003. Flavonoid inhibition of platelet procoagulant activity and phosphoinositide synthesis. J. Thromb. Haemost. JTH 1, 1820–1828. https://doi.org/10.1046/j.1538-7836.2003.00294.x

Bushell, S.R., Pike, A.C.W., Falzone, M.E., Rorsman, N.J.G., Ta, C.M., Corey, R.A., Newport, T.D., Christianson, J.C., Scofano, L.F., Shintre, C.A., Tessitore, A., Chu, A., Wang, Q., Shrestha, L., Mukhopadhyay, S.M.M., Love, J.D., Burgess-Brown, N.A., Sitsapesan, R., Stansfeld, P.J., Huiskonen, J.T., Tammaro, P., Accardi, A., Carpenter, E.P., 2019. The structural basis of lipid scrambling and inactivation in the endoplasmic reticulum scramblase TMEM16K. Nat. Commun. 10, 1–16. https://doi.org/10.1038/s41467-019-11753-1

Byrnes, J.R., Wolberg, A.S., 2017. Red blood cells in thrombosis. Blood 130, 1795–1799. https://doi.org/10.1182/blood-2017-03-745349

Cabrita, I., Benedetto, R., Schreiber, R., Kunzelmann, K., 2019. Niclosamide repurposed for the treatment of inflammatory airway disease. JCI Insight 4. https://doi.org/10.1172/jci.insight.128414

Caputo, A., Caci, E., Ferrera, L., Pedemonte, N., Barsanti, C., Sondo, E., Pfeffer, U., Ravazzolo, R., Zegarra-Moran, O., Galietta, L.J.V., 2008. TMEM16A, a membrane protein associated with calcium-dependent chloride channel activity. Science 322, 590–594. https://doi.org/10.1126/science.1163518

Chapin, J.C., Hajjar, K.A., 2015. Fibrinolysis and the control of blood coagulation. Blood Rev. 29, 17–24. https://doi.org/10.1016/j.blre.2014.09.003

Cheeseright, T., Mackey, M., Rose, S., Vinter, A., 2006. Molecular Field Extrema as Descriptors of Biological Activity: Definition and Validation. J. Chem. Inf. Model. 46, 665–676. https://doi.org/10.1021/ci050357s

Chen, Y., Yuan, Y., Li, W., 2018. Sorting machineries: how platelet-dense granules differ from α-granules. Biosci. Rep. 38. https://doi.org/10.1042/BSR20180458

Choo, H.-J., Kholmukhamedov, A., Zhou, C., Jobe, S., 2017. Inner mitochondrial membrane disruption links apoptotic and agonist-initiated phosphatidylserine externalization in platelets. Arterioscler. Thromb. Vasc. Biol. 37, 1503–1512. https://doi.org/10.1161/ATVBAHA.117.309473

Choo, H.-J., Saafir, T.B., Mkumba, L., Wagner, M.B., Jobe, S.M., 2012. Mitochondrial calcium and reactive oxygen species regulate agonist-initiated platelet phosphatidylserine exposure. Arterioscler. Thromb. Vasc. Biol. 32, 2946–2955. https://doi.org/10.1161/ATVBAHA.112.300433

Chua, B.A., Ngo, J.A., Situ, K., Morizono, K., 2019. Roles of phosphatidylserine exposed on the viral envelope and cell membrane in HIV-1 replication. Cell Commun. Signal. CCS 17, 132. https://doi.org/10.1186/s12964-019-0452-1

Curtis, M.J., Alexander, S., Cirino, G., Docherty, J.R., George, C.H., Giembycz, M.A., Hoyer, D., Insel, P.A., Izzo, A.A., Ji, Y., MacEwan, D.J., Sobey, C.G., Stanford, S.C., Teixeira, M.M., Wonnacott, S., Ahluwalia, A., 2018. Experimental design and analysis and their reporting II: updated and simplified guidance for authors and peer reviewers. Br. J. Pharmacol. 175, 987–993. https://doi.org/10.1111/bph.14153

Dadashpour, S., Tuylu Kucukkilinc, T., Unsal Tan, O., Ozadali, K., Irannejad, H., Emami, S., 2015. Design, synthesis and in vitro study of 5,6-diaryl-1,2,4-triazine-3-ylthioacetate derivatives as COX-2 and β-amyloid aggregation inhibitors. Arch. Pharm. (Weinheim) 348, 179–187. https://doi.org/10.1002/ardp.201400400

Daina, A., Michielin, O., Zoete, V., 2017. SwissADME: a free web tool to evaluate pharmacokinetics, drug-likeness and medicinal chemistry friendliness of small molecules. Sci. Rep. 7, 42717. https://doi.org/10.1038/srep42717

Daina, A., Zoete, V., 2016. A BOILED-Egg To Predict Gastrointestinal Absorption and Brain Penetration of Small Molecules. ChemMedChem 11, 1117–1121. https://doi.org/10.1002/cmdc.201600182

Dale, G.L., 2005. Coated-platelets: an emerging component of the procoagulant response. J. Thromb. Haemost. JTH 3, 2185–2192. https://doi.org/10.1111/j.1538-7836.2005.01274.x

Daleke, D.L., 2003. Regulation of transbilayer plasma membrane phospholipid asymmetry. J. Lipid Res. 44, 233–242. https://doi.org/10.1194/jlr.R200019-JLR200

Dang, S., Feng, S., Tien, J., Peters, C.J., Bulkley, D., Lolicato, M., Zhao, J., Zuberbühler, K., Ye, W., Qi, L., Chen, T., Craik, C.S., Jan, Y.N., Minor, D.L., Cheng, Y., Jan, L.Y., 2017. Cryo-EM structures of the TMEM16A calcium-activated chloride channel. Nature 552, 426–429. https://doi.org/10.1038/nature25024

de Witt, S.M., Swieringa, F., Cavill, R., Lamers, M.M.E., van Kruchten, R., Mastenbroek, T., Baaten, C., Coort, S., Pugh, N., Schulz, A., Scharrer, I., Jurk, K., Zieger, B., Clemetson, K.J.,

Farndale, R.W., Heemskerk, J.W.M., Cosemans, J.M.E.M., 2014. Identification of platelet function defects by multi-parameter assessment of thrombus formation. Nat. Commun. 5, 4257. https://doi.org/10.1038/ncomms5257

Deana, R., Turetta, L., Donella-Deana, A., Donà, M., Brunati, A.M., De Michiel, L., Garbisa, S., 2003. Green tea epigallocatechin-3-gallate inhibits platelet signalling pathways triggered by both proteolytic and non-proteolytic agonists. Thromb. Haemost. 89, 866–874.

Dekkers, D.W.C., Comfurius, P., Vuist, W.M.J., Billheimer, J.T., Dicker, I., Weiss, H.J., Zwaal, R.F.A., Bevers, E.M., 1998. Impaired Ca^{2+}-Induced Tyrosine Phosphorylation and Defective Lipid Scrambling in Erythrocytes From a Patient With Scott Syndrome: A Study Using an Inhibitor for Scramblase That Mimics the Defect in Scott Syndrome. Blood 91, 2133–2138.

Dias, E., Gomes, M., Domingues, C., Ramalheira, E., Morais, S., Pereira, M. de L., 2013. Subacute effects of the thiodicarb pesticide on target organs of male Wistar rats: biochemical, histological, and flow cytometry studies. J. Toxicol. Environ. Health A 76, 533–539. https://doi.org/10.1080/15287394.2013.785216

Durrant, T.N., van den Bosch, M.T., Hers, I., 2017. Integrin αIIbβ3 outside-in signaling. Blood 130, 1607–1619. https://doi.org/10.1182/blood-2017-03-773614

Egan, W.J., Merz, K.M., Baldwin, J.J., 2000. Prediction of drug absorption using multivariate statistics. J. Med. Chem. 43, 3867–3877. https://doi.org/10.1021/jm000292e

Emsley, J., Knight, C.G., Farndale, R.W., Barnes, M.J., Liddington, R.C., 2000. Structural Basis of Collagen Recognition by Integrin α2β1. Cell 101, 47–56. https://doi.org/10.1016/S0092-8674(00)80622-4

Falzone, M.E., Rheinberger, J., Lee, B.-C., Peyear, T., Sasset, L., Raczkowski, A.M., Eng, E.T., Di Lorenzo, A., Andersen, O.S., Nimigean, C.M., Accardi, A., 2019. Structural basis of Ca^{2+}-dependent activation and lipid transport by a TMEM16 scramblase. eLife 8. https://doi.org/10.7554/eLife.43229

Farndale, R.W., Sixma, J.J., Barnes, M.J., de Groot, P.G., 2004. The role of collagen in thrombosis and hemostasis. J. Thromb. Haemost. JTH 2, 561–573. https://doi.org/10.1111/j.1538-7836.2004.00665.x

Feng, S., Dang, S., Han, T.W., Ye, W., Jin, P., Cheng, T., Li, J., Jan, Y.N., Jan, L.Y., Cheng, Y., 2019. Cryo-EM Studies of TMEM16F Calcium-Activated Ion Channel Suggest Features Important for Lipid Scrambling. Cell Rep. 28, 567-579.e4. https://doi.org/10.1016/j.celrep.2019.06.023

Ferreira, L.G., dos Santos, R.N., Oliva, G., Andricopulo, A.D., 2015. Molecular Docking and Structure-Based Drug Design Strategies. Molecules 20, 13384–13421. https://doi.org/10.3390/molecules200713384

Feske, S., 2011. Immunodeficiency due to defects in store-operated calcium entry. Ann. N. Y. Acad. Sci. 1238, 74–90. https://doi.org/10.1111/j.1749-6632.2011.06240.x

Flores-Nascimento, M.C., Orsi, F.L.A., Yokoyama, A.P., Pereira, F.G., Lorand-Metze, I., De Paula, E.V., Castro, V., Annichino-Bizzacchi, J.M., 2012. Diagnosis of Scott syndrome in patient with bleeding disorder of unknown cause. Blood Coagul. Fibrinolysis Int. J. Haemost. Thromb. 23, 75–77. https://doi.org/10.1097/MBC.0b013e32834d0c81

Fujii, T., Sakata, A., Nishimura, S., Eto, K., Nagata, S., 2015. TMEM16F is required for phosphatidylserine exposure and microparticle release in activated mouse platelets. Proc. Natl. Acad. Sci. U. S. A. 112, 12800–12805. https://doi.org/10.1073/pnas.1516594112

Gasser, J.-P., Hehl, M., Millward, T.A., 2009. A homogeneous time-resolved fluorescence resonance energy transfer assay for phosphatidylserine exposure on apoptotic cells. Anal. Biochem. 384, 49–55. https://doi.org/10.1016/j.ab.2008.09.016

Ghose, A.K., Viswanadhan, V.N., Wendoloski, J.J., 1999. A knowledge-based approach in designing combinatorial or medicinal chemistry libraries for drug discovery. 1. A qualitative and quantitative characterization of known drug databases. J. Comb. Chem. 1, 55–68. https://doi.org/10.1021/cc9800071

Gieseler, F., Ungefroren, H., Settmacher, U., Hollenberg, M.D., Kaufmann, R., 2013. Proteinase-activated receptors (PARs) – focus on receptor-receptor-interactions and their physiological and pathophysiological impact. Cell Commun. Signal. 11, 86. https://doi.org/10.1186/1478-811X-11-86

Gurbel, P.A., Kuliopulos, A., Tantry, U.S., 2015. G-protein-coupled receptors signaling pathways in new antiplatelet drug development. Arterioscler. Thromb. Vasc. Biol. 35, 500–512. https://doi.org/10.1161/ATVBAHA.114.303412

Gyobu, S., Ishihara, K., Suzuki, J., Segawa, K., Nagata, S., 2017. Characterization of the scrambling domain of the TMEM16 family. Proc. Natl. Acad. Sci. 114, 6274–6279. https://doi.org/10.1073/pnas.1703391114

Halliez, M., Fouassier, M., Robillard, N., Ternisien, C., Sigaud, M., Trossaert, M., Bene, M.-C., 2015. Detection of phosphatidyl serine on activated platelets' surface by flow cytometry in whole blood: a simpler test for the diagnosis of Scott syndrome. Br. J. Haematol. 171, 290–292. https://doi.org/10.1111/bjh.13391

Harper, M.T., Londoño, J.E.C., Quick, K., Londoño, J.C., Flockerzi, V., Philipp, S.E., Birnbaumer, L., Freichel, M., Poole, A.W., 2013. Transient receptor potential channels function as a coincidence signal detector mediating phosphatidylserine exposure. Sci. Signal. 6, ra50. https://doi.org/10.1126/scisignal.2003701

Harper, M.T., Poole, A.W., 2011. PKC inhibition markedly enhances Ca^{2+} signaling and phosphatidylserine exposure downstream of protease-activated receptor-1 but not protease-activated receptor-4 in human platelets. J. Thromb. Haemost. JTH 9, 1599–1607. https://doi.org/10.1111/j.1538-7836.2011.04393.x

Harper, M.T., van den Bosch, M.T., Hers, I., Poole, A.W., 2015. Platelet dense granule secretion defects may obscure α-granule secretion mechanisms: evidence from Munc13-4-deficient platelets. Blood 125, 3034–3036. https://doi.org/10.1182/blood-2014-12-618439

Heemskerk, J.W., Vuist, W.M., Feijge, M.A., Reutelingsperger, C.P., Lindhout, T., 1997. Collagen but not fibrinogen surfaces induce bleb formation, exposure of phosphatidylserine, and procoagulant activity of adherent platelets: evidence for regulation by protein tyrosine kinase-dependent Ca^{2+} responses. Blood 90, 2615–2625.

Heemskerk, J.W.M., Mattheij, N.J.A., Cosemans, J.M.E.M., 2013. Platelet-based coagulation: different populations, different functions. J. Thromb. Haemost. JTH 11, 2–16. https://doi.org/10.1111/jth.12045

Hoizey, G., Canas, F., Binet, L., Kaltenbach, M.L., Jeunehomme, G., Bernard, M.-H., Lamiable, D., 2008. Thiodicarb and methomyl tissue distribution in a fatal multiple

compounds poisoning. J. Forensic Sci. 53, 499–502. https://doi.org/10.1111/j.1556-4029.2008.00676.x

Hu, Y., Kim, J.H., He, K., Wan, Q., Kim, J., Flach, M., Kirchhausen, T., Vortkamp, A., Winau, F., 2016. Scramblase TMEM16F terminates T cell receptor signaling to restrict T cell exhaustion. J. Exp. Med. 213, 2759–2772. https://doi.org/10.1084/jem.20160612

Iida, Y., Doi, T., Matsushima-Nishiwaki, R., Tokuda, H., Ogura, S., Kozawa, O., Iida, H., 2014. (-)-Epigallocatechin gallate selectively inhibits adenosine diphosphate-stimulated human platelet activation: suppression of heat shock protein 27 phosphorylation via p38 mitogen-activated protein kinase. Mol. Med. Rep. 10, 1383–1388. https://doi.org/10.3892/mmr.2014.2389

Jamasbi, J., Ayabe, K., Goto, S., Nieswandt, B., Peter, K., Siess, W., 2017. Platelet receptors as therapeutic targets: Past, present and future. Thromb. Haemost. 117, 1249–1257. https://doi.org/10.1160/TH16-12-0911

Janel, N., Leroy, C., Laude, I., Toti, F., Fressinaud, E., Meyer, D., Freyssinet, J.M., Kerbiriou-Nabias, D., 1999. Assessment of the expression of candidate human plasma membrane phospholipid scramblase in Scott syndrome cells. Thromb. Haemost. 81, 322–323.

Jiang, T., Yu, K., Hartzell, H.C., Tajkhorshid, E., 2017. Lipids and ions traverse the membrane by the same physical pathway in the nhTMEM16 scramblase. eLife 6, e28671. https://doi.org/10.7554/eLife.28671

Jin, Y.-R., Im, J.-H., Park, E.-S., Cho, M.-R., Han, X.-H., Lee, J.-J., Lim, Y., Kim, T.-J., Yun, Y.-P., 2008. Antiplatelet activity of epigallocatechin gallate is mediated by the inhibition of PLCgamma2 phosphorylation, elevation of PGD2 production, and maintaining calcium-ATPase activity. J. Cardiovasc. Pharmacol. 51, 45–54. https://doi.org/10.1097/FJC.0b013e31815ab4b6

Jobe, S.M., Wilson, K.M., Leo, L., Raimondi, A., Molkentin, J.D., Lentz, S.R., Di Paola, J., 2008. Critical role for the mitochondrial permeability transition pore and cyclophilin D in platelet activation and thrombosis. Blood 111, 1257–1265. https://doi.org/10.1182/blood-2007-05-092684

Jones, G., Willett, P., Glen, R.C., Leach, A.R., Taylor, R., 1997. Development and validation of a genetic algorithm for flexible docking11Edited by F. E. Cohen. J. Mol. Biol. 267, 727–748. https://doi.org/10.1006/jmbi.1996.0897

Joo, H.J., Park, J.-Y., Hong, S.J., Kim, K.-A., Lee, S.H., Cho, J.-Y., Park, J.H., Yu, C.W., Lim, D.-S., 2018. Anti-platelet effects of epigallocatechin-3-gallate in addition to the concomitant aspirin, clopidogrel or ticagrelor treatment. Korean J. Intern. Med. 33, 522–531. https://doi.org/10.3904/kjim.2016.228

Kajitani, K., Fujihashi, M., Kobayashi, Y., Shimizu, S., Tsujimoto, Y., Miki, K., 2008. Crystal structure of human cyclophilin D in complex with its inhibitor, cyclosporin A at 0.96-Å resolution. Proteins Struct. Funct. Bioinforma. 70, 1635–1639. https://doi.org/10.1002/prot.21855

Kalienkova, V., Clerico Mosina, V., Bryner, L., Oostergetel, G.T., Dutzler, R., Paulino, C., 2019. Stepwise activation mechanism of the scramblase nhTMEM16 revealed by cryo-EM. eLife 8, e44364. https://doi.org/10.7554/eLife.44364

Kang, W.S., Lim, I.H., Yuk, D.Y., Chung, K.H., Park, J.B., Yoo, H.S., Yun, Y.P., 1999. Antithrombotic activities of green tea catechins and (-)-epigallocatechin gallate. Thromb. Res. 96, 229–237. https://doi.org/10.1016/s0049-3848(99)00104-8

Katoh, Masuko, Katoh, Masaru, 2004. Identification and characterization of TMEM16E and TMEM16F genes in silico. Int. J. Oncol. 24, 1345–1349.

Keuren, J.F.W., Wielders, S.J.H., Ulrichts, H., Hackeng, T., Heemskerk, J.W.M., Deckmyn, H., Bevers, E.M., Lindhout, T., 2005. Synergistic effect of thrombin on collagen-induced platelet procoagulant activity is mediated through protease-activated receptor-1. Arterioscler. Thromb. Vasc. Biol. 25, 1499–1505. https://doi.org/10.1161/01.ATV.0000167526.31611.f6

Khelashvili, G., Falzone, M.E., Cheng, X., Lee, B.-C., Accardi, A., Weinstein, H., 2019. Dynamic modulation of the lipid translocation groove generates a conductive ion channel in Ca^{2+} -bound nhTMEM16. Nat. Commun. 10, 1–15. https://doi.org/10.1038/s41467-019-12865-4

Kmit, A., van Kruchten, R., Ousingsawat, J., Mattheij, N.J.A., Senden-Gijsbers, B., Heemskerk, J.W.M., Schreiber, R., Bevers, E.M., Kunzelmann, K., 2013. Calcium-activated and apoptotic phospholipid scrambling induced by Ano6 can occur independently of Ano6 ion currents. Cell Death Dis. 4, e611–e611. https://doi.org/10.1038/cddis.2013.135

Kojima, H., Newton-Nash, D., Weiss, H.J., Zhao, J., Sims, P.J., Wiedmer, T., 1994. Production and characterization of transformed B-lymphocytes expressing the membrane defect of Scott syndrome. J. Clin. Invest. 94, 2237–2244.

Le, T., Jia, Z., Le, S.C., Zhang, Y., Chen, J., Yang, H., 2019. An inner activation gate controls TMEM16F phospholipid scrambling. Nat. Commun. 10, 1846. https://doi.org/10.1038/s41467-019-09778-7

Lee, D.-H., Kim, Y.-J., Kim, H.-H., Cho, H.-J., Ryu, J.-H., Rhee, M.H., Park, H.-J., 2013. Inhibitory effects of epigallocatechin-3-gallate on microsomal cyclooxygenase-1 activity in platelets. Biomol. Ther. 21, 54–59. https://doi.org/10.4062/biomolther.2012.075

Libby, P., 2013. Mechanisms of acute coronary syndromes and their implications for therapy. N. Engl. J. Med. 368, 2004–2013. https://doi.org/10.1056/NEJMra1216063

Lill, G., Voit, S., Schrör, K., Weber, A.-A., 2003. Complex effects of different green tea catechins on human platelets. FEBS Lett. 546, 265–270. https://doi.org/10.1016/S0014-5793(03)00599-4

Lipinski, C.A., Lombardo, F., Dominy, B.W., Feeney, P.J., 2001. Experimental and computational approaches to estimate solubility and permeability in drug discovery and development settings. Adv. Drug Deliv. Rev. 46, 3–26. https://doi.org/10.1016/s0169-409x(00)00129-0

Lippi, G., Franchini, M., Targher, G., 2011. Arterial thrombus formation in cardiovascular disease. Nat. Rev. Cardiol. 8, 502–512. https://doi.org/10.1038/nrcardio.2011.91

Liu, F., Gamez, G., Myers, D.R., Clemmons, W., Lam, W.A., Jobe, S.M., 2013. Mitochondrially mediated integrin αIIbβ3 protein inactivation limits thrombus growth. J. Biol. Chem. 288, 30672–30681. https://doi.org/10.1074/jbc.M113.472688

Lukasik, M., Rozalski, M., Luzak, B., Michalak, M., Ambrosius, W., Watala, C., Kozubski, W., 2013. Enhanced platelet-derived microparticle formation is associated with carotid

atherosclerosis in convalescent stroke patients. Platelets 24, 63–70. https://doi.org/10.3109/09537104.2011.654292

Mallat Ziad, Benamer Hakim, Hugel Bénédicte, Benessiano Joëlle, Steg P. Gabriel, Freyssinet Jean-Marie, Tedgui Alain, 2000. Elevated Levels of Shed Membrane Microparticles With Procoagulant Potential in the Peripheral Circulating Blood of Patients With Acute Coronary Syndromes. Circulation 101, 841–843. https://doi.org/10.1161/01.CIR.101.8.841

Malvezzi, M., Andra, K.K., Pandey, K., Lee, B.-C., Falzone, M.E., Brown, A., Iqbal, R., Menon, A.K., Accardi, A., 2018. Out-of-the-groove transport of lipids by TMEM16 and GPCR scramblases. Proc. Natl. Acad. Sci. U. S. A. 115, E7033–E7042. https://doi.org/10.1073/pnas.1806721115

Malvezzi, M., Chalat, M., Janjusevic, R., Picollo, A., Terashima, H., Menon, A.K., Accardi, A., 2013. Ca^{2+}-dependent phospholipid scrambling by a reconstituted TMEM16 ion channel. Nat. Commun. 4, 2367. https://doi.org/10.1038/ncomms3367

Marcus, A.J., Broekman, M.J., Drosopoulos, J.H., Islam, N., Alyonycheva, T.N., Safier, L.B., Hajjar, K.A., Posnett, D.N., Schoenborn, M.A., Schooley, K.A., Gayle, R.B., Maliszewski, C.R., 1997. The endothelial cell ecto-ADPase responsible for inhibition of platelet function is CD39. J. Clin. Invest. 99, 1351–1360. https://doi.org/10.1172/JCI119294

Matsuno, K., Masuda, Y., Uehara, Y., Sato, H., Muroya, A., Takahashi, O., Yokotagawa, T., Furuya, T., Okawara, T., Otsuka, M., Ogo, N., Ashizawa, T., Oshita, C., Tai, S., Ishii, H., Akiyama, Y., Asai, A., 2010. Identification of a New Series of STAT3 Inhibitors by Virtual Screening. ACS Med. Chem. Lett. 1, 371–375. https://doi.org/10.1021/ml1000273

Mattheij, N.J.A., Braun, A., van Kruchten, R., Castoldi, E., Pircher, J., Baaten, C.C.F.M.J., Wülling, M., Kuijpers, M.J.E., Köhler, R., Poole, A.W., Schreiber, R., Vortkamp, A., Collins, P.W., Nieswandt, B., Kunzelmann, K., Cosemans, J.M.E.M., Heemskerk, J.W.M., 2016. Survival protein anoctamin-6 controls multiple platelet responses including phospholipid scrambling, swelling, and protein cleavage. FASEB J. Off. Publ. Fed. Am. Soc. Exp. Biol. 30, 727–737. https://doi.org/10.1096/fj.15-280446

McFadyen, J.D., Schaff, M., Peter, K., 2018. Current and future antiplatelet therapies: emphasis on preserving haemostasis. Nat. Rev. Cardiol. 15, 181–191. https://doi.org/10.1038/nrcardio.2017.206

McGann, M., 2011. FRED Pose Prediction and Virtual Screening Accuracy. J. Chem. Inf. Model. 51, 578–596. https://doi.org/10.1021/ci100436p

Miletich, J.P., Kane, W.H., Hofmann, S.L., Stanford, N., Majerus, P.W., 1979. Deficiency of factor Xa-factor Va binding sites on the platelets of a patient with a bleeding disorder. Blood 54, 1015–1022.

Millington-Burgess, S.L., Harper, M.T., 2019. Gene of the issue: ANO6 and Scott Syndrome. Platelets 1–4. https://doi.org/10.1080/09537104.2019.1693039

Millington-Burgess, S.L., Bonna, A.M., Rahman, T., Harper, M.T., 2020. R5421 is not a selective inhibitor of platelet phospholipid scramblase activity. Br. J. Pharmacol. https://doi.org/10.1111/bph.15152

Montague, S.J., Delierneux, C., Lecut, C., Layios, N., Dinsdale, R.J., Lee, C.S.-M., Poulter, N.S., Andrews, R.K., Hampson, P., Wearn, C.M., Maes, N., Bishop, J., Bamford, A., Gardiner, C., Lee, W.M., Iqbal, T., Moiemen, N., Watson, S.P., Oury, C., Harrison, P.,

Gardiner, E.E., 2018. Soluble GPVI is elevated in injured patients: shedding is mediated by fibrin activation of GPVI. Blood Adv. 2, 240–251. https://doi.org/10.1182/bloodadvances.2017011171

Moroi, M., Jung, S.M., 2004. Platelet glycoprotein VI: its structure and function. Thromb. Res. 114, 221–233. https://doi.org/10.1016/j.thromres.2004.06.046

Morton, L.F., Hargreaves, P.G., Farndale, R.W., Young, R.D., Barnes, M.J., 1995. Integrin alpha 2 beta 1-independent activation of platelets by simple collagen-like peptides: collagen tertiary (triple-helical) and quaternary (polymeric) structures are sufficient alone for alpha 2 beta 1-independent platelet reactivity. Biochem. J. 306 (Pt 2), 337–344. https://doi.org/10.1042/bj3060337

Muegge, I., Heald, S.L., Brittelli, D., 2001. Simple selection criteria for drug-like chemical matter. J. Med. Chem. 44, 1841–1846. https://doi.org/10.1021/jm015507e

Munnix, I.C.A., Harmsma, M., Giddings, J.C., Collins, P.W., Feijge, M.A.H., Comfurius, P., Heemskerk, J.W.M., Bevers, E.M., 2003. Store-mediated calcium entry in the regulation of phosphatidylserine exposure in blood cells from Scott patients. Thromb. Haemost. 89, 687–695.

Muszbek, L., Bereczky, Z., Bagoly, Z., Komáromi, I., Katona, É., 2011. Factor XIII: a coagulation factor with multiple plasmatic and cellular functions. Physiol. Rev. 91, 931–972. https://doi.org/10.1152/physrev.00016.2010

Nadaud, S., Poirier, O., Girerd, B., Blanc, C., Montani, D., Eyries, M., Imbert-Bismut, F., Pacheco, A., Vigne, J., Tregouet, D.-A., Humbert, M., Soubrier, F., 2013. Small platelet microparticle levels are increased in pulmonary arterial hypertension. Eur. J. Clin. Invest. 43, 64–71. https://doi.org/10.1111/eci.12018

Namkung, W., Thiagarajah, J.R., Phuan, P.-W., Verkman, A.S., 2010. Inhibition of Ca^{2+}-activated Cl− channels by gallotannins as a possible molecular basis for health benefits of red wine and green tea. FASEB J. 24, 4178–4186. https://doi.org/10.1096/fj.10-160648

Nanetti, L., Sarto, E., Castaldo, A., Magri, S., Mongelli, A., Rossi Sebastiano, D., Canafoglia, L., Grisoli, M., Malaguti, C., Rivieri, F., D'Amico, M.C., Di Bella, D., Franceschetti, S., Mariotti, C., Taroni, F., 2019. ANO10 mutational screening in recessive ataxia: genetic findings and refinement of the clinical phenotype. J. Neurol. 266, 378–385. https://doi.org/10.1007/s00415-018-9141-z

Navarro-Núñez, L., Langan, S.A., Nash, G.B., Watson, S.P., 2013. The physiological and pathophysiological roles of platelet CLEC-2. Thromb. Haemost. 109, 991–998. https://doi.org/10.1160/TH13-01-0060

Nechipurenko, D.Y., Receveur, N., Yakimenko, A.O., Shepelyuk, T.O., Yakusheva, A.A., Kerimov, R.R., Obydennyy, S.I., Eckly, A., Léon, C., Gachet, C., Grishchuk, E.L., Ataullakhanov, F.I., Mangin, P.H., Panteleev, M.A., 2019. Clot Contraction Drives the Translocation of Procoagulant Platelets to Thrombus Surface. Arterioscler. Thromb. Vasc. Biol. 39, 37–47. https://doi.org/10.1161/ATVBAHA.118.311390

Nieman, M.T., 2016. Protease-activated receptors in hemostasis. Blood 128, 169–177. https://doi.org/10.1182/blood-2015-11-636472

Nishimura, T., Yamamoto, T., Komuro, Y., Hara, Y., 1995. Antiplatelet functions of a stable prostacyclin analog, SM-10906 are exerted by its inhibitory effect on inositol 1,4,5-

trisphosphate production and cytosolic Ca++ increase in rat platelets stimulated by thrombin. Thromb. Res. 79, 307–317. https://doi.org/10.1016/0049-3848(95)00117-a

Nofer, J.-R., Herminghaus, G., Brodde, M., Morgenstern, E., Rust, S., Engel, T., Seedorf, U., Assmann, G., Bluethmann, H., Kehrel, B.E., 2004. Impaired Platelet Activation in Familial High Density Lipoprotein Deficiency (Tangier Disease). J. Biol. Chem. 279, 34032–34037. https://doi.org/10.1074/jbc.M405174200

O'Boyle, N.M., Banck, M., James, C.A., Morley, C., Vandermeersch, T., Hutchison, G.R., 2011. Open Babel: An open chemical toolbox. J. Cheminformatics 3, 33. https://doi.org/10.1186/1758-2946-3-33

Obydennyy, S.I., Sveshnikova, A.N., Ataullakhanov, F.I., Panteleev, M.A., 2016. Dynamics of calcium spiking, mitochondrial collapse and phosphatidylserine exposure in platelet subpopulations during activation. J. Thromb. Haemost. JTH 14, 1867–1881. https://doi.org/10.1111/jth.13395

O'Donnell, V.B., Murphy, R.C., Watson, S.P., 2014. Platelet lipidomics: a modern day perspective on lipid discovery and characterization in platelets. Circ. Res. 114, 1185–1203. https://doi.org/10.1161/CIRCRESAHA.114.301597

Ok, W.-J., Cho, H.-J., Kim, H.-H., Lee, D.-H., Kang, H.-Y., Kwon, H.-W., Rhee, M.H., Kim, M., Park, H.-J., 2012. Epigallocatechin-3-gallate has an anti-platelet effect in a cyclic AMP-dependent manner. J. Atheroscler. Thromb. 19, 337–348. https://doi.org/10.5551/jat.10363

Ousingsawat, J., Wanitchakool, P., Schreiber, R., Wuelling, M., Vortkamp, A., Kunzelmann, K., 2015. Anoctamin-6 controls bone mineralization by activating the calcium transporter NCX1. J. Biol. Chem. 290, 6270–6280. https://doi.org/10.1074/jbc.M114.602979

Parry, D.H., Giddings, J.C., Bloom, A.L., 1980. Familial Haemostatic Defect Associated with Reduced Prothrombin Consumption. Br. J. Haematol. 44, 323–334. https://doi.org/10.1111/j.1365-2141.1980.tb01215.x

Pasalic, L., Wing-Lun, E., Lau, J.K., Campbell, H., Pennings, G.J., Lau, E., Connor, D., Liang, H.P., Muller, D., Kritharides, L., Hogg, P.J., Chen, V.M., 2018. Novel assay demonstrates that coronary artery disease patients have heightened procoagulant platelet response. J. Thromb. Haemost. JTH 16, 1198–1210. https://doi.org/10.1111/jth.14008

Patrono, C., Morais, J., Baigent, C., Collet, J.-P., Fitzgerald, D., Halvorsen, S., Rocca, B., Siegbahn, A., Storey, R.F., Vilahur, G., 2017. Antiplatelet Agents for the Treatment and Prevention of Coronary Atherothrombosis. J. Am. Coll. Cardiol. 70, 1760–1776. https://doi.org/10.1016/j.jacc.2017.08.037

Paulino, C., Kalienkova, V., Lam, A.K.M., Neldner, Y., Dutzler, R., 2017a. Activation mechanism of the calcium-activated chloride channel TMEM16A revealed by cryo-EM. Nature 552, 421–425. https://doi.org/10.1038/nature24652

Paulino, C., Neldner, Y., Lam, A.K., Kalienkova, V., Brunner, J.D., Schenck, S., Dutzler, R., 2017b. Structural basis for anion conduction in the calcium-activated chloride channel TMEM16A. eLife 6. https://doi.org/10.7554/eLife.26232

Payrastre, B., Missy, K., Trumel, C., Bodin, S., Plantavid, M., Chap, H., 2000. The integrin αIIb/β3 in human platelet signal transduction. Biochem. Pharmacol. 60, 1069–1074. https://doi.org/10.1016/S0006-2952(00)00417-2

Petkovic, M., Oses-Prieto, J., Burlingame, A., Jan, L.Y., Jan, Y.N., 2020. TMEM16K is an interorganelle regulator of endosomal sorting. Nat. Commun. 11, 3298. https://doi.org/10.1038/s41467-020-17016-8

Pettersen, E.F., Goddard, T.D., Huang, C.C., Couch, G.S., Greenblatt, D.M., Meng, E.C., Ferrin, T.E., 2004. UCSF Chimera--a visualization system for exploratory research and analysis. J. Comput. Chem. 25, 1605–1612. https://doi.org/10.1002/jcc.20084

Podoplelova, N.A., Sveshnikova, A.N., Kotova, Y.N., Eckly, A., Receveur, N., Nechipurenko, D.Y., Obydennyi, S.I., Kireev, I.I., Gachet, C., Ataullakhanov, F.I., Mangin, P.H., Panteleev, M.A., 2016. Coagulation factors bound to procoagulant platelets concentrate in cap structures to promote clotting. Blood 128, 1745–1755. https://doi.org/10.1182/blood-2016-02-696898

Pomorski, T., Menon, A.K., 2006. Lipid flippases and their biological functions. Cell. Mol. Life Sci. CMLS 63, 2908–2921. https://doi.org/10.1007/s00018-006-6167-7

Preston Richard A., Jy Wenche, Jimenez Joaquin J., Mauro Lucia M., Horstman Lawrence L., Valle Madelyn, Aime Gerard, Ahn Yeon S., 2003. Effects of Severe Hypertension on Endothelial and Platelet Microparticles. Hypertension 41, 211–217. https://doi.org/10.1161/01.HYP.0000049760.15764.2D

Prodan, C.I., Dale, G.L., 2008. Coated-Platelets in Ischemic Stroke – Potential Insight into the Etiology of Stroke Subtypes. Int. J. Stroke 3, 249–250. https://doi.org/10.1111/j.1747-4949.2008.00223.x

Prodan, C.I., Vincent, A.S., Dale, G.L., 2011. Coated-platelet levels are elevated in patients with transient ischemic attack. Transl. Res. J. Lab. Clin. Med. 158, 71–75. https://doi.org/10.1016/j.trsl.2011.02.010

Quek, L.S., Bolen, J., Watson, S.P., 1998. A role for Bruton's tyrosine kinase (Btk) in platelet activation by collagen. Curr. Biol. CB 8, 1137–1140. https://doi.org/10.1016/s0960-9822(98)70471-3

Ramstrom, S., O'Neill, S., Dunne, E., Kenny, D., 2010. Annexin V binding to platelets is agonist, time and temperature dependent. Platelets 21, 289–296. https://doi.org/10.3109/09537101003660564

Remenyi, G., Szasz, R., Friese, P., Dale, G.L., 2005. Role of mitochondrial permeability transition pore in coated-platelet formation. Arterioscler. Thromb. Vasc. Biol. 25, 467–471. https://doi.org/10.1161/01.ATV.0000152726.49229.bf

Ren, J.-X., Li, L.-L., Zheng, R.-L., Xie, H.-Z., Cao, Z.-X., Feng, S., Pan, Y.-L., Chen, X., Wei, Y.-Q., Yang, S.-Y., 2011. Discovery of novel Pim-1 kinase inhibitors by a hierarchical multistage virtual screening approach based on SVM model, pharmacophore, and molecular docking. J. Chem. Inf. Model. 51, 1364–1375. https://doi.org/10.1021/ci100464b

Rush, T.S., Grant, J.A., Mosyak, L., Nicholls, A., 2005. A shape-based 3-D scaffold hopping method and its application to a bacterial protein-protein interaction. J. Med. Chem. 48, 1489–1495. https://doi.org/10.1021/jm040163o

Sabatier, F., Darmon, P., Hugel, B., Combes, V., Sanmarco, M., Velut, J.-G., Arnoux, D., Charpiot, P., Freyssinet, J.-M., Oliver, C., Sampol, J., Dignat-George, F., 2002. Type 1 And Type 2 Diabetic Patients Display Different Patterns of Cellular Microparticles. Diabetes 51, 2840–2845. https://doi.org/10.2337/diabetes.51.9.2840

Savage, J.S., Williams, C.M., Konopatskaya, O., Hers, I., Harper, M.T., Poole, A.W., 2013. Munc13-4 is critical for thrombosis through regulating release of ADP from platelets. J. Thromb. Haemost. JTH 11, 771–775. https://doi.org/10.1111/jth.12138

Schaff, M., Tang, C., Maurer, E., Bourdon, C., Receveur, N., Eckly, A., Hechler, B., Arnold, C., de Arcangelis, A., Nieswandt, B., Denis, C.V., Lefebvre, O., Georges-Labouesse, E., Gachet, C., Lanza, F., Mangin, P.H., 2013. Integrin α6β1 is the main receptor for vascular laminins and plays a role in platelet adhesion, activation, and arterial thrombosis. Circulation 128, 541–552. https://doi.org/10.1161/CIRCULATIONAHA.112.000799

Schick, P.K., Kurica, K.B., Chacko, G.K., 1976. Location of phosphatidylethanolamine and phosphatidylserine in the human platelet plasma membrane. J. Clin. Invest. 57, 1221–1226. https://doi.org/10.1172/JCI108390

Schmitz, G., Schambeck, C.M., 2006. Molecular defects in the ABCA1 pathway affect platelet function. Pathophysiol. Haemost. Thromb. 35, 166–174. https://doi.org/10.1159/000093563

Schoenwaelder, S.M., Yuan, Y., Josefsson, E.C., White, M.J., Yao, Y., Mason, K.D., O'Reilly, L.A., Henley, K.J., Ono, A., Hsiao, S., Willcox, A., Roberts, A.W., Huang, D.C.S., Salem, H.H., Kile, B.T., Jackson, S.P., 2009. Two distinct pathways regulate platelet phosphatidylserine exposure and procoagulant function. Blood 114, 663–666. https://doi.org/10.1182/blood-2009-01-200345

Schreuder, M., Reitsma, P.H., Bos, M.H.A., 2019. Blood coagulation factor Va's key interactive residues and regions for prothrombinase assembly and prothrombin binding. J. Thromb. Haemost. JTH 17, 1229–1239. https://doi.org/10.1111/jth.14487

Schwarz, U.R., Walter, U., Eigenthaler, M., 2001. Taming platelets with cyclic nucleotides. Biochem. Pharmacol. 62, 1153–1161. https://doi.org/10.1016/s0006-2952(01)00760-2

Scudieri, P., Caci, E., Venturini, A., Sondo, E., Pianigiani, G., Marchetti, C., Ravazzolo, R., Pagani, F., Galietta, L.J.V., 2015. Ion channel and lipid scramblase activity associated with expression of TMEM16F/ANO6 isoforms. J. Physiol. 593, 3829–3848. https://doi.org/10.1113/JP270691

Shi, J., Shi, Y., Waehrens, L.N., Rasmussen, J.T., Heegaard, C.W., Gilbert, G.E., 2006. Lactadherin detects early phosphatidylserine exposure on immortalized leukemia cells undergoing programmed cell death. Cytom. Part J. Int. Soc. Anal. Cytol. 69, 1193–1201. https://doi.org/10.1002/cyto.a.20345

Shimizu, T., Iehara, T., Sato, K., Fujii, T., Sakai, H., Okada, Y., 2013. TMEM16F is a component of a Ca^{2+}-activated Cl- channel but not a volume-sensitive outwardly rectifying Cl- channel. Am. J. Physiol. Cell Physiol. 304, C748-759. https://doi.org/10.1152/ajpcell.00228.2012

Siess, W., Lapetina, E.G., 1989. Platelet aggregation induced by alpha 2-adrenoceptor and protein kinase C activation. A novel synergism. Biochem. J. 263, 377–385.

Sims, P.J., Wiedmer, T., Esmon, C.T., Weiss, H.J., Shattil, S.J., 1989. Assembly of the platelet prothrombinase complex is linked to vesiculation of the platelet plasma membrane. Studies in Scott syndrome: an isolated defect in platelet procoagulant activity. J. Biol. Chem. 264, 17049–17057.

Solari, F.A., Mattheij, N.J.A., Burkhart, J.M., Swieringa, F., Collins, P.W., Cosemans, J.M.E.M., Sickmann, A., Heemskerk, J.W.M., Zahedi, R.P., 2016. Combined Quantification

of the Global Proteome, Phosphoproteome, and Proteolytic Cleavage to Characterize Altered Platelet Functions in the Human Scott Syndrome. Mol. Cell. Proteomics 15, 3154–3169. https://doi.org/10.1074/mcp.M116.060368

Soulard, C., Salsac, C., Mouzat, K., Hilaire, C., Roussel, J., Mezghrani, A., Lumbroso, S., Raoul, C., Scamps, F., 2020. Spinal Motoneuron TMEM16F Acts at C-boutons to Modulate Motor Resistance and Contributes to ALS Pathogenesis. Cell Rep. 30, 2581-2593.e7. https://doi.org/10.1016/j.celrep.2020.02.001

Stefanini, L., Bergmeier, W., 2019. Small GTPases in megakaryocyte and platelet biology. Platelets 30, 7–8. https://doi.org/10.1080/09537104.2018.1560938

Stefanini, L., Bergmeier, W., 2016. RAP1-GTPase signaling and platelet function. J. Mol. Med. Berl. Ger. 94, 13–19. https://doi.org/10.1007/s00109-015-1346-3

Steinhubl, S.R., Moliterno, D.J., 2005. The role of the platelet in the pathogenesis of atherothrombosis. Am. J. Cardiovasc. Drugs Drugs Devices Interv. 5, 399–408. https://doi.org/10.2165/00129784-200505060-00007

Stierand, K., Rarey, M., 2007. From modeling to medicinal chemistry: automatic generation of two-dimensional complex diagrams. ChemMedChem 2, 853–860. https://doi.org/10.1002/cmdc.200700010

Stuart, M.C.A., Reutelingsperger, C.P.M., Frederik, P.M., 1998. Binding of annexin V to bilayers with various phospholipid compositions using glass beads in a flow cytometer. Cytometry 33, 414–419. https://doi.org/10.1002/(SICI)1097-0320(19981201)33:4<414::AID-CYTO4>3.0.CO;2-H

Supuran, C.T., 2012. Structure-based drug discovery of carbonic anhydrase inhibitors. J. Enzyme Inhib. Med. Chem. 27, 759–772. https://doi.org/10.3109/14756366.2012.672983

Suzuki, J., Fujii, T., Imao, T., Ishihara, K., Kuba, H., Nagata, S., 2013. Calcium-dependent phospholipid scramblase activity of TMEM16 protein family members. J. Biol. Chem. 288, 13305–13316. https://doi.org/10.1074/jbc.M113.457937

Suzuki, J., Imanishi, E., Nagata, S., 2014. Exposure of phosphatidylserine by Xk-related protein family members during apoptosis. J. Biol. Chem. 289, 30257–30267. https://doi.org/10.1074/jbc.M114.583419

Suzuki, J., Umeda, M., Sims, P.J., Nagata, S., 2010. Calcium-dependent phospholipid scrambling by TMEM16F. Nature 468, 834–838. https://doi.org/10.1038/nature09583

Suzuki, T., Suzuki, J., Nagata, S., 2014. Functional Swapping between Transmembrane Proteins TMEM16A and TMEM16F. J. Biol. Chem. 289, 7438–7447. https://doi.org/10.1074/jbc.M113.542324

Suzuki-Inoue, K., Inoue, O., Frampton, J., Watson, S.P., 2003. Murine GPVI stimulates weak integrin activation in PLCgamma2-/- platelets: involvement of PLCgamma1 and PI3-kinase. Blood 102, 1367–1373. https://doi.org/10.1182/blood-2003-01-0029

Swieringa, F., Kuijpers, M.J.E., Heemskerk, J.W.M., van der Meijden, P.E.J., 2014. Targeting platelet receptor function in thrombus formation: The risk of bleeding. Blood Rev. 28, 9–21. https://doi.org/10.1016/j.blre.2013.12.001

Tang, X., Halleck, M.S., Schlegel, R.A., Williamson, P., 1996. A subfamily of P-type ATPases with aminophospholipid transporting activity. Science 272, 1495–1497. https://doi.org/10.1126/science.272.5267.1495

Toti, F., Satta, N., Fressinaud, E., Meyer, D., Freyssinet, J.M., 1996. Scott syndrome, characterized by impaired transmembrane migration of procoagulant phosphatidylserine and hemorrhagic complications, is an inherited disorder. Blood 87, 1409–1415.

Trott, O., Olson, A.J., 2010. AutoDock Vina: improving the speed and accuracy of docking with a new scoring function, efficient optimization and multithreading. J. Comput. Chem. 31, 455–461. https://doi.org/10.1002/jcc.21334

Tsuji, T., Cheng, J., Tatematsu, T., Ebata, A., Kamikawa, H., Fujita, A., Gyobu, S., Segawa, K., Arai, H., Taguchi, T., Nagata, S., Fujimoto, T., 2019. Predominant localization of phosphatidylserine at the cytoplasmic leaflet of the ER, and its TMEM16K-dependent redistribution. Proc. Natl. Acad. Sci. U. S. A. 116, 13368–13373. https://doi.org/10.1073/pnas.1822025116

Tucker, K.L., Sage, T., Stevens, J.M., Jordan, P.A., Jones, S., Barrett, N.E., St-Arnaud, R., Frampton, J., Dedhar, S., Gibbins, J.M., 2008. A dual role for integrin-linked kinase in platelets: regulating integrin function and alpha-granule secretion. Blood 112, 4523–4531. https://doi.org/10.1182/blood-2008-03-148502

Valaydon, Z.S., Lee, P., Dale, G.L., Januszewski, A.S., Rowley, K.G., Nandurkar, H., Karschimkus, C., Best, J.D., Lyons, T.J., Jenkins, A.J., 2009. Increased coated-platelet levels in chronic haemodialysis patients. Nephrol. Carlton Vic 14, 148–154. https://doi.org/10.1111/j.1440-1797.2008.01026.x

van der Meijden, P.E.J., Heemskerk, J.W.M., 2019. Platelet biology and functions: new concepts and clinical perspectives. Nat. Rev. Cardiol. 16, 166–179. https://doi.org/10.1038/s41569-018-0110-0

van Kruchten, R., Mattheij, N.J.A., Saunders, C., Feijge, M.A.H., Swieringa, F., Wolfs, J.L.N., Collins, P.W., Heemskerk, J.W.M., Bevers, E.M., 2013. Both TMEM16F-dependent and TMEM16F-independent pathways contribute to phosphatidylserine exposure in platelet apoptosis and platelet activation. Blood 121, 1850–1857. https://doi.org/10.1182/blood-2012-09-454314

van Montfort, R.L.M., Workman, P., 2017. Structure-based drug design: aiming for a perfect fit. Essays Biochem. 61, 431–437. https://doi.org/10.1042/EBC20170052

Vane, J.R., Anggård, E.E., Botting, R.M., 1990. Regulatory functions of the vascular endothelium. N. Engl. J. Med. 323, 27–36. https://doi.org/10.1056/NEJM199007053230106

Varga-Szabo David, Pleines Irina, Nieswandt Bernhard, 2008. Cell Adhesion Mechanisms in Platelets. Arterioscler. Thromb. Vasc. Biol. 28, 403–412. https://doi.org/10.1161/ATVBAHA.107.150474

Veber, D.F., Johnson, S.R., Cheng, H.-Y., Smith, B.R., Ward, K.W., Kopple, K.D., 2002. Molecular properties that influence the oral bioavailability of drug candidates. J. Med. Chem. 45, 2615–2623. https://doi.org/10.1021/jm020017n

Versteeg, H.H., Heemskerk, J.W.M., Levi, M., Reitsma, P.H., 2013. New Fundamentals in Hemostasis. Physiol. Rev. 93, 327–358. https://doi.org/10.1152/physrev.00016.2011

Wang, G.R., Zhu, Y., Halushka, P.V., Lincoln, T.M., Mendelsohn, M.E., 1998. Mechanism of platelet inhibition by nitric oxide: in vivo phosphorylation of thromboxane receptor by cyclic GMP-dependent protein kinase. Proc. Natl. Acad. Sci. U. S. A. 95, 4888–4893. https://doi.org/10.1073/pnas.95.9.4888

Watanabe, R., Sakuragi, T., Noji, H., Nagata, S., 2018. Single-molecule analysis of phospholipid scrambling by TMEM16F. Proc. Natl. Acad. Sci. 115, 3066–3071. https://doi.org/10.1073/pnas.1717956115

Watson, S.P., Auger, J.M., McCARTY, O.J.T., Pearce, A.C., 2005. GPVI and integrin αIIbβ3 signaling in platelets. J. Thromb. Haemost. 3, 1752–1762. https://doi.org/10.1111/j.1538-7836.2005.01429.x

Wei, H., Malcor, J.-D.M., Harper, M.T., 2018. Lipid rafts are essential for release of phosphatidylserine-exposing extracellular vesicles from platelets. Sci. Rep. 8, 9987. https://doi.org/10.1038/s41598-018-28363-4

Weiss, H.J., Lages, B., 1997. Family Studies in Scott Syndrome. Blood 90, 475–476.

Weiss, H.J., Turitto, V.T., Baumgartner, H.R., 1986. Role of shear rate and platelets in promoting fibrin formation on rabbit subendothelium. Studies utilizing patients with quantitative and qualitative platelet defects. J. Clin. Invest. 78, 1072–1082.

Weiss, H.J., Vicic, W.J., Lages, B.A., Rogers, J., 1979. Isolated deficiency of platelet procoagulant activity. Am. J. Med. 67, 206–213. https://doi.org/10.1016/0002-9343(79)90392-9

Wesseling, M.C., Wagner-Britz, L., Nguyen, D.B., Asanidze, S., Mutua, J., Mohamed, N., Hanf, B., Ghashghaeinia, M., Kaestner, L., Bernhardt, I., 2016. Novel Insights in the Regulation of Phosphatidylserine Exposure in Human Red Blood Cells. Cell. Physiol. Biochem. Int. J. Exp. Cell. Physiol. Biochem. Pharmacol. 39, 1941–1954. https://doi.org/10.1159/000447891

White, M.J., Schoenwaelder, S.M., Josefsson, E.C., Jarman, K.E., Henley, K.J., James, C., Debrincat, M.A., Jackson, S.P., Huang, D.C.S., Kile, B.T., 2012. Caspase-9 mediates the apoptotic death of megakaryocytes and platelets, but is dispensable for their generation and function. Blood 119, 4283–4290. https://doi.org/10.1182/blood-2011-11-394858

WHO, n.d. Cardiovascular diseases (CVDs) [WWW Document]. URL https://www.who.int/news-room/fact-sheets/detail/cardiovascular-diseases-(cvds) (accessed 12.10.19).

Wlodawer, A., Vondrasek, J., 1998. Inhibitors of HIV-1 protease: a major success of structure-assisted drug design. Annu. Rev. Biophys. Biomol. Struct. 27, 249–284. https://doi.org/10.1146/annurev.biophys.27.1.249

Wu, N., Cernysiov, V., Davidson, D., Song, H., Tang, J., Luo, S., Lu, Y., Qian, J., Gyurova, I.E., Waggoner, S.N., Trinh, V.Q.-H., Cayrol, R., Sugiura, A., McBride, H.M., Daudelin, J.-F., Labrecque, N., Veillette, A., 2020. Critical Role of Lipid Scramblase TMEM16F in Phosphatidylserine Exposure and Repair of Plasma Membrane after Pore Formation. Cell Rep. 30, 1129-1140.e5. https://doi.org/10.1016/j.celrep.2019.12.066

Yang, H., Kim, A., David, T., Palmer, D., Jin, T., Tien, J., Huang, F., Cheng, T., Coughlin, S.R., Jan, Y.N., Jan, L.Y., 2012. TMEM16F forms a Ca^{2+}-activated cation channel required for lipid scrambling in platelets during blood coagulation. Cell 151, 111–122. https://doi.org/10.1016/j.cell.2012.07.036

Yang, Y.D., Cho, H., Koo, J.Y., Tak, M.H., Cho, Y., Shim, W.-S., Park, S.P., Lee, J., Lee, B., Kim, B.-M., Raouf, R., Shin, Y.K., Oh, U., 2008. TMEM16A confers receptor-activated calcium-dependent chloride conductance. Nature 455, 1210–1215. https://doi.org/10.1038/nature07313

Ye, W., Han, T.W., He, M., Jan, Y.N., Jan, L.Y., 2019. Dynamic change of electrostatic field in TMEM16F permeation pathway shifts its ion selectivity. eLife 8, e45187. https://doi.org/10.7554/eLife.45187

Younan, P., Iampietro, M., Santos, R.I., Ramanathan, P., Popov, V.L., Bukreyev, A., 2018. Role of Transmembrane Protein 16F in the Incorporation of Phosphatidylserine Into Budding Ebola Virus Virions. J. Infect. Dis. 218, S335–S345. https://doi.org/10.1093/infdis/jiy485

Yu, K., Whitlock, J.M., Lee, K., Ortlund, E.A., Cui, Y.Y., Hartzell, H.C., 2015. Identification of a lipid scrambling domain in ANO6/TMEM16F. eLife 4, e06901. https://doi.org/10.7554/eLife.06901

Zarubica, A., Trompier, D., Chimini, G., 2007. ABCA1, from pathology to membrane function. Pflugers Arch. 453, 569–579. https://doi.org/10.1007/s00424-006-0108-z

Zhang, Y., Le, T., Grabau, R., Mohseni, Z., Kim, H., Natale, D.R., Feng, L., Pan, H., Yang, H., 2020. TMEM16F phospholipid scramblase mediates trophoblast fusion and placental development. Sci. Adv. 6, eaba0310. https://doi.org/10.1126/sciadv.aba0310

Zhao, J., Gao, Q.-Y., 2019. TMEM16F inhibition limits pain-associated behavior and improves motor function by promoting microglia M2 polarization in mice. Biochem. Biophys. Res. Commun. 517, 603–610. https://doi.org/10.1016/j.bbrc.2019.07.070

Zhou, Q., Sims, P.J., Wiedmer, T., 1998. Expression of Proteins Controlling Transbilayer Movement of Plasma Membrane Phospholipids in the B Lymphocytes From a Patient With Scott Syndrome. Blood 92, 1707–1712.

Zhou, Q., Zhao, J., Stout, J.G., Luhm, R.A., Wiedmer, T., Sims, P.J., 1997. Molecular cloning of human plasma membrane phospholipid scramblase. A protein mediating transbilayer movement of plasma membrane phospholipids. J. Biol. Chem. 272, 18240–18244. https://doi.org/10.1074/jbc.272.29.18240

Zhou, Q., Zhao, J., Wiedmer, T., Sims, P.J., 2002. Normal hemostasis but defective hematopoietic response to growth factors in mice deficient in phospholipid scramblase 1. Blood 99, 4030–4038. https://doi.org/10.1182/blood-2001-12-0271

Zwaal, R.F., Comfurius, P., Bevers, E.M., 1998. Lipid-protein interactions in blood coagulation. Biochim. Biophys. Acta 1376, 433–453. https://doi.org/10.1016/s0304-4157(98)00018-5

Appendix

Automated analysis of docking poses

Written by Tom Millington

```
import re, os, sys, random, datetime, numpy, copy

from math import pow, sqrt


MAX_RADIUS = 11.0


class Position:

    def __init__(self, x = 0.0, y = 0.0, z = 0.0):

        self.x = x

        self.y = y

        self.z = z


    def set_pos(self, x, y, z):

        self.x = x

        self.y = y

        self.z = z


    def copy_pos(self, pos):

        self.set_pos(pos.x, pos.y, pos.z)


    def equals(self, pos):

        return (self.x == pos.x) and (self.y ==
pos.y) and (self.z == pos.z)


    def add_pos(self, pos):

        self.set_pos(self.x + pos.x, self.y + pos.y,
self.z + pos.z)


    def div_by_const(self, const):

        self.set_pos(self.x / const, self.y / const,
self.z / const)


    def distance(self, pos):

        return sqrt(pow(self.x - pos.x, 2) +
pow(self.y - pos.y, 2) +

                    pow(self.z - pos.z, 2))

    # Apply a transformation matrix to a
coordinate and return a new Position

    # object

    def apply_matrix(self, matrix):

        v = numpy.array([self.x, self.y, self.z, 1.0])

        result = matrix.dot(v)

        assert(result[3] == 1.0)

        return Position(result[0], result[1],
result[2])


    # Apply a transformation matrix to a
coordinate and modify the object

    def transform(self, matrix):

        new_pos = self.apply_matrix(matrix)

        self.copy_pos(new_pos)


class Atom:

    def __init__(self, x, y, z):

        self.pos = Position(x, y, z)


class Pose:

    def __init__(self, filename, run, rank,
energy):

        self.name = os.path.basename(filename)

        self.atoms = []

        self.run = run

        self.rank = rank

        self.energy = energy

        file = open(filename, 'r')

        lines = file.readlines()

        file.close()
```

```
        # Parse the PDB file and extract the atom positions
        for line in lines:
            if line.startswith("REMARK"):
                continue
            if line.startswith("HEADER"):
                continue
            if line.startswith("TER"):
                break
            if line.startswith("END"):
                break
            if (line.startswith("ATOM")):

self.atoms.append(Atom(float(line[31:39]), float(line[39:47]),
                                   float(line[47:55])))
                continue
            if (line.startswith("HETATM")):

self.atoms.append(Atom(float(line[31:39]), float(line[39:47]),
                                   float(line[47:55])))
                continue
            assert(0)


        # Calculate the centre of the pose by averaging the positions of the
        # atoms
        self.recalc_centre()


    def recalc_centre(self):
        self.centre = Position(0.0, 0.0, 0.0)
        for atom in self.atoms:
            self.centre.add_pos(atom.pos)
        self.centre.div_by_const(len(self.atoms))

    # Apply a transformation matrix to every atom in the pose and recalculate
    # the centre.
    def transform(self, matrix):
        for atom in self.atoms:
            atom.pos.transform(matrix)
        self.recalc_centre()


    # Transform a pose by a matrix and its inverse, then take the average of the
    # two resultant poses
    def transform_by_avg(self, matrix, inv_matrix):
        for atom in self.atoms:
            pos1 = atom.pos.apply_matrix(matrix)
            pos2 = atom.pos.apply_matrix(inv_matrix)
            pos1.add_pos(pos2)
            pos1.div_by_const(2)
            atom.pos.copy_pos(pos1)
        self.recalc_centre()


    # Find the maximum distance between any two atoms in the pose
    def max_dimension(self):
        max_dist = 0
        for atom1 in self.atoms:
            for atom2 in self.atoms:
                dist = atom1.pos.distance(atom2.pos)
                if dist > max_dist:
                    max_dist = dist
        return max_dist


class Cluster:
```

```
    def __init__(self, pose=None):
        self.shadow_poses = []
        self.centre = Position(0.0, 0.0, 0.0)
        self.std_dev = 0.0
        if pose is not None:
            self.poses = [pose]
            self.centre.copy_pos(pose.centre)
            self.avg_energy = pose.energy
            self.avg_rank = pose.rank
        else:
            self.poses = []
            self.avg_energy = 0.0
            self.avg_rank = 0.0


    # Remove all poses and move them to the
shadow array for reference
    def move_poses_to_shadow(self):
        self.shadow_poses = self.poses[:]
        self.poses = []


    def add_pose(self, pose):
        self.poses.append(pose)
        # Return true if the pose was not in this
cluster in the last round
        return pose not in self.shadow_poses


    def distance_from_centre(self, pos):
        dist = pow(self.centre.x - pos.x, 2) +
pow(self.centre.y - pos.y, 2) + \
                pow(self.centre.z - pos.z, 2)
        return sqrt(dist)


    # Find maximum distance of any atom in a
given pose from the centre of the
    # cluster
    def pose_max_distance(self, pose):
        max_dist = 0
        for atom in pose.atoms:
            dist =
self.distance_from_centre(atom.pos)
            if dist > max_dist:
                max_dist = dist
        return max_dist


    def recalc_centre(self):
        self.centre.set_pos(0.0, 0.0, 0.0)
        self.avg_energy = 0.0
        self.avg_rank = 0.0
        for pose in self.poses:
            self.centre.add_pos(pose.centre)
            self.avg_energy += pose.energy
            self.avg_rank += pose.rank
        self.centre.div_by_const(len(self.poses))
        self.avg_energy /= len(self.poses)
        self.avg_rank /= len(self.poses)


        sum_sqrs = 0.0
        for pose in self.poses:
            sum_sqrs +=
pow(self.distance_from_centre(pose.centre),
2)
        sum_sqrs /= len(self.poses)
        self.std_dev = sqrt(sum_sqrs)


    # Find the maximum distance of any atom in
the cluster from the centre of
    # the cluster
    def max_distance(self):
        max_dist = 0
        for pose in self.poses:
            dist = self.pose_max_distance(pose)
            if dist > max_dist:
```

```
            max_dist = dist
        return max_dist


    # Find the maximum distance between any
two atoms in the cluster
    def max_dimension(self):
        max_dist = 0
        for pose1 in self.poses:
            for atom1 in pose1.atoms:
                for pose2 in self.poses:
                    for atom2 in pose2.atoms:
                        dist =
atom1.pos.distance(atom2.pos)
                        if dist > max_dist:
                            max_dist = dist
        return max_dist


    # Take an equivalent cluster in the opposite
chain, transform each pose and
    # add it to the current cluster
    def absorb(self, cluster2, matrix):
        for pose in cluster2.poses:
            pose.transform(matrix)
            self.add_pose(pose)
        self.recalc_centre()


    # Transform a cluster by a matrix and
inverse matrix then take the average
    # of the two results
    def transform_by_avg(self, matrix,
inv_matrix):
        for pose in self.poses:
            pose.transform_by_avg(matrix,
inv_matrix)
        self.recalc_centre()
```

```
class Compound:
    def __init__(self, name):
        self.name = name
        self.poses = []
        self.clustering = []
    def add_pose(self, filename, run, rank,
energy):
        self.poses.append(Pose(filename, run,
rank, energy))


# Take two clusters in opposite chains,
transform one of them, then calculate
# the maximum distance of any atom from the
combined centre
def max_dist_for_clusters(cluster1, cluster2,
matrix):
    # Calculate the centre of the new cluster
    new_centre = Position()
    for pose in cluster1.poses:
        new_centre.add_pos(pose.centre)
    for pose in cluster2.poses:

new_centre.add_pos(pose.centre.apply_matrix
(matrix))

new_centre.div_by_const(len(cluster1.poses)
+ len(cluster2.poses))


    max_dist = 0
    for pose in cluster1.poses:
        for atom in pose.atoms:
            dist = new_centre.distance(atom.pos)
            if dist > max_dist:
                max_dist = dist
    for pose in cluster2.poses:
        for atom in pose.atoms:
```

```
            dist =
new_centre.distance(atom.pos.apply_matrix(m
atrix))
            if dist > max_dist:
                max_dist = dist
    return max_dist


cmA = Position()
cmB = Position()


def is_in_chainA(pos):
    return (pos.distance(cmA) <=
pos.distance(cmB))


def main():
    if len(sys.argv) != 2:
        print("Pass directory name as command
line argument")
        sys.exit()
    dirname = sys.argv[1]
    filenames = os.listdir(dirname)
    compound_names = []
    compounds = []
    matrix = None
    inv_matrix = None


    outputfile = open(dirname +
"clustering_results.csv", "w")


    #Read matrix
    for filename in filenames:
        dummy, file_extension =
os.path.splitext(filename)
        if file_extension != ".txt":
            continue
        file = open(dirname + filename, 'r')
        lines = file.readlines()
        file.close()
        parse_matrix = False
        match = False
        i = 0
        elements = [[0.0,0.0,0.0,0.0],
[0.0,0.0,0.0,0.0], [0.0,0.0,0.0,0.0],
                [0.0,0.0,0.0,0.0]]
        for line in lines:
            if parse_matrix and i <= 3:
                str_elements = line.split(",")
                for j in range(0,4):
                    elements[i][j] =
float(str_elements[j])
                i += 1
            if line == "Transformation (TTT)
matrix\n":
                parse_matrix = True
                match = True
            if line.startswith("Centre of mass A:"):
                pos = line.replace("Centre of mass
A:","").split(",")
                cmA.set_pos(float(pos[0]),
float(pos[1]), float(pos[2]))
            if line.startswith("Centre of mass B:"):
                pos = line.replace("Centre of mass
B:","").split(",")
                cmB.set_pos(float(pos[0]),
float(pos[1]), float(pos[2]))


        if match:
            matrix = numpy.array(elements)
            inv_matrix = numpy.linalg.inv(matrix)
            break


    # Read each pose and assign to a
compound base on the filename
```

```
    for filename in filenames:
        dummy, file_extension =
os.path.splitext(filename)
        if file_extension != ".pdb":
            print("skipping", filename)
            continue
        # Filename must be
[run_number]_[protein_name]_optimised_[com
pound_name]_[rank]_[energy].pdb
        regex = re.compile("([0-9]+)_([0-9A-Za-
z]+)_optimised_([a-zA-Z0-9_]+)_([0-9]+)_-([0-
9\.]+).pdb")
        regex_result = regex.match(filename)
        if regex_result is None:
            print("Filename", filename, "does not
match pattern")
        assert(regex_result is not None)
        run = int(regex_result.group(1))
        compound_name = regex_result.group(3)
        rank = int(regex_result.group(4))
        energy = float(regex_result.group(5))

        if compound_name in compound_names:
            for comp in compounds:
                if comp.name == compound_name:
                    comp.add_pose(dirname +
filename, run, rank, energy)
        else:

compound_names.append(compound_name)
            new_comp =
Compound(compound_name)
            new_comp.add_pose(dirname +
filename, run, rank, energy)
            compounds.append(new_comp)


    for compound in compounds:
        best_clustering = None
        best_k = 0xffffffff
        for iters in range(0, 1000):
            # Display progress
            if iters % 100 == 0:
                print(str(datetime.datetime.now()) +
":", compound.name,
                      "iteration", iters)
            k = 1
            clusters = []
            while True:
                # Assign initial cluster values, they
must not share the same
                # position
                clusters = []
                pose_pool = compound.poses[:]
                while len(clusters) < k:
                    seed = random.choice(pose_pool)
                    clusters.append(Cluster(seed))
                    for pose in pose_pool:
                        if
pose.centre.equals(seed.centre):
                            pose_pool.remove(pose)


                # Iterate through K-means until there
is no change
                change = True
                while change:
                    change = False
                    for cluster in clusters:

cluster.move_poses_to_shadow()
                    for pose in compound.poses:
                        best_cluster = None
                        best_distance = 0xffffffff
                        for cluster in clusters:
```

```
                    distance = cluster.distance_from_centre(pose.centre)
                    if distance < best_distance:
                        best_distance = distance
                        best_cluster = cluster
                change |= best_cluster.add_pose(pose)
            for cluster in clusters:
                if len(cluster.poses) == 0:
                    clusters.remove(cluster)
                    continue
                cluster.recalc_centre()


        # Check all clusters are less than 10 in radius
        clusters_in_limit = True
        for cluster in clusters:
            if cluster.max_distance() > MAX_RADIUS:
                if len(cluster.poses) == 1:
                    print("ALERT: Pose %s does not fit in a cluster of 1. Pose width is %f, cluster radius %f" \
                          %(cluster.poses[0].name, cluster.poses[0].max_dimension(), cluster.max_distance()))
                    sys.exit(1)
                clusters_in_limit = False
        if clusters_in_limit:
            break
        k += 1
    #} while True


    new_clustering = copy.deepcopy(clusters)


    # Merge equivalent clusters
    for cluster1 in new_clustering:
        if not is_in_chainA(cluster1.centre):
            continue
        for cluster2 in new_clustering:
            if is_in_chainA(cluster2.centre):
                continue
            dist1 = max_dist_for_clusters(cluster1, cluster2, matrix)
            dist2 = max_dist_for_clusters(cluster1, cluster2, inv_matrix)
            if (dist1 < MAX_RADIUS) and (dist1 <= dist2):
                cluster1.absorb(cluster2, matrix)

assert(is_in_chainA(cluster1.centre))

new_clustering.remove(cluster2)
            elif (dist2 < MAX_RADIUS) and (dist2 < dist1):
                cluster1.absorb(cluster2, inv_matrix)

assert(is_in_chainA(cluster1.centre))

new_clustering.remove(cluster2)


    #Move all unpaired clusters in chain B into chain A
    for cluster in new_clustering:
        if is_in_chainA(cluster.centre):
            continue
        new_cluster = copy.deepcopy(cluster)

new_cluster.transform_by_avg(matrix, inv_matrix)
        if not is_in_chainA(new_cluster.centre):
            continue
```

```
            cluster.transform_by_avg(matrix,
inv_matrix)


            # If this clustering has fewer cluster
than the previous best then
            # this becomes the new best clustering
            if len(new_clustering) < best_k:
                best_k = len(new_clustering)
                best_clustering = new_clustering


        #} for iters in range(0, 1000)
        compound.clustering = best_clustering
    #} for compound in compounds


    # Print out info to the terminal and output
csv data to log file
    for compound in compounds:
      nice_name =
compound.name.replace("_"," ").capitalize()


outputfile.write(str(i)+","+str(len(cluster.poses))
+","+str(cluster.std_dev)+","+str(rank_0_poses
)+","+str(cluster.avg_energy)+","+str(cluster.ce
ntre.x)+","+str(cluster.centre.y)+","+str(cluster.
centre.z)+"\n")
          i += 1
      print("")
      outputfile.write("\n")


print("\n\n\n|{0:>22}|{1:>12}|{2:>12}|{3:>14}|{4:
>16}|{5:>13}|{6:>15}|{7:>13}|{8:>20}|{9:>8}|{10:
>8}|{11:>8}|{12:>40}|".format( \
        "Compound", "Num clusters", "Num R0 in
C0", "Avg rank in C0", "Avg energy of C0",
"Std dev of C0", "Num poses in C0", \
        "Max dim in C0", "Avg max dim of poses",
"C0 X", "C0 Y", "C0 Z", "Closest R0 pose"))


print("|"+'='*22+"|"+'='*12+"|"+'='*12+"|"+'='*14+
      print("Analysed", nice_name, "found",
len(compound.clustering), "clusters:")
      outputfile.write(nice_name+"\n")
      i = 0
      outputfile.write("Cluster index, Num poses,
Cluster std dev, Rank 0 poses, Average
energy, Centre x, Centre y, Centre z\n")
      for cluster in compound.clustering:
          rank_0_poses = 0
          for pose in cluster.poses:
              if pose.rank == 0:
                  rank_0_poses += 1
          print("  Cluster", i, "has",
len(cluster.poses), "poses and",
cluster.std_dev, "std dev and", rank_0_poses,
"rank 0 poses and avg energy",
cluster.avg_energy, "centred on",
cluster.centre.x, ", ", cluster.centre.y, ", ",
cluster.centre.z)


"|"+'='*16+"|"+'='*13+'|'+'='*15+'|'+'='*13+'|'+'='*
20+'|'+'='*8+"|"+'='*8+"|"+'='*8+"|"+'='*40+"|")
    outputfile.write("\nCompound,Num
clusters,Num R0 in C0,Avg rank in C0,Avg
energy of C0,Std dev of C0,Num poses in
C0,"+ \
                "Max dim in C0,Avg max dim of
poses,C0 X,C0 Y,C0 Z,Closest R0 pose\n")
    for compound in compounds:
        best_poses = 0
        avg_size = 0
        for pose in compound.poses:
            avg_size += pose.max_dimension()
        avg_size /= len(compound.poses)
        for cluster in compound.clustering:
            if len(cluster.poses) > best_poses:
                best_poses = len(cluster.poses)
        for cluster in compound.clustering:
```

```
            if len(cluster.poses) == best_poses:
                r0_poses = 0
                min_dist = MAX_RADIUS
                closest_pose = None
                for pose in cluster.poses:

                    if pose.rank == 0:
                        if
cluster.distance_from_centre(pose.centre) <
min_dist:
                            min_dist =
cluster.distance_from_centre(pose.centre)
                            closest_pose = pose
                        r0_poses += 1
                if closest_pose is not None:
                    best_pose_name =
closest_pose.name
                else:
                    best_pose_name = "(None)"

print("|{0:>22}|{1:>12}|{2:>12}|{3:>14.4}|{4:>16.
4}|{5:>13.4}|{6:>15}|{7:>13.4}|{8:>20.4}|{9:>8.5
}|{10:>8.5}|{11:>8.5}|{12:>40}|".format( \
                    compound.name,
len(compound.clustering), r0_poses,
cluster.avg_rank, cluster.avg_energy,
cluster.std_dev, len(cluster.poses), \
                    cluster.max_dimension(),
avg_size, cluster.centre.x, cluster.centre.y,
cluster.centre.z, best_pose_name))

outputfile.write(compound.name.replace("_","
").capitalize()+","+str(len(compound.clustering)
)+","+str(r0_poses)+","+str(cluster.avg_rank)+"
,"+str(cluster.avg_energy)+","+str(cluster.std_d
ev)+","+str(len(cluster.poses))+","+\

str(cluster.max_dimension())+","+str(avg_size)
+","+str(cluster.centre.x)+","+str(cluster.centre.
y)+","+str(cluster.centre.z)+","+best_pose_na
me+"\n")
    outputfile.close()



# Separate entry point to apply a matrix to a
single pose file
def transform_pose(pose_file, matrix_file):
    dummy, file_extension =
os.path.splitext(pose_file)
    pose = Pose(pose_file, 0, 0, 1)
    pose2 = copy.deepcopy(pose)
    pose3 = copy.deepcopy(pose)


    dummy, file_extension =
os.path.splitext(matrix_file)
    if file_extension != ".txt":
        print("not a txt file:", filename)
        sys.exit()
    file = open(matrix_file, 'r')
    lines = file.readlines()
    file.close()
    matrix = None
    inv_matrix = None
    parse_matrix = False
    match = False
    i = 0
    elements = [[0.0,0.0,0.0,0.0],
[0.0,0.0,0.0,0.0], [0.0,0.0,0.0,0.0],
                [0.0,0.0,0.0,0.0]]
    for line in lines:
        if parse_matrix and i <= 3:
            str_elements = line.split(",")
            for j in range(0,4):
                elements[i][j] = float(str_elements[j])
            i += 1
        if line == "Transformation (TTT) matrix\n":
            parse_matrix = True
```

```
            match = True
        if line.startswith("Centre of mass A:"):
            pos = line.replace("Centre of mass
A:","").split(",")
            cmA.set_pos(float(pos[0]),
float(pos[1]), float(pos[2]))
        if line.startswith("Centre of mass B:"):
            pos = line.replace("Centre of mass
B:","").split(",")
            cmB.set_pos(float(pos[0]),
float(pos[1]), float(pos[2]))


    if match:
        matrix = numpy.array(elements)
        inv_matrix = numpy.linalg.inv(matrix)


    print("pose centroid is %.4f %.4f %.4f\n"
%(pose.centre.x,
                                    pose.centre.y,
                                    pose.centre.z))
    pose2.transform(matrix)
    print("transformed centroid is %.4f %.4f
%.4f\n" %(pose2.centre.x,

pose2.centre.y,

pose2.centre.z))
    pose3.transform(inv_matrix)
    print("inverse transformed centroid is %.4f
%.4f %.4f\n" %(pose3.centre.x,

pose3.centre.y,

pose3.centre.z))



if __name__ == "__main__":
    main()
```